Granite petrogenesis and crustal evolution studies in the Damara Pan-African orogenic belt, Namibia

Thesis

Granite petrogenesis and crustal evolution studies in the Damara Pan-African orogenic belt, Namibia

A thesis submitted for the degree of Ph. D.

by

Patrick Francis Mc Dermott

November 1986

Dept. of Earth Sciences

The Open University

ON INSTRUCTION

FROM

THE UNIVERSITY THE

PUBLISHED PAPERS

HAVE NOT BEEN

SCANNED

EX12

HIGHER DEGREES OFFICE

LIBRARY AUTHORISATION FORM

STUDENT: Mr. P.F. McDermott SERIAL NO: HDM 66462.

DEGREE: PhD.

TITLE OF THESIS: Granite Petrogenesis & Crustal Evolution Studies in the Damara - Pan-African Orogenic Belt Namibia.

I confirm that I am willing that my thesis be made available to readers and maybe photocopied, subject to the discretion of the Librarian.

SIGNED: Frank M Dermott DATE: 21/8/87

ABSTRACT

Major and trace element data for Damara granitoids distinguish three geochemically distinct granitoid groups, - crustal-melt granitoids, calc-alkaline granitoids and within-plate granitoids. The overwhelming majority of the Damara granitoids are peraluminous crustal-melt leucogranites which have elevated $^{87}Sr/^{86}Sr$ ratios (> 0.710) and old model Nd ages (~ 2.0 Ga).

Calc-alkaline diorites are metaluminous and have the lowest $^{87}Sr/^{86}Sr$ ratios (0.704 - 0.707) and model Nd ages (DM) in the range 1.1 - 1.7 Ga. Within-plate granitoids are characterised by elevated high-field strength (HFS) abundances and have model Nd ages (DM) in the range 1.1 - 1.6 Ga.

All Damara granitoids have model Nd ages (DM) older than about 1.0 Ga suggesting that intracrustal reworking was the dominant process and crustal growth was negligible.

Damara granitoids define a hyperbola on an ε Sr vs. ε Nd diagram but cannot be modelled as simple binary mixtures between old continental crust and depleted mantle end-members. An episodic intracrustal remobilisation model is proposed to explain the hyperbola defined by granitoid data on an ε Sr vs. ε Nd diagram.

Within the 10 km thick Damara metasedimentary pile $^{87}Sr/^{86}Sr$ ratios increase systematically with depth. This trend is accompanied by a decrease in $^{143}Nd/^{144}Nd$ ratios. Model Nd ages (CHUR) for the stratigraphically oldest Damara metasediments (Nosib Group) are about 2.0 Ga whereas the younger metasediments (Kuiseb Formation and Nama Group) have model Nd ages (CHUR) about 1.0 Ga reflecting sediment input from younger source terrains. The ratio of model ages ($T^{Nd}_{CHUR}/T^{Sr}_{BE}$) is used as an index of intracrustal reworking since it provides a measure of Rb/Sr fractionation (increases) relative to Sm/Nd fractionation. The older Damara metasediments (Nosib Group) have the highest model age ratios suggesting that their source terrains have suffered the largest amount of intracrustal reworking. However, the rate of intracrustal reworking was greatest in source terrains sampled by the younger Damara metasediments (Kuiseb Formation and Nama Group). This suggests that the rate of intracrustal reworking increased through time in the interval (2.0 - 1.0 Ga) in this segment of continental crust.

CONTENTS

Chapter 1 Introduction

Chapter 2 Palmental area field study

Chapter 3 Granitoid petrography and field relations

Chapter 4 Granitoid geochemistry

Chapter 5 Isotope geochemistry

Chapter 6 Summary and Conclusions

LIST OF FIGURES

LIST OF TABLES

Appendix A

LIST OF PLATES

Chapter 2

Chapter 3

Acknowledgements

This project would not have been possible without the help of several people. Firstly, I wish to thank my supervisors Drs. Chris Hawkesworth and Nigel Harris for guidance and encouragement throughout the project. I am particularly grateful for their speedy return of chapters while the thesis was been written. I am also indebted to Dr G.D. Sevastopulo of Trinity College Dublin for getting me interested in geological research and to Dr. C.J. Hawkesworth for suggesting this project and for the opportunity to do research at the Open University.

The help and considerable logistical support of Dr. R. Mc G. Miller and the staff of the Geological Survey in Windhoek are gratefully acknowledged. Drs. Wolf Hegenberger, Roy Miller and Rolf Brandt of the Geological survey in Windhoek are thanked for several field excursions and for introducing me to Damaran geology. Peter Van Calsteren, Chris Hawkesworth, Nigel Harris and John Barber are thanked for companionship in the field and for cheerfully surviving the rigours of Namibian fieldwork. Mr. Heinz Berens and his wife on farm Palmental are thanked for their hospitality and for rescuing my jeep from the sand when it refused to start!

Peter Van Calsteren and Andrew Gledhill are thanked for their help in the radiogenic isotope lab and Andrew Gledhill provided some metasediment Sr and Nd isotope data. Zenon Palacz helped get me started in the lead isotope lab and Dave Mattey is thanked for his help with the oxygen isotope analyses. Andy Tindle is thanked for instruction in the use of the microprobe. John Watson is thanked for running the X.R.F. analyses and Drs. Brian Atkin and Peter Harvey of Nottingham University provided wavelength dispersive X.R.F. Nick Rogers is thanked for help with neutron activation analyses. John Taylor patiently provided cartographic advise. Ian Chaplin is thanked for preparing thin-sections. This project also benefited from discussions with other research students and staff at the O.U. - Nick Rogers, Gareth Davies, Seifa Berhe, Bram Murton, Kirsten Fraser, Zenon Palacz and Andy Tindle are especially thanked.

I wish to gratefully acknowledge my parents for their encouragement, patience and interest throughout this project. Finally, I thank Deirdre for her encouragement and for patiently preparing the reference list and for helping with the editing.

CHAPTER 1

Introduction

1.1 Significance of orogenic events

Orogenesis has long been recognised as a critical process in the evolution of the earth's continental crust. Tectonic and thermal activity during orogenesis reshapes and rejuvenates portions of the continental crust. In the geological record, orogenic events are recognised and deciphered by detailed investigations of their tectonic, metamorphic and magmatic products. Magmatism associated with orogenesis may result in a nett transfer of material from the mantle to the continental crust, thereby contributing to crustal growth (e.g. Allegre and Ben Othmann, 1980).

In addition to the well documented geomorphological rejuvenation (e.g. Holmes,1964), orogenesis produces more subtle effects which result in a geochemical rejuvenation of the continental crust. Several studies (e.g. Chappell and White,1974 ; Allegre and Ben Othman,1980 ; Fourcadre and Allegre, 1981 ; Pearce *et al*, 1984) have focussed on granitoid geochemistry to assess how trace elements are redistributed during, and subsequent to, orogenic events.

1.2 Why study the Damara orogen ?

The Pan-African Damara orogen of central Namibia (Fig. 1.1) is a well exposed, deeply eroded orogenic belt which provides an excellent opportunity to study the temporal relationship between deformation, regional metamorphism and magmatism during a late Precambrian orogenic event.

The Damara orogen has been the subject of a co-ordinated programme of geological research over the past decade. This research has provided a sound geological and geochronological framework within which more detailed geochemical studies may be carried out. The voluminous syn- to post-tectonic granitoids which out-crop in the central portions of

the orogen (Fig. 1.3) display a broad compositional range which facilitates granitoid petrogenetic studies.

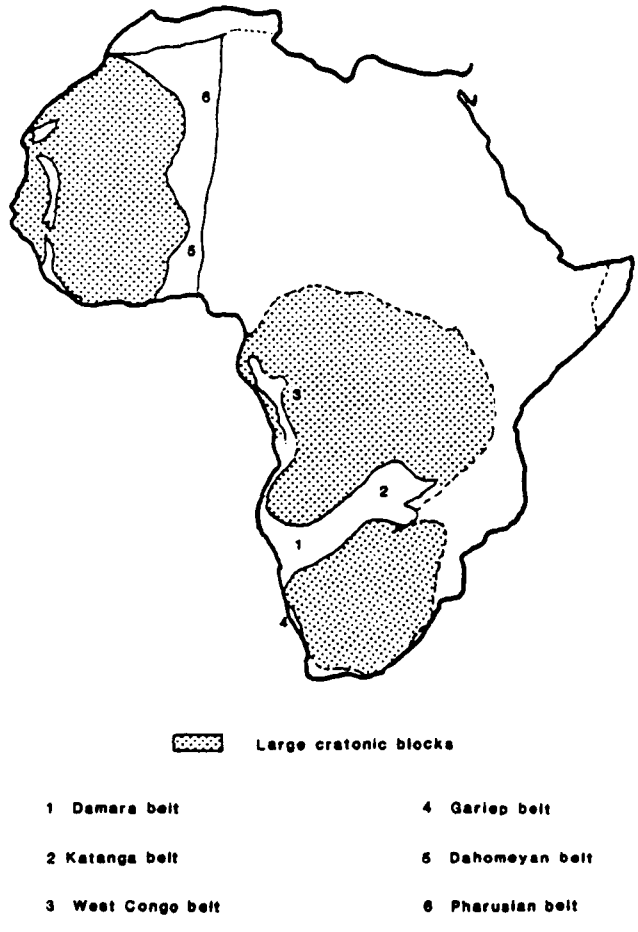

Fig. 1.1 Map showing the Pan-African mobile belts referred to in text.

The selection of individual granitoid intrusions for detailed geochemical investigations was aided by previous geochronological studies (e.g. Kroner *et al.*,1978 ; Blaxland *et al.*,1979 ; Haack *et al.*,1980 ; Kroner,1982 ; Marlow,1981 ; Hawkesworth *et al.*,1981 ; Downing,1982 ; Hawkesworth *et al.*,1983 ; Hawkesworth and Marlow,1983).

Detailed geological maps are available for large portions of the orogen (e.g. Smith,1965 ; Martin,1965 ; Nash,1971 ; Jacob,1974 ; Downing,1982) as well as a geological map for the entire country at a scale of 1:1,000,000 (Geological Survey of South West Africa/Namibia,1980). In addition, a geological map of the orogen at a scale of 1:500,000 has been published (Special Publication No.11 of the Geological Society of South Africa, 1983).

The Damara orogen provides an opportunity to investigate granitoid geochemistry in the context of orogenic evolution. The Damara orogen also preserves a

sequence of relatively undisturbed molasse-type sediments (Mulden Group and the Fish-River Subgroup of the Nama Group) which are suitable for Nd isotopic investigations. These studies are used to evaluate the effect of the Damara orogeny on the evolution of a relatively large crustal segment sampled by these sediments.

1.3 Objectives of this study

This study was undertaken to improve our understanding of how the Damara orogen evolved and to explore the implications for the Pan-African "event". An improved understanding of how the late Precambrian-early Palaeozoic Damara belt evolved provides an insight to the style of large scale tectonics at this transitional stage of earth history. The study also investigates the effect of orogenesis on the redistribution of trace elements within the crust and assesses the implications for granitoid petrogenetic and crustal evolution models. A number of priorities were identified ;

1. To constrain the sources of the voluminous granitoids which outcrop in central Namibia (Fig.1.3)
2. To evaluate the significance of diorites in central Namibia which were thought to be subduction related (Miller,1983)
3. To investigate the redistribution of trace elements during crustal anatexis and to assess the implications for granitoid petrogenesis
4. To investigate variations in Nd and Sr isotopes within the Damara metasedimentary pile and associated molasse sediments in order to assess the effect of a single orogeny on crustal evolution
5. To extend previous geothermometry studies (e.g. Puhan and Hoffer, 1983) in order to further constrain the thermal evolution of the orogen
6. To propose a geotectonic model for the evolution of the Damara orogen which can explain the observed relationship between metamorphism and deformation as well as temporal variations in granitoid geochemistry.

1.4 Geological framework

The Damara orogen consists of two tectonothermal branches which appear to border older cratons (Fig.1.1). The north-south trending coastal branch parallels the present South-Atlantic coastline in north-east Namibia before attaining a south-westerly strike and disappearing offshore as the better exposed north-east trending intracontinental branch is approached.

Pre-drift reconstructions of Africa and South-America indicate that the Damara coastal branch is part of the Ribeiro orogen of Brazil. Thus, the Ribeiro orogen delimits the western margin of the Damara coastal branch (Porada,1977)

The 400km wide intracontinental branch is well exposed for some 500km northwestwards from the coast before any significant younger cover rocks are encountered, thus providing a well exposed cross-section through a deeply eroded orogenic belt. Extensions of the coastal and intracontinental branches of the orogen remain speculative although geophysical evidence (Reeves,1978), suggests that the Damara structural trends extend into northern Botswana and south-western Zambia.

The Gariep belt which forms an arcuate shaped re-entrant south of Luteritz in southern Namibia is believed to be the southern extension of the coastal branch of the Damara orogen (Fig 1.1). Miller (1983) speculates that the West Congo and possibly the Dahomeyan and Pharusian belts (Fig.1.1) represent northerly extensions of the Damara coastal branch. On a regional scale the coastal and intracontinental branches of the Damara orogen form part of a larger network of late Precambrian - early Palaeozoic mobile belts for which Kennedy (1964) coined the term "Pan-African".

The Damara orogen has been divided into a number of zones on the basis of stratigraphy, structure, metamorphic grade, plutonic rocks, geochronology and geophysical expression (Fig. 1.2 ; Miller,1983).

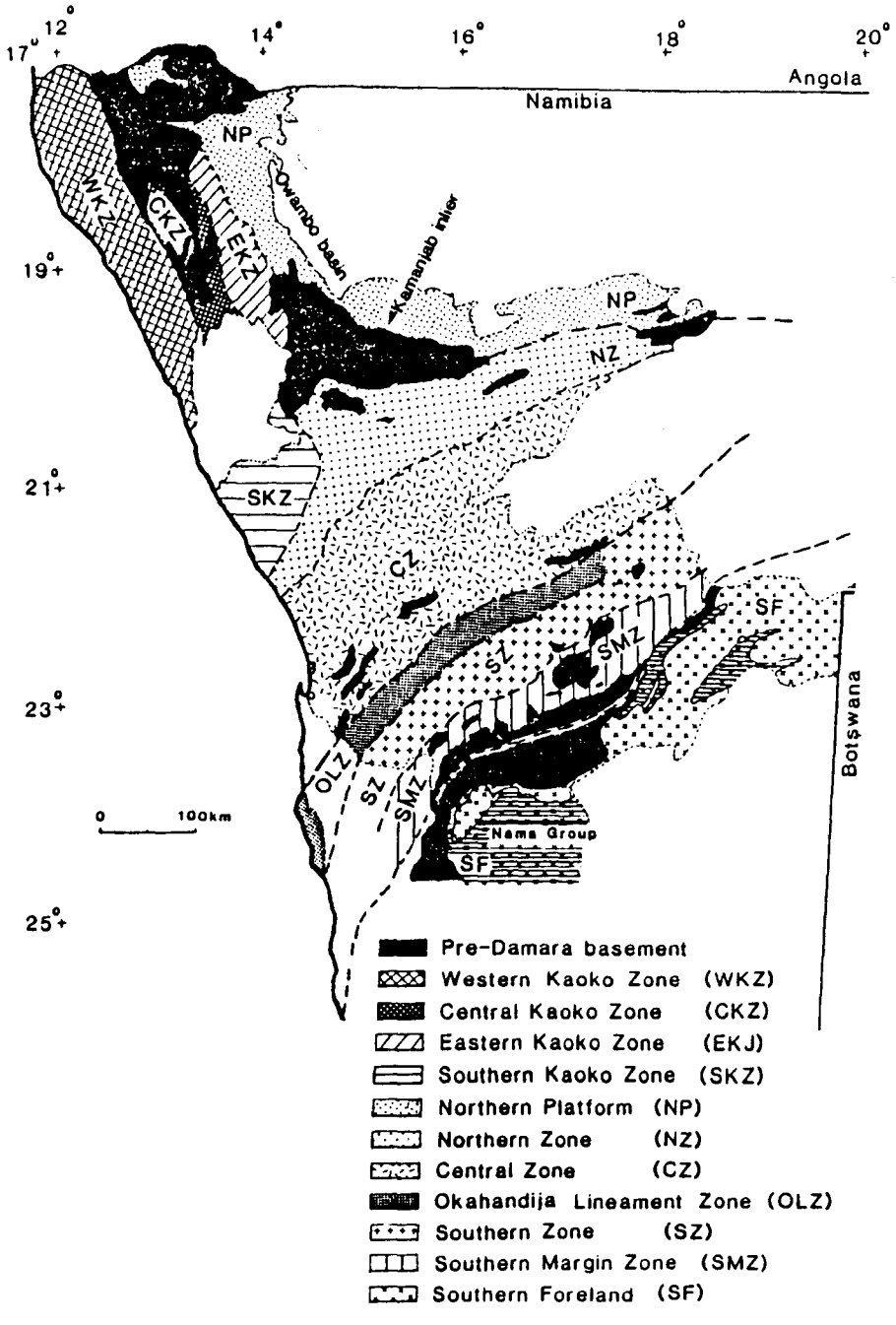

Fig. 1.2 Map of the Damara orogen showing the main structural zones referred to in text (after Miller, 1983). In text, the term coastal branch is used to refer collectively to the Kaoko belt zones shown in N.W. Namibia.

1.4.1 Stratigraphy

The Nosib Group rocks form the basal portions of the Damara succession and were deposited unconformably on the Pre-Damara basement in three major graben systems (Martin and Porada,1977). The dominant lithology is pinkish, coarse to medium grained feldspathic quartzite. In the Central Zone (Fig.1.2) the Nosib Group may be subdivided into a basal quartzitic succession (Etusis Formation) which is overlain by feldspathic quartzites, schists and minor carbonates (Khan Formation). In the Northern Zone (Fig.1.2) the Nosib Group includes abundant alkaline volcanics (Naauwpoort volcanics). Evaporites occur extensively in the Nosib Group of the Southern Margin Zone (Fig. 1.2).

The Nosib Group is unconformably overlain by an extensive carbonate sequence with variable amounts of associated clastics (Otavi Group). This succession includes an extensive marker mixtite deposit (Chuos Formation).

The overlying Swakop Group consists of a thick sequence of dolomites, limestones, schists, and calc-silicates (Khan Formation). This predominantly carbonate sequence is overlain by a thick sequence (up to 10Km thick) of biotite schists (Kuiseb Formation).

This succession forms the upper part of the Swakop Group and includes the amphibolites of the Matchless Member (Matchless belt, Fig.1.2). The Kuiseb Formation schists are overlain by the weakly metamorphosed Mulden Group siltstones, greywackes, sandstones and phyllites which form a molasse sequence in northern Namibia. In southern Namibia a slightly younger molasse sequence (Fish-River Subgroup of the Nama Group) consists of red feldspathic sandstones and shales.

Nosib Group deposition occurred between about 1000 - 900 Ma ago (Miler, 1983). The Otavi Group and most of the Swakop Group had been deposited before about 650 Ma ago and the northern molasse (Mulden Group) was deposited between about 650 and 630 Ma ago (Miller, *op. cit.*). Deposition of the Nama Group and southern molasse (Fish River Subgroup) occurred in the period 650 - 540 Ma (Miller, 1983).

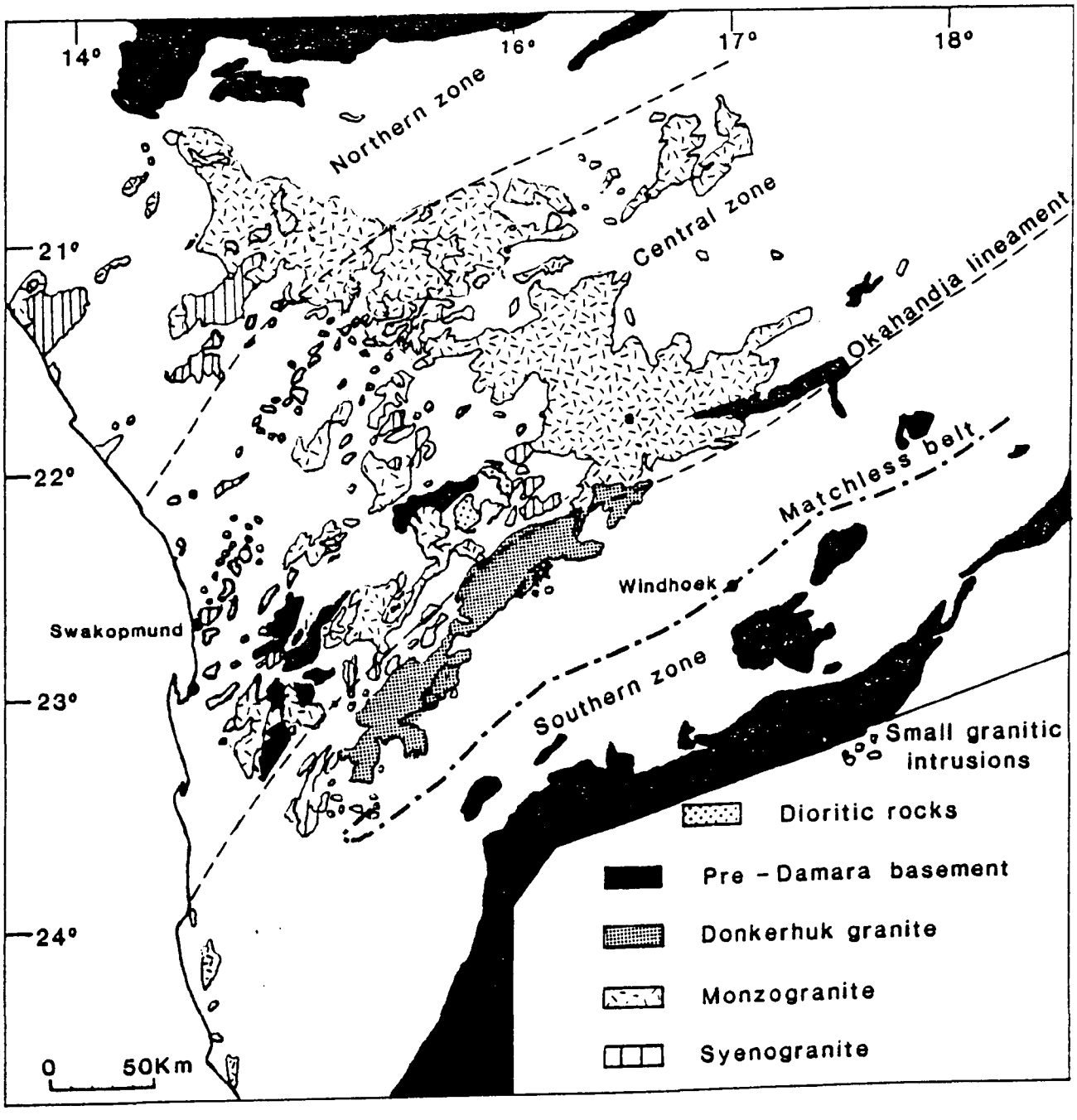

Fig. 1.3 Map of the intracontinental branch of the Damara orogen showing the distribution of Damara granitoids (after Miller 1983). The positions of the Okahandja lineament and the Matchless belt are also shown.

1.4.2 Damara granitoids

Syn- to post- tectonic granitoids outcrop over large areas in the Central Zone of the Damara orogen (Fig.1.2). Granitoids range in composition from diorites to granites (sensu-stricto) and at present exposure levels the aerial proportions of gabbro/diorite : tonalite/granodiorite : granite is 2 : 2 : 96 with monzogranite being the predominant rock type (Miller,1983).

Marlow (1981) proposed a fourfold classification of Damara granitoids into syn- to post-tectonic Salem-type granitoids and red granites, and late- to post-tectonic leucogranites and alaskites (Ch. 3). The term Salem granite is a "sack" name frequently used to describe biotite rich porphyritic granitoids which include granodiorites, granites and adamellites. The typical Salem granite from the type example in the Swakop river on Farm Salem 102 contains large K-feldspar phenocrysts in a biotite-rich but muscovite-free matrix. Detailed petrographic descriptions of the granitoids as well as their field relationships are given in Ch. 3.

Damara granitoids range in age from 650 Ma to 460 Ma (Downing and Coward, 1981; Kroner, 1982 ; Hawkesworth *et al.*, 1983). Magmatic activity prior to about 650 Ma was confined to alkaline volcanism and intrusion of relatively minor syenite intrusions (e.g. Oas syenite and Lofdal nepheline syenite which yield ages of 840 $\pm$12 and 764 $\pm$ 60 Ma respectively, Kroner, 1982 ; Hawkesworth *et al.*,1983).

Most of the voluminous Salem-type granitoids were intruded in the period 600-550 Ma. This suite of Salem-type granitoids is post-tectonic in the Northern Zone (Fig. 1.2), (Miller, 1983). Damara diorites of the Central Zone have been deformed by the main deformation event in the intracontinental branch of the orogen (e.g. the Palmental diorite, Ch 2). Most red granites and leucogranites (e.g. the post-tectonic Donkerhuk granite, Fig.1.3) were intruded from 550 to 460 Ma ago. The youngest intrusions emplaced between 490 and 460 Ma ago are confined to the Central Zone (Fig.1.2). Many of these post-490 Ma granitoids are highly potassic alaskite intrusions, some of which are associated with economic uranium mineralisation (Berning *et al.*, 1976).

Although a wealth of isotopic data had been obtained (e.g. Clifford, 1967 ; Blaxland *et al.*, 1979 ; Haack *et al.*, 1980 ; Hawkesworth *et al.*, 1981 ; Marlow, 1981; Downing, 1982 ; Kroner, 1982 ; Hawkesworth *et al.*, 1983 ; Hawkesworth and Marlow, 1983) relatively little was known about the trace element geochemistry of the Damara granitoids prior to this study.

Miller (1983) compiled the available major element data for the Damara granitoids and showed that the majority of the intrusions are peraluminous and have a composition intermediate between typical calc-alkaline batholiths and intraplate granitoids. Miller (*op. cit.*) pointed out that the Otjimbingwe Complex and the Dachsberg granite (Fig. 1.3) are alkaline while syn-tectonic diorites at Palmental (Fig. 1.3) are calc-alkaline.

Hawkesworth *et al.*, (1983) alluded to the intraplate character of many Damara granitoids which display the lowest initial $^{87}Sr/^{86}Sr$ ratios and pointed out that some Damara granitoids are enriched in Nb, Ce and the LREE compared to typical calc-alkaline granitoids. Detailed descriptions of Damara granitoid geochemistry and classification are given in Ch. 4.

1.4.3 Damara P/T variations

Two distinct prograde patterns have been recognised in the intracontinental branch of the Damara orogen (e.g. Jacob, 1974 ; Puhan, 1976 ; Haack and Hoffer, 1976 ; Puhan, 1983 ; Kasch, 1983 ; Hartmann *et al.*, 1983). South of the Okahandja lineament, (Fig. 1.3) reactions in pelitic rocks indicate a typical Barrovian progression (Fig. 1.4). Metamorphic grade increases in a north-westerly direction through biotite, garnet, staurolite and kyanite isograds. The Okahandja lineament is a large monocline-like downfold of the Damara succession from the Central Zone to the Okahandja lineament zone (Fig. 1.2 ; Miller, 1979).

As the Okahandja lineament is approached from the south-east kyanite is replaced by andalusite. The andalusite isograd (Fig. 1.4) is located within the thermal aureole of the Donkerhuk granite (Fig. 1.3) which was intruded just after the peak of metamorphism in this area (Blaxland *et al.*, 1979). There is textural evidence that andalusite formation was a

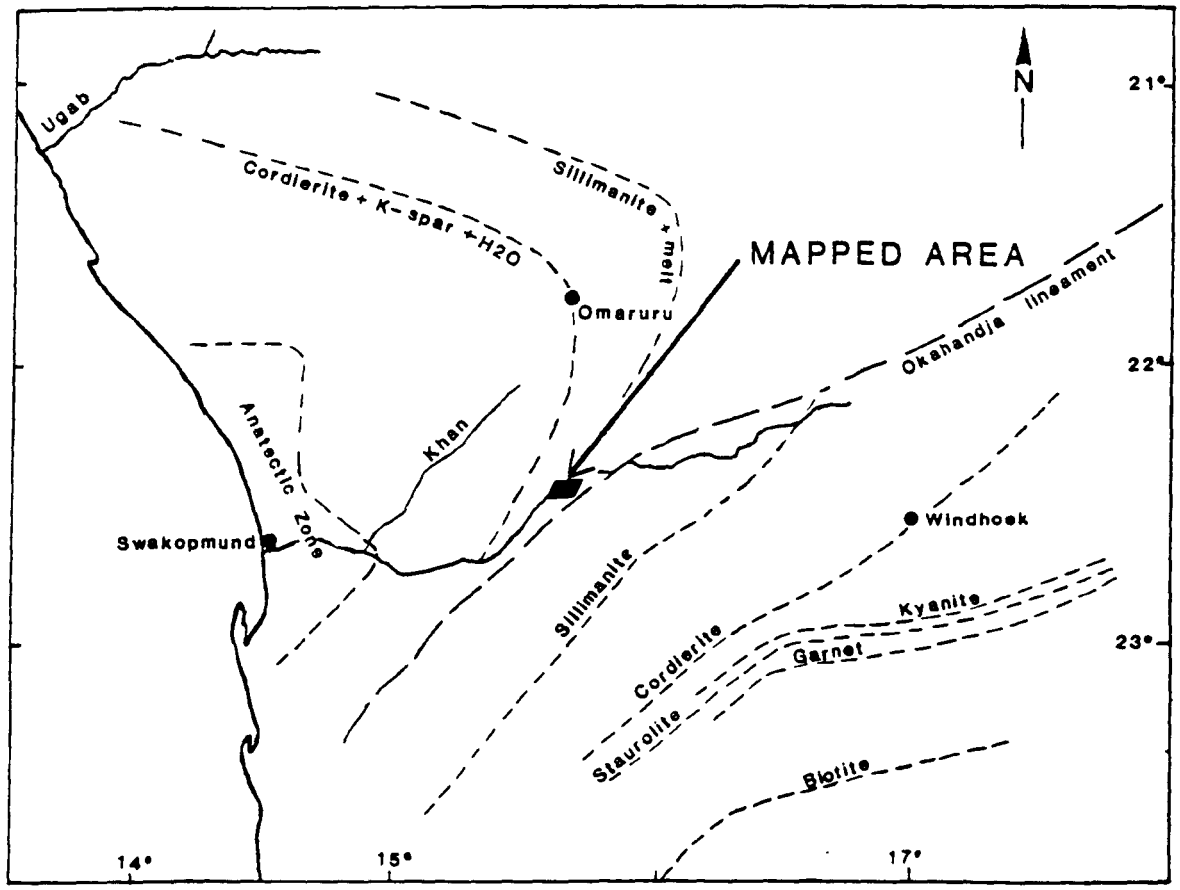

Fig. 1.4 Map of the Damara orogen showing the main reaction isograds in metapelites (after Kasch, 1983). South of the Okahandja lineament a Barrovian type sequence occurs whereas the region north of the lineament is characterised by high-T, low-P conditions. The location of the area mapped around Palmental (Chapter 2) is also shown.

consequence of regional metamorphism as well as Donkerhuk granite contact metamorphism (Hartmann *et al.*, 1983). Close to the Okahandja lineament sillimanite is found on the periphery of andalusite porphyroblasts, indicating the reaction andalusite = sillimanite. The sillimanite isograd south of the lineament shown in Fig. 1.4 represents sillimanite formation as a result of staurolite breakdown according to the reaction staurolite + muscovite + quartz = sillimanite +

biotite + H_2O (Hartmann *et al.*, *op. cit.*).

Northwest of the Okahandja lineament in the Central Zone (Fig.1.2), isograds in pelitic rocks indicate distinctly lower pressure and higher temperature conditions than to the south-east of the lineament. Andalusite is replaced by sillimanite, and at higher metamorphic grades cordierite appears, reflecting lower pressure conditions than south of the lineament. Anatectic conditions are reached in an area northeast of Swakopmund (Fig.1.4) according to the reaction biotite + K-feldspar + plagioclase = melt + garnet (Hartmann *et al.*, 1983).

P/T estimates using a variety of geothermometers and geobarometers indicate that high temperature metamorphism in the Central Zone occurred at relatively low pressures whereas in southern Namibia high pressure, relatively low temperature conditions prevailed. Pressure estimates for the Southern Magin Zone are in the range 7-10 Kb whereas those from the Central Zone are about 2.5-4 Kb. Temperature estimates are in the range 580°– 660 °C for the Central Zone and 340°– 570° C for the Southern Margin Zone (Kasch, 1981,1983 ; Sawyer, 1981 ; Hoernes and Hoffer, 1979).

Microtextural evidence suggests that there were two metamorphic peaks. Index minerals are frequently formed syn- as well as post-kinematically suggesting that two generations of index minerals were formed, implying two distinct metamorphic peaks (e.g. Nash, 1971 ; Kasch, 1983). However the interpretation of these microtextures remain equivocal. Hartmann *et al.* (1983) argue that the apparent presence of two generations of certain index minerals (e.g. cordierite) is a reflection of slow reaction rates (relative to rates of deformation), or the generation of the same index mineral by two different reactions during a single prograde metamorphic event.

1.4.4 Structural history

Three major deformation events have been recognised in the Damara orogen (Guj, 1970 ; Jacob, 1974 ; Halbich, 1977 ; Haack, 1980 ; Downing and Coward, 1981 ; Coward, 1981 ; Coward, 1983). The timing of deformation was strongly diachronous on either side of the Okahandja lineament (Fig 1.3), (Miller, 1983).

Northwest of the Okahandja lineament in the coastal branch of the orogen, D_1 structures are north-south trending, south-east verging recumbent folds. D_2 structures in the coastal branch are large-scale eastward recumbent folds and nappes (Guj, 1970). This was the last major deformation event to affect the coastal branch of the orogen. D_2 deformation in the intracontinental branch north of the Okahandja lineament was broadly coeval with the D_2 event in the coastal branch and produced the main north-east trending penetrative fabric of the intracontinental branch. F_2 structures in the Central Zone are south-west verging sheath-folds (Coward, 1983). Coward (1983) argued that the second major deformation event was produced by oblique convergence across the intracontinental branch of the orogen. D_3 deformation in the Central Zone (Fig.1.2) produced tight upright structures and domes (Downing and Coward, 1981).

Southeast of the Okahandja lineament, structural evolution was later than to the northwest of the lineament. The S_3 foliation northwest of the lineament can be traced into the S_1 foliation southeast of the lineament (Jacob, 1974 ; Blaine, 1977 ; Miller, 1979 ; Sawyer, 1981 ; Downing and Coward, 1981 ; Downing, 1982 ; Miller *et al.*, 1983).

Southeast of the lineament, D_1 produced intense southeast thrusting and nappe formation in the Southern Margin Zone (Fig.1.2). D_2 deformation increased in intensity southwards from the lineament towards the Southern Margin Zone (Fig.1.2). F_2 folds are open in the area to the south of the lineament but are tight and are associated with thrusting in the Southern Margin Zone (Fig. 1.2, Hoffmann, 1983). D_3 deformation produced minor crenulation folding in the Southern Zone, while northeast and east-west trending domes were formed in the Southern Margin Zone.

1.5 Previous models

Published models for the geotectonic evolution of the Damara orogen are outlined in order to place this study in the context of previous work. Models for the evolution of the orogen are of two types - those which involve subduction of oceanic crust and those which envisage orogenic evolution in an entirely intracratonic, ensialic setting. Finally, a more recently published model which combines features of both types (Kasch, 1983 ; Miller, 1983) is outlined.

1.5.1 Ensialic models

Models proposed by Martin and Porada (1977) and Kroner (1980) envisage orogenic evolution in an ensialic setting. Both models invoke an early stage of rifting followed by crustal downwarping and sedimentation. In these models, subsequent compression produces crustal thickening, deformation, metamorphism and crustal anatexis. Martin and Porada (*op. cit.*) suggest that the initial rifting stage was in response to the intrusion of an "asthenolith" beneath the lower crust. This model also requires the intrusion of a second "asthenolith" to produce high temperature metamorphism and crustal anatexis in the Central Zone.

The model of Kroner (1982) is similar to that of Martin and Porada (*op. cit.*). However, in Kroner's model initial rifting is in response to a mantle plume and subsequent delamination of the sub-crustal lithosphere allowed the intrusion of hot asthenospheric material to produce lower crustal melting and intrusion of syn-tectonic granites. According to Kroner's model, compression resulted in crustal underthrusting and "A - type" subduction. In this model, crustal thickening by underthrusting and interstacking produced intense deformation, metamorphism and crustal anatexis.

1.5.2 Ocean - floor subduction models

Models which invoke ocean-floor subduction have been proposed by Blaine, 1977 ; Hartnady, 1978,1979 ; Kasch, 1979,1981 ; Sawyer, 1981 ; Barnes and Sawyer, 1980 and Barnes, 1982. These models differ from ensialic models since they all involve an early rifting stage which leads to continental separation and ocean-floor spreading followed by subduction of oceanic crust. In these models, continental convergence and collision produced crustal thickening and metamorphism and the Matchless amphibolite belt is interpreted as the site of a continent-continent suture.

1.6 Alternative models

None of the previously published models adequately explain all the geological, geochronological and geochemical data. Ensialic models fail to explain the following ;

1. The marked structural asymmetry of the intracontinental branch of the orogen
2. The fact that the Matchless amphibolite (Fig. 1.2) has the geochemical affinities of MORB.
3. The development of high-T, low-P and low-T, high-P terrains in the Central and Southern Zones respectively.

Problems with ocean - floor subduction models include ;

1. The apparent absence of island-arc volcanism or significant volumes of calc - alkaline granitoids which appear to characterise modern-day subduction related magmatism.
2. The lack of complete ophiolite sequences which may mark the site of obducted oceanic crust.
3. Carbonates may be correlated across the width of the intracontinental branch (Martin, 1983). This argues against models which require wide oceans prior to continental convergence and collision.

A more recently published model (Miller, 1983) is presented here as an introductory model. According to this model, a phase of intracontinental rifting between 1000 and 900 Ma marked the beginning of the Damara event (Martin and Porada, 1977). The end of orogenic activity is recorded by biotites which yield Rb/Sr cooling ages of 455 - 420 Ma in the Central Zone (Fig. 1.2) (Haack, 1976 ; Hawkesworth, 1983). Details of orogenic evolution based on Miller's (1983) model are as follows ;

1.6.1 Early rifting and sedimentation

Three elongate northeasterly trending graben systems developed above rising asthenospheric diapirs between 1000 and 900 Ma ago (Martin and Porada, 1977). Crustal thinning led to the merging of the graben systems to form a wide geosyncline in which extensive fluviatile sedimentation occurred (Nosib Group). Extensive alkaline magmatism (Naauwpoort volcanics) occurred in the northern rift over a period of at least 110 Ma (840 - 730 Ma) (Kroner, 1982 ; Miller and Burger, 1983 ; Hawkesworth *et al.*, 1983) whereas the southern rift was characterised by widespread evaporite formation (Behr *et al.*, 1983).

In this model, Nosib igneous activity (c. 840 - 730 Ma) was followed by a general subsidence across the entire geosyncline and extensive carbonate deposition. Subsequent to carbonate deposition the northern and southern grabens deepened and were the sites of turbidite deposition whereas the Central Zone (Fig.1.2) was characterised by rapid facies changes indicative of variable depositional conditions.

In contrast, the Northern Platform (Fig.1.2) was characterised by extremely stable conditions in which about 1700m of carbonates accumulated (Sohnge, 1964).

In this model, the initial phase of relative stability in which carbonates were deposited across the entire geosyncline was followed by a period of crustal instability during which mixtites were deposited (Chuos Formation). Mixtite deposition was followed by a period of relatively stable depositional conditions in which carbonates of the Karibib Formation and Tsumeb Subgroups were deposited. Deep-water fan deposits (Tinkas turbidites) which

interfinger with pelitic schists of the Kuiseb Formation south of the Okahandja lineament (Fig. 1.3) are the only siliceous equivalents of the ubiquituous carbonates deposited at this stage. Variations in stratigraphic thickness across the orogen suggest that the Central Zone (Fig.1.2) remained a relatively shallow-water area, separating deep-water basins until at least the end of Kuiseb Formation deposition (i.e. until about 650 Ma ago ; Miller, 1983).

According to this model, crustal stretching and thinning eventually led to continental separation and the Matchless belt (Fig. 1.3) amphibolites which have mid-ocean ridge chemistry (Finnemore, 1978 ; Miller, 1983) are interpreted as obducted oceanic crust.

1.6.2 Compressional tectonics

In this model, (Miller, *op. cit*) the structural asymmetry across the intracontinental branch of the orogen is a result of north-westward subduction beneath the Congo craton to the north. D_1 deformation produced a well developed bedding parallel S_1 foliation in the coastal branch of the orogen and in the Central Zone of the intracontinental branch (Fig.1.2). D_1 uplift in north-west Namibia resulted in deep erosion of Damara and Pre-Damara rocks (Martin, 1965 ; Frets, 1969 ; Hedberg, 1979) and consequent deposition of the northern molasse sequence (Mulden Group). Calc-silicate assemblages which yield an age of 650 Ma (Kroner, 1982) were produced during D_1 deformation in the Central Zone (Klein, 1980).

Recumbent folds and thrusts in the Central Zone are interpreted as D_2 deformation in this model. The D_2 event occurred at about 600 Ma and was broadly coeval in the coastal and intracontinental branches of the orogen. D_2 deformation in the coastal belt produced large scale eastward recumbent folds and nappes (Guj, 1970). In this model, the D_2 event in both the coastal branch and the Central Zone were produced by one intense south-east directed deformational pulse which was a result of north-westward subduction of the Southern Zone beneath the Congo craton.

Following the emplacement of the 550 Ma granitoids, the D_3 event produced numerous elongate and diapir like domes. D_3 deformation is dated by the Ida-dome alaskite (542 ± 33 Ma) which was intruded during the D_3 doming event (Marlow, 1981, 1983). The

youngest post- D_2, pre- D_3 granite in the Central Zone has an age of 554 ± 33 Ma (Downing and Coward, 1981).

The S_3 fabric of the Central Zone can be traced into the S_1 fabric south of the Okahandja lineament reflecting the later structural evolution of the region south of the lineament (Jacob, 1974 ; Blaine, 1977 ; Miller, 1979 ; Sawyer, 1981 ; Downing and Coward, 1981 ; Downing, 1982 ; Miller *et al.*, 1983). D_1 deformation south of the lineament occurred about 540 Ma ago (i.e. syn-D_3 north of the lineament). However the large Donkerhuk granite (south of the lineament) is clearly post-tectonic and yields an age of 523 ± 8 Ma (Blaxland *et al.*, 1979). Therefore, in this model deformation south of the lineament occurred rapidly within the period 540-520 Ma (Miller, 1983).

D_1 deformation south of the Okahandja lineament produced open to tight folds in the area immediately south of the lineament, culminating in intense thrusting to the south-east in the Southern Margin Zone (Fig.1.2). D_3 deformation produced minor crenulation folding in the Southern Zone and east-west trending domes in the Southern Margin Zone (Miller, *op. cit.*)

1.6.3 Molasse deposition

In this model, D_1 uplift in north-west Namibia resulted in extensive erosion of Damara and pre-Damara rocks (Hedberg,1979). Material derived from this erosion was deposited as a discordant intramontane molasse in the west and as a concordant distal molasse in the east to form the Mulden Group (Miller, *op. cit.*). This c. 650 Ma deposition occurred in an extensive basin covering the Northern Platform (Fig. 1.2).

According to Miller's (*op. cit.*) model the Southern Zone ocean had closed by about 540 Ma ago allowing the transport of feldspar rich detritus from the granitic source terrains of the Central Zone into the Nama basin of southern Namibia. This feldspathic detritus formed the Fish-River Subgroup of the Nama group (Germs, 1983). Deposition of this southern molasse occurred before the deformation of the Southern Foreland (Fig. 1.2) , i.e. before about 534 Ma ago.

1.7 Summary

In summary, none of the published models adequately explain all the geological, geochronological and geochemical data. The main shortcomings of each type of model have been outlined above. Models for the evolution of the Damara orogen must satisfactorily explain the following observations

1. Damara granitoid magmatism resulted in no detectable crustal growth (Chs. 4 and 5) i.e. magmatism resulted in remobilisation of pre-existing crustal material

2. The development of high-pressure (up to 10 Kb) kyanite bearing assemblages in the Southern and Southern Margin Zones (Fig. 1.3)

3. In the western Central Zone crustal melting occurred at relatively shallow depths (pressures of 2.5 - 4 Kb). Crustal melting appears to have occurred at progressively shallower crustal levels with time, culminating in near in-situ anatexis of lower Damara metasediments

5. The apparent delay between the end of sedimentation in the Central Zone (at about 650 Ma ago, Miller, 1983) and high-T, low-P regional metamorphism (about 560 - 530 Ma ago, Miller, *op. cit.*). This is in marked contrast to the contemporaneous sedimentation and high-T, low-P regional metamorphism recently documented for the Hercynian of the Pyrenees for which a rift model has been proposed (Wickham and Oxburgh, 1985).

CHAPTER 2

A study of deformation, metmorphism and magmatism in the Palmental area, Central Namibia.

2.1 Introduction

Field-work was carried out over a total period of about three months, in 1984 and 1985. The area investigated consists of about 30 km^2 and is located some 50 km south of Karibib, close to the Karibib-Anschluss road. The topography consists of low hills, cut by streams which drain into the nearby Swakop river. Vegetation is sparse and consists mainly of bush and a thin cover of dry grass. Apart from the dry stream and river beds which are blanketed by alluvial sand deposits, rock exposure is excellent (Plate 2.1).

Plate 2.1 Part of the Palmental area, looking S.W. along strike of the Tinkas Member metasediments. The strike of the regional foliation is folded around into an approximately E-W direction in the background (see enclosed map)

2.1.1 Previous studies

The area was mapped to a scale of 1 : 125,000 by Smith (1965) as part of a regional mapping study. More recently, several mining companies have prospected in the area for skarn-hosted mineralisation but the results of these investigations remain unpublished.

2.1.2 Objectives

The primary objective was to establish the relationship between granitoid magmatism, metamorphism and deformation and to relate the timing of these events to those documented in regional studies e.g. Jacob, 1974 ; Downing and Coward, 1981 ; Kasch, 1981, 1983 ; Coward, 1981 and Hartmann *et al.* 1983.

Previously published ages for the Palmental diorite of about 750 Ma (Kroner, 1982) appeared to be too old since the early stages of rifting were occurring in the northern part of the orogen at this time (Miller, 1983) . Such an old age for the Palmental diorite would require extreme diachronism of events across the intracratonic belt which was thought to be unlikely since there is no geological evidence for such diachronism at this stage. In addition, the Palmental locality provided an excellent opportunity to establish the field relationships between examples of the three major granitoid types recognised in this study i.e. calc-alkaline diorites, within-plate granitoids and leucogranites. These are represented by the Palmental diorite, Otjimbingwe syenite and Palmental leucogranite respectively. Particular emphasis was placed on unravelling the fabric relationships between granitoids in order to place constraints on the interpretation of geochronological results.

Contact metamorphic effects of the granitoids were investigated and microtextural studies of metamorphic mineral assemblages developed in pelitic rocks were carried out to determine the relative ages of deformation and regional metamorphism.

Finally, garnet-biotite Fe/Mg exchange geothermometers were used to compare temperatures of regional metamorphism recorded in the Palmental area with those estimated by previous workers from elsewhere in the Central Zone.

2.2 Methodology

Geological mapping was carried out on a scale of 1: 14,400 using aerial photographs as base maps (see enclosed map). Emphasis was placed on unravelling the structural history of the area and there was little attempt to map out small-scale lithological variations within the metasediments except insofar as lithological variations and markers (e.g. marble bands) were mapped out to delineate structures.

All foliation data are presented using the convention that a plane dips clockwise when viewed towards the chosen azimuth of strike (e.g. a plane with a strike of 290° which dips at 40° to the north is shown as 290/40 whereas a plane with the same strike which dips at 40° to the south is shown as 110/40). Linear data (e.g. mineral lineations and fold axes) are recorded as dips towards the azimuth of dip when viewed in plan.

Fold style was used to identify folds generated during the same phase of folding, while the criterion of refolding was used to determine the relative ages of folds and associated fabrics. Cleavage/bedding relationships and the asymmetry of parasitic folds were used to elucidate the forms of major overturned folds. Asymmetric parasitic folds were recorded as S or Z folds (anticlockwise and clockwise verging respectively) using the convention that fold shape is recorded when viewed down the plunge of the fold axis.

All stereonets are Schmidt equal-area nets in which data are projected in the lower hemisphere. Foliation data are presented as π-type diagrams in which orthogonal poles to planes are plotted.

2.2.1 Terminology

A deformation phase (D) is defined as an event which produces structures which are related in both time and space. The term foliation (S) is used to describe all mesoscopically recognisable planes and S_0 is used to denote original bedding. The term lineation (l) is used to describe linear structures produced by the intersection of two foliations or by linear mineral alignment. D, S and l designations are numbered with subscripts to denote consecutive deformation phases. Fold phases (F) and their respective fold axes (B) are similarily numbered.

2.3 Major lithological units

The area is dominated by metsediments of the Tinkas Member which is stratigraphically equivalent to the upper portion of the Karibib Formation and most of the Kuiseb Formation (Table 2.1), (S.A.C.S., 1980 ; Hoffman, 1983).

Central zone			
GROUP		Formation	Lithology
SWAKOP	KHOMAS	Kuiseb	Mica-schist / Tinkas member (1000)
		Karibib (500)	Schist / Limestone
		Chuos (600)	Mixtite
	UGAB	Rossing (180)	Dolomite calc-silicate
NOSIB		Khan (50) / Etusis (3000)	Feldspathic quartzite

Table 2.1 Stratigraphy of the Central Zone of the Damara orogen (after South African Comittee for Stratigraphy, 1980 ; Hoffmann, 1983). Maximum thickness in metres of the Formations are shown in parentheses.

The Tinkas Member consists predominantly of pelitic to semi-pelitic schists and calc-silicates with several distinctive marble bands. The entire sequence is less than 1km thick (Downing, 1982). The base of the Tinkas Member is marked by a 50m thick amphibolite horizon (Downing, *op. cit.*) which is occasionally observed in the study area and marks a change from pelitic schists of the Kuiseb Formation to interbedded schists and calc-silicate/marble bands of the Tinkas Member. Individual marble units may be up to 20m thick. No sedimentary structures are preserved in the Tinkas Member of the study area, so that "way-up" criteria are difficult to establish. However, purple semi-pelitic layers of the Tinkas Member occasionally have relatively pelitic tops which contain cordierite porphyroblasts, while these are absent in the more psammitic bases of these units. Quartzite layers up to 3m thick occur locally but the succession is dominated by semi-pelites and calc-silicates with occasional interbedded marbles.

Sawyer (1976, 1981) and Miller (1979) have interpreted the Tinkas Member as a deep-water turbidity deposit. However Downing (1982) pointed out that the presence of interbedded mature quartzite units is inconsistent with such an interpretation. Downing (1982) suggested that the presence of interbedded carbonates and quartzites is indicative of a mixed clastic-carbonate shelf sequence.

The Palmental diorite which contains a strong penetrative foliation is volumetrically the most important intrusive rock in the study area. Xenoliths of pelitic schists and calc-silicates are common in the diorite, and hornblendite clots similar to those interpreted elsewhere as "autoliths" (Tindle, 1982) occur locally. The north-east segment of the area is dominated by the Otjimbinwge syenite which is characterised by large (up to 5 cm long) phenocrysts of K-feldspar. The Otjimbingwe syenite is a zoned pluton with a ~50m wide marginal facies of leucocratic syenite (Otjimbingwe leucocratic syenite). Amphibole-rich enclaves (autoliths ?) occur locally, and the entire syenite suite is cut by late pegmatite and aplite dykes. The strong penetrative fabric in the Otjimbingwe syenite has been mapped into the fabric of the Palmental diorite so that the two fabrics are indistinguishable. The Palmental leucogranite which outcrops in the west of the area post-dates the deformation fabric observed

in the diorite and syenite and therefore is post-tectonic. In contrast to xenoliths in the Palmental diorite which clearly have been partially assimilated, pelitic xenoliths in the Palmental granite have knife-sharp contacts with their host granite.

2.4 Geochronological studies

Rb/Sr whole rock age determinations have been carried out on intrusive rocks from the Palmental area. The results are summarised in Table 2.2 and are discussed in detail in Ch. 5.

Table 2.2 - Summary of Rb/Sr whole-rock ages from the Palmental area.

	Age in Ma	**Initial $^{87}Sr/^{86}Sr$**
Palmental roadside diorite	568 ± 53	0.7070 ± .0003
Swakop river diorite	451 ± 27	0.7089 ± .0001
Otjimbingwe syenite	403 ± 14	0.7086 ± .0002
Leucocratic Otj. syenite	510 ± 32	0.7067 ± .0001
Palmental leucogranite	546 ± 45	0.7200 ± .0001

The 568 ± 53 Ma age obtained for the Palmental "roadside" diorite contrasts sharply with the 756 ± 35 and 749 ± 34 Ma isochrons reported by Kroner (1982). However four of the five samples which define Kroner's (*op. cit.*) 749 ± 34 Ma isochron are co-linear on a 1/Sr vs. $^{87}Sr/^{86}Sr$ diagram (Fig. 5.5) which suggests that this "isochron" is a mixing line and does not have any direct age significance. Similarily, four of the five samples which define Kroner's (*op. cit.*) 756 ± 35 Ma isochron show a strong correlation (three are co-linear) between $^{87}Sr/^{86}Sr$ and 1/Sr suggesting that this "isochron" is also a mixing line. It is argued (Ch. 5) that

the 568 ± 53 Ma "errorchron" obtained here is a more accurate age estimate.

The Swakop river diorite intrudes the Palmental "roadside" diorite although is unlikely to be younger than about 520 Ma since it is cut by pegmatite dykes which are presumed to be part of the Donkerhuk granite. The Donkerhuk granite outcrops less than 1km south of the sampled locality (age = 521 ± 15 Ma, Blaxland et al., 1979). The 451 ± 27 Ma errorchron obtained here for the Swakop river diorite is interpreted as reflecting the time at which the small sampled volume became a closed system with respect to Sr. The 510 ± 32 Ma (MSWD = 2.3) six point isochron obtained for the leucocratic Otjimbingwe syenite may reflect the age of intrusion and it is noted that this age is indistinguishable from that of the Donkerhuk granite. The 403 ±14 Ma isochron obtained for the Otjimbingwe syenite may reflect partial resetting of the Sr isotopic systematics. This intrusion must be older than about 520 Ma since xenoliths of this syenite occur in the c.520 Ma old Donkerhuk granite (this study and R. Mc G. Miller, pers. comm.). The 545 ± 46 Ma age obtained for the Palmental granite is within error of the 521 ± 15 Ma age reported for the nearby Donkerhuk granite (Blaxland et al., *op. cit.*). The Donkerhuk and Palmental granites have similar major and trace element geochemistry (Ch. 4) suggesting that they may be co-magmatic, although initial $^{87}Sr/^{86}Sr$ ratios calculated for 521 Ma show that those of Palmental granite samples (~ 0.723) are slightly higher than those of Donkerhuk granite samples (~ 0.712).

2.5 Granitoid/Metasediment field relations

As shown on the enclosed geological map, the Palmental diorite and Otjimbingwe syenite intrusions preserve the regional penetrative fabric of their host metasediments. The Swakop river diorite is younger than the Palmental "roadside" diorite and does not have a strong penetrative fabric. The Palmental leucogranite is post-tectonic, although locally a weak non-penetrative fabric defined by mica alignment is just discernable.

All the granitoids studied have clear contact aureoles. The Palmental diorite causes migmatisation of semi-pelitic schists and cordierite growth in the more pelitic units.

Garnet/amphibole/epidote skarns are frequently observed where the diorite is in contact with calc-silicates. The Otjimbingwe syenite causes local migmatisation of semi-pelites, although on the southern margin of the intrusion this effect may be partly due to contact metamorphism by the Donkerhuk batholith. The Palmental leucogranite intrudes the Palmental diorite and contacts between these intrusions are sharp. Although some migmatites occur near the northern margin of the Palmental leucogranite, these are thought to be due to diorite contact metamorphism. Xenoliths of pelitic schists in the Palmental leucogranite have sharp contacts with their host granite. In contrast, calc-silicate and pelitic schist xenoliths in the Palmental diorite show evidence of reaction with their host magma, possibly reflecting higher magma temperatures (Plate 2.2).

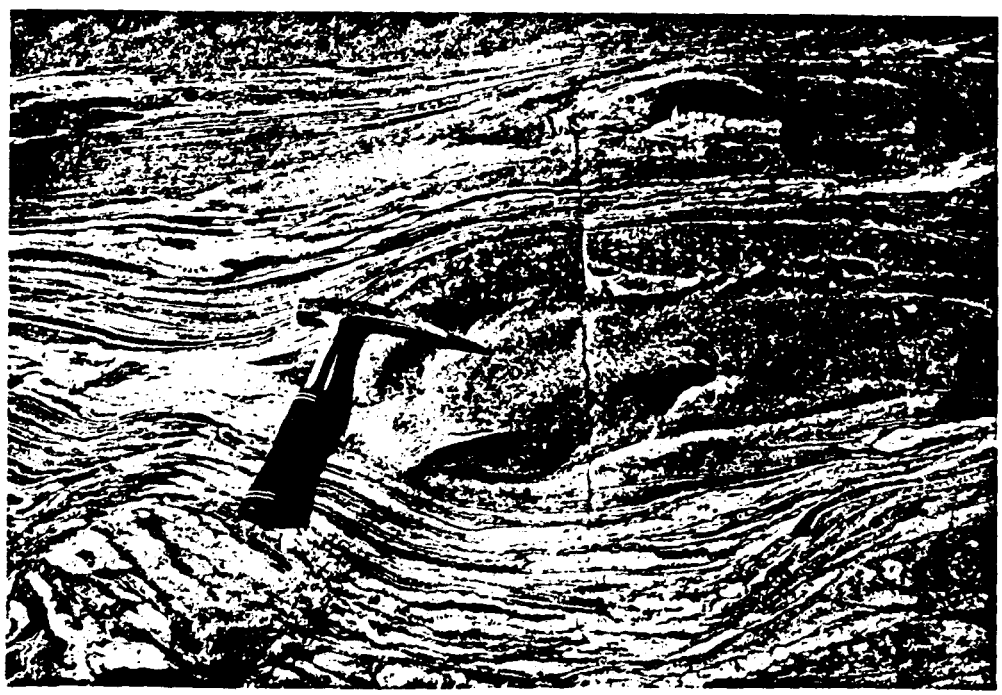

Plate 2.2 Migmatised calc-silicate and pelitic xenoliths in the Palmental diorite. In contrast, xenoliths in the Palmental granite have knife-sharp contacts with their host magma.

2.6 Structural evolution

Three major episodes of deformation have been identified. Fold styles are distinctive for each deformation episode and are broadly similar to those identified by previous workers in the Central Zone (e.g. Jacob, 1974 ; Downing and Coward, 1981; Downing, 1982). D_2 deformation produced the regional penetrative fabric, although the major structural features observed on aerial photographs are due to D_3 deformation.

2.6.1 The first phase of deformation

F_1 folds are tight to isoclinal overturned symmetrical folds. Apart from a few well exposed F_1 fold closures (e.g. Plate 2.3) F_1 folds are not well represented on outcrop scale.

Plate 2.3 F_1 folds are well exposed in the centre of the area as tight to isoclinal symmetrical folds. F_1 limbs are often attenuated and form boudins of purple pelitic schist in calc-silicates and marbles.

F_1 folds produce a weak S_1 spaced cleavage locally, which is sub-parallel to original bedding (S_o). F_1 folds are readily identified in the interbedded marble/calc-silicate/schist units of the Tinkas Member by the presence of protrusions of calc-silicate material into adjacent semi-pelites near F_1 fold closures. These "interface-spurs" (Plates 2.4 and 2.5), characterise F_1 fold closures in interbedded calc-silicate/semi-pelite units throughout the Central Zone (Klein, 1980 ; Miller, 1983).

2.6.1.1 S_1 fabric

F_1 folding produced a weak non-penetrative bedding-parallel spaced cleavage which may be due to a mass-transfer process (Grey, 1977). The cleavage is only observed close to the closures of F_1 folds although it is developed locally as a weak fabric in schist xenoliths in the Palmental diorite. This fabric results from a compositional segregation defined by alternating quartz-rich and mica-rich bands up to 3 mm wide in semi-pelitic schists. Occasionally, this spaced cleavage is observed as a macroscopic banding of alternating dark and light coloured layers. In calc-silicates the S_1 fabric is defined by carbonate rich/amphibole rich alternating bands.

2.6.1.2 F_1 folds - mesoscopic features

F_1 fold closures are commonly observed as refolded isoclinal folds in hand-specimens, but occasionally can be traced in outcrop for tens of metres. F_1 fold closures (Plate 2.3) are best exposed in the central part of the area where north-south trending foliations are dominant. In this area, F_1 fold axes plunge gently to the north-east, although the orientation of these early folds has undoubtedly been modified by subsequent deformation events. Fig. 2.1 is an equal area stereonet, lower hemisphere projection showing the dominant plunge direction of F_1 fold axes in the central part of the area.

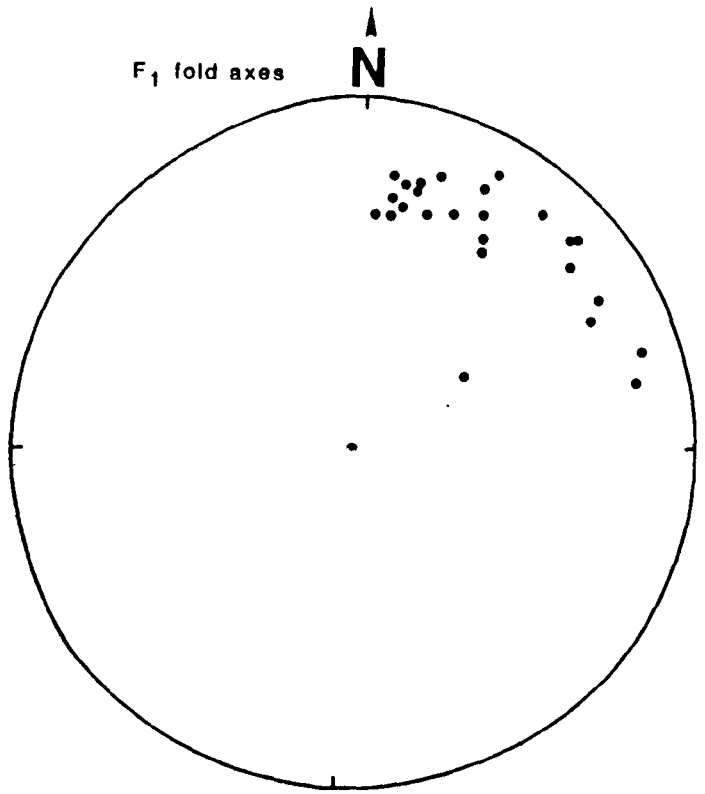

Fig. 2.1 Equal area stereonet, lower hemisphere projection of F_1 fold axes in the central part of the study area where N-S foliations are dominant

Mesoscopic F_1 fold closures are recognised by the presence of interface spurs which are described in detail by Klein (1980). Interface spur formation is due to the viscosity contrast between adjacent calc-silicate and semi-pelite layers. Klein (*op. cit.*) argues that interface spurs are formed by the migration of a fluid phase towards the fold hinge during deformation. Fluid expulsion towards fold-hinges is an irreversible process which occurs only during the earliest stages of F_1 folding (Klein, 1980). Parish *et al.* (1976) note that in addition to the role of fluid migration towards fold hinges, a viscosity contrast between layers of contrasting competency is critical to the process of interface-spur formation. Parish *et al.* (*op. cit.*) argue that relatively high temperatures are required to maintain large viscosity contrasts between adjacent layers.

2.6.1.3 F_1 folds - macroscopic features

F_1 folds are never directly observed on a macroscopic scale but are inferred to be several km in amplitude. Since major rotations of these structures have occurred during F_2 and F_3 events it is not possible to determine the original vergence direction of the large-scale F_1 folds. It is also likely that F_1 folds have been tightened during subsequent deformation events.

2.6.2 The second phase of deformation

2.6.2.1 Introduction

The second phase of deformation produced the intense penetrative foliation of the study area. This penetrative foliation (S_2) is the regional foliation recognised by other workers (e.g. Jacob, 1974 ; Downing and Coward 1981; Kasch, 1981; Downing, 1982). In contrast to F_1 folds, the F_2 folds are well developed on a mesoscopic scale where they form asymmetric parasitic folds. The large scale F_2 folds have been elucidated by mapping out changes in vergence directions of mesoscopic F_2 parasitic folds. The major asymmetric folds shown in cross-sections of the mapped area (see enclosed map) are F_2 folds.

2.6.2.2 F_2 folds - microscopic scale

F_2 folds produced a strong axial planar foliation which almost totally obliterates the earlier S_1 fabric. At fold closures the earlier S_1 spaced cleavage is refolded by F_2 folds. In metapelites, garnet porphyroblasts are enclosed by the penetrative S_2 fabric. This porphyroblast / fabric relationship suggests that prograde regional metamorphism had already commenced prior to D_2 deformation.

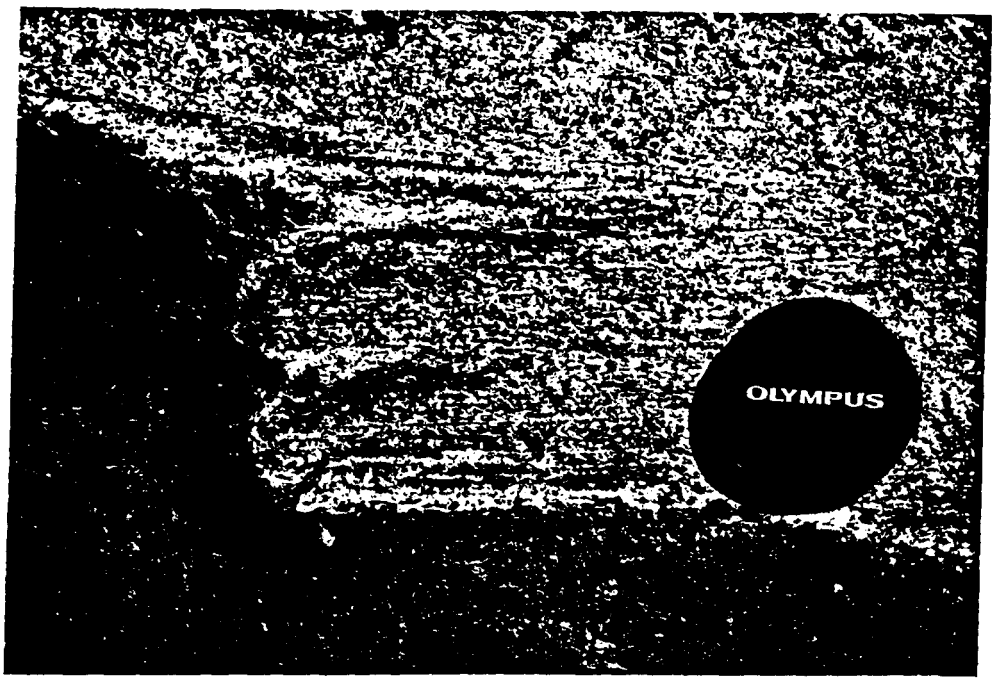

Plate 2.4 Interface-spurs near an F_1 fold closure (to the right of the area photographed). Interface spurs occur at pelitic schist/calc-silicate contacts near F_1 fold closures. Spur formation is a result of viscosity contrasts and fluid migration between adjacent layers and occurs only during the earliest stages of deformation (Klein, 1980).

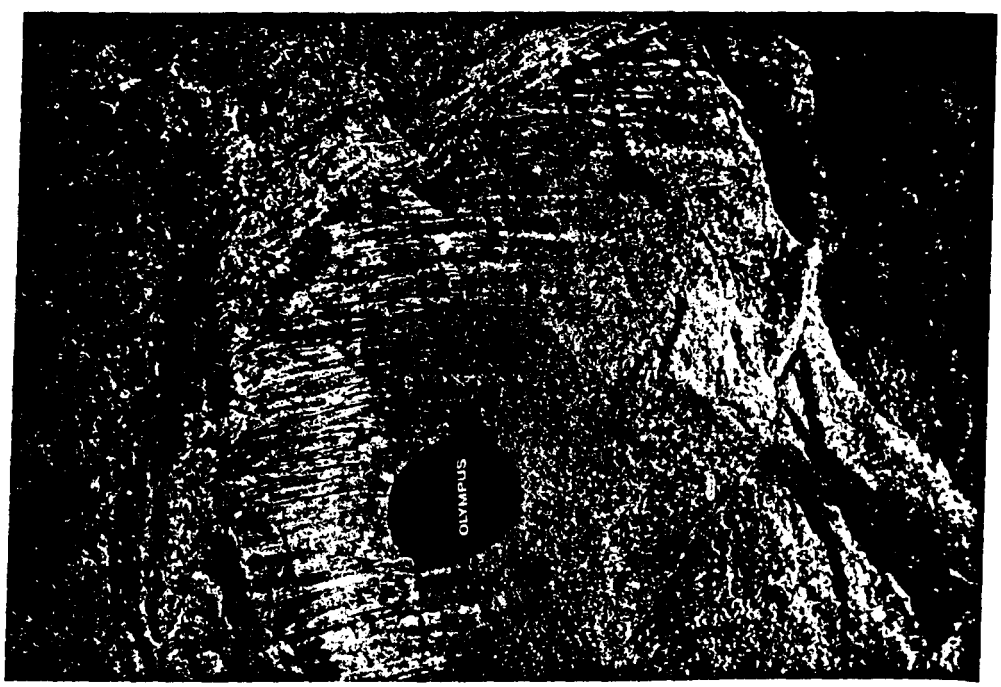

Plate 2.5 Interface spurs at an F_1 fold closure in the Palmental area.

2.6.2.3 F_2 folds - mesoscopic scale

Asymmetric F_2 folds occur ubiquituously throughout the study area as 0.5-5m parasitic folds on the limbs of major F_2 overturned folds (e.g. Plate 2.6). The change from Z (clockwise verging) to S (anticlockwise verging) folds were mapped out over distances of 0.5-1km across strike, (see enclosed map and cross-section A - B). Frequently, extreme viscosity contrasts between adjacent layers of the interbedded calc-silicate/marble succession results in disharmonic folds in which layers of similar viscosity and competence buckle independently of each other, (Plates 2.10 to 2.11).

Plate 2.6 F_2 asymmetric "S" fold in interbedded calc-silicates and pelites of the Tinkas Member. A strong axial-planar fabric is developed. Axial-planar fabrics associated with F_2 folds form the penetrative foliation of the area. (hammer for scale).

Plate 2.7 F_2 symmetric "M" fold in interbedded metapelites and calc-silicates of the Tinkas Member. F_2 "M" folds mark the hinge areas of major F_2 folds when the vergence directions of parasitic F_2 folds change.

Plate 2.8 Symmetric F_1 fold closure refolded by an F_2 asymmetric "S" fold. The pencil is parallel to the axial planar cleavage of the F_1 fold. The hammer handle parallels the axial planar cleavage of the F_2 "S" fold

Plate 2.9 Asymmetric F_2 "Z" folds in interbedded calc-silicates and marbles of the Tinkas Member. The lower calc-silicate layer (below hammer) is folded whereas the upper calc-silicate layer is relatively undeformed, reflecting the extreme ductility contrast between calc-silicates and adjacent marbles.

Plate 2.10 Close-up photograph of folded calc-silicate layer showing the ductility contrast between adjacent calc-silicate and marble layers.

2.6.2.4 F_2 folds-macroscopic scale

Large-scale F_2 folds have amplitudes of several km and are overturned to the north. Traces of major F_2 folds and cross-sections of macroscopic F_2 folds are shown on the enclosed geological map.

2.6.2.5 S_2 fabric

At a few localities (e.g. Plate 2.11) the axial planar fabric of F_2 asymmetric folds can be seen to produce the penetrative fabric in the Palmental diorite.

Plate 2.11 F_2 asymmetric "Z" fold at a contact between calc-silicates of the Tinkas Member and the Palmental diorite. The pencil marks the contact and it parallels the strike of the penetrative foliation of the diorite and the axial-planar fabric of the calc-silicates (below and above the pencil respectively). This demonstrates that the penetrative foliation in the diorite is the axial-planar cleavage of F_2 asymmetric folds i.e. the diorite foliation is S_2

This implies that the penetrative regional fabric preserved in intrusive rocks and metasediments of the study area is S_2 i.e. produced during D_2 deformation. This fabric produced a slaty cleavage in pelitic rocks and a strong penetrative fabric in intrusives, (i.e. the Palmental diorite

and Otjimbingwe syenite). The S_2 fabric is defined by a strong parallelism of micas in pelitic rocks, and in the biotite rich Otjimbingwe syenite intrusion. In the Palmental diorite the penetrative fabric is defined by amphibole alignment.

Equal area stereonets (Figs. 2.2 and 2.3) show the orientation of the S_2 fabric in the Palmental diorite and in the Otjimbingwe syenite respectively. Both intrusions preserve the same (S_2) foliation, the difference in orientation is due to refolding by later (D_3) deformation.

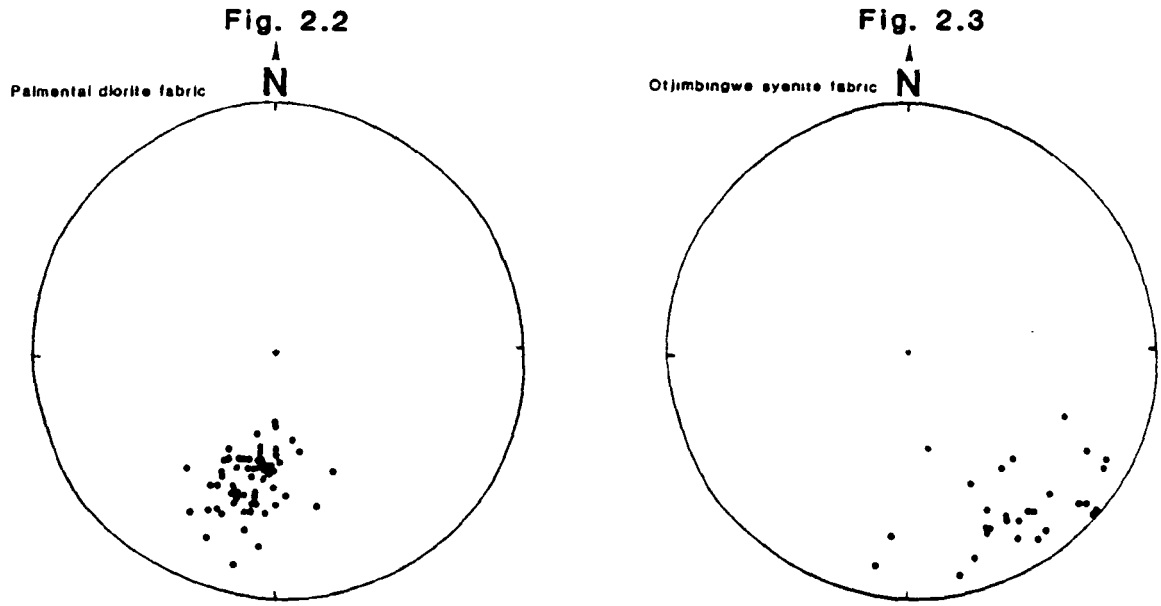

Figs. 2.2 and 2.3 Equal area stereonets (lower hemisphere projection) of orthogonal poles to the S_2 penetrative fabric in the Palmental diorite and Otjimbingwe syenite respectively.

Variations in the strike of the regional (S_2) fabric are shown in Fig. 2.4a - 2.4c. The foliation "swings" from east-west (Fig. 2.4a), through northeast-southwest (Fig. 2.4b) to north-south (Fig 2.4c) in the south, south-east and central portions of the area respectively.

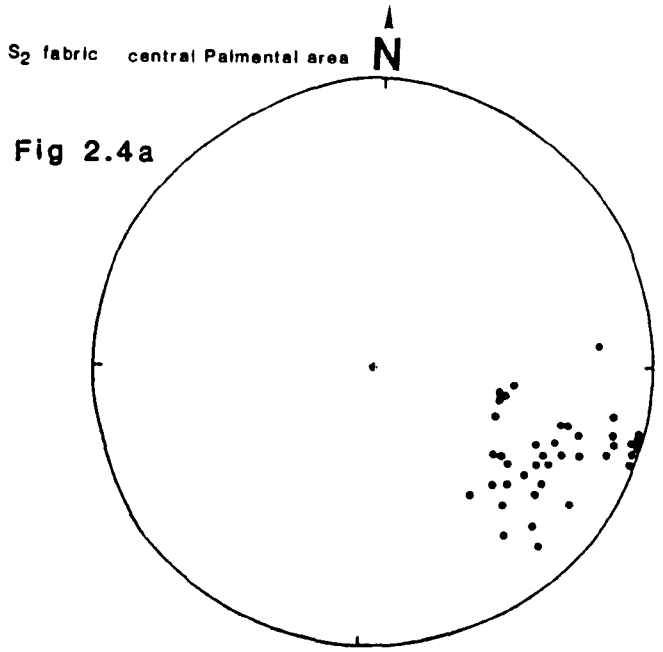

Fig 2.4a

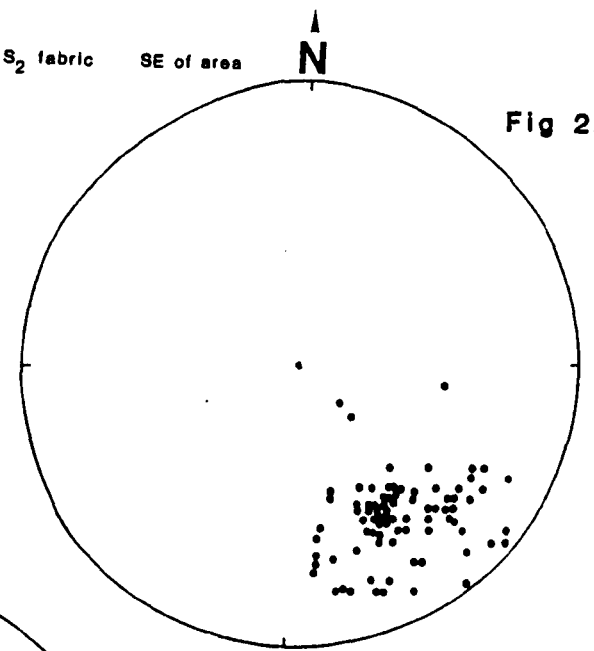

Fig 2.4b

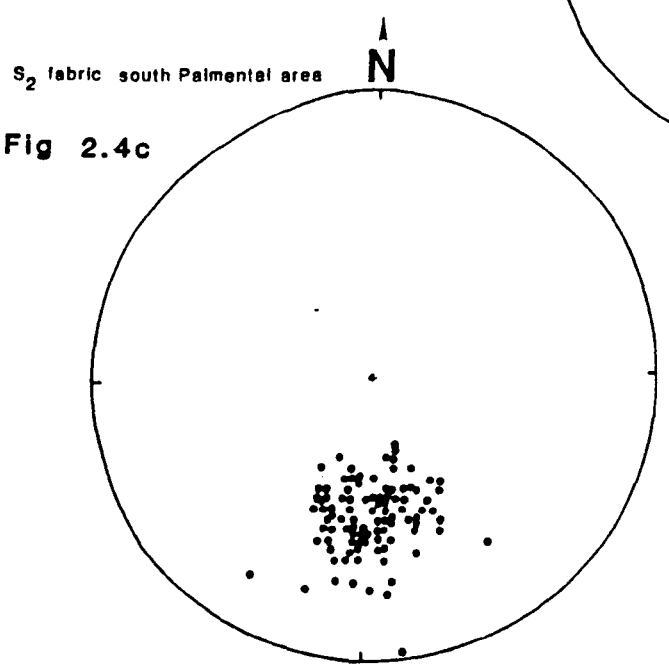

Fig 2.4c

Figs. 2.4a - 2.4c Equal area stereonet, lower hemisphere projection of orthogonal poles to the regional S_2 fabric in different parts of the study area. The S_2 fabric swings from N-S trending to to ENE-WSW to E-W trending in the central, south-east and southern parts of the mapped area. This is due to D_3 deformation.

2.6.2.6 Lineations

Both mineral lineations and lineations defined by the intersections of planes have been observed and recorded in the Palmental area. Most lineations result from the intersections of F_2 axial planes (S_2) and bedding parallel S_1 . Lineations are plotted on an equal area stereonet (Fig. 2.3) which shows that most lineations plunge at 25 - 40^o north, reflecting the dominant plunge direction of F_2 fold hinges.

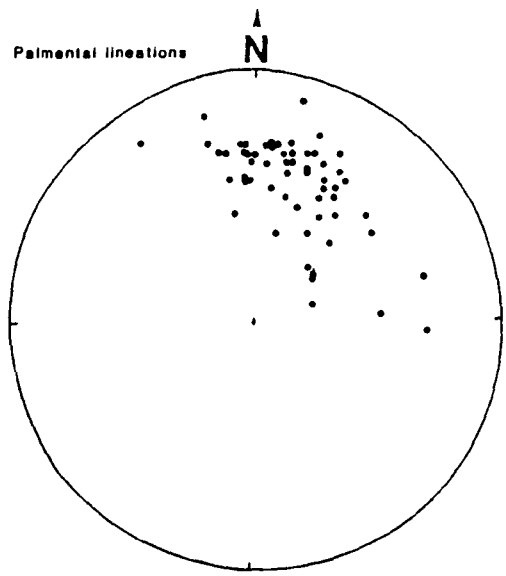

Fig. 2.5 Equal area stereonet lower hemisphere projection of lineations measured in the Palmental area.

2.6.3 The third phase of deformation

2.6.3.1 Introduction

D_3 deformation produced the major structural features observed on aerial photographs of the study area. F_3 folds are open, upright folds which refold the penetrative S_2 regional foliation. Locally, an axial planar cleavage is developed but does not form a penetrative fabric. Since F_3 folds are open and do not produce a penetrative fabric D_3 deformation is not well represented on microscopic or mesoscopic scales. Occasionally however F_3 folds are

observed on the scale of a single outcrop (30 - 50m, Plate 2.12) where they refold the regional S_2 foliation. Frequently F_3 folds result in changes in strike of the regional foliation of up to 90° over distances of a few tens of metres.

Plate 2.12 F_3 open fold in interbedded purple pelites and calc-silicates of the Tinkas Member. The penetrative S_2 fabric (parallel to hammer handle in the lower middle part of the photograph) is folded around by this F_3 fold. F_3 folds result in changes in the strike of the regional foliation of up to 90° over distances of a few tens of metres. An F_1 fold closure marked by a yellow pencil can be seen in the upper-middle part of the photograph.

2.6.3.2 F_3-Macroscopic scale

Major variations in the strike of the regional foliation (see enclosed geological map) are largely due to F_3 folding. F_3 folds change the strike of the regional fabric from east-west along the southern boundary of the mapped area to north-south in the central portion of the area. The change in strike of the regional foliation north of the Swakop river from northwest-southeast in the N.W. corner of the area to northeast-southwest in the N.E. part of the area is due to F_3 folding. Similarily F_3 folds change the strike of the diorite foliation from a predominantly east-west direction to a northeast-southwest trend in the Otjimbingwe syenite.

Perhaps the most striking effect of F_3 folding was to produce variations in the directions of plunge of F_2 fold axes. Fig. 2.6 shows how F_3 folding changed the direction of plunge of F_2 fold axes from northwest through north to northeast in the southern, central and southeast boundary segments of the area.

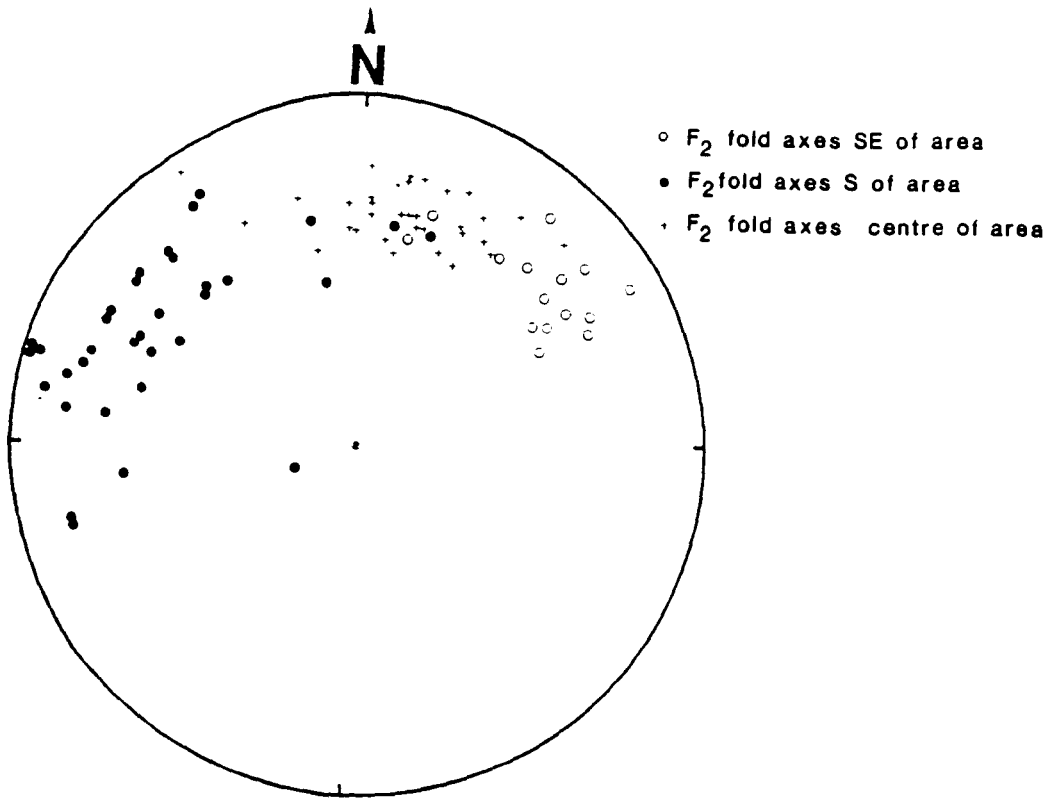

Fig. 2.6 Equal area stereonet, lower hemisphere projection of F_2 fold axes, showing how F_2 fold axes change in direction in different parts of the study area due to F_3 folding. The plunge direction of F_2 fold axes change from northwest through north to northeast in the southern, central and southeastern parts of the area.

2.7 Petrography and metamorphic petrology

2.7.1 Introduction

Field and thin-section studies indicate that a single episode of regional metamorphism may have produced the regional metamorphic assemblages observed in the study area. This area is east of (i.e. downgrade from) the sillimanite-in isograd reported by Hartmann *et al.* (1983). In pelitic rocks of the study area garnet is the only porphyroblastic mineral which may be unequivocally attributed to regional metamorphism. Locally, contact metamorphism has produced cordierite, and K-feldspar bearing assemblages. Contact metamorphic effects have produced localised skarns where calc-silicates are in contact with the Palmental diorite. Metamorphic mineral assemblages developed in marbles, calc-silicates and semi-pelites are discussed below.

2.7.2 Marbles

Marble horizons occur as interbedded layers within the mixed calc-silicate/mica schist succession of the Tinkas Member. Individual marbles may be up to 20m thick and are particularly well exposed in the western portion of the area in Farm Tsaobismund 85. Marbles are usually white although locally the presence of graphite and disseminated pyrite gives them a greyish appearance. In the central part of the area where north-south trending foliations are dominant several pale-green/yellowish marble bands occur. The green colouration is due to the presence of serpentine after olivine.

Marble bands are coarse grained and have a granular texture (grain size 0.2 - 2 cms.) and often exhibit a nearly perfect granoblastic texture. In general, the marbles do not preserve a foliation suggesting that significant post-tectonic recrystallisation occurred.

However, most samples have some calcite grains which have deformation twins and lamellae suggesting that at least some strain has been recorded.

Both calcite and dolomite occur, although calcite is dominant in most samples. Diopside, tremolite and serpentine (after olivine) occur in impure marbles. Wollastonite occurs locally as a contact metamorphic mineral close to diorite contacts. Accessory phases include graphite, pyrite, muscovite and chlorite. The mineral assemblages in marble samples are listed in Table 2.3.

Table 2.3 Summary of Calc-silicate/Marble assemblages

Sample	Qtz	K-spar	Plag.	Hble	Dio.	Calcite	Scap.	Ep.	Sph.	Others
FC11	√		√	√	√	√		√		
FC2b	√	√	√	√	√	√			√	
FC2c	√		√	√		√				idocrase
P321	√		√	√	√	√				biotite
Loc137	√		√	√		√			√	biotite
P122	√		√	√	√					
Loc85	√	√	√	√	√	√	√		√	
P320b	√		√	√	√	√				
2137					√	√		√		garnet
321b	√			√	√	√				
FC5	√	√	√	√	√	√				
FC1B	√			√	√				√	
FC10	√			√	√	√		√		
FC4b	√			√	√		√			
FC4c	√		√	√	√	√	√			chlorite
FC2a	√		√	√	√	√	√	√		

Marble mineral assemblages

Sample	Qtz.	Calcite	Olivine	Serp.	Talc	Trem.	Musc.	Others
Loc511		√	√	√			√	
FC4a	√	√				√		biotite
FC4c	√	√	√					

2.7.3 Calc-silicates

Locally, calc-silicates constitute up to about 50% of the Tinkas Member and are frequently interbedded with marble layers. Calc-silicates are typically massive in appearance and vary in colour from buff-colour to dark brown. Individual calc-silicate layers are up to 10m thick and grain-size is in the range 0.05-2mm. Occasionally, good granoblastic textures are developed but these are due to a thermal overprint by contact metamorphic effects. A penetrative fabric is usually lacking although amphiboles and/or pyroxenes are often aligned in thin sections. Representative mineral assemblages observed in calc-silicates are listed in Table 2.3.

Calcite is the dominant carbonate mineral. Quartz almost invariably shows undulose extinction and there is a complete gradation from relatively pure quartzite layers to calc-silicates. Plagioclase is usually present and K-feldspar has been observed in one thin-section. Scapolite is present in several thin sections. Diopside is present in most samples as poikiloblastic grains enclosing polygonal quartz grains. Two generations of hornblende are present. A dark green, strongly pleochroic variety occurs as rims on diopside grains, some of which are almost completely replaced by hornblende. Euhedral grains of hornblende which are yellow in p.p.l. are are often rimmed by dark-green strongly pleochroic hornblende. Epidote has been observed in several samples. Biotite is present locally, in samples which are close (a few cms.) to calc-silicate/mica schist contacts. Garnet and idocrase are present in contact metamorphosed calc-silicates only.

2.7.4 Pelitic and semi-pelitic association

Semipelitic to pelitic schists of the Kuiseb Formation and the Tinkas Member occur in the study area. Metapelites are of fine grained schists with a strong penetrative (S_2) fabric. Grain size varies from 0.01- 2 mm becoming coarser locally due to contact thermal

effects. The schists with more pelitic compositions are commonly porphyroblastic. Porphyroblasts of garnet, cordierite and K-feldspar occur, although cordierite and K-feldspar bearing assemblages appear to be restricted to contact metamorphic assemblages since they are found close to diorite contacts only. Fabric/porphyroblast relationships consistently indicate that the porphyroblasts pre-date the major fabric-forming deformation event (D_2) since the porphyroblasts disrupt and are enclosed by the penetrative fabric, suggesting that prograde regional metamorphism had commenced prior to D_2 deformation.

In the regionally metamorphosed metapelites quartz, biotite and plagioclase are invariably present. The penetrative S_2 fabric is defined by biotite alignment. Occasionally, a weak S_1 spaced cleavage is preserved as compositional segregation banding. Garnet occurs both as equidimensional porphyroblasts and as elongate tabular shaped grains. There is no evidence for two generations of garnet growth and the differences in shape probably reflect local strain variations in the metapelites. Biotites which occur close to garnet porphyroblasts commonly have a darker colour than those which occur in the semi-pelite matrix. Garnets usually have abundant inclusions of quartz, plagioclase and biotite with some carbonate material occurring locally. Chlorite and muscovite are present in some samples as late alteration minerals.

Cordierite occurs in purple pelitic schists of the Tinkas Member, close to intrusive rock contacts where it forms porphyroblasts up to 1 cm across and is enclosed by the S_2 penetrative fabric. Inclusions of quartz, biotite and muscovite occur in cordierite porphyroblasts.

K-feldspar occurs in pelitic schists as altered cloudy porphyroblasts enclosed by the penetrative fabric, close to granite pegmatite dykes in the central part of the study area. Garnet is the only porphyroblastic mineral which can definitely be attributed to regional metamorphism since it occurs outside thermal aureoles of the intrusives. Mineral assemblages of pelitic to semipelitic schists are listed in Table 2.4.

Table 2.4 Summary of mineral assemblages in pelites

Sample	Qtz.	Bi.	Plag.	K-spar.	Mu.	Cd.	Gt.	Opa.	Chl.	Others
FC13	√	√	√					√	R	
FC13a	√	√	√					√		
FC15	√	√	√				√			
FC11	√	√	√		R		√	√	R	Zircon
FDP12	√	√	√	√	√	√				
P361	√	√	√				√	√		
P782	√	√	√				√			
P481	√	√	√	√			√	√		
P966	√	√		√						
PG15	√	√	√				√	√		apatite
P879	√	√	√	√			√			
P135	√	√	√		R					
P392	√	√	√							
FC10	√	√	√							
FC12	√	√	√		R				R	
FC8	√	√	√		R					
P4	√	√	√	√			√			
FC7	√	√	√		R				R	calcite

R = present as a retrogressive phase. Mineral abbreviations are given in Table 2.4

Table 2.5 Mineral abbreviations used in this Chapter.

Abbreviation	Mineral
Tre	Tremolite
Di	Diopside
Dol	Dolomite
Fo	Forsterite
Cc	Calcite
Qtz	Quartz
Woll	Wollastonite
An	Anorthite
K-Spar	K-feldspar
Sph	Sphene
Ep	Epidote
Plag	Plagioclase
Mu	Muscovite
Mic	Microcline
Hble	Hornblende
Zoi	Zoisite
Gros	Grossular
Graph	Graphite
Chl	Chlorite
Mag	Magnetite
Gt	Garnet
Bi	Biotite

2.7.5 Interpretation of metamorphic mineral assemblages

Numerous reaction equations may be written to describe reactions between minerals of assemblages observed in pelitic and calc-silicate rocks. Many of these reactions have been studied either by experimental or thermodynamic methods so that if mineral reactions can be demonstrated texturally, constraints may be placed on the physical conditions of metamorphism. On the basis of experimental and thermodynamic results several

petrogenetic grids have been published which may yield pressure and temperature estimates for equilibrium assemblages.

The presence and composition of fluid phases is critical to the P/T conditions at which several metamorphic reactions occur and although the effects of H_2O and CO_2 have been investigated experimentally there are inadequate data on the effects of other fluid phases such as HCl, HF, SO_2 etc. It is noted that most experimental data assume that $P_f = P_{tot.}$ so that this assumption is inherent in applying the published experimental data. For the purposes of these discussions P_{tot} is assumed to be 4Kb since this is the pressure estimated by Downing (1982) for the area just north of the Okahandja lineament some 20km along strike from the study area. Mineral abbreviations used in this study are listed in Table 2.5.

2.7.5.1 Interpretation of marble mineral assemblages

Several marble samples studied have tremolite and serpentine after olivine. Occasionally wollastonite is present but this is interpreted as a contact metamorphic mineral since it occurs in marbles close to diorite contacts only. Olivine bearing marble samples contain the assemblage calcite + olivine.

Possible olivine producing reaction are (Eggert and Kerrick, 1981 ; Fig. 2.7).

$Tre + 11\ Dol = 8\ Fo + 13\ Cc + 9\ CO_2 + H_2O$ ..... (1)

$3\ Dol + Di = 4\ Cc + 2\ Fo + 2CO_2$ ..... (2)

The absence of tremolite, dolomite or diopside in olivine bearing marbles (e.g. sample 511) suggests that these reactions have gone to completion. These olivine producing reactions are indicative of regional metamorphic temperatures of 600-670°C at 4Kb depending on $X(CO_2)$, (Eggert and Kerrick, *op. cit.*).

Diopside occurs in several marble/calc-silicate samples and a typical assemblage is diopside + calcite + dolomite + quartz + tremolite. Therefore diopside was probably produced by the reaction

$Tre + 3Cc + 2\,Qtz = 5Dio + 3CO_2 + H_2O$ .....(3).

Dioposide is produced by this reaction at temperatures in the range 560 - 590°C depending on $X(CO_2)$. Irrespective of $X(CO_2)$ this reaction is indicative of temperatures in excess of 560°C (Eggert and Kerrick, *op. cit.*).

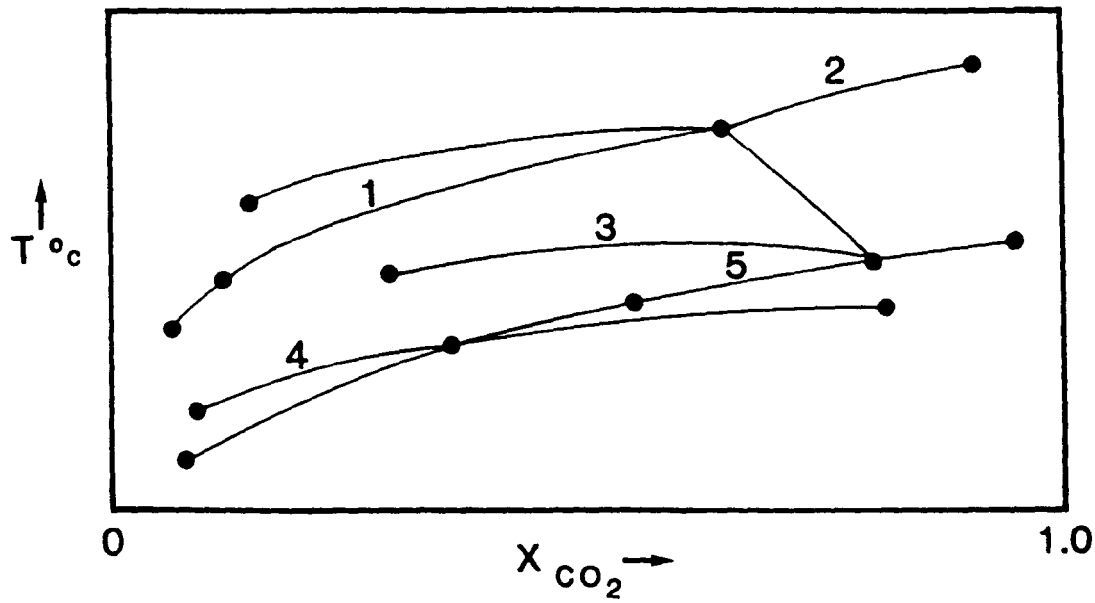

Fig. 2.7 Schematic T - X (CO_2) diagram (after Eggert and Kerrick, 1981) showing important mixed volatile equilibria in the siliceous dolomite system. Reaction numbers correspond to those in text.

In samples where tremolite is observed the equilibrium assemblage is quartz + calcite + dolomite + tremolite (e.g. sample FC4a). Possible tremolite producing reactions are

$2\,Talc + 3\,Cc = Tre + Dol + CO_2 + H_2O$ ..... (4)

$5\,Dol + 8\,Qtz + H_2O = Tre + 3\,Cc + 7\,CO_2$ ..... (5)

Reaction 5 in the most likely tremolite producing reaction since talc is not observed in tremolite bearing samples whereas calcite is always present. Reaction 5 occurs at high $X(CO_2)$, (Eggert and Kerrick, op. cit. ; Fig. 2.7). These reactions are indicative of minimum temperatures in the range 530 -570°C, depending on $X(CO_2)$.

In summary, the presence of olivine bearing assemblages in marbles indicate minimum regional metamorphic temperatures in the range 550-590°C, depending on $X(CO_2)$.

Mineral assemblages observed in calc-silicate assemblages have been tabulated in Table 2.3. Epidote, scapolite, chlorite and K-feldspar occur locally whereas quartz, plagioclase, hornblende and diopside occur in most samples. There is good textural evidence for replacement of diopside by hornblende but this is interpreted as a retrogressive effect. Diopside and prograde hornblende are usually poikoblastic. Garnet occurs only in contact metamorphosed / skarn-type assemblages.

Petrogenetic grids for calc-silicate systems have been constructed by Thompson (1975) and Hoschek (1980) both of which are used to interpret the observed assemblages. However Hoschek's grid does not include high grade, diopside bearing assemblages so it is of limited use in the interpretation of most calc-silicates of the study area. Thompson's (*op.cit.*) grid is constructed for P (H_2O) = 5 Kb which is probably slightly too high for assemblages produced in the Palmental area. Since all the reactions have positive slopes in P,T space the temperatures estimated by Thompson's (*op. cit.*) grid may be too high. A further difficulty in using published grids is that previous work considers tremolite as the dominant amphibole phase generated by prograde metamorphism of calcareous metasediments. However hornblende is the dominant amphiobole observed in calc-silicates. The presence of hornblende instead of tremolite possibly reflects a more aluminous bulk chemical composition of calc-silicates in the Palmental area. For the purposes of this discussion hornblende is treated as tremolite. This will affect the positions of reaction curves in P,T space so that no reliable P/T estimates can be made on the basis of mineral reactions involving tremolite.

Epidote occurs in trace amounts in most calc-silicate samples studied. The presence of epidote in calc-silicate assemblages is indicative of relatively high X (H_2O) (Hewitt, 1973 ; Thompson, 1975 ; Hoschek, 1980). At $P_{tot.}$ = 5Kb Hoschek calculated that X (H_2O) must be greater than 0.75 for the assemblage biotite + zoisite + quartz.

Diopside-free calc-silicate assemblages which have the assemblage calcite + quartz + tremolite lie on the low-temperature side of the reaction

$$Tre + 3\ Cc + Qtz = 5\ Di + 3\ CO_2 + H_2O \quad \text{..... (3) (Fig. 2.7)}$$

This reaction is shown in Fig. 2.8 after Thompson (1975). Clearly the presence of diopside is strongly dependent on X (CO_2) (Fig. 2.8) so that no reliable temperature estimates may be made since X (CO_2) is not known.

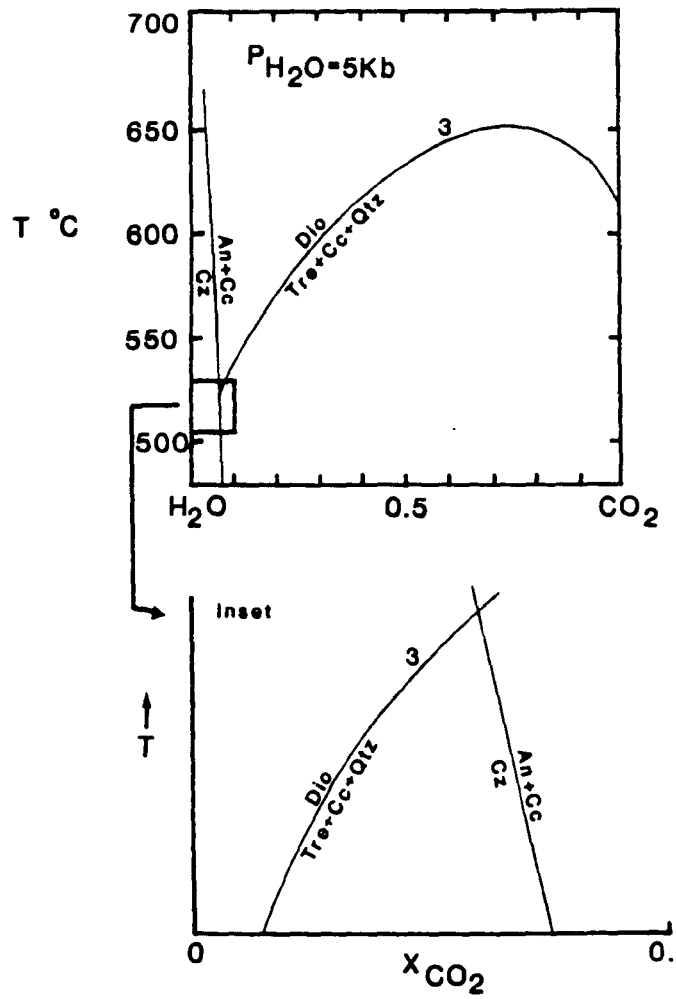

Fig. 2.8 T-X (H_2O -CO_2) diagram for reaction 3, (after Thompson, 1975) for the system CKMASH at 5Kb.

Microcline occurs locally in samples with the assemblage calcite + quartz + plagioclase + microcline and was probably produced by the reaction

Mu + Cc + Qtz = Mic + An + CO_2 + H_2O ..... (6)

since microcline and muscovite do not co-exist.

Wollastonite is observed in marbles and calc-silicates close to diorite contacts and is interpreted as a contact metamorphic mineral. Wollastonite was probably produced by the reaction

Cc + Qtz = Woll + CO_2 ..... (7)

Greenwood (1967) calculated a curve in T, X (CO_2) space for this reaction (Fig. 2.9). Wollastonite is stable only at temperatures above about 600°C if X (CO_2) is low. The stability temperature increases dramatically at higher X (CO_2) values. The high temperatures required for wollastonite stability probably explains why it is found locally, only within the thermal aureole of the Palmental diorite.

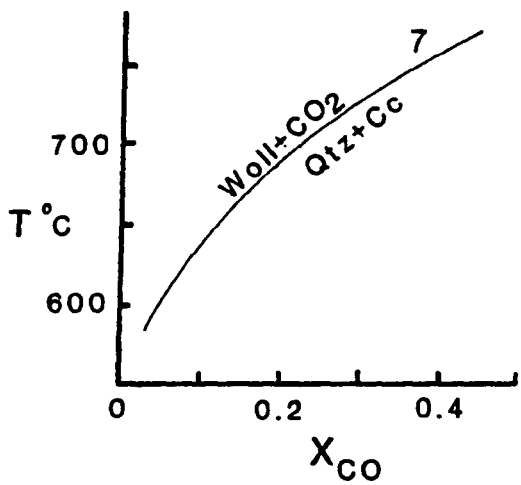

Fig. 2.9 T - X (CO_2) diagram adapted from Gordon and Greenwood (1970) for the reaction Qtz + Cc = Woll + CO_2 which illustrates the effect of variable XCO_2 on the temperature at which reaction 7 occurs.

2.7.5.2 Summary of calc-silicate assemblages

A sequence of prograde metamorphic mineral assemblages for calc-silicate rocks may be worked out. Increasing metamorphic grade is accompanied by the following "index mineral" reactions ; epidote-out, amphibole-in, clinopyroxene and K-feldspar-in. Wollastonite and garnet occur only in contact metamorphosed calc-silicates in the Palmental area.

Comparisons of mineral assemblages and reactions observed in marbles with published experimental and thermodynamic data suggest regional metamorphic temperatures in the range 600-680 °C while contact metamorphism may have produced temperatures of at least 700 °C locally (wollastonite formation). However, there are several difficulties in applying published petrogenetic grids to estimate P T conditions for calc-silicate assemblages.

1. Most reactions are highly sensitive to $X(CO_2)$. Since $X(CO_2)$ is likely to be very variable locally, temperature estimates may be unreliable.

2. Experimental and thermodynamic data and published petrogenetic grids consider tremolite as the dominant amphibole in calc-silicate systems whereas hornblende is the dominant amphibole in calc-silicates of the Palmental area.

3. Conditions of $X(CO_2)$ and $X(H_2O)$ are difficult to estimate and may be highly variable locally. It is probable that $X(CO_2)$ was high in thick marble units during metamorphism whereas thin calc-silicate layers may have had higher $X(H_2O)$ and lower $X(CO_2)$. The presence of pelitic layers interbedded with calc-silicates may have caused high $X(H_2O)$, so that these parameters may have been largely controlled by layer thickness and the proximity of pelitic layers.

2.7.5.3 Interpretation of semi-pelitic mineral assemblages

The metamorphic "index" minerals observed are chlorite, biotite, garnet and cordierite. No Al_2SiO_5 polymorphs have been observed. Locally, pelites are extensively migmatised by contact metamorphism.

In metapelites the penetrative fabric is defined by parallel alignment of biotites. Garnet occurs as a pre-D_2 mineral and is always enclosed by the penetrative schistosity. Cordierite occurs locally within the thermal aureoles of granitoids both as a pre- and a syn-D_2 mineral. Chlorite and muscovite occur as retrogressive phases and often cross-cut the schistosity. Metapelite mineral assemblages have been sumarised in Table 2.4.

In garnet bearing pelites, the typical mineral assemblage is quartz + garnet + biotite so that garnet was probably produced by the continuous reaction

Chl + Mu + Qtz = Gt + Bi + H_2O ..... (8) (Thompson and Norton, 1968).

Using a general pelite petrogenetic grid (Harte, 1975) the assemblage cordierite,

biotite and garnet reflect temperatures of about 580 °C at 4Kb during regional metamorphism. Migmatisation at 4Kb by the reaction Ab + Qtz + V = Liq (Thompson, 1982) requires temperatures in excess of 650 °C.

2.7.5.4 Summary

Comparisons of mineral assemblages and reactions observed in carbonate rocks with published experimental and thermodynamic data suggest temperatures in the range 600-680 °C, (depending on $X(CO_2)$) assuming a pressure of about 4 Kb. Locally, contact metamorphism may have produced temperatures up to 700 °C. Migmatisation of pelitic schists by the Palmental diorite and Otjimbingwe syenite indicate temperatures of at least 650 °C. The presence of pre-D_2 garnets in metapelites indicates that regional metamorphism had commenced prior to D_2 deformation although the peak of regional metamorphism post-dates D_2 deformation (Miller, 1983).

2.8 Biotite -garnet geothermometry

Microprobe analyses of co-existing biotite and garnet pairs in nine semi-pelite samples from the intracontinental branch of the orogen have been used to estimate peak temperatures reached during regional metamorphism. The primary objective of this study was to compare metamorphic temperatures recorded by pelitic rocks from the Palmental area with those from elsewhere in the intracontinental branch of the orogen. In addition to estimating the maximum metamorphic temperature recorded by each sample, zoning patterns in metamorphic garnets are used to characterise portions of metamorphic paths by studying rim to core variations in calculated temperatures. Sample localities are shown in Fig. 2.10. All temperature estimates are calculated at 4 Kb, although these thermometers are rather insensitive to pressure variations.

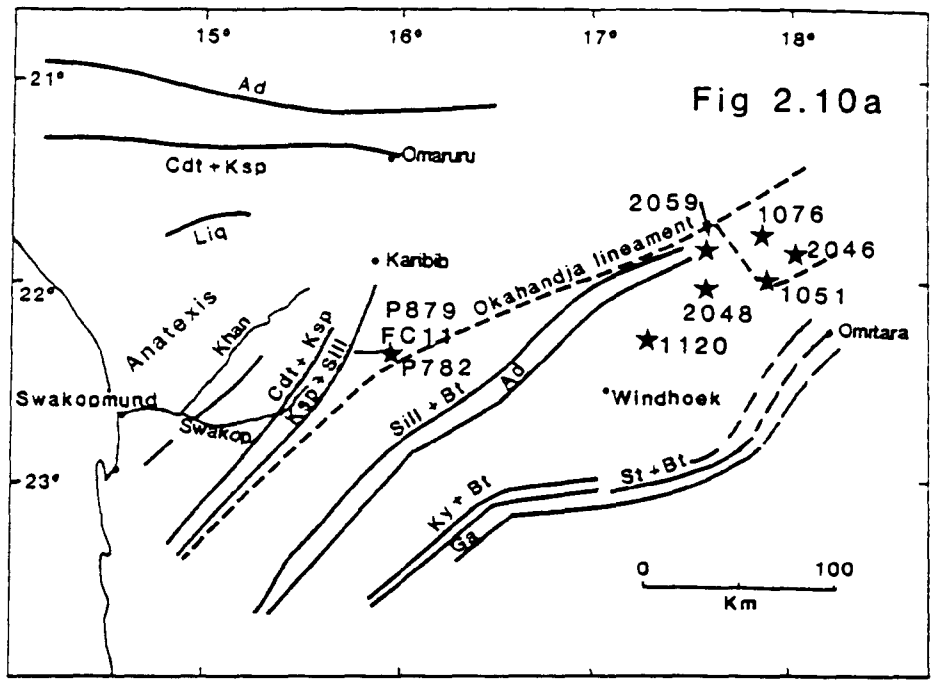

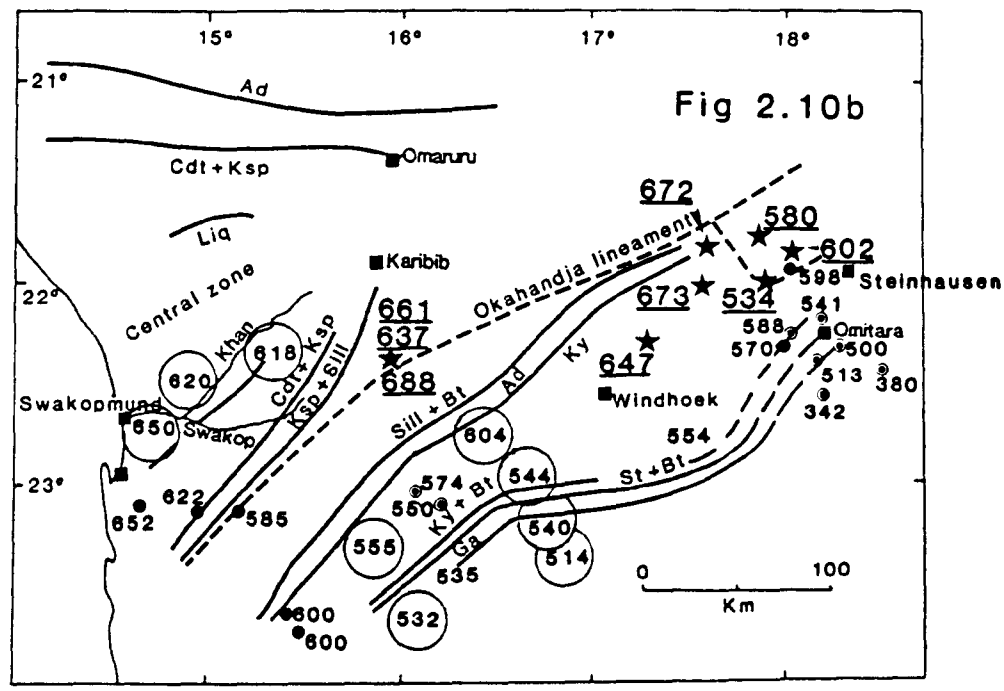

Fig. 2.10a Map showing localities of samples used in geothermometry study.
Fig. 2.10b Metamorphic isograd map of the intracontinental branch of the Damara orogen showing temperature estimates from this and previous studies.

★Localities from which M_1 temperature estimates in metapelites have been determined (this study) by Fe-Mg biotite/garnet exchange geothermometry. Temperature estimates from this study are shown underlined in large type and are based on the calibration of Indares and Martignole (I + M $_B$,1985). Oxygen isotope temperature estimates from Hoernes and Hoffer (1979) are shown in circles. Biotite/garnet temperature estimates for M_2 are shown as ◉ Calcite - dolomite temperatures are shown as • (after Kasch, 1983).

2.8.1 Methodology

Each sample used for geothermometry studies was examined in thin section to establish the microtextural relationships between garnet porphyroblasts and biotite grains. Although perfect granoblastic textures were not observed in all samples there is no textural evidence for disequilibrium between co-existing minerals. A short petrographic description of each sample is given below.

Traverses across individual garnet grains were analysed to assess compositional zoning patterns. Several biotite grains (~20) were analysed in each thin section to establish the range in biotite compositions present. Ranges in Mg/(Fe + Mg) ratios of biotites used in temperature determinations are shown in Fig. 2.11.

Since garnet cores and isolated biotite grains are most likely to preserve compositions attained at peak metamorphic conditions all temperature determinations are based on average compositions of matrix biotites and garnet cores.

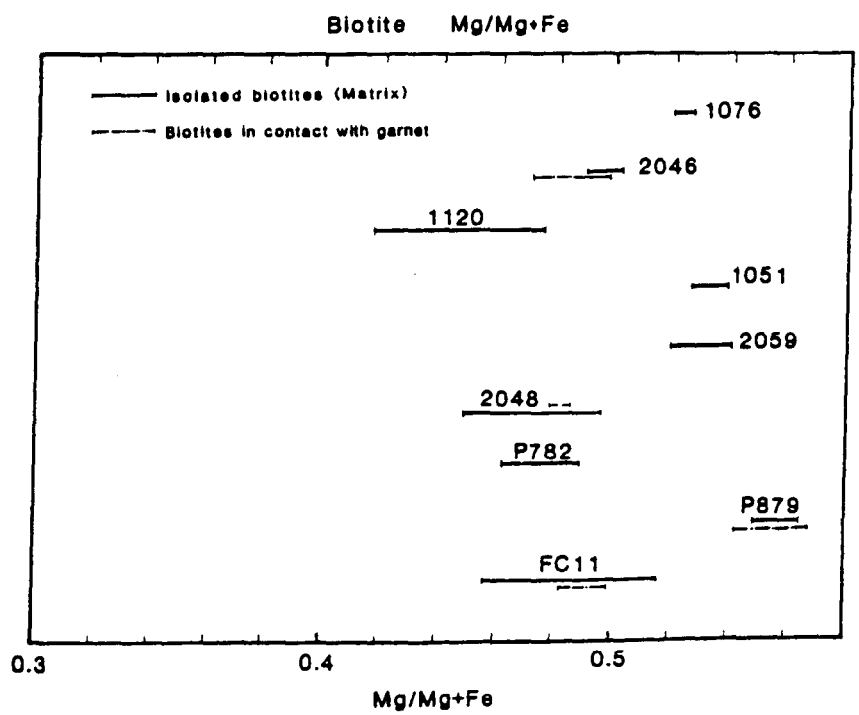

Fig. 2.11 Variations in Mg/Mg + Fe for biotites analysed in different samples to investigate the range in biotite compositions between different samples.

2.8.2 Petrography of metapelites

All the metapelites studied have the mineral assemblage quartz, plagioclase, biotite and garnet. Secondary chlorite and muscovite are present in some samples. With the exception of sample 1051, which also contains kyanite, (from the Steinhausen area of NE Namibia, Fig. 2.10) all garnet porphyroblasts have grown early in the metamorphic history of the samples since the garnet porphyroblasts are characteristically enclosed by the penetrative fabric. Occasionally, garnets preserve inclusion trails which mimic an earlier schistosity. Garnet in samples from the Palmental area contain abundant quartz and biotite inclusions. Petrographic descriptions are given for each sample in approximate order of increasing metamorphic grade, as estimated from the various geothermometers (Table 2.6).

Table 2.6

Sample No.	Th.	F+S	H+S	G+S	I+M_A	I+M_B
1051	542	515	571	514	526	534
1076	581	565	616	567	560	580
P 879	586	570	598	601	546	661
2059	591	578	620	607	566	672
2046	612	604	646	606	584	602
FC11	666	674	700	635	626	637
1120	665	676	702	656	640	647
2048	682	699	725	675	670	673
P 782	711	739	759	688	664	688

Table 2.6 showing peak metamorphic temperatures as recorded by each geothermometer using garnet core / matrix biotite pairs.Calibrations are by Thompson ,1976 (Th.) ; Ferry and Spear ,1978 (F+S) ; Hodges and Spear, 1982 (H+S) ; Ganguly and Saxena, 1984 (G+S) and calibrations A and B of Indares and Martignole, 1985 (I+M_A and I+M_B respectively).

Sample 1051

Mineralogy : Quartz, plagioclase, biotite, muscovite, garnet, kyanite

Grain size : Coarse grained, 0.5 - 2mm with kyanite porphyroblasts up to 20mm long

Texture : A polygonal, almost granoblastic texture is developed. A strong schistosity is defined by parallel alignment of micas. Two generations of garnet porphyroblasts are present. One garnet population have well developed inclusion trails which suggest syn-tectonic garnet growth. In contrast, post-kinematic garnets are almost totally free of inclusions. Kyanite is present as a post-kinematic mineral which has grown obliquely to the penetrative fabric.

Interpretation : The mineral assemblages in this rock record two metamorphic peaks which were syn- and post-tectonic respectively. Garnets with "snowball" type inclusion trails record syn-tectonic metamorphism while post-kinematic garnets and kyanite are indicative of a post-tectonic metamorphic peak. In this sample garnets analysed for geothermometry are post-kinematic and so record a later metamorphic "event".

Sample P879

Mineralogy : Quartz, plagioclase, biotite, chlorite, garnet

Grain size : 0.2 - 3mm.

Texture : Garnets form porphyroblasts up to 3 mm across. Biotites define a strong penetrative fabric which encloses the garnet porphyroblasts. Garnet inclusions consist of oriented biotite grains and quartz pools, which define an earlier foliation.

Sample 1076

Mineralogy : Quartz, plagioclase, biotite, garnet and muscovite

Grain size : 0.1 - 5mm

Texture : A polygonal texture is developed. Biotites are strongly aligned and enclose earlier garnet porphyroblasts. Most garnet porphyroblasts are inclusion-free.

Sample 2059

Mineralogy : Quartz, plagioclase, biotite, garnet and chlorite

Grain size : 0.5 - 5mm

Texture : Biotites define a very strong fabric which wraps around garnet porphyroblasts. Garnet grains are riddled with inclusions of quartz and biotite. Secondary chlorite (after biotite) is present.

Sample 2046

Mineralogy : Quartz, plagioclase, biotite, muscovite and garnet

Grain size : 0.1 - 3mm

Texture : Quartz grains form a polygonal texture. Garnet porphyroblasts pre-date the penetrative schistosity which is defined by biotite alignment. Garnets are usually idioblastic in outline but some are partly replaced by quartz.

Sample FC11

Mineralogy : Quartz, plagioclase, biotite and garnet

Grain size : Relatively fine grained - 0.01 -1mm, with garnet porphyroblasts up to 3mm across.

Texture : There is no evidence for textural equilibrium. Compositional banding is defined by quartz-rich and biotite-rich layers. The schistosity is weakly developed and many biotite grains are not aligned parallel to the main schistosity. Garnets are pre- to syn-kinematic and have abundant quartz and biotite inclusions.

Sample 1120

Mineralogy : Quartz, plagioclase, biotite and garnet

Grain size : 0.05 -1mm. Garnet porphyroblasts are up to 3 mm across.

Texture : Garnet porphyroblasts preserve curved inclusion trails indicative of syn-kinematic garnet growth.

Sample 2048

Mineralogy : Quartz, biotite, plagioclase, garnet, muscovite, chlorite

Grain size : Coarse grained - 0.5 to 2mm with garnet porphyroblasts up to 5mm in diameter

Texture : A granoblastic texture is well developed. Garnet porphyroblasts are clearly pre-kinematic. Secondary chlorite and biotite are present.

Sample P782

Mineralogy : Quartz, biotite, plagioclase, chlorite and garnet

Grain size : 0.2 -1mm. Garnets are up to 1mm in diameter

Texture : Quartz grains interlock to form a weak granoblastic texture. Garnet porphyroblasts are enclosed by the penetrative foliation. Inclusions of quartz are common in garnet porphyroblasts.

Table 2.7 Summary of metapelite mineral assemblages

Sample No.	Qtz.	Plag.	Biotite	Garnet	Musc.	Chlorite	Kyanite
1051	√	√	√	√	√	√	√
P879	√	√	√	√		√	
1076	√	√	√	√	√		
2059	√	√	√	√		√	
2046	√	√	√	√	√	√	
FC11	√	√	√	√			
1120	√	√	√	√			
2048	√	√	√	√	√	√	
P782	√	√	√	√			

2.8.3 Limitations of Fe-Mg exchange geothermometry

Although textural equilibrium may have been achieved at peak metamorphic conditions it is difficult to assess the degree to which chemical equilibrium was attained. Furthermore, the compositions of co-existing minerals may undergo retrograde re-equilibration so that the mineral compositions of peak metamorphic conditions may not be retained. If minerals continued to equilibrate after the metamorphic maximum, geothermometers based on exchange equilibria may record temperatures which are lower than those reached at the metamorphic maximum. However, this problem may be partly resolved by estimating temperatures based on garnet cores and matrix (isolated) biotites, since retrograde re-equilibration is likely to be restricted to garnet rims and adjacent biotite grains.

Apart from the problems of defining equilibrium criteria and the effects of retrograde re-equilibration, geothermometers may yield inconsistent or geologically unreasonable results because of shortcomings in the published calibrations. For the purposes of this study the calibrations of Thompson (1976), Ferry and Spear (1978), Hodges and Spear (1982) and Indares and Martignole (1985) are used to estimate peak metamorphic temperatures.

The calibration of Thompson (1976) differs from other published geothermometers since it is purely an empirical calibration, which is based on the observed linear relationship between Ln (K_d) and 1/T, (K_d = $(Mg/Fe)_{garnet}$ / $(Mg/Fe)_{biotite}$). This calibration is based on naturally occurring low to medium grade metapelite assemblages and on independent temperature estimates obtained from metamorphic reactions. Since this calibration is based on naturally occurring assemblages it does not suffer from many of the problems associated with calibrations based on pure binary Fe/Mg mixtures.

Ferry and Spear's (1978) calibration is based on an experimental study using pure Fe-Mg binary mixtures. Although this calibration has serious shortcomings insofar as it does not take minor constituents (e.g. Al^{VI}, Ti), or non-ideal solid solutions into account, it nevertheless

remains the basis for several more recent, improved thermometers. While the calibration does not take account of the effect of minor constituents, indices of non-ideality have been defined which give a measure of how far biotite or garnet compositions deviate from ideal Fe-Mg mixtures. Ferry and Spear (*op. cit.*) suggest that biotites with non-ideality indices (defined as $(Al^{VI} + Ti) / (Al^{VI} + Ti + Fe + Mg)$) greater than 0.15 are unsuitable for use with this calibration. With the exception of two samples from the Palmental area (samples P872 and FC11) the non-ideality index exceeds 0.15 in all biotites analysed. Non-ideality indices are typically in the range 0.16 - 0.20. High Ti and Al^{VI} contents of biotites lower K_d values, and result in an overestimation of temperatures.

The calibration of Hodges and Spear (1982) which is closely based on that of Ferry and Spear (1978) consistently yields the highest temperature estimates for the samples studied (Table 2.6). Sample P879 is the only exception - the thermometer of Indares and Martignole (1985) yields a higher temperature estimate for this sample. Unlike the calibration of Ferry and Spear (*op. cit.*) the calibration of Hodges and Spear (*op. cit.)* takes account of non-ideality in pyrope-grossular solid solutuion. Like the Ferry and Spear calibration however, the presence of minor constituents (e.g. Ti in biotite) is not taken into consideration.

While the calibration of Ganguly and Saxena (1984) does not allow for non-ideal biotite compositions the calibration is more refined than that of Ferry and Spear (*op. cit.*) since the asymmetric non-ideal mixing behaviour of Fe and Mg in garnet is taken into account. However this calibration does not allow for the effects of minor constituents in biotite and so suffers from many of the shortcomings of earlier calibrations.

Indares and Martignole (1985) proposed two calibrations based on the experimental data of Ferry and Spear (*op. cit.*). However these calibrations are unlike previously published thermometers since corrections are applied for non-ideality in biotite e.g. Al^{VI} and Ti substitution) and non-ideality in garnet solid-solution. Indares and Martignole (1985) offer two equations based on different garnet solid-solution models. These are referred to as calibrations A and B (after Indares and Martignole, *op. cit.*) and are distinguished as $I + M_A$ and $I+M_B$ in Table

2.6. Calibration A is based on thermodynamic data from Newton and Haselton (1981) which accounts for non-ideality in Fe/Mg/Ca garnet solid solution, neglecting the effect of Mn. Calibration B (which consistently yields higher temperature estimates) is based on thermodynamic data and takes non-ideality of a quaternary garnet solid solution into account. Since the calibration of Indares and Martignole (*op. cit.*) corrects for non-ideality in both biotite and garnet it is likely to yield the most accurate temperature estimates. It should be noted however that the corrections applied for Ti and Al^{VI} in biotite are based on the empirical observations. Unlike non-ideality in garnet which can be modelled thermodynamically, the energetics of mixing in biotite are poorly understood so that corrections are empirical.

Since most samples studied have non-ideality indices >0.15 temperature estimates based on calibrations which do not correct for Al^{VI} and Ti in biotite (e.g. Ferry and Spear, 1978 ; Hodges and Spear, 1982 ; Ganguly and Saxena, 1984) are likely to be too high. However this effect is compensated for, to some extent, by retrograde re-equilibration between biotite and garnet grains. In summary, the calibrations of Indares and Martignole (1985), ($I+M_B$, Table 2.6) in which corrections for non-ideality in biotite and garnet are applied, and that of Thompson (1976) based on natural assemblages, are preferred. Since most biotites have non-ideality indices in excess of 0.15 calibrations which do not correct for non-ideality may yield unreliable temperature estimates.

2.8.4 Mineral chemistry

Representative analyses of biotites and garnets are given in Appendix 1. In general, biotites have relatively low TiO_2 contents (< 2.2%) although one sample from the Palmental area (FC11) has biotites which contain up to 3.5% TiO_2. Biotites are usually unzoned, whereas most garnets exhibit measurable core to rim variations in composition.

2.8.4.1 Garnet

Traverses across garnet grains were analysed to assess compositional heterogeneity between garnet rims and cores. Compositional zoning is most clearly observed for Fe, Mn, Mg and Ca. Although the core sections of many garnets are homogeneous, small variations in Mn, Mg, Fe and Ca are almost invariably observed close to garnet rims (e.g. sample P872, Fig. 2.12).

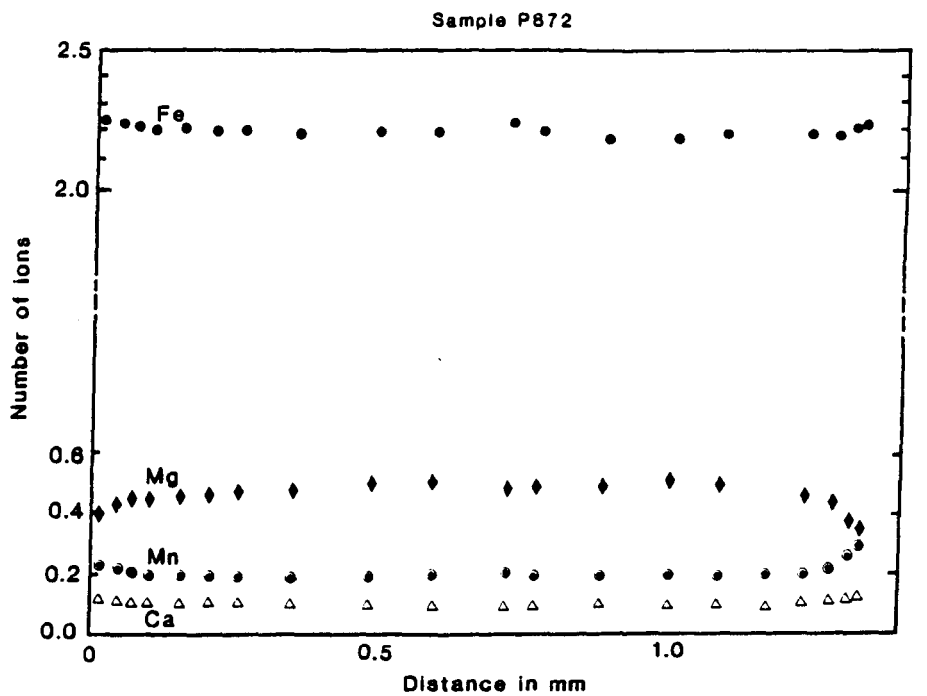

Fig. 2.12 Fe, Mg, Mn and Ca variations in a traverse across a garnet from sample P872. Garnets in most samples are relatively homogeneous and show minor compositional variations close to garnet rims only. Garnet formula contains 12 oxygens.

With the exception of sample 1051 (Fig. 2.14) which shows spectacular depletions in Mn in garnet rims, all samples have higher Mn contents in garnet rims. Ca content remains relatively constant across most garnet grains with a slight tendancy to increase in rims relative to cores. Exceptions to this trend are samples 1076,1051 (Fig. 2.14) and 2048 (Fig. 2.15) in which garnets have Ca depleted rims.

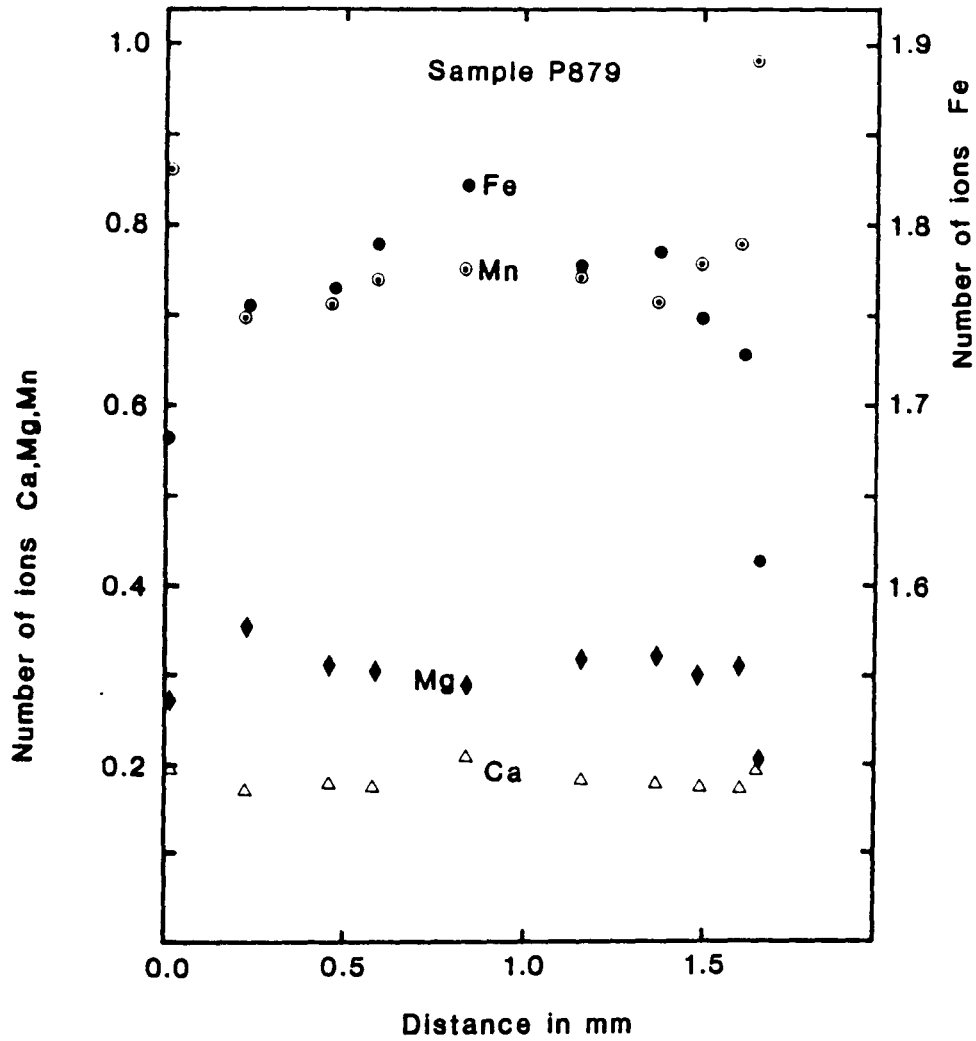

Fig. 2.13 Traverse across a garnet in sample P879. The Fe profile in this garnet is unusual since Fe content decreases towards the rims - the opposite to that observed in other samples.

The zoning patterns observed in most garnets analysed (e.g. Fig. 2.12) is similar to those commonly observed in high-grade metamorphic terrains (e.g. Hess, 1971 ; Grant and Weiben, 1971 ; Yardley, 1977 ; Barber and Yardley, 1985). In addition to the observed core to rim variations in Mn, Mg, Ca and Fe, the relatively flat compositional profiles of most samples (e.g. Fig 2.12) are characteristic of high grade terrains (Yardley, 1977).

Samples P879 and 1051 (Figs. 2.13 and 2.14) which yield the lowest temperature estimates (Table 2.6) also exhibit greatest compositional heterogeneity across individual grains. This observation is consistent with Yardley's (1977) conclusion that homogenisation of garnet compositions is due to self-diffusion of the cations which is a

temperature dependent process. Garnets from sample 1051 (Fig. 2.14) are strongly zoned in a reverse sense to that which is commonly observed in garnets from high grade terrains. This sample preserves garnets with "bell-shaped" (e.g. Mn profile) profiles which are usually attributed to fractionation during garnet growth (Hollister, 1966 ; Atherton, 1968) and is in marked contrast to the zoning patterns observed in all other samples studied.

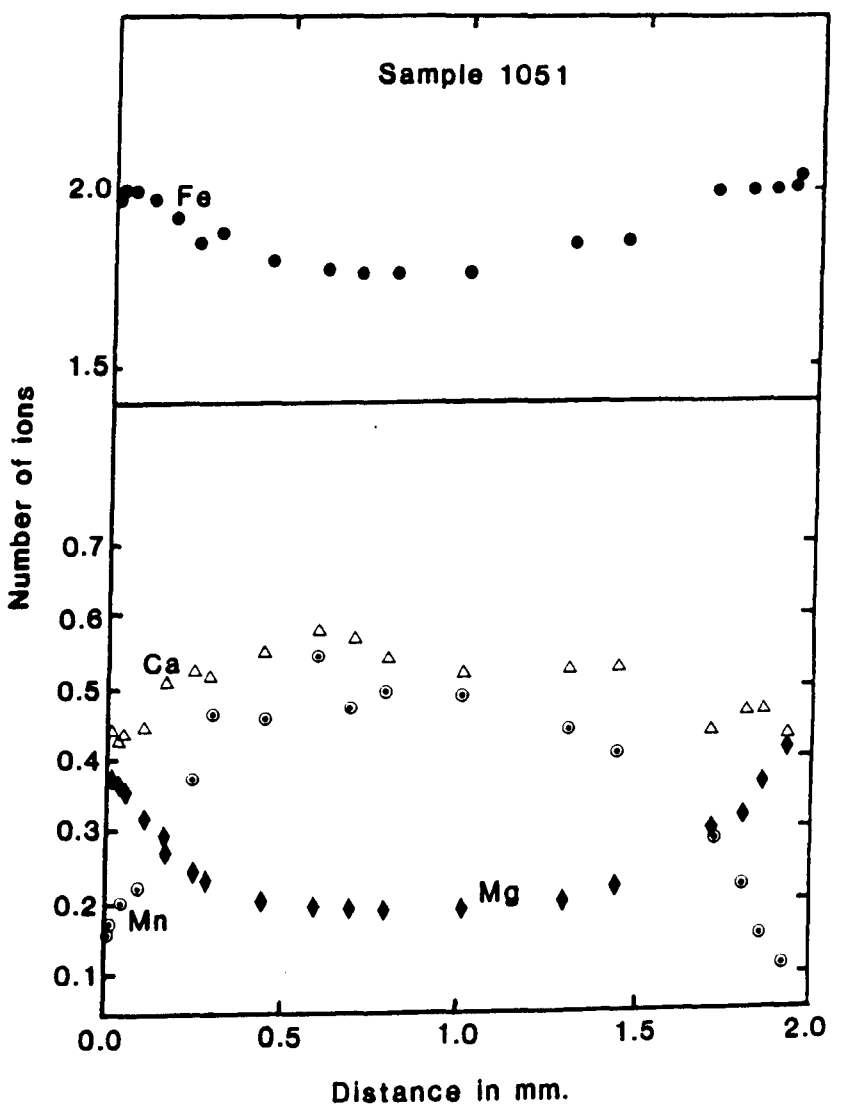

Fig. 2.14 Traverse across a post-kinematic garnet in sample 1051 showing extreme variations in Mg, Mn, Ca and Fe between rim and core sections. This "bell shaped" zoning is typical of garnets from low grade metamorphic terrains. Garnet formula contains 12 oxygens.

2.8.4.2 Biotite

No significant zoning was detected within individual biotite grains. Mg/(Fe + Mg) ratios have been calculated for biotites analysed in each sample and the range in compositions are shown in Fig. 2.11. Samples which yield the lowest temperatures have highest Mg/(Fe + Mg) ratios. In general, biotite grains in contact with garnet grains exhibit a greater range in Mg/(Mg + Fe) ratios than that recorded by matrix biotites. Mean Mg/(Mg +Fe) ratios are somewhat higher for biotites in contact with garnet grains although the values for contact and matrix grains overlap for most samples.

2.8.5 Garnet core to rim temperature profiles

Variations in temperature estimates along traverses analysed across individual garnet grains have been investigated. In general the highest temperature estimates occur close to or at the centres of garnet grains, while temperature estimates decrease on either sides towards garnet rims. Sample 1051 is an exception to this general trend since garnets from this sample record higher rim temperatures relative to those recorded by cores. However these garnets are post-tectonic and reflect a post-tectonic M_2 metamorphic peak.

If it is assumed that an individual garnet grain grew from core to rim while maintaining equilibrium with matrix biotites it is possible to infer temperature variations with time, by examining core to rim variations in recorded temperatures.

With the exception of sample 1051, garnets from all samples appear to have grown under conditions of decreasing temperature. Sample 1051 in contrast, records higher rim temperatures relative to those recorded by cores suggesting garnet growth under conditions of increasing temperature. This is consistent with the microtextural evidence, since these post-kinematic M_2 garnets may have grown in response to increasing temperature subsequent to the M_1 metamorphic peak. However, an alternative explaination is that the M_2

garnets in sample 1051 simply reflect the preservation of low-temperature "bell-shaped" profiles and the apparent increase in calculated temperatures towards garnet cores is an artifact of these "reverse zoning" low-temperature profiles.

2.8.6 Regional variations in estimated temperatures

Five of the nine samples studied are from the area around Steinhausen (Fig. 2.10) where Damara metasediments disappear beneath younger cover rocks to the north-east. Calculated temperatures suggest that M_1 temperatures reached at least 600 °C in this area (Fig. 2.10). These temperatures are consistent with the 588 °C temperature estimate obtainted by Kasch (1983, Fig. 2.10), from the area about 40km south of the sampled locality.

M_1 temperatures of at least 600°C in this region, strongly suggest that the mapped isograds (Fig. 2.10, after Kasch, 1983) may extend north-eastwards for a considerable distance beneath the younger calcrete deposits. This is consistent with the occurrence of garnet in isolated outcrops of pelitic schists around Steinhausen (Fig. 2.10).

Samples collected from the Palmental area (P782, FC11, P879) record a range of temperatures, (546 - 751°C). All samples were collected within an area of about 20km^2 and care was taken to ensure that the samples had not been affected by local contact metamorphic effects. The variations in recorded temperatures from this relatively small area highlight the difficulty in using geothermometers to document regional variations in metamorphic temperatures. However, if the two calibrations which consistently yield the lowest and highest temperatures (Indares and Martignole, 1985 ; calibration A and Hodges and Spear, 1982 respectively) are eliminated most temperature estimates are in the range 600 - 700°C.These estimates suggest that M_1 metamophic temperatures of the Palmental area exceeded those recorded in the north-west (Steinhausen area) where most estimates are about 600°C.

2.8.7 Conclusions from geothermometry studies

1. M_1 temperatures of about 600°C were reached at the northeastern extremity of the Damara metasediment outcrop in the area around Steinhausen. M_2 temperature estimates are in the range 514 - 571°C for this region (sample 1051 and Kasch, 1983).

2. Samples from the Palmental area record temperatures in the range 600-700°C, significantly higher than those of the Steinhausen area, but comparable to those recorded by sample 1120 (30km notrtheast of Windhoek, Fig. 2.10).

3. M_1 garnets appear to have grown under conditions of decreasing temperature while M_2 garnets (1051) retain bell-shaped (low-grade terrain zoning) profiles suggesting that significant cation self-diffusion did not occur during M_2 metamorphism.

4. Recorded temperatures are consistent with observed garnet zoning patterns. Samples which yield the highest temperature estimates have unzoned garnet profiles, intermediate temperature samples show "normal" high grade garnet zoning profiles (e.g. Hess, 1971 ; Yardley, 1977 ; Barber and Yardley, 1985 ; e.g. Fig. 2.12) while sample 1051 which records the lowest temperatures (of M_2) has a bell shaped profile (Fig. 2.14) characteristic of low-grade terrains (Yardley, 1977).

2.9 Summary of the geological history of the Palmental area

~ 700-650 Ma - Following deposition and burial of the Tinkas Member, D_1 deformation produced (tight ?) symmetrical folds which resulted in large scale stratigraphic repetitions and inversions. D_1 produced a weak spaced cleavage (S_1). Interface-spur formation between marbles and adjacent calc-silicate layers must have occurred during the earliest stages of D_1 while pore-fluids were still available for expulsion towards the extrados regions of F_1 fold closures.

~ 570 Ma - Intrusion of the Palmental diorite and Otjimbingwe syenite followed D_1 deformation. The Palmental diorite is intruded by the Otjimbingwe syenite on the west bank of the river Audawib. Contact metamorphism of metasediments by these intrusions produced skarns and migmatites locally.

~ 600-550 Ma - D_2 deformation produced an intense penetrative regional fabric in metasediments, diorite and syenite. Associated F_2 folds are large (several km amplitude) overturned asymmetric folds. The S_2 penetrative fabric encloses pre-D_2 garnet porphyroblasts. Locally syn- to post- D_2 diorite veins and dykes are intruded (e.g. the Swakop river diorite). This small diorite intrusion does not have a penetrative fabric.

~ 530 Ma - D_3 deformation produced open upright folds. D_3 deformation pre-dated the intrusion of the Donkerhuk granite, (age = 521 ± 15 Ma, Blaxland et al. 1979).

~ 520 Ma - Intrusion of the post-tectonic Donkerhuk granite about 1km south of the study area. Numerous post-tectonic pegmatite and two-mica granite dykes were intruded in the Palmental area.

CHAPTER 3

Granitoid petrography and field relations

3.1 Introduction

Syn- to post-tectonic Damara granitoids outcrop over an area of some 74,000 km^2 in central Namibia (Miller, 1983). Granitoids range in composition from syenites to diorites and granites (sensu-stricto), and at present exposure levels the aerial proportions of gabbro/diorite : tonalite/granodiorite : granite are 2 : 2 : 96 (Miller, *op. cit.*). The distribution of granitoids is shown in Fig. 3.3.

Granitoids range in age from about 650 Ma to 460 Ma (Downing and Coward, 1981 ; Marlow, 1981; Downing, 1982 ; Kroner, 1982 ; Hawkesworth *et al.*, 1983). Prior to 650 Ma syenites were intruded e.g. the Oas and Lofdal syenites which yield ages of 840 $\pm$ 12 Ma and 764 $\pm$ 60 Ma respectively, (Kroner, 1982 ; Hawkesworth *et al,* 1983). Post-D_1 pre-D_2 diorites were intruded at about 600 Ma (Ch. 5). Leucogranites are typically post-D_2 whereas most alaskites were intruded during D_3 in the Central Zone (Fig. 3.3) about 500 Ma ago.

3.2 Granitoid classification - previous work

Smith (1965) and Jacob (1974) subdivided the Damara granitoids on the basis of macroscopic appearance, intrusive relationships, mineralogy and colour. Smith (*op. cit.*) classified the syn-tectonic granitoids into red "gneissic" granite and grey biotite-rich gneiss and granite. Smith (*op. cit.*) recognised a stratigraphic control on the distribution of the different granitoid types and argued that the red granite-gneiss occurs in the cores of antiforms below the stratigraphic level of the Karibib Formation while the Salem-type granite suite occurs predominantly above the Karibib Formation. Smith (*op.cit.*) distinguished diorite gneiss and "homogenous intrusive granites" as well as late pegmatites and aplites.

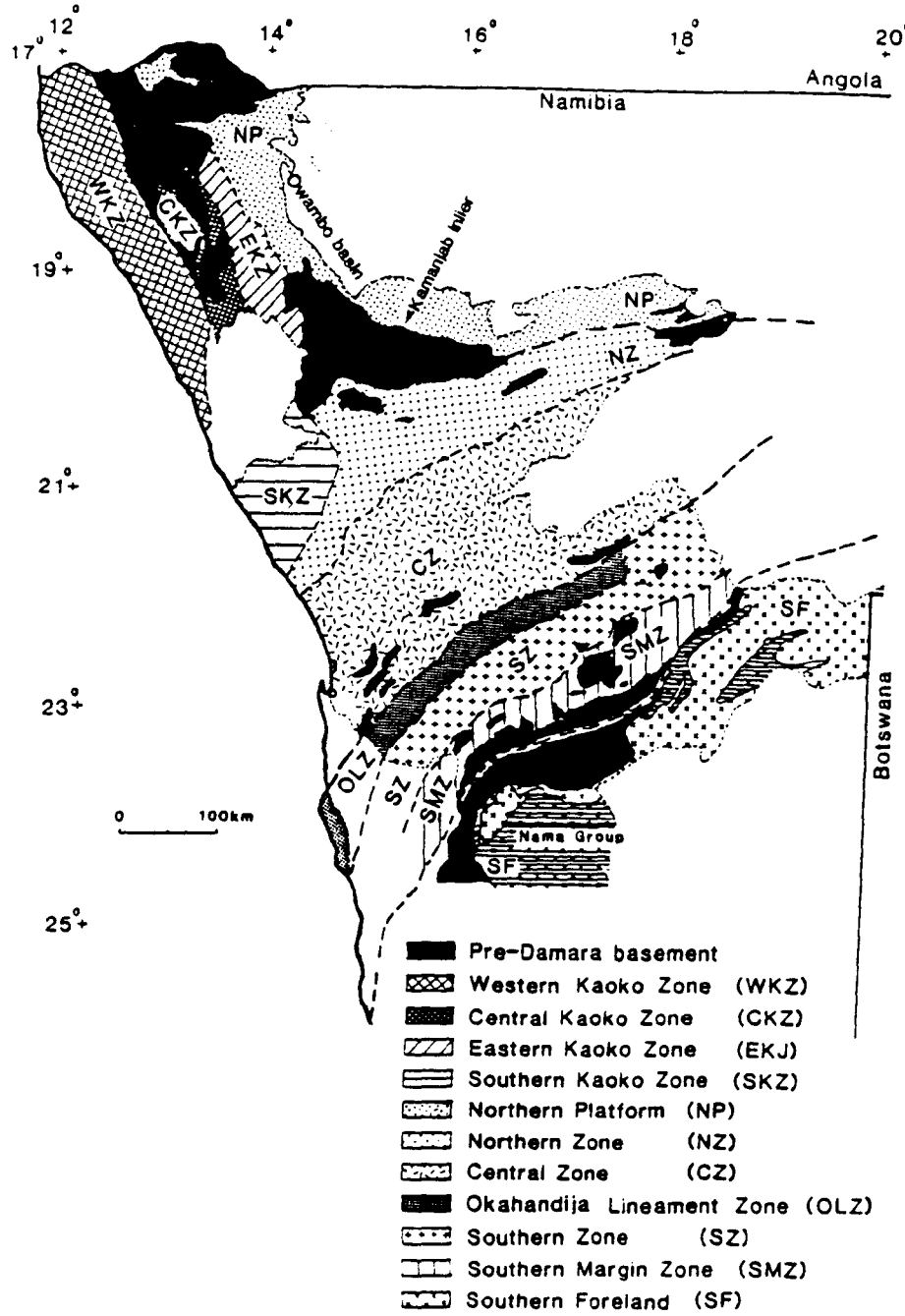

Fig. 3.1 Map of the Damara orogen showing the main structural zones referred to in text (after Miller, 1983). In text, the term coastal branch is used to refer collectively to the Kaoko belt zones shown in N.W. Namibia.

The term "Salem granite" has been used to describe biotite-rich porphyritic granitoids which include granodiorites, granites and adamellites. Typical Salem granite from the type example in the Swakop river on Farm Salem 102 contains large K-feldspar phenocrysts in a biotite-rich, but muscovite-free matrix (Jacob, 1974).

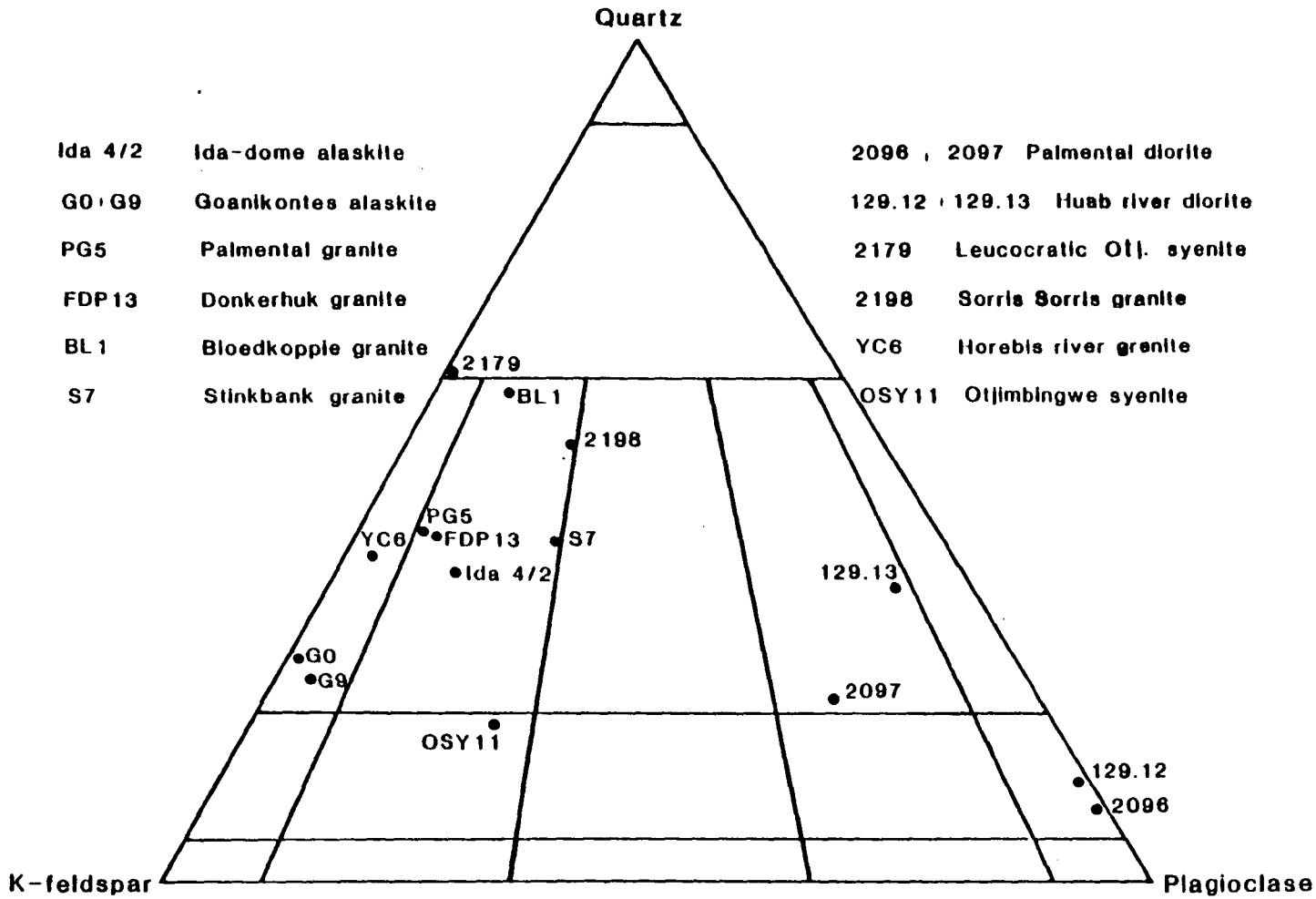

Fig. 3.2 Streckeisen diagram showing representative samples from Damara granitoids. Modal analyses are based on 1500-2000 point counts per thin section.

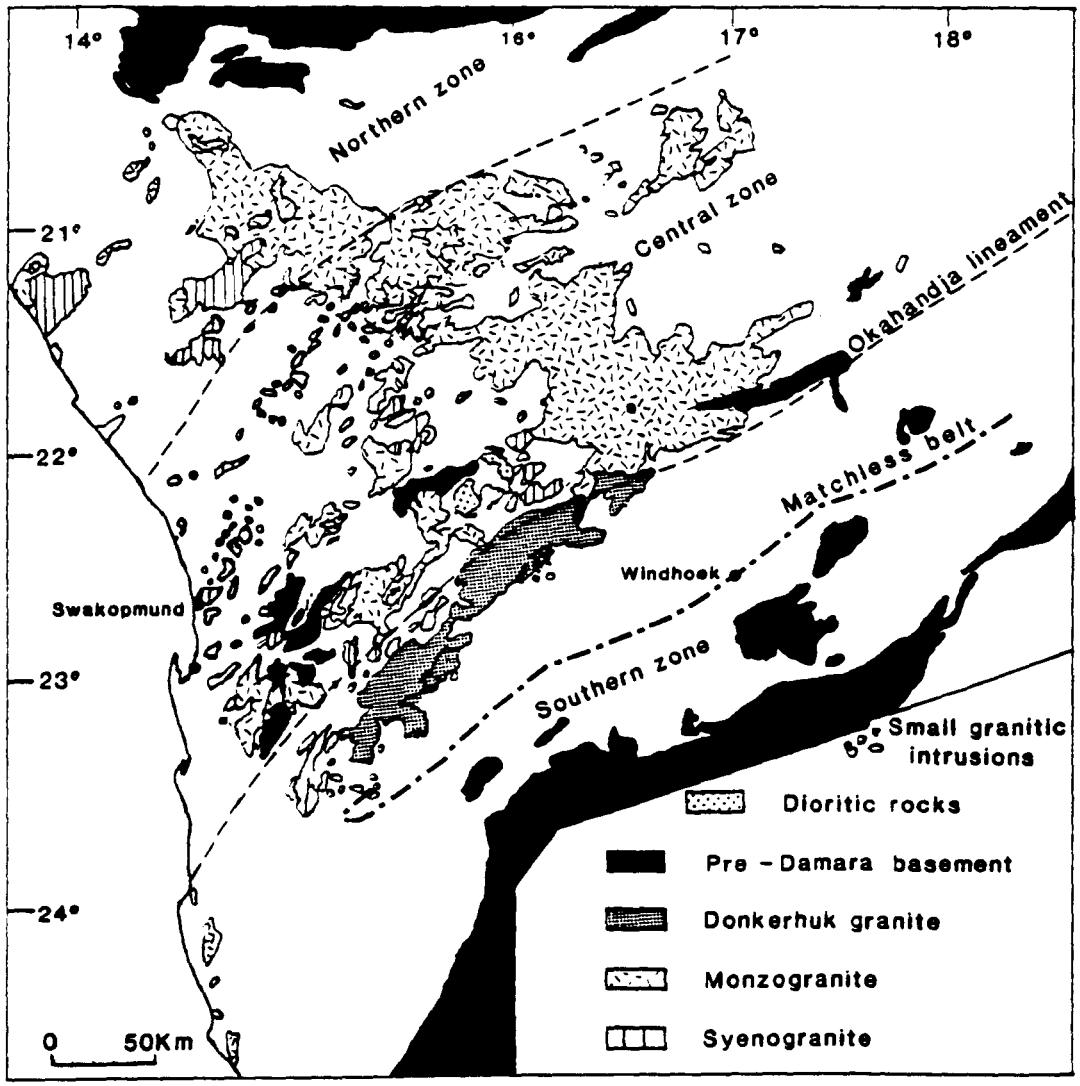

Fig. 3.3 Map of the intracontinental branch of the Damara orogen showing the distribution of Damara granitoids (after Miller 1983). The positions of the Okahandja lineament and the Matchless belt are also shown.

Jacob (*op. cit.*) pointed out that the term "red gneissic granite" is difficult to apply in the field because of the difficulty in distinguishing between intrusive red-granite, red gneissic pre-Damara basement, and late leucocratic alaskites. Marlow (1981) rejected Smith's (*op. cit.*) classification and pointed out that there is not a total stratigraphic control on the

distribution of the red gneissic granites and Salem-type granitoids. Marlow (*op. cit.*) proposed a four-fold classification of the Damara granitoids into syn- to post-tectonic Salem-type granitoids and red granites, and late- to post-tectonic leucogranites and alaskites.

3.2.1 A revised classification scheme

It is proposed that the term "red granite" should be discontinued as a field classification term. The other three granitoid groups identified by Marlow (*op. cit.*) i.e. leucogranites, alaskites and Salem-type granitoids remain as useful field terms. The term "Salem-type granitoid" is preferred to "Salem granite" because although readily identifiable in the field, the Salem-type granitoids are heterogeneous geochemically (Ch. 4).

The term "red-granite" should be discontinued because it lumps together granitoids which are petrogenetically unrelated. For example, the red-granite from the Horebis River locality (Downing, 1982 ; YC series samples) is extremely enriched in high field strength (HFS) elements and is classified as a within-plate granite according to the scheme of Pearce *et al.* (1984) for the tectonic interpretetion of granitic rocks. On the other hand, the red granite from Farm Otjua 37 (Marlow, 1981) has the trace-element characteristics of a crustal melt.

The term leucogranite is a useful field term and characteristic mineralogies may be used as descriptive prefixes (e.g. 2 mica leucogranite, cordierite bearing leucogranite etc). The term "alaskite", though often rather loosely applied (strictly an alaskite plots in the alkali-feldspar granite field of a "Streckeisen diagram", Streckeisen, 1975) remains a useful field-term in the Central Zone. It is suggested that diorites and quartz-diorites be distinguished as a separate class and should not be lumped together with the Salem-type granitoids when porphyritic.

In summary, it is proposed that the leucogranite, alaskite and Salem-type groupings be retained as useful field terms and that the term red-granite should be abandoned. Diorites and quartz-diorites form an additional class which may be readily distinguished in the field.

3.3 Compositional types - Petrography and field-relations

Petrographic descriptions are given for representative samples from each of the granitoids which will be discussed in detail in Ch. 4. Each granitoid has been classified according to the Streckeisen classification scheme (Streckeisen, 1975) on the basis of 1500-2000 point counts per thin section (Fig 3.2).

Since the leucogranites, alaskites and Salem-type granitoids have similar geochemical affinities and will be discussed as a group in Ch. 4 their mineralogical features are discussed together here. The principal mineralogical characteristics of this granitoid group are summarised in Table 3.1.

Table 3.1 Summary of mineralogy of leucogranites, Alaskites and Salem-type granitoids

	Leucogranites	**Alaskites**	**Leucocratic Salem-type**
Major phases	quartz, K-feldspar perthite, plagioclase muscovite	quartz, microcline orthoclase, plagioclase	quartz, K-feldspar plagioclase, biotite
Minor phases	biotite, muscovite hornblende, garnet	biotite, muscovite	myrmekite, hornblende
Accessory phases	zircon, apatite, sphene	zircon, sphene	zircon, monazite, apatite

3.3.1 The leucogranites

Leucogranites are characterised by quartz, K-feldspar, plagioclase (usually albite), muscovite and minor amounts of biotite. In strongly peraluminous leucogranites, garnet is sometimes present in addition to muscovite and biotite. Cordierite has not been observed. Modal analyses are given in Table 3.2.

Table 3.2 Modal analyses of the Damara granitoids

Sample	Quartz	K- Spar	Plag.	Hble.	Biotite	Musc.	Chlorite	Cpx.	Opaq.
Alaskites									
Ida 4/2	36 %	57 %	6 %	-	-	-	-	-	1 %
G0	27 %	72 %	0.6 %	-	-	-	-	-	0.4%
G9	25 %	72 %	1 %	-	1.5 %	0.25 %	-	-	Tr.
Leucogranites									
PG5	38 %	47 %	6 %	-	8.0 %	1.0 %	-	-	-
FDP 13	40 %	47 %	7 %	-	4 %	0.8 %	(also ~ 1.2% sillimanite)		
BL1	58 %	33 %	7 %	-	1 %	1 %	-	-	-
S7	39 %	37 %	19 %	-	4 %	1 %	-	-	
Diorites									
P2096	4 %	0.4 %	41 %	51 %	0.6 %	-	2 %	0.5 %	0.5%
P2097	11 %	11 %	30 %	48 %	-	-	-	-	Tr.
129.12	8 %	-	58 %	22 %	10 %	-	(1% epidote)	0.6	0.4
129.13	31 %	7 %	51 %	8 %	2 %	-	-	0.3 %	0.7 %
Syenites / intraplate granitoids.									
Osy 11	17 %	47 %	20 %	14 %	0.5 %	-	0.9 %	0.5 %	0.1 %
SOR 2198	50 %	29 %	15 %	-	4.0 %	1.0 %	0.5 %	-	0.5 %
OT2179	44 %	27 %	-	10 %	-	15 %	-	3.0 %	1.0 %
YC 6	39 %	56 %	3 %	-	1.0 %	-	-	-	1.0 %

The Bloedkoppie leucogranite consists of quartz, microcline, plagioclase (An_{20}) and biotite, with minor muscovite and accessory sphene, zircon and apatite. Grain size is in the range 0.02-3mm and no fabric is developed. Symplekitic intergrowths of quartz and feldspar are occasionally observed. Sample BL1 is a representative sample for which the proportions of minerals have been determined by point counting. Quartz, K-feldspar, plagioclase and biotite are in the proportions 58 : 33 : 7 : 2.6, and this sample plots in the granite field in Fig. 3.2. Some alkali feldspars are slightly sericitised although feldspar alteration is generally not severe.

The Palmental granite consists of quartz, K-feldspar, biotite, primary muscovite and minor amounts of albite. A good igneous texture is preserved. Grain size is in the range 0.1-5mm. K-feldspar grains are sericitised but biotites are fresh. Accessory phases include zircon, apatite and monazite. Modal analysis indicates that the rock is a granite sensu-stricto (Fig. 3.2).

The Stinkbank leucogranite consists of quartz, K-feldspar, plagioclase, biotite and muscovite. Muscovite is generally primary though some is associated with minor alteration. Biotite is unaltered and contains abundant zircon inclusions. Minor sericitisation of plagioclase and K-feldspar is observed and occasionally non-sericitised albite rims occur around sericitised cores. Plagioclase is typically about An_{10} in composition. Perthite is occasionally observed. Accessories include apatite, zircon and monazite.

The equigranular Otjua red granite consists of quartz, microcline, orthoclase and plagioclase with minor amounts of biotite and muscovite. Feldspars are slightly sericitised. Accessories include Fe oxides, monazite and zircon. Plagioclase is about An_{18}.

The leucogranites are typically late- to post-tectonic and commonly have a batholithic style of intrusion. However, numerous narrow (<1m wide) two mica leucogranite dykes occur (e.g. in the Palmental area). The Donkerhuk granite forms a large batholith with a thermal aureole. Migmatites are observed at granite/Kuiseb schist contacts near the margins of the batholith.

In the high-T Central Zone (Fig. 3.4) alaskites have been generated by anatexis of pre-Damara basement and Nosib Group rocks, and nebulous transition zones exist between the alaskites and their precursors (Smith, 1965 ; Jacob, 1974 ; Sawyer,1976,1981; Bunting,1977). Leucogranites frequently contain enclaves (usually xenoliths of pelitic schists), many of which have sharply defined contacts with their granite hosts (e.g. pelitic xenoliths in the Palmental granite, Ch.2).

In the southern Central Zone foliated red granites occur as concordant bodies in the cores of antiforms in the stratigraphic position of the pre-Damara basement and the Nosib Group (Miller, 1983).

3.3.2 Alaskites

All the alaskite intrusions are similar mineralogically. Petrographic studies of alaskite samples from the Rossing, Valencia, Ida-Dome and Goanikontes localities of the Central Zone (Fig.3.1) allow the following generalisations to be made. Alaskites consist almost entirely of quartz and K-feldspar, usually microcline. Biotite is the only ferromagnesian observed and is present only in small amounts (< 2%). Most alaskites show little sign of alteration although minor sericitisation is sometimes observed and secondary muscovite is occasionally developed. Plagioclase is usually present (An_{10}). Myrmekitic textures and perthite are present in the Goanikontes alaskite. Alaskites are generally coarse grained, sometimes with K-feldspar grains up to several cms across. Modal analyses of alaskites are given in Table 3.2 and are plotted in Fig 3.2.

Alaskites occur only in the Central Zone and the Northern Zone, i.e. north-west of the Okahandja lineament and are characterised by their extremely leucocratic nature as well as their anastomosing vein-like style of intrusion. Alaskites occur mainly in the Khan Formation, but also intrude the pre-Damara basement and the base of the Swakop Group (Jacob,1974 ; Berning et al , 1976 ; Corner,1983 ; Marlow,1983). Occasionally migmatites derived from both

the pre-Damara basement and the Nosib Group rocks are indistinguishable from alaskite dykes (Plate 3.1).

Plate 3.1 Alaskite dykes in the Khan Gorge area of the Central Zone. Alaskites are formed by near in-situ melting of Damara metasediments and pre-Damara basement.

3.3.3 Salem-type granitoids

Goas Salem-type granitoid : This porphyritic intrusion consists of zoned K-feldspar phenocrysts up to 30mm long, set in a matrix of quartz and biotite. There is no microscopic fabric and feldspar sericitisation is minimal. Symplektite is frequently developed.

Onanis Salem-type granitoid : This intrusion consists of quartz, biotite, plagioclase (An_{30}), K-feldspar and minor muscovite. Grain size is in the range 1-10mm. K-feldspars are occasionally slightly sericitised and myrmekitic textures are present. Quartz shows undulose extinction. Accessory minerals include secondary chlorite, apatite, opaques and zircon.

Valencia Salem-type granitoid : This granitoid consists of quartz, K-feldspar (mostly orthoclase), plagioclase (An_{31}), biotite and accessory Fe-oxides, monazite and zircon . In general, feldspars are extremely fresh with no evidence for significant sericitisation. Grain size is in the range 1-10mm. Perthite is developed locally.

The Salem-type granitoids occur predominantly above the Karibib marbles in the stratigraphic position of the Kuiseb schist. Miller (1983) noted that the syn-tectonic and late- to post-tectonic Salem-type granitoids have different styles of intrusion. Many pre-D_3 syn-tectonic Salem-type intrusions closely follow the irregular forms of synformal domains and often surround F_3 domal structures (Smith,1965 ; Jacob,1974 ; Klein,1980). The margins of pre-D_3 plutons have an intense foliation which often becomes less penetrative towards the centre of the intrusion. In contrast, the post-tectonic Salem-type granitoids in contrast, generally have a fairly rounded form and many are virtually enclosed by Kuiseb schist, (Miller, 1983). Salem-type granitoids are frequently surrounded by wide migmatitic thermal aureoles (Miller, 1980) when intruded into Kuiseb schist.

3.3.4 The diorites

In the Palmental diorite amphiboles are the dominant constituent and are yellowish-green to dark-green in p.p.l. Plagioclase (An_{41}) is frequently altered and generally has a "dusty" appearance. Small, but variable amounts of quartz and K-feldspar are present in some thin sections. Secondary muscovite is observed as an alteration product of feldspar. Accessory minerals include sphene and epidote. Samples plot in the diorite/granodiorite fields of Fig. 3.2.

The Huab-river diorite consists of hornblende and plagioclase (An_{37}) with minor amounts of clinopyroxene, quartz, biotite, chlorite, muscovite, sphene and epidote. Feldspars are extensively sericitised and secondary muscovite is present. Original igneous zoning in preserved in some plagioclase grains. The rock is dioritic to granodioritic in composition (Fig. 3.2).

Diorites which outcrop in the Central Zone preserve a strong penetrative S_2 fabric and are pre- to syn-D_2. An earlier, non-penetrative weak S_1 fabric associated with F_1 folds occurs in pelitic xenoliths within the Palmental diorite suggesting that diorite intrusion was post-D_1 but pre-D_2 (Ch. 2). Diorites have sharp contacts with Damara metasediments and frequently have migmatitic contacts and skarns where diorites intrude pelites and calc-silicates of the Tinkas Formation (Plate 2.2, Ch. 2). Detailed descriptions of diorite field relations from the Palmental area are given in Ch 2.

3.3.5 Other granitoids

Granitoids from the Sorris-Sorris, Horebis River, Dachsberg and Otjimbingwe syenite complex display similar geochemical affinities (Ch.4) and are discussed together here.

The post-tectonic porphyritic Sorris-Sorris granitoid consists of quartz, K-feldspar,

plagioclase (An_{12}), biotite and secondary muscovite. Relatively large K-feldspar phenocrysts (up to 10 mm across) give the rock a porphyritic appearance in thin section. A good igneous texture is preserved. Locally, K-feldspar sericitisation is quite intense. Accessory phases include zircon, apatite and monazite. Sample no. 2198 from the Sorris-Sorris intrusion plots in the granite (sensu-stricto) field on a Streckeisen diagram (Fig 3.2).

The post-D_1, pre-D_2 Horebis-river granitoid consists of quartz, K-feldspar, plagioclase, biotite and muscovite with minor magnetite and haematite. Grain size is very variable within the range 0.02-10mm. Large phenocrysts of K-feldspar up to 5mm across are slightly sericitised although the rock is generally unaltered. Biotites show a weak preferential alignment and define a weak microscopic fabric. Perthite is occasionally observed. Sample YC 6 from this intrusion plots in the alkali-feldspar granite field on a Streckeisen diagram (Fig 3.2).

The Dachsberg granite which forms a small plug-like intrusion consists almost entirely of K-feldspar and quartz. Spectacular symplekitic and graphic textures are developed suggesting simultaneous crystallisation of quartz and alkali-feldspar. Feldspars are fresh and there is no evidence for sericitisation. Grain size is in the range 0.2-5mm.

The Otjimbingwe syenite has a strong penetrative fabric formed during the major regional D_2 deformation in this part of the Central Zone (Ch. 2). The mineralogy of this intrusion consists of K-feldspar, hornblende, biotite, clinopyroxene and minor amounts of quartz (Sample OT 2179, Table 3.2). Other minerals are hornblende, clinopyroxene and minor amounts of quartz. Amphiboles are buff coloured to light green in p.p.l. and biotites appear fresh in thin section. Minor sericitization of orthoclase is observed in some samples. Sphene and zircon are present as accessories.

The leucocratic Otjimbingwe syenite is equigranular and consists of K-feldspar, plagioclase, quartz and hornblende. K-feldspars are extensively sericitised in some samples. Grain size is in the range 0.1-2mm. Sample OSY 11 (Table 3.2) from this intrusion plots in the syenite field in Fig. 3.2.

3.4 Regional metamorphism and granitoid genesis

In general, temperatures of regional metamorphism increased westwards from the margins of the orogen both in the intracontinental and coastal branches (Fig 3.3). Most authors (e.g. Jacob ,1974 ; Hoffer, 1977 ; Blaine, 1977 ; Puhan, 1979 ; Haack *et al* 1980 and Hartmann *et al* 1983) argue that metamorphism occurred as a single event which commenced syn-tectonically with D_1 deformation (Jacob, 1974 ; Klein, 1980) and culminated in a syn- to post-tectonic peak. The highest grades were reached in the Central Zone (Fig 3.4) and culminated in syn-D_2 partial melting (Jacob, 1974).

Sawyer (1981) argued that a second metamorphic peak produced garnet-cordierite assemblages during late D_3 deformation in the Central Zone. Temperatures of at least 650°C were reached in the Central Zone at pressures of between 2.5-4 kb. In contrast, the Southern Margin Zone was characterised by high pressure, relatively low temperature metamorphic conditions of up to 580°C at 8-10 kb (Kasch 1983).

In general, the plutonic rocks of the Central Zone form permissive intrusions and frequently lack thermal aureoles, reflecting intrusion into relatively hot country rocks. High grade metamorphism in the Central Zone has produced near in-situ anatexis of metasediments to produce alaskites. Leucogranites have been formed by anatexis of both Pre-Damara basement and Nosib Group metasediments (Smith,1965 ; Jacob,1974 ; Sawyer, 1976,1981 ; Bunting, 1977). Several in-situ migmatites have been produced by partial-melting of pre-Damara basement and Damara metasediments (Sawyer, 1976 ; Bunting, 1977 ; Jacob *et al.*, 1983).

The Salem-type granitoids of the Central Zone typically have wide migmatitic thermal auleoles and are often surrounded by in-situ migmatites, injection migmatites and pegmatite intrusions (Miller, 1980).

In summary, plutons in the Central Zone were intruded into a relatively high temperature enviroment so that thermal aureoles are generally lacking.

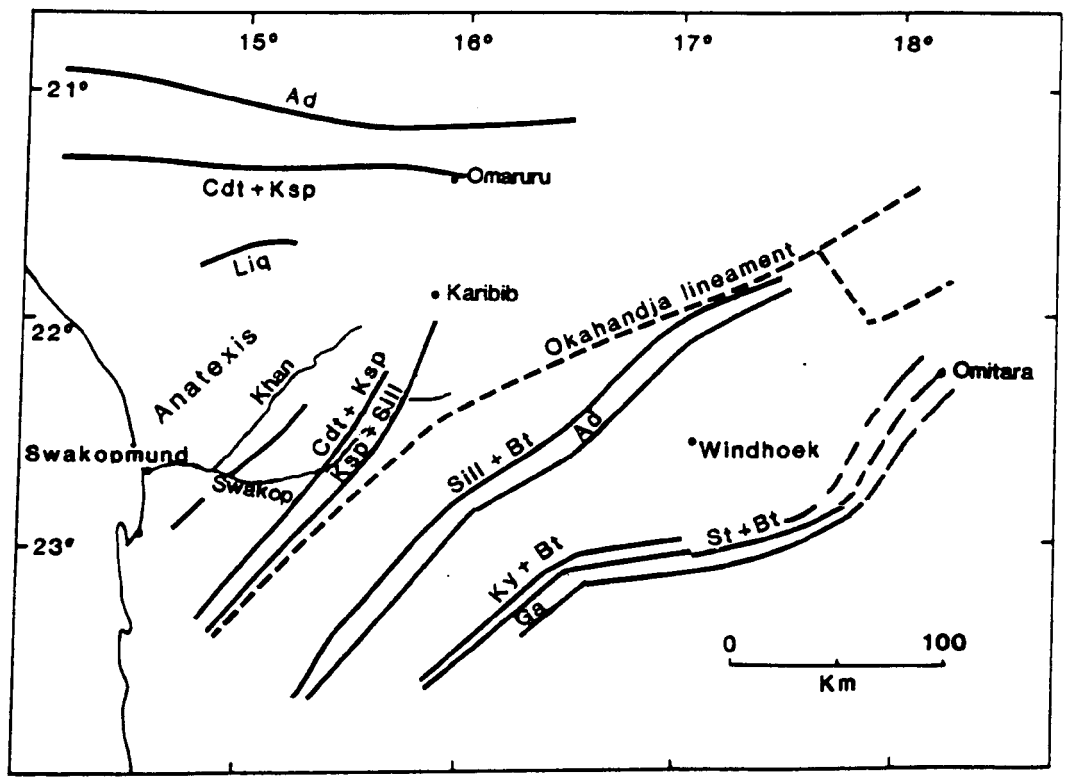

Mineral abbreviations

Ky - Kyanite	St - Staurolite
Ad - Andalusite	Ksp - K-feldspar
Sill - Sillimanite	Ga - Garnet
Cdt - Cordierite	Bt - Biotite
Liq - Liquid	

Fig. 3.4 Map of the Damara orogen showing the main reaction isograds in metapelites (after Kasch, 1983). South of the Okahandja lineamant a Barrovian-type sequence occurs whereas the region north of the lineament is characterised by high -T, low-P conditions.

High grade metamorphism has produced migmatites and granitoid formation by near in-situ anatexis (e.g. the alaskites of the Central Zone). The Salem-type granitoids were apparently derived from deeper structural levels since they are intrusive at all crustal levels and are accompanied by thermal aureoles. In contrast, granitoids emplaced in the relatively low temperature Northern Zone (Fig. 1.2) are accompanied by wide thermal aureoles.

3.5 Timing of deformation and intrusive events

The earliest Damara magmatism e.g. Oas syenite, Abbabis felsite dykes, Lofdal nepheline syenite and Naauwpoort lavas (840-728 Ma) (Kroner, 1982 ; Hawkesworth et al. 1981,1983 ; Miller and Burger, 1983) pre-dates major deformation events.

In the period 650-630 Ma intense D_1 deformation occurred in the coastal and intracontinental belts of the orogen (Miller, 1983). Several intrusions of diorite to granodioritic composition (e.g. Palmental diorites, Okombahe Salem-type granodiorite and the Otjosondjou quartz monzonite are post-D_1 and pre-D_2. Detailed descriptions of the relationship between deformation and diorite intrusion in the Palmental area are given in Ch. 2.

D_2 deformation was strongly diachronous, occurring at about 600 Ma in the Northern and southern Central Zones and at about 540 Ma in the Southern and Southern Margin Zones (Fig 3.4). Voluminous Salem-type granitoids which were intruded at about 550 Ma are post-D_1 and pre-D_2 in the northern Central Zone and post-D_2 in the southern Central Zone (Miller, 1983).

D_3 deformation in the southern Central Zone occurred at about 540 Ma and was followed by the post-D_3 peak of regional metamorphism in the Central Zone and Southern Zone. However D_3 deformation in the northern Central Zone (at about 470 Ma) occurred later than in the southern Central Zone (Miller, *op. cit.*).

Granitoids intruded after about 540 Ma in the southern Central Zone and later than 470 Ma in the northern Central Zone post-date all major episodes of deformation. Most

leucogranites (e.g. the Donkerhuk granite, Bloedkoppie leucogranite, Otjua red granite and Stinkbank leucogranite) post-date the major D_2 fabric forming deformation event in the Central Zone. Alaskites in the Central Zone were intruded after the main D_2 deformation episode and many are syn-D_3 e.g. the Goanikontes, Valencia and late Rossing alaskites. (Marlow, 1981 ; Briqueu *et al*, 1982 ; Downing, 1982; Hawkesworth and Marlow, 1983 ; Hawkesworth et al 1983). A fracture cleavage in the post-D_2 Ida-Dome alaskite which has an age of 542 ± 33 Ma is due to D_3 doming (Marlow, 1981,1983).

3.6 Summary and conclusions

A revised granitoid classification scheme is proposed. It is suggested that the term "red granite" should be abandoned as a field classification term. The term "Salem granite" should be discontinued although "Salem-type granitoid" is a useful field term to describe porphyritic biotite-rich leucocratic granitoids. Wherever possible however, more specific petrologic names should be applied. In particular diorites and granodiorites should be distinguished as a separate group and should not be lumped together with Salem-type granitoids when porphyritic.

The diorites and Salem-type granitoids are typically pre- to syn-tectonic while most leucogranites and alaskites are post-tectonic. In general, granitoids which outcrop in the high temperature Central-Zone lack thermal aureoles. High grade metamorphism in the Central Zone produced incipient anatexis and locally, alaskites were formed by near in-situ anatexis of Damara metasediments.

The Salem-type granitoids are always clearly intrusive however, and usually have thermal aureoles. Modal analyses (Fig 3.2) confirm that the Huab-river and Palmental intrusions are dioritic to granodioritic in composition. Most granitoids plot in the granite (sensu-stricto) field on a Streckeisen diagram. Alaskite samples are alkali-feldspar granites i.e. alaskites sensu-stricto.

CHAPTER 4

Granitoid major and trace element geochemistry

4.1 Introduction

Major and trace element data are presented for a wide range of Damara granitoids. Smooth inter-element variation patterns on Harker diagrams reflect primary igneous processes and suggest that element redistribution by subsolidus alteration is minimal for most intrusions. Petrographic studies (Ch. 3) confirm that most Damara granitoids are relatively unaffected by subsolidus alteration.

In general, the classification of granitoids has proved problematical and several classification schemes have been published (e.g. Peacock, 1931; Shand, 1951 and Pearce *et al.*, 1984). These geochemical classifications distinguish more than twelve different granitoid types! Clearly there is a need for a unifying approach which seeks to understand petrogenetic processes and so make links between the various granite types. Petrologists and geochemists concerned with granite petrogenesis must seek to answer two key questions

1. What are the petrogenetic processes which produce the systematic geochemical variations on which classification schemes have relied?

2. Can apparent links between different classification schemes (e.g. the tendancy for many peralkaline granites to be enriched in high field strength (HFS) elements and so plot as within-plate granites) be a reflection of a common petrogenetic process?

The approach adopted here is to combine several geochemical parameters which form the basis of the previously published classifications. Combining major and trace element variations in the Damara granitoids has led to the identification of three geochemically distinct granitoid end-member compositions. Division of the Damara granitoids into three groups is also

supported by isotopic data (Ch. 5). This approach seeks to establish links between the previously published granitoid types and to explain them in terms of petrogenetic processes.

4.2 The three granitoid groups

Three geochemically distinct granitoid types have been identified by combining some of the geochemical parameters from previously published granitoid classification schemes. With some exceptions which are discussed below, these three granitoid types - crustal-melt granitoids, calc-alkaline granitoids and within-plate granitoids broadly coincide with the syn-collision, volcanic-arc, and within-plate groups of Pearce *et al.*, (1984). Fig 4.1 is a plot of the Shand index (Shand, 1951) against the HFS elements Nb+Y (Pearce *et al.*, 1984).

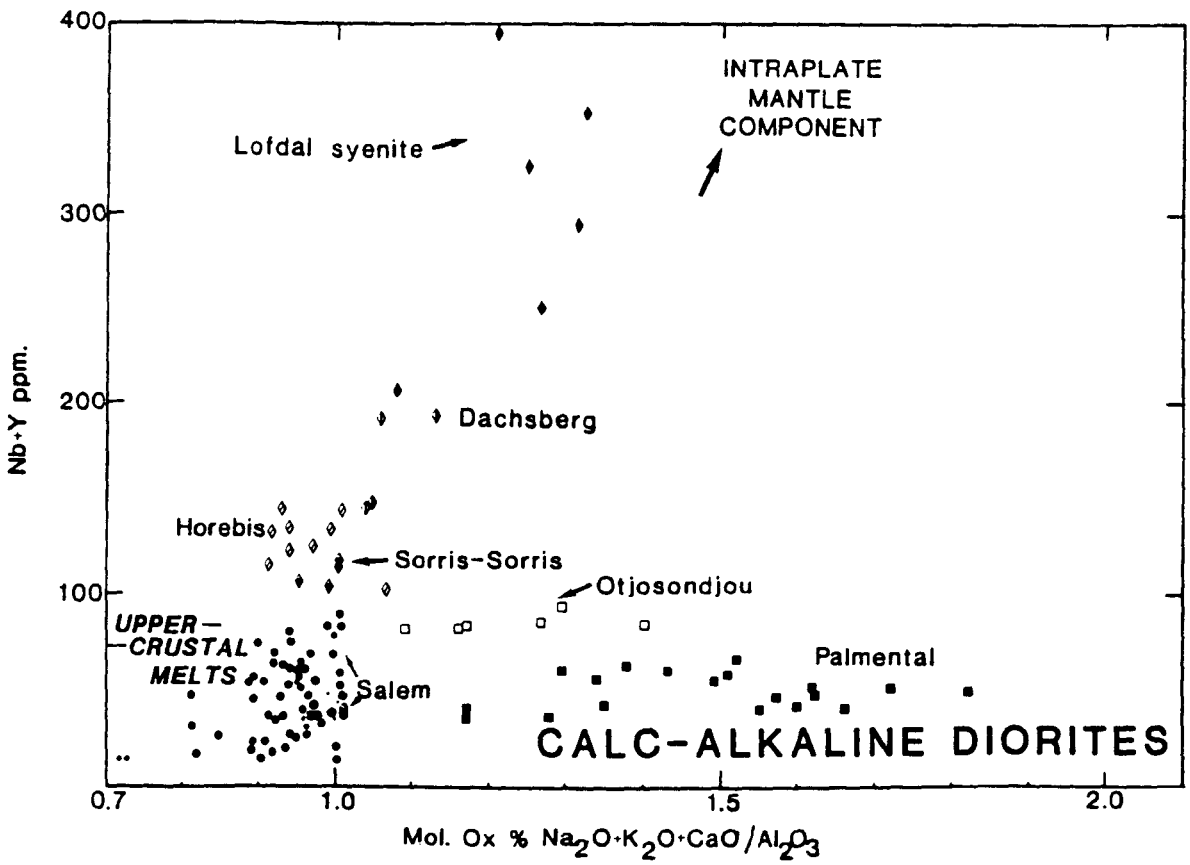

Fig 4.1 Plot of 1/Shand index (CNK/A) Vs. the high field strength (HFS) elements Nb + Y. Upper crust melt granitoids (alaskites and leucogranites) are peraluminous whereas within-plate granitoids and calc-alkaline diorites are characterised by high and low HFS element abundances respectively. The Dachesberg and Lofdal syenite intrusions are typical within-plate granitoids while the Otjosondjou and Palmental intrusions are calc-alkaline diorites.

Crustal-melt granitoids are characterised by high alumina contents and low HFS element abundances. Calc-alkaline diorites also have low HFS element abundances but have lower alumina contents relative to other major element oxides and exhibit a fractionation style which distinguishes them as "calc-alkaline" (Peacock, 1927), (Fig. 4.2). Within-plate granitoids are characterised by elevated HFS element contents, low CaO and relatively low alumina contents.

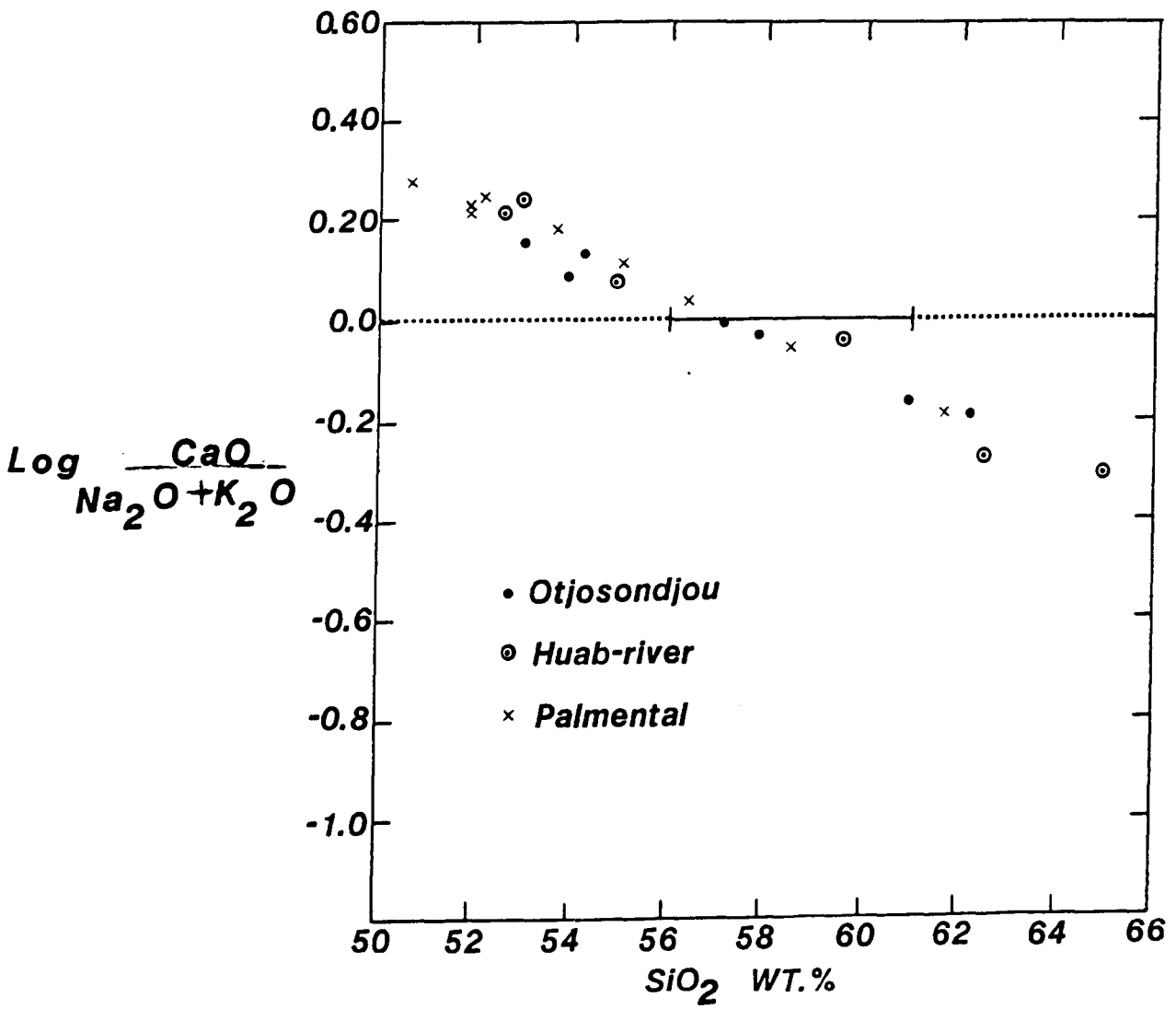

Fig. 4.2 Calcium oxide / alkalis Vs. silica diagram for Damara diorites (after Brown, 1979). Damara diorites have alkali-lime indices (Peacock, 1931) in the range 57-61, i.e. they are calc-alkaline.

Isotopic data, which are discussed in detail in Ch. 5 also distinguish the three granitoid types. Fig 4.3 is a plot of Ɛ Sr Vs. Nb+Y. The crustal-melt granitoids are characterised by high Ɛ Sr and low HFS abundances. This implies that crustal-melt granitoids have had high time-integrated Rb/Sr ratios. It is argued in Ch.5 that high time-integrated Rb/Sr ratios and depletions in HFS elements reflect the same petrogenetic process i.e. intracrustal reworking of crustal-melt granitoid precursors. Similarily, relatively low Ɛ Sr and elevated HFS abundances in within-plate granitoids reflect a single petrogenetic process (Ch. 5).

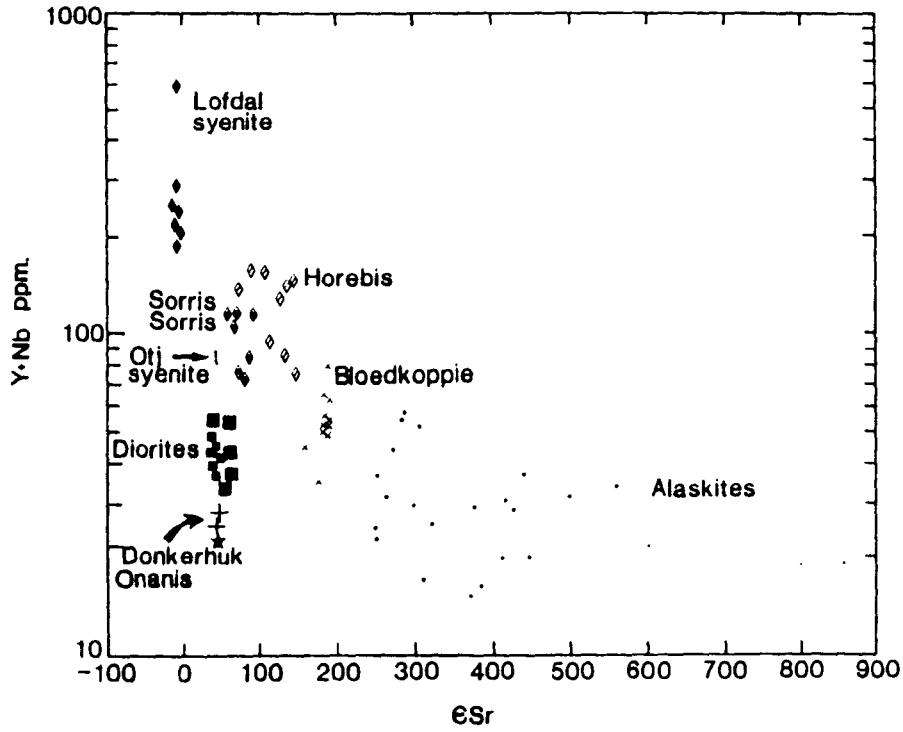

Fig. 4.3 Plot of εSr vs. the HFS elements Nb + Y. Upper crustal melt granitoids have high εSr values and low HFS abundances while the within-plate and calc-alkaline diorites are characterised by high HFS and low HFS element abundances respectively.

In summary, three geochemically distinct granitoid types have been distinguished. This simple three-fold classification offers the possibility of explaining the links between previously published classifications in terms of petrogenetic processes. The three-fold classification is also reflected in radiogenic and stable isotope variations which are discussed in Ch.5.

The principal geochemical characteristics of each granitoid type are summarised in Table 4.1.

Table 4.1 Summary of the geochemical characteristics of the three granitoid groups

	Crustal-melt granitoids	Calc-alkali diorites	Within-plate granitoids
Major elements	Peraluminous	Metaluminous	Extremely low CaO
Trace elements	high Rb low Nb, Y, Zr (high Th,U)	low Rb/Sr low HFS	High Nb, Zr, Hf, Y, High REE
Sr isotopes	high initial $^{87}Sr/^{86}Sr$ (> 0.710)	low initial $^{87}Sr/^{86}Sr$ (< 0.710)	variable $^{87}Sr/^{86}Sr$
Model Nd ages	~ 2.0 Ga.	~ 1.0-1.4 Ga	~1.2Ga.
O isotopes	high $\delta^{18}O$	variable $\delta^{18}O$	low $\delta^{18}O$

4.3 Significance of alumina saturation in granitoids

The degree of alumina saturation allows a first order classification of granitoids (e.g. Shand, 1927 ; Shand, 1951 ; White and Chappell, 1974 ; Bowden *et al.*, 1984 ; White *et al*, 1986). The A/CNK ratio i.e. molecular % $Al_2O_3/CaO+Na_2O+K_2O$, is used to quantify the degree of alumina saturation. Peraluminous, metaluminous and peralkaline granites (Shand, 1951) are distinguished as follows ;

Peraluminous granitoids - $Al_2O_3 > Na_2O + K_2O + CaO$

Metaluminous granitoids - $Na_2O + K_2O < Al_2O_3 < Na_2O + K_2O + CaO$

Peralkaline granitoids - $Al_2O3 < Na_2O + K_2O$.

(All the above constituents are expressed as molecular oxide %)

The significance of alumina oversaturation in granitoids has been discussed by several authors e.g. Chappell and White, 1974 ; Cobbing, 1982 ; Brown *et al*, 1984 ; Bowden *et al*, 1984 ; Miller, 1985 and White, 1986. The term peraluminous (Shand, 1927) is applied to granitoids which have a molecular excess of alumina over the amount necessary to co-ordinate with the available Ca, K and Na to yield feldspar, after CaO is reduced by the amount necessary to combine with P_2O_5 to form apatite.

There is little consensus on whether peraluminous granitoids require peraluminous sources, or the extent to which granitoid major element chemistry is a reflection of source region bulk chemistry.

Experimental data (e.g. Helz,1976 ; Stern and Wyllie,1978 ; Sekine *et al*,1982 ; Naney,1983) demonstrate that peraluminous magmas may be generated from a variety of source materials. Helz (1976) carried out melting experiments at PH_2O = 5Kb on three basalts - a tholeiite, an olivine tholeiite and an alkali basalt. Irrespective of variations in the composition of the initial basaltic material all the melts produced were quartz normative and the overwhelming majority were corundum normative. Within the hornblende stability field, melt composition is largely insensitive to changes in basalt composition although the TiO_2, FeO and MgO contents of the melt increase sharply in the temperature interval 1000-1045°C as hornblende begins to melt extensively (Helz, *op.cit.*).Similarily Holloway and Burnham (1972) and Green and Ringwood (1968) reported peraluminous compositions for all melts co-existing with appreciable amounts of hornblende.

However Kushiro and Yoder (1972) generated peraluminous melts by melting an

ultramafic peridotite source at PH_2O = 10 Kb, at a temperature of 1025°C. This $CaO\text{-}MgO\text{-}Al_2O_3\text{-}SiO_2$ system contains no alkalis and does not involve hornblende, suggesting that the presence of excess alumina is not peculiar to hornblende bearing systems.

Clearly then, peraluminous magmas can be generated by melting a variety of source materials. In addition, fractional crystallisation of alumina-poor phases e.g. amphiboles, pyroxenes, epidote and sphene may generate weakly peraluminous magmas from metaluminous calc-alkaline magmas.

While experimental studies have demonstrated that it is possible to generate peraluminous melts from a variety of source materials there is abundant field evidence that large volumes of peraluminous granites are derived by anatexis of peraluminous sources, an observation which led Chappell and White (1974) to equate strongly peraluminous granites with metasedimentary or "S - type" sources. Moreover, much of the experimental data discussed above relates to melting experiments carried out at relatively high temperatures (>1000°C). Since these melting experiments were conducted at temperatures well above the granite solidus the results are not generally applicable to granite genesis by crustal anatexis during high temperature regional metamorphism

However, classification schemes which equate peraluminous compositions with a metasedimentary source are oversimplistic. Miller (1985) argues that while most peraluminous granitoids are derived from continental crustal material a sedimentary source is not required to generate peraluminous magmas. (White *et. al,* 1986) argue that only strongly peraluminous, cordierite bearing granites require a sedimentary source. Although the majority of the Damara granitoids are peraluminous they are not strongly peraluminous and with the exception of the Donkerhuk batholith are not S-type granites as defined by Chappell and White (1974). Fig 4.4 demonstrates that most Damara granitoids have A/CNK ratios greater than 1 but less than 1.1.

Several authors (e.g. Pitcher,1979 ; Brown *et. al.*,1984) have debated the

tectonic settings in which peraluminous granitoids are generated. Pitcher (*op. cit.*) and Brown *et. al.* (*op. cit.*) noted that peraluminous granitoids are characteristic of orogenic belts located within ancient continental crust i.e. the Hercynotype belts of Pitcher (*op. cit.*). Although the genetic link between the generation of large volumes of peraluminous granitoids and high temperature/low pressure regional metamorphism has been established (e.g. Le Fort,1981 ; Miller,1982 ; De Paolo and Farmer,1984), there is little concensus on the the tectonic settings which produce "Hercynotype" orogenies. Although high-temperature regional metamorphism and crustal anatexis is frequently associated with crustal thickening (e.g. England and Thompson, 1984), recent work by Wickham and Oxburgh (1985) suggests that high temperature/low pressure metamorphic belts and associated peraluminous granitoids can result from crustal thinning and so may be indicative of a tensional tectonic regime.

In summary, it is argued that large volumes of peraluminous magmas produced during high-grade regional metamorphism are derived by partial melting of upper-crustal materials but only strongly peraluminous magmas require metasedimentary sources. For this reason the term crustal-melt granitiod is preferred to S-type granite. Most Damara granitoids are peraluminous but A/CNK ratios are less than 1.1 for most intrusions.

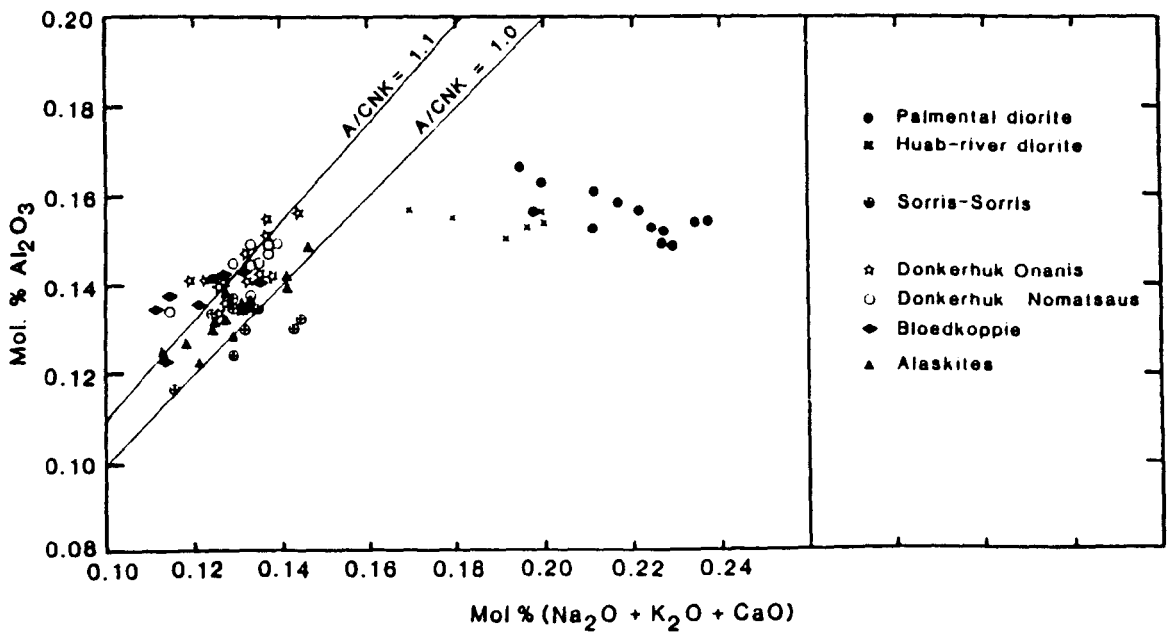

Fig. 4.4 Molecular % Al_2O_3 Vs. mol. % (Na_2O + K_2O + CaO) for selected Damara granitoids. Most Damara granioids are peraluminous (A/CNK > 1) but are not sufficiently alumina oversaturated to be classified as S-type granitoids (Chappell and White, 1974), i.e. A/CNK is < 1.1 for most intrusions.

4.3.1 A/CNK variations in the Damaran granitoids.

Variations in the molecular proportions of alumina, alkalis and CaO are shown as triangular diagrams in Figs. 4.5a to 4.5e. The crustal-melt granitoids i.e. leucogranites, Salem-type granitoids and alaskites (Ch. 3) are peraluminous (Fig. 4.5a - 4.5c).

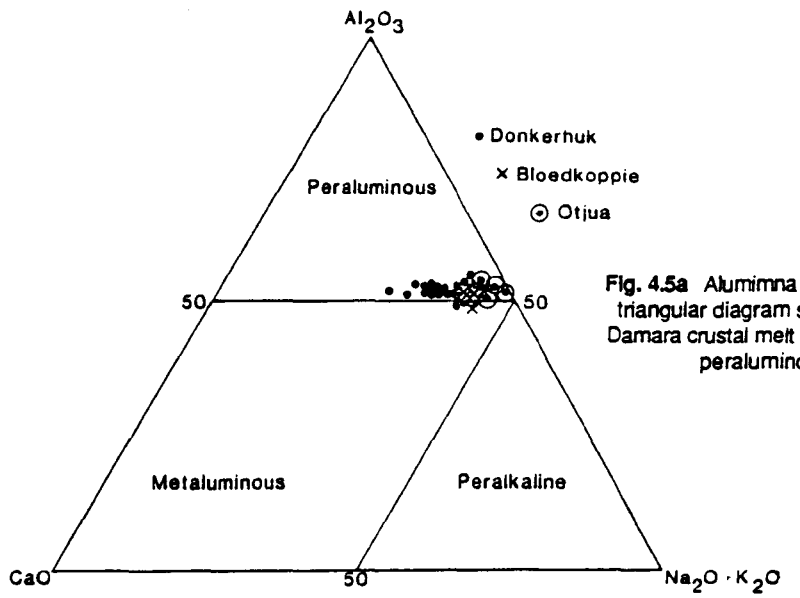

Fig. 4.5a Alumimna / CaO / alkalis triangular diagram showing that Damara crustal melt granitoids are peraluminous.

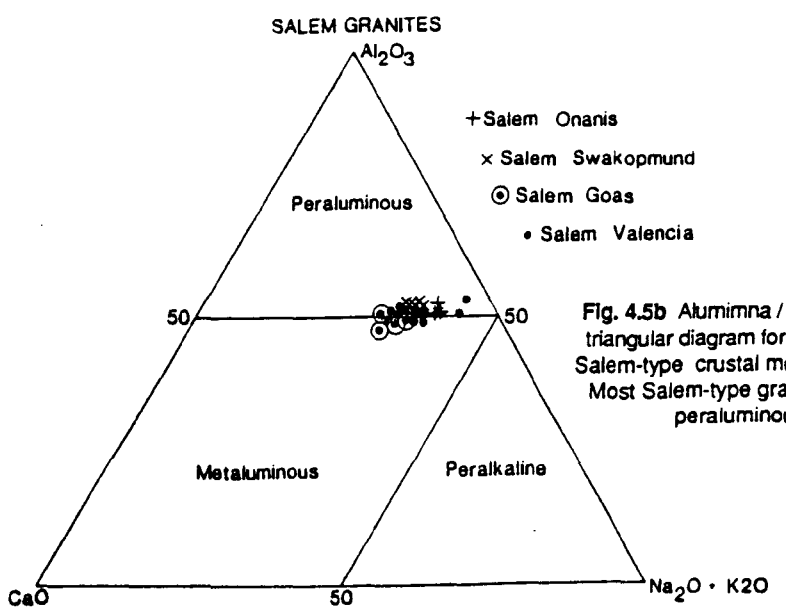

Fig. 4.5b Alumimna / CaO / alkalis triangular diagram for the Damara Salem-type crustal melt granitoids. Most Salem-type granitoids are peraluminous.

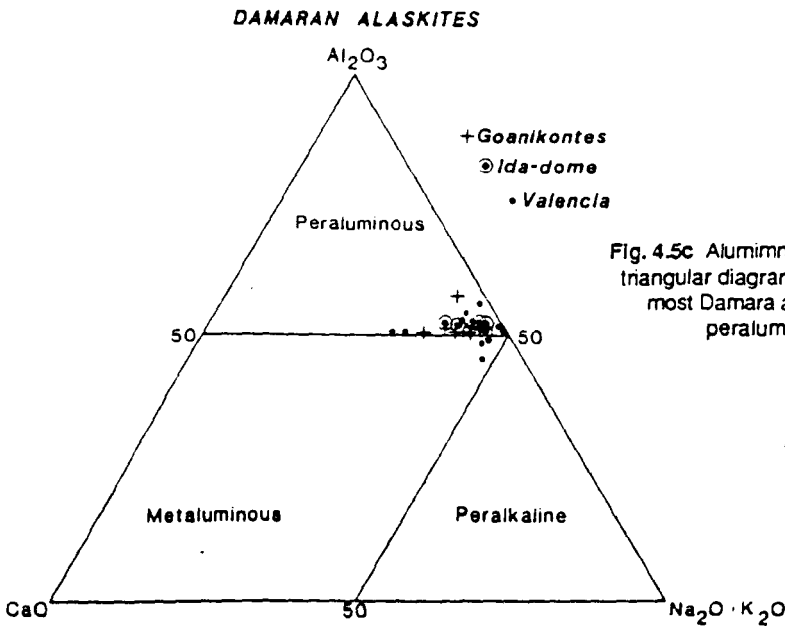

Fig. 4.5c Alumimna / CaO / alkalis triangular diagram showing that most Damara alaskites are peraluminous.

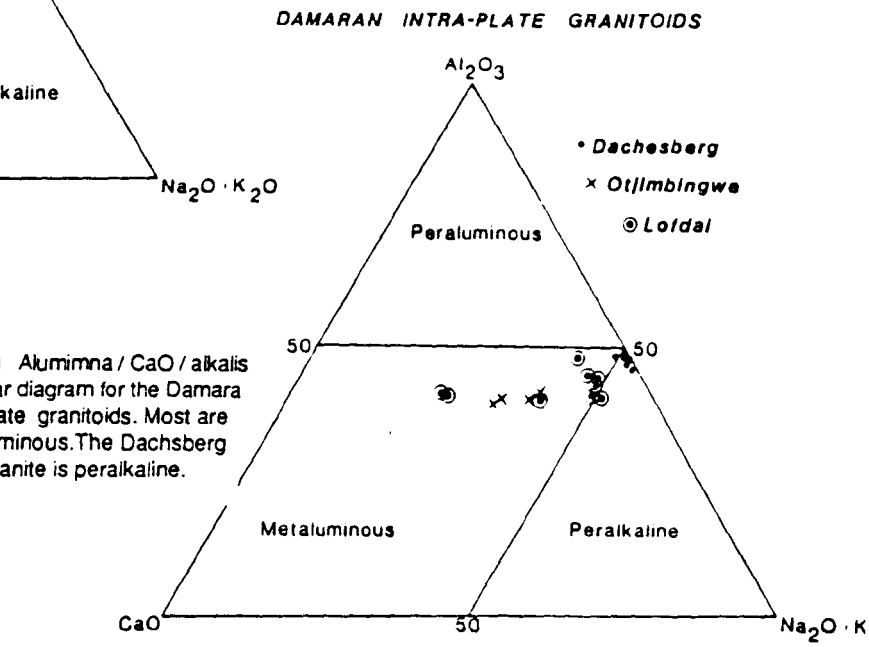

Fig. 4.5d Alumimna / CaO / alkalis triangular diagram for the Damara within plate granitoids. Most are peraluminous.The Dachsberg granite is peralkaline.

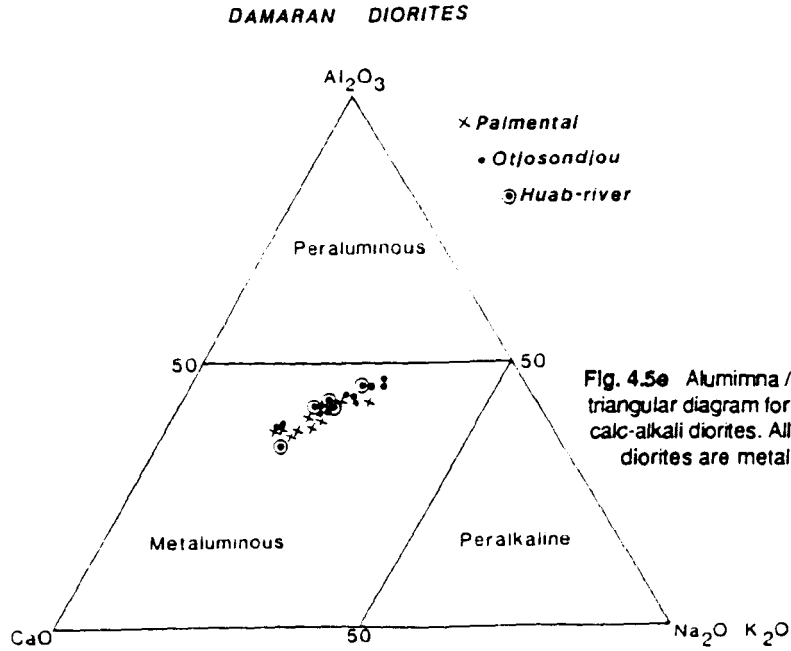

Fig. 4.5e Alumimna / CaO / alkalis triangular diagram for the Damara calc-alkali diorites. All the Damara diorites are metaluminous.

The calc-alkaline diorites from the Otjosondjou, Huab and Palmental localities are metaluminous (Fig. 4.5d). The majority of the within-plate granitoids are metaluminous (Fig.4.5e) although the samples from the Dachsberg and Horebis-river red granite (Downing,1982) are peraluminous. The extremely low CaO content of the Dachsberg intrusion makes it difficult to classify using triangular A/CNK diagrams because small changes in the Al_2O_3/ alkalis ratio can result in samples with very similar major element chemistry plotting in any of the peraluminous, metaluminous or peralkaline fields.

4.4 Harker variation diagrams

Harker variation diagrams are presented for several granitoids from each of the three major granitoid types identified i.e. crustal-melt granitoids, calc-alkaline granitoids and within-plate granitoids. These diagrams suggest that major and trace elements in individual granitoids behave in a coherent manner and systematically reflect igneous processes - an assumption which is inherent in the use of trace elements to quantitatively model petrogenetic paths for each of the three granitoid types.

4.4.1 Crustal-melt granitoids

Two suites of samples have been analysed from the strongly peraluminous Donkerhuk intrusion, from farms Nomatsaus and Wilsonfontein, which will be referred to as the Nomatsaus and Wilsonfontein segments of the Donkerhuk batholith. Blaxland *et al.* (1979) obtained whole-rock Rb/Sr ages of 523 ± 8 and 521 ± 15 with initial $^{87}Sr/^{86}Sr$ ratios of 0.70740 and 0.71170 for the Nomatsaus and Wilsonfontein segments respectively.

The Wilsonfontein segment was sampled over a distance of 30km (Blaxland *et. al., op. cit.*) and exhibits a wide compositional variation. SiO_2 values vary from 64.5 to 76.6 wt.%. Plots of SiO_2 against MgO, TiO_2, Fe_2O_3, MnO and CaO exhibit tightly defined linear trends (Fig 4.6), while the Nomatsaus suite is compositionally restricted (71.0 to 74.15 wt.% SiO_2) and with the exception of Fe_2O_3 does not show smooth inter-element co-variation patterns. The Nomatsaus suite is more compositionally "evolved" than the Wilsonfontein suite (e.g. higher SiO_2 and lower contents of P_2O_5, Fe_2O_3, TiO_2, MnO and MgO, Fig. 4.6).

The distribution of trace elements in the Donkerhuk granite clearly discriminates between the two segments recognised in the major element variations. The Wilsonfontein segment is characterised by higher Rb and lower Sr contents than the Nomatsaus segment . Sr decreases at higher silica contents in the more evolved Wilsonfontein segment. The LREE 's La and Ce as well as Zr and Y, decrease as SiO_2 increases (Fig. 4.6).

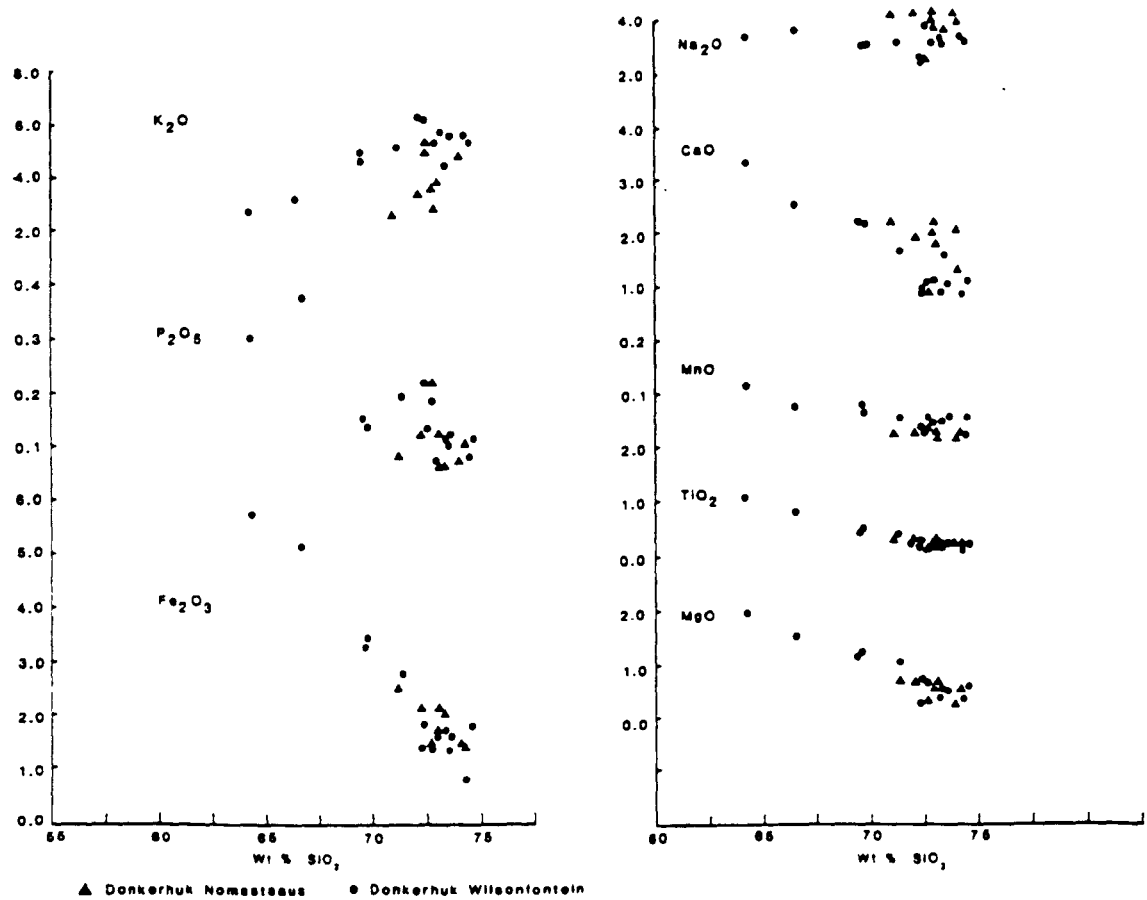

Fig. 4.6 Harker variation diagrams for the Donkerhuk granite. The Nomatsaus and Wilsonfontein segments (Blaxland *et al*, 1979) are shown as triangles and circles respectivelv.

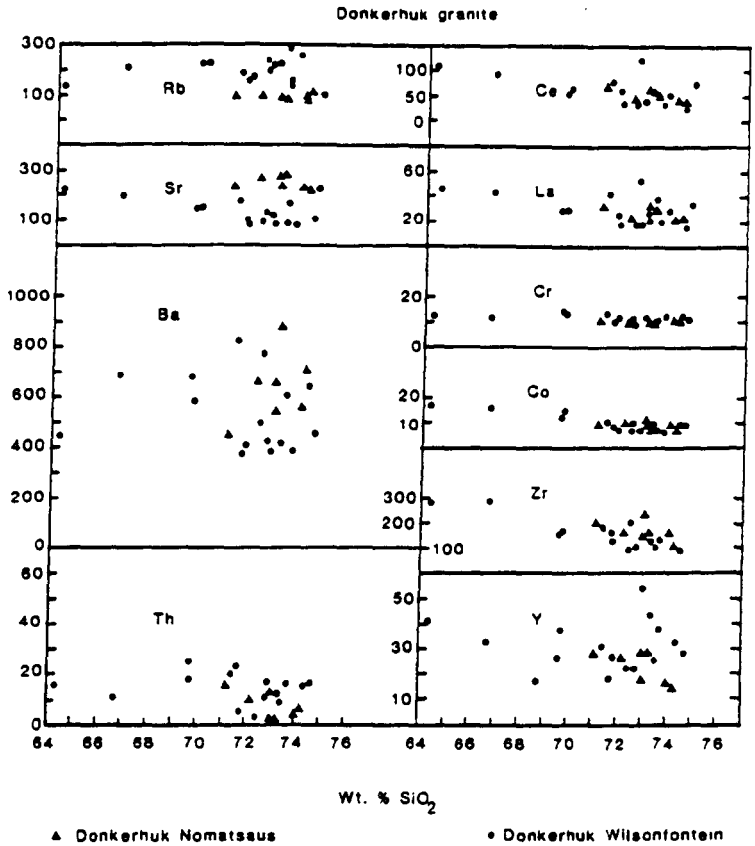

Fig. 4.6 (Contd.) Trace element variations in the Donkerhuk crustal-melt leucogranite.

Twelve samples from the Bloedkoppie leucogranite have SiO_2 values in the range 73.5 to 76.3 wt.%. Plots of silica against CaO, Fe_2O_3, K_2O and TiO_2 (Fig. 4.7) show that these elements decrease sharply with increasing silica. Sr and Ba abundances decrease in samples with higher silica contents. Rb behaves as an incompatible trace element while Ce, Zr, Cr, La and Th abundances decrease in the more evolved samples. Since this intrusion shows coherent trace element patterns it is selected for more detailed trace element modelling.

The alaskite samples from Goanikontes,Valencia, Ida-Dome and Rossing are discussed together because of their similar major and trace element geochemistry. SiO_2 contents are in the range 70-77 wt.%. TiO_2, MnO, MgO and CaO abundances are typically less than 1wt.% and show no systematic variation over the observed silica range (e.g. Fig. 4.8). The alaskites are characteristically enriched in alkalis with up to 8% K_2O and 4% Na_2O. Sr contents

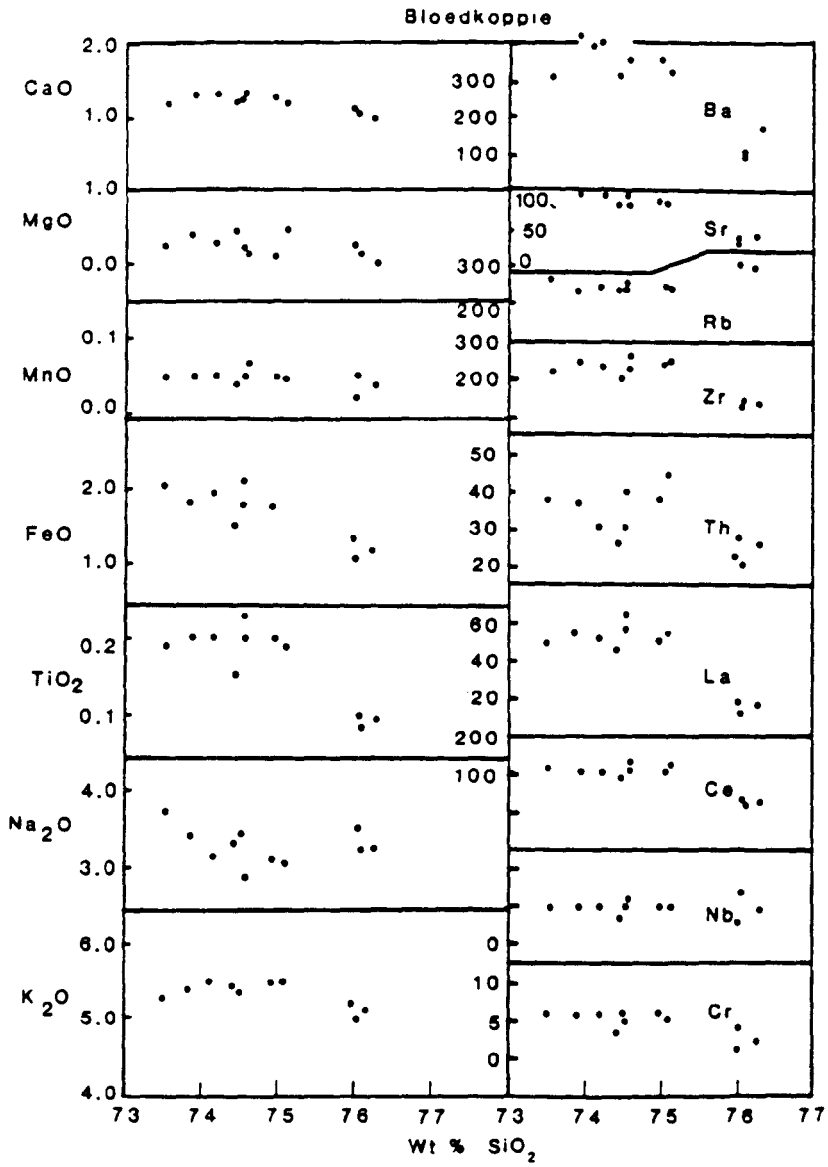

Fig. 4.7 Harker variation diagrams for the Bloedkoppie crustal-melt leucogranite.

decrease as silica increases while Rb does not show any systematic variation. Ni, Co, Nb and Sr decrease as SiO_2 increases in the Goanikontes alaskite, while other trace elements do not show any systematic variation. Trace elements in the Valencia alaskites (Fig. 4.81) show considerable scatter though La, Ce and Th abundances decrease in the more "evolved" samples. Ba, Sr and Rb decrease as silica increases in the Ida-Dome alaskite samples while Th and U behave as incompatible trace elements.

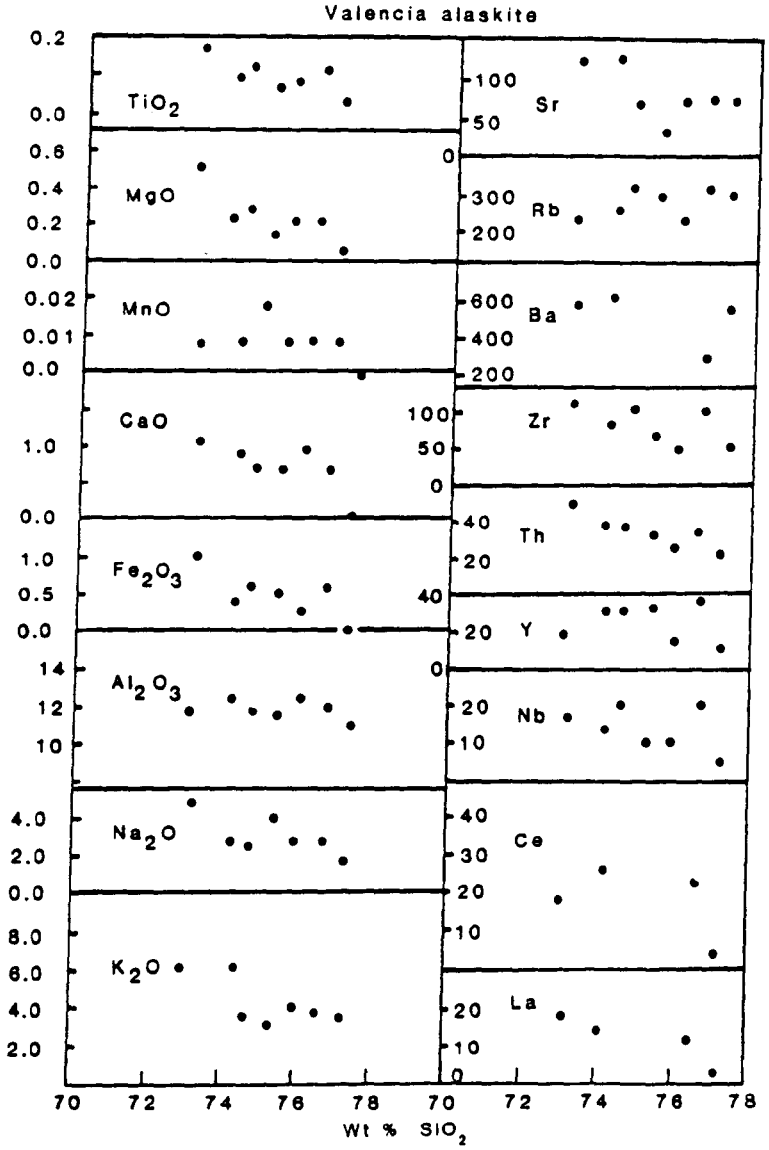

Fig. 4.8 Harker variation diagram for the Valencia alaskite intrusion.

The Salem-type granitoid from Onanis (Downing,1982 ; GG series samples) has SiO_2 contents in the range 70.56-73.3 wt.%. CaO, Fe_2O_3, Al_2O_3 and Na_2O contents decrease as SiO_2 increases. Sr is compatible while Rb, Ba, Zr, Nb, Y and the LREE's La and Ce are incompatible. Cr, Ni and V decrease steadily as silica increases.

SiO_2 contents vary from 67.56 to 70.51 wt.% in the Salem-type granitoid from Goas. CaO, MnO, TiO_2 and MgO define tight trends and decrease slightly with increasing silica. K_2O increases sharply over the observed silica range. Sr and Rb as well as La, Ce, Zr, Y and Nb

decrease as silica increases.

The Salem-type granitoid from the Stinkbank locality (Marlow, *op. cit.* ; S series samples) exhibits smooth major-element variation trends. Ba, Sr and Rb abundances decrease reflecting feldspar and biotite removal while Zr and Y decrease in the more evolved samples reflecting zircon crystallization, (Fig 4.9).

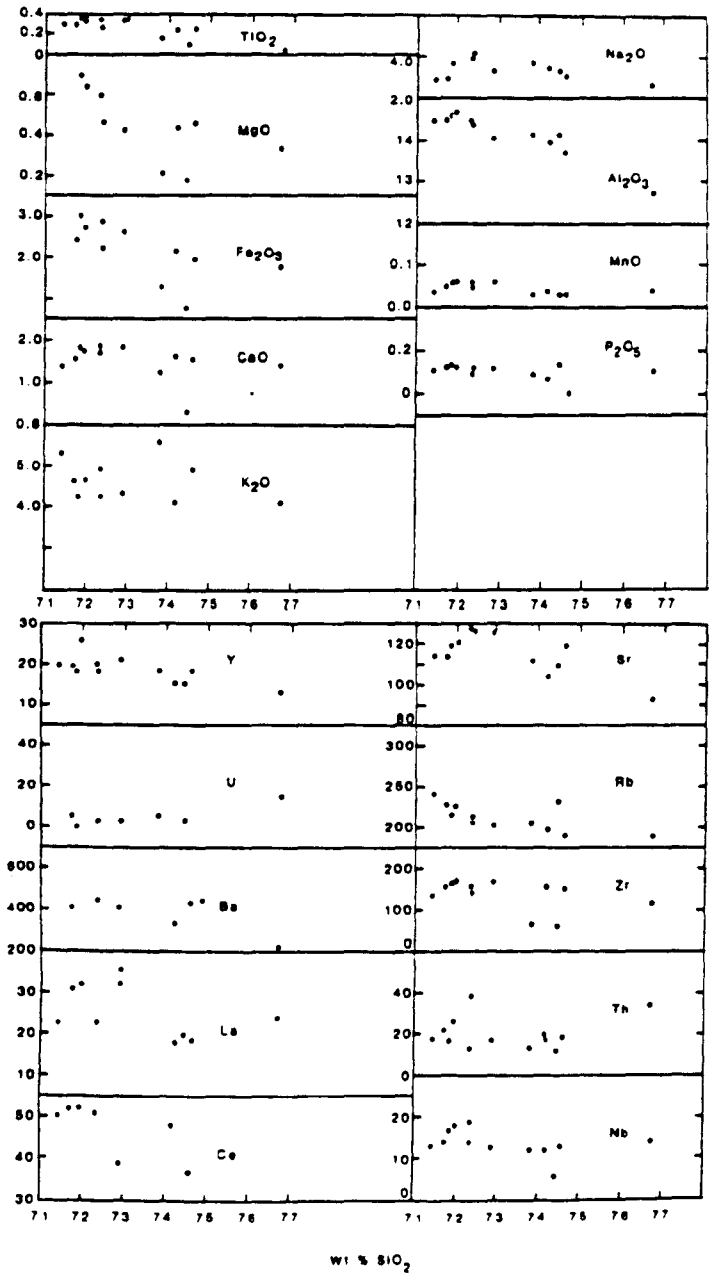

Fig. 4.9 Harker variation diagrams for the Stinkbank Salem-type granite.

4.4.2 The calc-alkaline diorites

All the Damara diorites studied i.e. from the Otjosondjou, Huab river and Palmental localities are metaluminous (Fig. 4.5d). Diorites are calc-akaline as defined by Peacock (1931), (Fig. 4.2) and define tight linear trends on a triangular alumina/CaO/alkalis diagram (Fig. 4.5d) which are interpreted as reflecting the removal of a CaO rich, alumina poor phase (e.g. pyroxene) from the magma combined with the effect of variable modal proportions of pyroxenes, amphiboles and plagioclase in the analysed samples from individual intrusions.

The Palmental diorite displays a wide compositional range (51.7 to 62.4 wt% SiO_2). Major element oxides show systematic linear trends when plotted against silica (Fig. 4.10). MgO, Fe_2O_3, TiO_2 and CaO decrease with increasing silica while Na_2O and K_2O contents increase. P_2O_5 increases initially as silica increases, and then decreases sharply reflecting apatite crystallization (Ch.3). Sr abundances increase slightly as silica increases suggesting that plagioclase removal was not a major petrogenetic process over the observed compositional range. Rb remains relatively constant while Nb, Zr and Th are incompatible.

In the calc-alkaline Otjosondjou diorite silica values are in the range 51.75 to 64.5 wt%. P_2O_5, TiO_2, MgO and CaO decrease with increasing silica. Sr decreases sharply with increasing silica suggesting that plagioclase removal was an important petrogenetic process. Rb, Y, and Zr are incompatible and show moderate increases with increasing SiO_2.

The calc-alkaline Huab-river diorite (sampled 15km north of the mouth of the Huab-river R. Mc G Miller, pers. comm.) has silica values in the range 57.2 to 61.8 wt.%. TiO_2, MgO, CaO, and P_2O_5 decrease as silica increases while Na_2O and K_2O contents increase. Sr is compatible while Rb and Th are incompatible. Decreases in Zr and Y concentration with increasing silica content reflect zircon removal (Ch. 3).

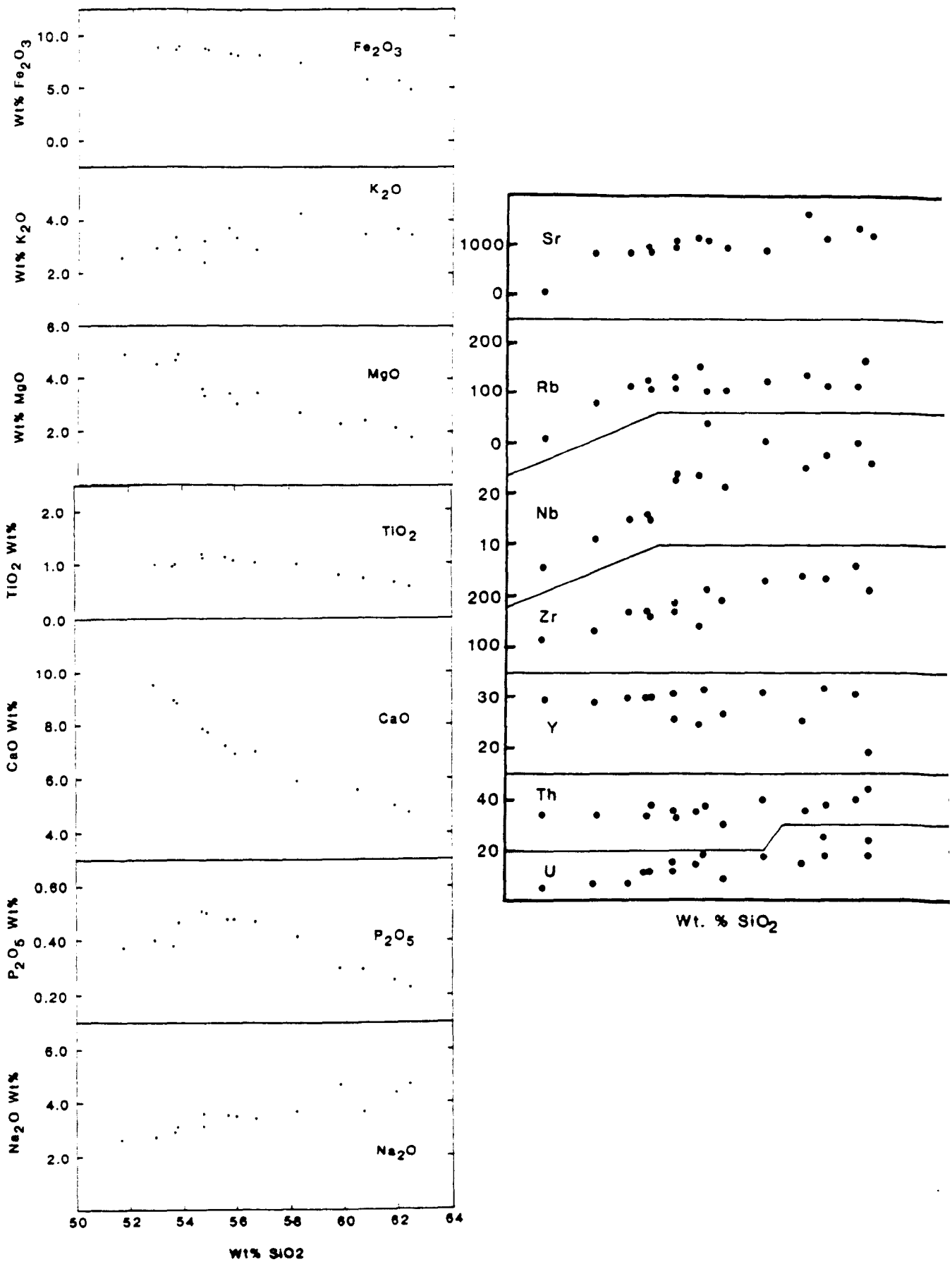

Fig. 4.10 Harker variation diagrams for the calc-alkaline Palmental diorite.

4.4.3 Within-plate granitoids

In the Horebis-river red granite Fe_2O_3, MgO and TiO_2 decrease smoothly as SiO_2 increases. Ba and Sr abundances decrease with increasing SiO_2 reflecting K-feldspar fractional crystallization. Rb shows considerable scatter while the LREE 's La and Ce decrease slightly as SiO_2 increases. Zirconium decreases with increasing silica reflecting ziron removal.

In the within-plate Sorris-Sorris granitoid (Fig. 4.11) CaO, TiO_2, Fe_2O_3, Al_2O_3 and MnO decrease as silica increases. Ba and Sr abundances decrease as SiO_2 increases reflecting K-feldspar fractional crystallization. Zr also decreases sharply reflecting zircon crystallization. La is compatible while Yb and Lu increase as silica increases.

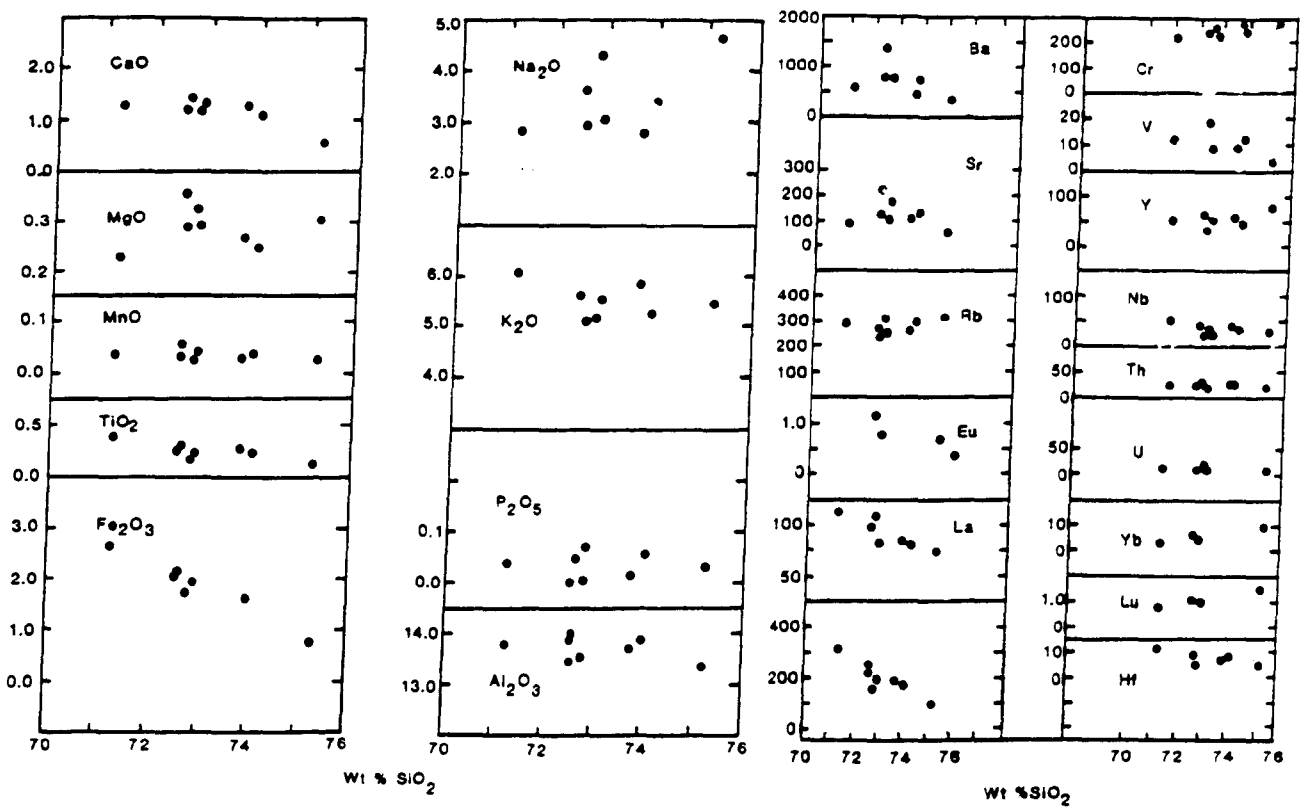

Fig. 4.11 Harker variation diagrams for the within-plate Sorris-Sorris granitoid.

Similarily the within-plate Salem-type granite from the Swakopmund area shows a decrease in Ba, Sr and the LREE 's as SiO_2 increases. Both Rb and Sr decrease with increasing silica in the Dachsberg granite while Nb and Zr increase slightly in the samples with highest silica contents.

4.5 Application of trace elements to granitoid petrogenetic studies

Several authors (e.g. Arth and Hanson,1975 ; Barker *et. al.*,1976 ; Condie and Hunter,1976 ; Hanson,1978 ; Fourcadre and Allegre,1981 ; Pearce *et. al.*,1984) have demonstrated that trace elements have considerable potential for characterising granitoid sources. However, a number of problems arise which are not usually encountered when applying trace elements to basaltic systems.

In general, the observed trace element variations are a result of several superimposed petrogenetic processes e.g. crystal fractionation, volatile fluxing and heterogeneous sources. Furthermore, minor phases often control the distribution of trace elements in granitoids. The following aspects of granitoid petrogenesis should be considered when interpreting trace element variations in granitoids.

1. In high-viscosity granitic melts there is no clear distinction between "cumulate" and "liquid" fractions. Unequivocal cumulate textures are rare and most granitoids are "mushes" with variable mixtures of "cumulate" crystals and trapped interstitial melt (Mc Carthy and Grooves, 1979)

2. In high-silica magmas the effects of melt composition on trace element partition coefficients are critical (Watson,1979). In general, distribution coefficients are affected much more by minor compositional variations in highly silicic magmas than by temperature variations (Hart and Davis ; 1978, Takahashi,1978). Mahood and Hildreth (1983) argue that in highly silicic magmas "liquid structure" becomes the most important control on trace element partitioning.

3. In high silica magmas partition coefficients may be exceedingly high, reflecting the strongly polymerised nature of the alkali-aluminosilicate liquid and may show marked variability due to differences in the concentrations of complexing ligands and/or different degrees of polymerisation (Mahood and Hildreth,1981).

4. The distribution of many trace elements in granitic rocks is controlled by minor phases. The role of minor phases has been highlighted by Fourcadre and Allegre (1981). Fourcadre and Allegre (*op. cit.*) showed that the light rare earth elements (LREE), as well as Hf, Zr, Th, U and Ta are largely controlled by allanite, zircon, sphene and apatite although some major mineral constituents, notably hornblende and biotite contain a large proportion of the trace elements in the absence of allanite. LREE'S are stoichiometric constituents comprising about 20% and 50% of allanite and monazite respectively. Thus allanite and monazite have effective "Kd_{REE}" in the range 10^3 to 10^4 (Miller and Mittlefehldt, 1982). In contrast, sphene and apatite have Kd_{REE} in the range 20-60 and would need to be removed in relatively large quantities (more than 1%) to deplete significantly the liquid in LREE. Gromet and Silver (1983) concur with Fourcadre and Allegre (*op. cit.*) that hornblende is the only major mineral constituent that hosts significant quantities of the REE'S in granitoids.

Watson and Harrison (1984) identified the most important factors in determining the role of accessory minerals during crustal remelting events. Redistribution of trace elements largely depends on the solubility of accessory phases in crustal-melts, the partitioning characteristics of trace elements between accessory phases and melt and the diffusivities of the chemical species in the accessory phases. Zircon solubility is lower in highly silicic melts than in more intermediate melts at the same temperature (Watson and Harrison, 1983), while apatite is generally insoluble during crustal melting. Partitioning of the REE'S into sphene and allanite is enhanced as granitic magmas become progressively more silicic (Gromet and Silver, 1983).

While minor phases control the distribution of many trace elements in granitic rocks partitioning of trace elements into small grains of accessory minerals does not necessarily produce significant alterations in trace element distribution patterns as granitic liquids become more evolved, because solid/liquid (crystal/melt) separation is likely to be rather sluggish in highly viscous granitic magmas (Rice, 1981). Miller and Mittlefehldt (1982) argue that trace-element enriched minor phases can only be removed from viscous high-silica magmas by removal within larger host grains (e.g. as inclusions in biotite).

5. Volatile constituents may exert a fundamental control on the behavior of trace elements in granitic magmas. Harris (1981) pointed out that F and Cl behave differently in granitic magmas. F tends to concentrate in the residual fluid whereas Cl is concentrated in the co-existing volatile phase, an observation which is in agreement with the experimental data of Van Groos and Wyllie (1968, 1969). Fractionation of peralkaline magmas leads to an increase in F accompanied by an increase in alkalis and an increase in HREE/LREE (Harris, *op. cit.*).

Since the solubility of CO_2 is relatively low in granitic systems many granitic magmas are accompanied by a CO_2-H_2O fluid phase during ascent in the crust (Holloway, 1976). The effect of CO_2 in the source region of alkali rich silica melts was investigated by Wendlandt and Harrison (1979). At crustal pressures a CO_2 rich vapour in equilibrium with silicate melts is LREE enriched. Volatiles, notably CO_2 play an important role in the petrogenesis of alkaline to peralkaline granites resulting in enrichments in a range of elements which are atypical of igneous enrichment trends (Taylor *et. al.*, 1981). Light to middle REE'S are concentrated by Cl bearing fluids whereas the heavy REE'S are concentrated by F and CO_2 bearing fluids (Flynn and Burnham, 1978). The carbonate complexes of the HREE and uranyl ions are stable under alkaline conditions perhaps accounting for U enrichment in some alkaline granites (e.g. the Damara Lofdal syenite).

4.5.1 Trace element variations between the three granitoid groups

Trace-element distribution patterns for representative intrusions of each of the three major granitoid groups are illustrated in Figs. 4.12a and 4.12b.

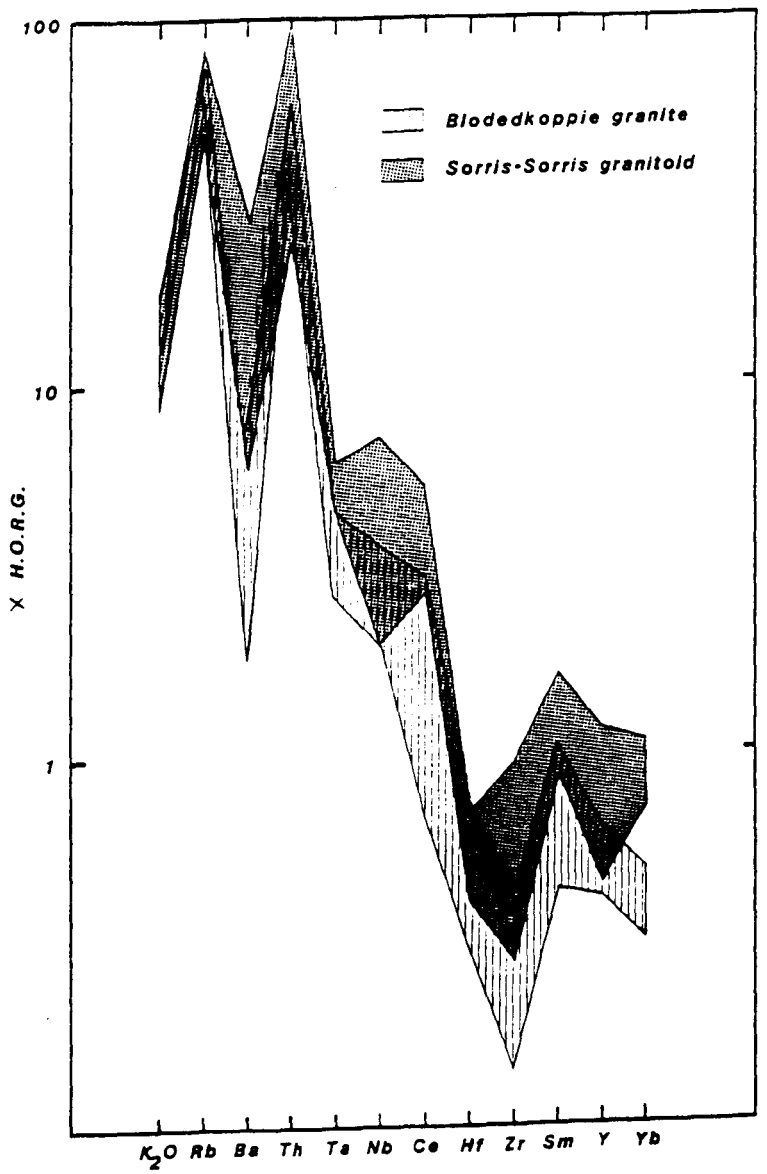

Fig. 4.12a "Spider diagrams" for the crustal-melt Bloedkoppie crustal melt granite and the within-plate Sorris-Sorris granitoid. The Sorris-Sorris granitoid is enriched in the HFS elements Ta, Nb and Y as well as the REE's.

Trace element abundances are normalised to the trace element composition of a hypothetical ocean ridge granite (HORG) , (Pearce *et al*, 1984). The trace element abundances of HORG have been calculated by Pearce *et al.* (*op. cit.*) by assuming 75% Rayleigh fractional-crystallisation of a magma with a mid-ocean ridge basalt composition.

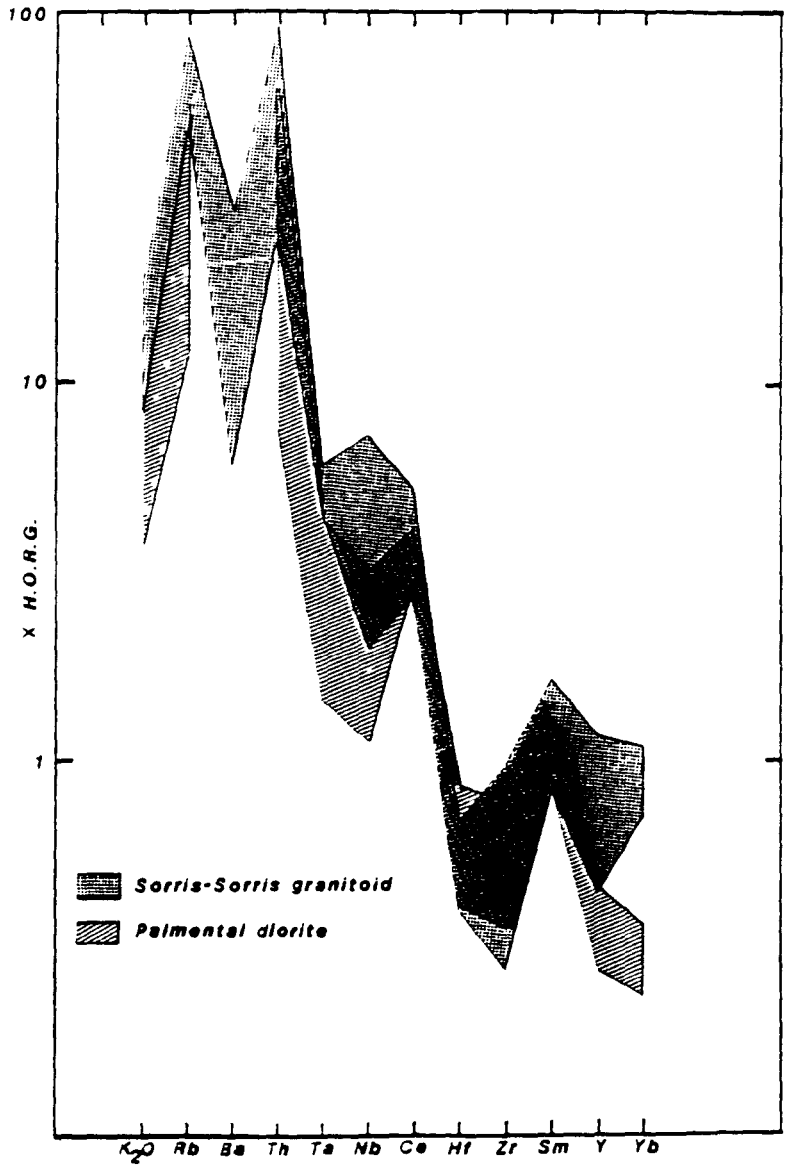

Fig. 4.12b Trace element abundances in the within-plate Sorris-Sorris granitoid compared with those of the calc-alkaline Palmental diorite.

Fig. 4.12a compares the trace-element distribution patterns of a typical crustal melt (the Bloedkoppie leucogranite) to that of the within-plate Sorris-Sorris granitoid. The most striking difference between within-plate granitoids and crustal-melt granitoids is the elevated high-field strength (HFS) element (e.g. Ta, Nb, Zr, Y) and Ba abundances of within-plate granitoids. Similarily, within-plate granitoids are characteristically enriched in the REE 's relative to other granitoid types. Trace element distribution patterns of the within-plate Sorris-Sorris granite and the calc-alkaline Palmental diorite are compared in Fig. 4.12b. The Palmental diorite has lower K_2O than either the within-plate or crustal-melt granitoid types (Fig. 4.12b). Crustal -melt granitoids and in particular the alaskites, have elevated K_2O contents. In general, the calc-alkaline diorites have lower HFS elements and REE than the within-plate granitoids but are slightly enriched in these elements relative to crustal-melt granitoids.

The relatively high K_2O and low HFS contents of crustal-melt granitoids is demonstrated in Fig. 4.13. Of the crustal-melt granitoids, alaskites characteristically have highest K_2O contents (up to 8 wt. % K_2O). Within-plate granitoids typically have high Y contents whereas calc-alkaline diorites have relatively low Y and K_2O abundances, (Fig. 4.13).

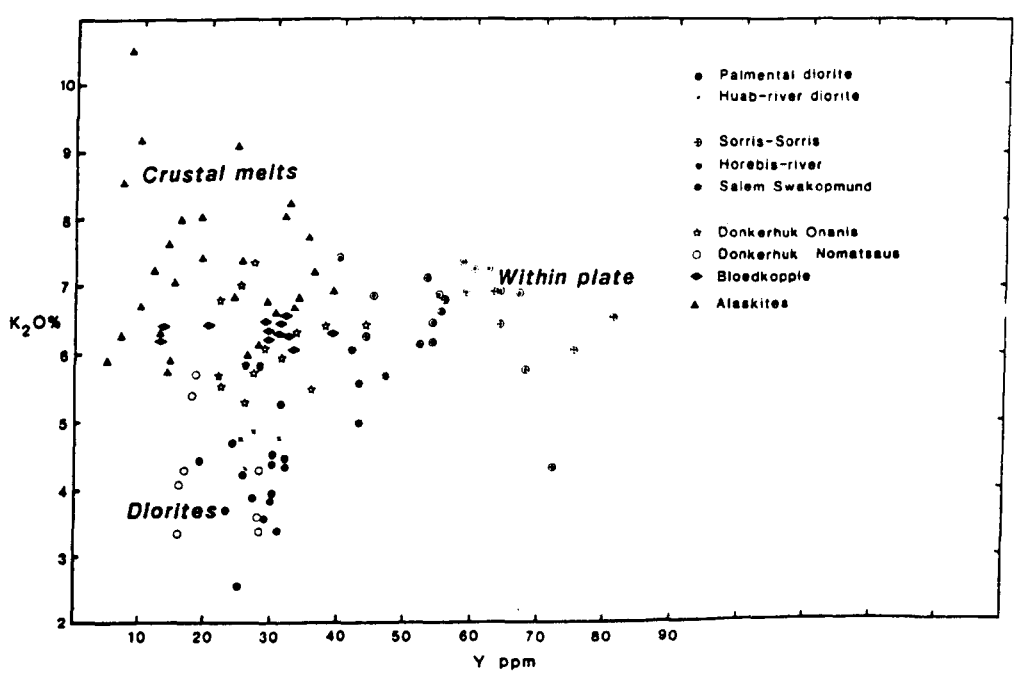

Fig. 4.13 K_2O vs. Y diagram for Damara granitoids. Crustal-melt granitoids have high K_2O contents and low Y abundances. Within-plate granitoids are characterised by high Y abundances whereas calc-alkaline diorites have low Y and K_2O contents.

The calc-alkaline diorites are characterised by low Rb/Sr ratios compared to the within-plate or crustal-melt groups. Typically, the Damara calc-alkaline diorites have Rb/Sr ratios lower than about 0.2. The ratio Nb/Rb effectively discriminates between within-plate granitoids (Nb/Rb > 0.1) and crustal-melt granitoids which have low Nb/Rb ratios (< 0.1), (Fig. 4.14).

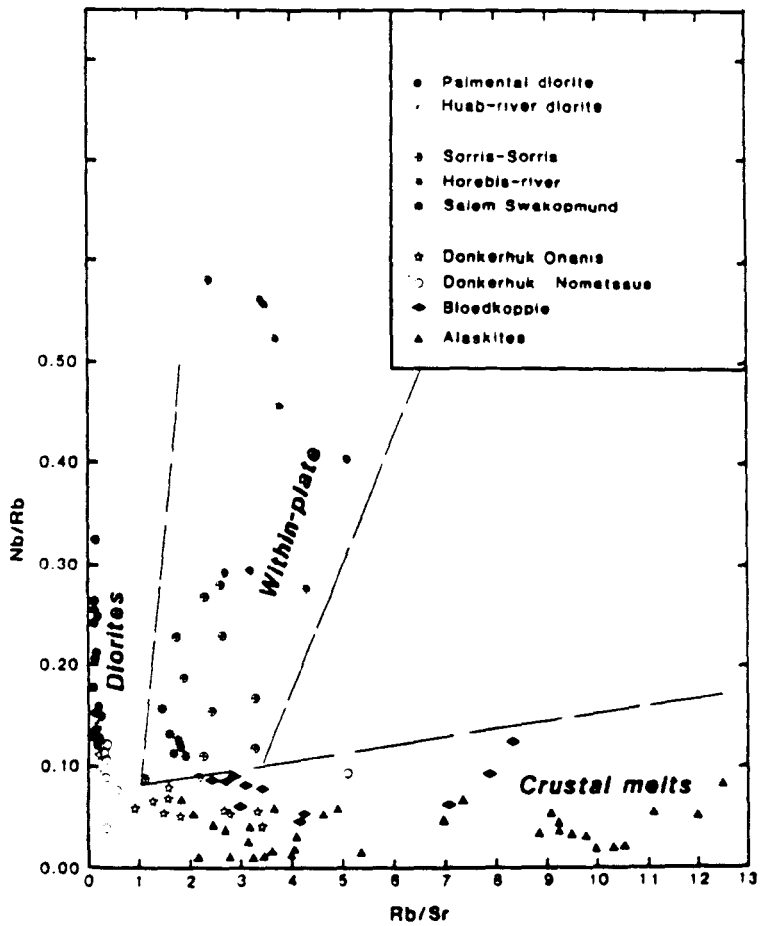

Fig. 4.14 Nb/Rb vs. Rb/Sr diagram for Damara granitoids. Within-plate granitoids have high Nb/Rb ratios whereas crustal-melt granitoids have low Nb/Rb ratios. Crustal-melt granitoids have high Rb/Sr ratios while calc-alkaline diorites have low Rb/Sr ratios.

Representative REE profiles for the three granitoid groups are shown as chondrite normalised diagrams, (Figs. 4.15- 4.18). Crustal-melt granitoids, typified by the alaskites and Bloedkoppie leucogranite (Fig. 4.15 and 4.16) have low REE abundances. The alaskites characteristically have U shaped REE profiles (Fig. 4.15) and have small negative or

positive Eu anomalies (Eu/Eu* = 0.34-0.47) , (Fig. 4.15a and 4.15b) and a LREE enriched profile. The positive Eu anomalies of some alaskite samples and one Bloedkoppie leucogranite sample in Fig 4.15b (Samples 26/69 78m , G0, KND 1.5), is interpreted as reflecting feldspar accumulation.

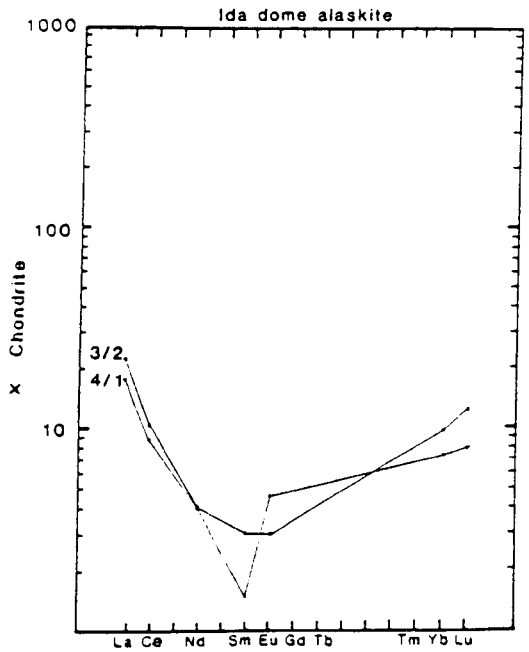

Fig. 4.15 Chondrite normalised REE diagram for Ida-Dome alaskite samples.

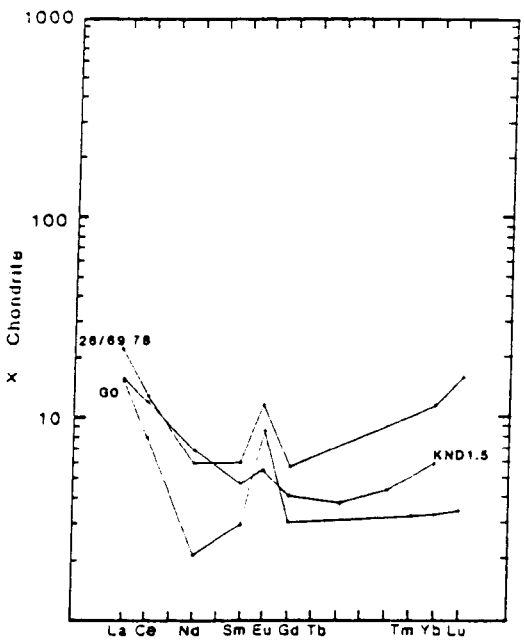

Fig. 4.15a Chondrite normalised REE diagram for alaskite and Bloedkoppie crustal-melt granitoids which show positive Eu anomalies.

In marked contrast to crustal-melt granitoids, within-plate granitoids have high REE abundances with a LREE enriched profile (e.g. the Sorris-Sorris granite, Fig. 4.17). Relatively large negative Eu anomalies (Eu/Eu* = 0.25 - 0.3) and high (up to 300 times chondrite) LREE are characteristic of within-plate granitoids.

Calc-alkaline granitoids (e.g. the Palmental diorite, Fig. 4.18) typically have steep LREE enriched profiles and relatively small, negative Eu anomalies (Eu/Eu* = 1.08 - 1.2).

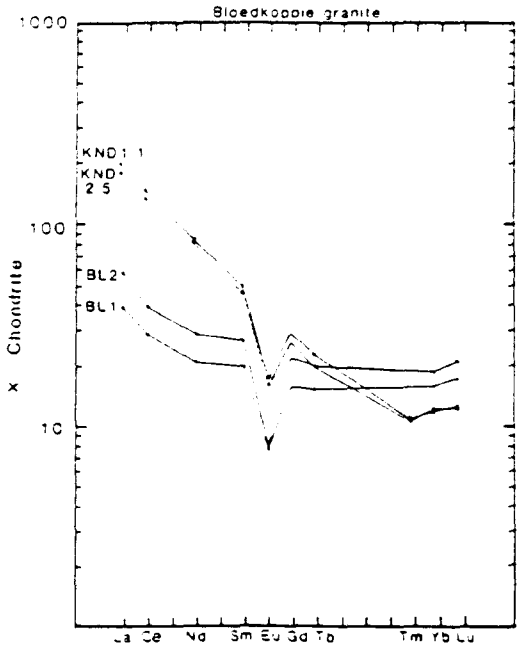

Fig. 4.16 Chondrite normalised REE diagram for the Bloedkoppie crustal-melt leucogranite.

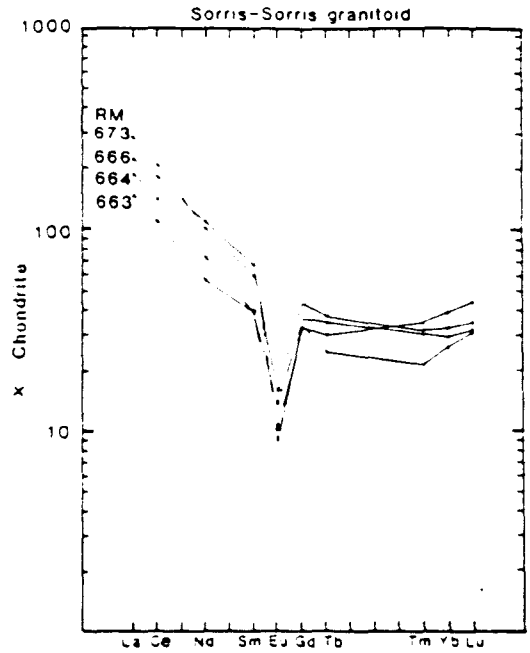

Fig. 4.17 Chondrite normalised REE diagram for the within-plate Sorris-Sorris granitoid.

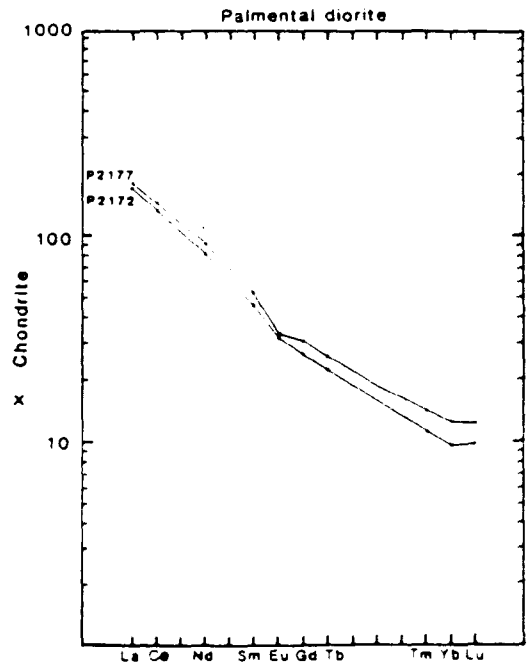

Fig. 4.18 Chondrite normalised REE diagram for the calc-alkaline Palmental diorite.

4.5.3 Tectonic discriminant diagrams

Pearce *et al.* (1984) proposed a granite classification scheme which assigns granites (sensu-lato) to one of four possible tectonic settings. Discrimination boundaries are drawn empirically but have a petrogenetic basis (Pearce *et al.*, *op. cit.*). Post-collision granites are the most difficult group to classify since their precise trace-element characteristics depend on the nature and timing of the collision event as well as lithospheric thickness and composition. Tectonic discriminant diagrams should be regarded as guides to the nature of source regions of granitoid magmas and should be used in conjunction with geological constraints (Pearce *et al.*,*op. cit.*).

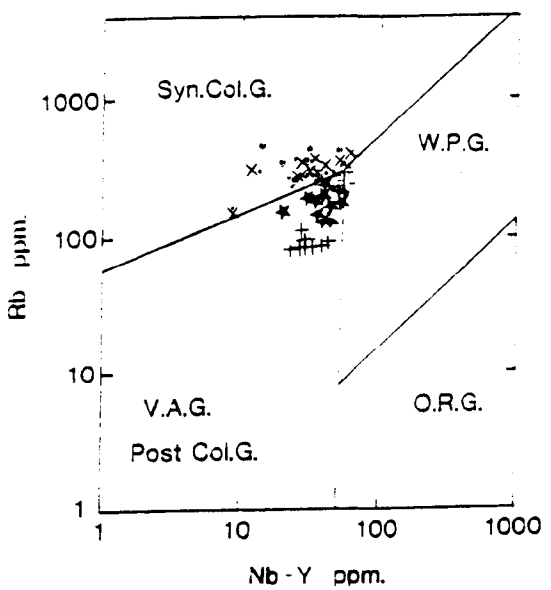

Fig. 4.19 Rb vs. (Nb + Y) diagram for the Damara crustal-melt granitoids. With the exception of the Donkerhuk granite, crustal-melt granitoids plot in the syn-collision field. The high initial $^{87}Sr/^{86}Sr$ ratio of the post-tectonic Donkerhuk granite indicates that this is a post-collision granite

• Goanikontes alaskite + Donkerhuk Nomatsa

· Valencia alaskite * Donkerhuk Onanis

× Rössing alaskite △ Bloedkoppie

Damara granitoids plot in the syn-collision, within-plate and post-collision granitoid fields. The crustal-melt granitoid group (e.g. alaskites and two-mica granitoids plot in the syn-collision

granitoid field (Fig. 4.19) while the large Donkerhuk batholith plots in the volcanic-arc/post-collision field. Post-collision granitoids are distinguished from volcanic-arc granitoids on the basis of initial $^{87}Sr/^{86}Sr$ ratio (Pearce *et al.,op. cit.*). The relatively high initial $^{87}Sr/^{86}Sr$ ratio of the post-tectonic Donkerhuk granite (up to 0.7117) suggests that this intrusion should be classed as a post-collision granite according to the scheme of Pearce *et al.*, 1984. Damara calc-alkaline diorites display both intra-plate and volcanic-arc affinities (Fig. 4.20). Diorites from the Palmental and Huab-River localities have volcanic-arc granite trace element affinities whereas the diorite from Otjosondjou (Miller, 1973) plots in the within-plate granite field (Fig. 4.21). The Lofdal syenite and granitoids from the Sorris-Sorris, Dachsberg, Horebis, Otjosondjou and Swakopmund intrusions are enriched in HFS elements and plot in the within-plate granitoid field on discriminant diagrams e.g. Fig. 4.21.

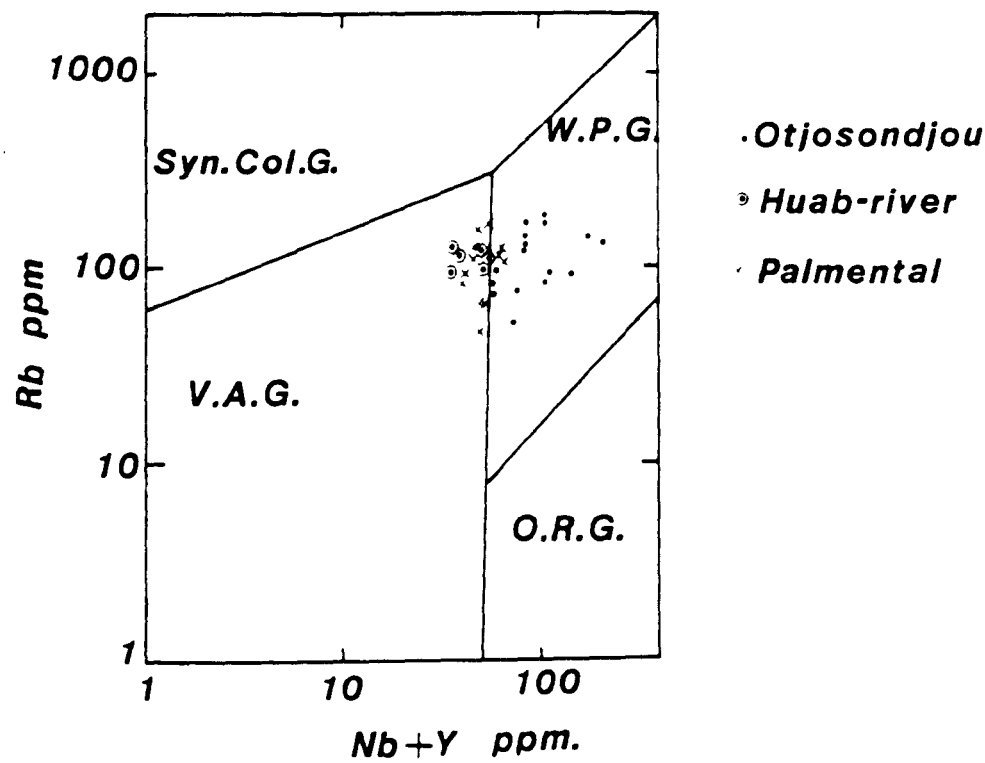

Fig. 4.20 Rb vs. Nb + Y granite discriminant diagram (Pearce *et al.*, 1984) for Damara calc-alkali diorites. The Huab-river and Palmental diorites are "volcanic-arc" granites whereas the Otjosondjou diorite plots in the within-plate granitoid field.

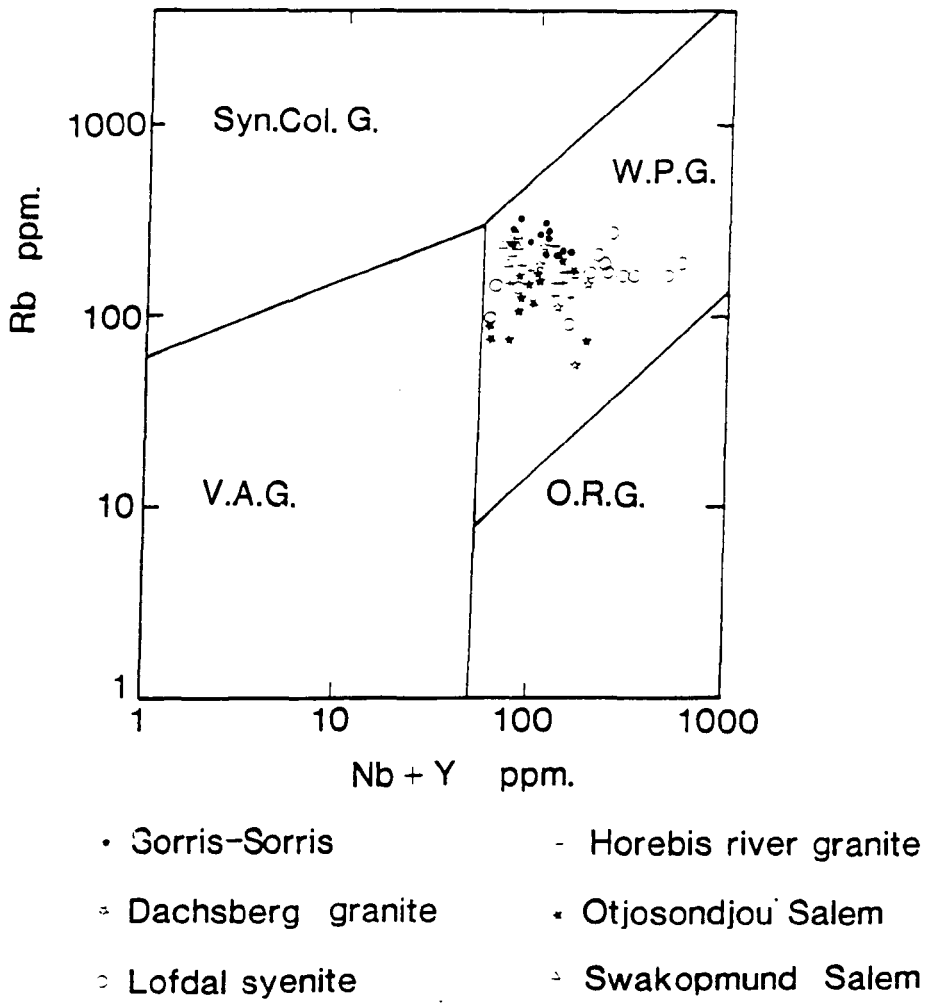

Fig. 4.21 Rb Vs. Nb + Y granite discriminant diagram (Pearce *et al.*, 1984) for Damara within-plate granitoids.

4.6 Trace-element modelling

One intrusion from each of the three major granitoid groups has been selected for detailed trace element modelling. Granitoid intrusions from Bloedkoppie, Sorris-Sorris and Palmental (diorite) were selected to represent crustal-melts, within-plate granitoids and calc-alkaline diorites respectively. In addition, the Goanikontes alaskite (Marlow,1981) was selected for detailed trace element modelling in order to assess differences between alaskite and leucogranite petrogenesis.

4.6.1 The Bloedkopple granite

Large-ion lithophile (LIL) element modelling has been carried out to assess the covariation between Sr, Ba and Rb which are largely partitioned into major silicate phases in granitic systems. The observed variations in LIL elements are primarily a reflection of high-level crustal processes dominated by feldspar fractional crystallisation. LIL data are presented as logarithmic plots of Ba vs Sr and Ba vs Rb (Fig. 4.22) . Both Ba and Sr behave as compatible trace elements while Rb is incompatible (Fig. 4.22).

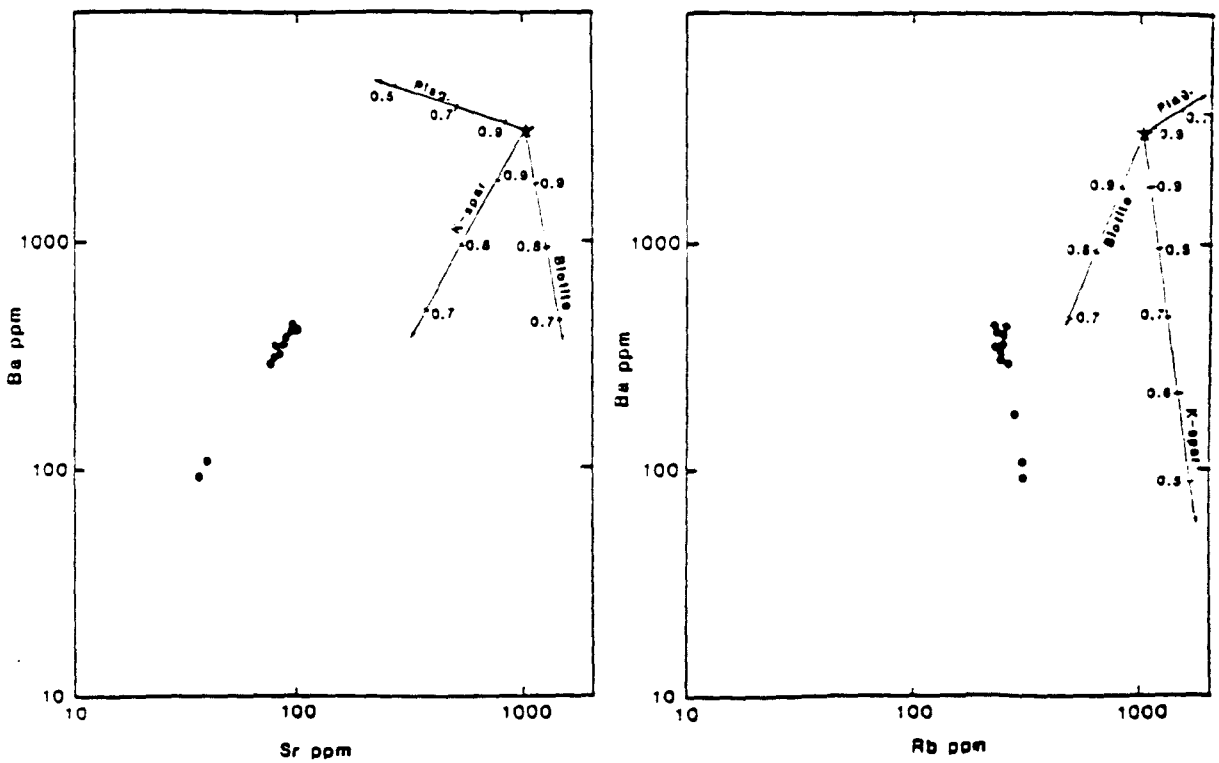

Fig. 4.22 Ba Vs. Sr and Ba Vs. Rb log-log diagrams for the Bloedkoppie crustal melt granitoid.

Since perfect equilibrium crystallisation is considered to be unlikely the modelled variations are based on Rayleigh fractional crystallisation using the equation :

$C^i_l = C^i_{o\,l} F^{(Di-1)}$ where i is the trace element of interest e.g. Ba, Sr, Rb

C^i_l is the concentration of the trace element i in the "final liquid"

C^i_{ol} is the concentration of trace element i in the "original liquid"

F is the weight fraction of the liquid remaining

D_i is the bulk distribution coefficient for trace element i.

Fractionation vectors have been superimposed on the log-log plots of LIL elements (Fig 4.22). F values are shown at 0.1 intervals along each vector. Inspection of the trend of the data points and of the mineral vectors on both Rb vs Ba and Sr vs Ba diagrams suggest that LIL element variations are strongly controlled by K-feldspar fractional crystallisation. The distribution coefficients used for trace element modelling are given in table 4.2.

Table 4.2 Distribution co-efficients used in LIL modelling

	Plagioclase	K- feldspar	Biotite
Ba	0.36	6.12	6.36
Sr	2.94	3.87	0.12
Rb	0.05	0.34	3.26

(K_d values after Arth and Hanson,1975 and Hanson, 1978)

LIL element concentrations in the Bloedkoppie granite primary magma are assumed to be 424 ppm Ba, 98 ppm Sr and 269 ppm Rb i.e. the concentrations of these elements in the least "evolved" sample (KND 1.1). Assuming that sample KND 1.1 and BL2 (the least and most evolved samples respectively on the basis of major and trace element data) are related by simple Rayleigh fractional crystallisation and represent the initial and final liquid respectively, the degree of fractional crystallisation required to produce the observed variation in LIL elements may be calculated.

$\text{Log } C^i_l = \text{Log } C^i_{o,l} + (D - 1)\text{Log } F$ ..... Rayleigh fractional crystallisation equation

$\text{Log } F = (\text{Log } C^i_l - \text{Log } C^i_{o,l}) / D-1$ .....equation 4.1

In order to use equation 4.1 to estimate F, D must be estimated for each trace element. The approach of Allegre *et al.* (1977) is used to estimate bulk distribution coefficients for a range of trace elements during fractional crystallisation of a primary magma. The technique is based on hygromagmatophile element systematics (Treuil and Varet,1973) and is adapted here for use in granitic systems. Since most trace elements behave compatibly during fractional crystallisation of granitic magmas several elements were used as H elements ($D << 1$) in order to assess which trace element most closely approached ideal incompatible behavior during fractional crystallisation of granitic magmas. In the Bloedkoppie granite Lu, Yb and Nb were found to most closely approximate ideal hygromagmatophile element behaviour i.e. D close to zero. Lu is the most incompatible trace element and D values calculated for other trace elements using Lu as a hygromagmatophile (H) element will be used in subsequent calculations.

Assuming Rayleigh fractional crystallisation $C^i_l = C^i_{o,l}\ F^{(D-1)}$

In the case of hygromagmatophile trace elements which are designated as H in the following equations, $D << 1$ therefore (D-1) approaches -1.

$F^{(D-1)} \sim = F^{-1}$ i.e. $1 / F$

substituting $1 / F$ for $F^{(D-1)}$ in $C^H_l = C^H_{o,l} F^{(D-1)}$ we get $F = C^H_{O,l} / C^H_l$

The validity of the approximation $F^{(D-1)} = 1 / F$ is shown in Fig. 4.23. In general, the approximation is valid for high values of F ($F > \sim 0.5$) when D is small (< 0.05, i.e. a hygromagmatophile trace element). Considering a trace element i (e.g. Ba, Sr, Eu) and writing the Rayleigh law in the form $C^i_l = C^i_{o,l,} (C^H_{o,l} / C^H_l)^{(Di-1)}$ (i.e. substituting $C^H_{o,l} / C^H_l$ for F)

$\text{Log } C^i_l = \text{Log } C^i_{o,l} + \text{Log } (C^H_{o,l} - C^H_l)^{(Di-1)}$

$\text{Log } C^i_l = \text{Log } C^i_{o,l} + (D^i - 1)\ (\text{Log } C^H_{o,l} - \text{Log } C^H_l)$

$$D^i = (\text{Log } C^i_l - \text{Log } C^i_{o,l} \; / \text{Log } C^H_{o,l} - \text{Log } C^H_l) + 1 \text{ ..... equation 4.2.}$$

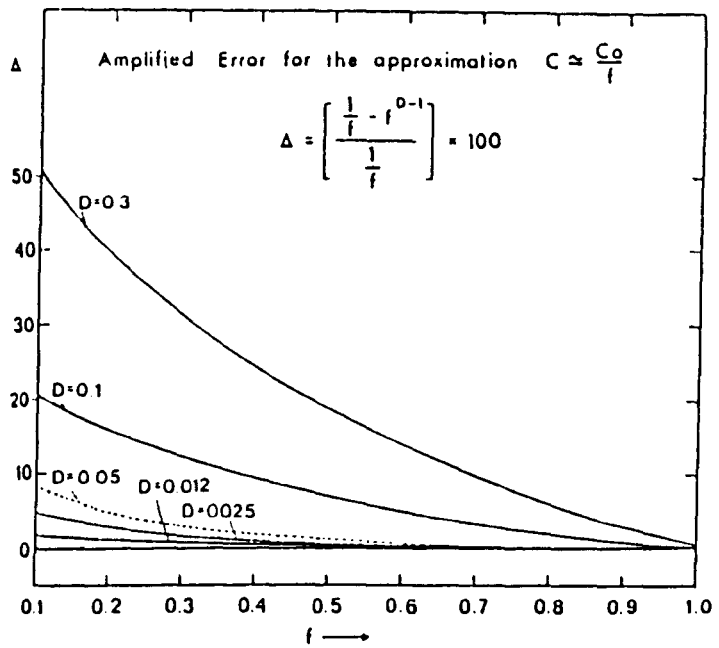

Fig. 4.23 Diagram showing the amplified error for the approximation $C = C_o/F$ as a function of D and F, (Allegre *et al.*, 1977). This shows that the approximation is valid for the Rayleigh law when D is <<1.

Therefore if the concentration of H elements in the original and final liquids are known, the average bulk D values for other trace elements may be calculated. Calculated D values are average bulk D values since they are based on the assumption that bulk D remains constant for a given trace element during the entire fractional crystallisation process. These calculations yield average bulk D values for each trace element over the observed compositional range and are based on trace element abundances in samples KND 1.1 and BL2 which on the basis of major and trace element geochemistry are assumed to represent the initial and final liquids respectively. Table 4.3 shows the average bulk D values calculated for a range of trace elements using the H elements shown in the left hand column. Since Lu is the element which most closely approximates hygromagmatophile element behaviour, D values calculated using Lu as a H element are used in subsequent calculations.

Table 4.3 Average D values calculated for Bloedkoppie granite fractional crystallisation

	Eu	Sr	Ba	La	Ce	Nd	Sm	Gd	Yb	Lu
Lu	2.24	2.74	3.64	3.21	3.12	2.67	2.01	1.41	0.10	-
Yb	2.38	2.93	3.94	3.46	3.36	2.85	2.18	1.46	-	0.11
Nb	2.56	3.18	4.33	3.78	3.67	3.10	2.27	1.52	-0.1	-0.26

	Zr	Rb	Pb	Cs	Hf	Nb	Y	Th	U	Ta
Lu	3.07	0.81	0.75	0.87	2.09	0.21	0.32	0.98	0.82	0.70
Yb	3.30	0.70	0.73	0.85	2.21	0.12	0.24	0.98	0.80	0.67
Nb	3.60	0.76	0.69	0.83	2.37	-	0.14	0.97	0.78	0.63

Ba, Sr, LREE and Zr are highly compatible trace elements while U, Th, Y, Rb, Pb, Ta and Cs are incompatable during fractional crystallisation of the Bloedkoppie magma. These bulk D values (based on Lu as a H element) are used to constrain the F value (weight fraction of remaining liquid) which can account for the observed trace element variations. The observed variation in all trace elements for which D values have been estimated, (Table 4.3) may be accounted for by about 44% fractional crystallisation - for example in the case of Ba :

$$\text{Log } F = \text{Log } C^{i}_{o,l} - \text{Log } C^{i}_{o,l} / (D^{i} - 1) \quad \text{....equation 4.1}$$

$$\text{Log } F = (\text{Log } 92 - \text{Log } 424) / 2.64 \quad \text{.... where } C^{i}_{l} = \text{i in sample BL2}$$

and $C^{i}_{o,l}$ = i in sample KND 1.1

$F = 0.56$ i.e. ~ 44% fractional crystallisation.

4.6.2 Melting models to produce the Bloedkoppie primary magma

It is assumed that the peraluminous Bloedkoppie granite was derived by anatexis of crustal rocks (section 4.3). For the purposes of this modelling an average Kuiseb schist composition (Haack *et al.*, 1984 and this work) is used as a starting material. The trace element abundances of this average schist are as shown in Table 4.4. For comparison, trace element abundances of average upper crust (Taylor and Mc Clennan, 1985) is shown in parentheses in Table 4.4.

Table 4.4 Trace element abundances of average Kuiseb schist and average upper crust

Ba	Sr	Rb	Eu	La	Ce	Nd	Sm	Tb	Ho	Tm
509	93	132	1.45	38	77	39	7.76	1.12	1.65	0.53
(550)	(350)	(112)	(0.88)	(30)	(64)	(26)	(4.45)	(0.64)	-	(0.33)

Yb	Lu	Y	Zr	Ta	U	Th	Pb	Hf	Nb	Cs
3.27	0.54	45	187	0.99	3.9	13.75	29	7.5	21	5.09
(2.2)	(0.32)	(22)	(190)	(2.2)	(2.8)	(10.7)	(20)	(5.8)	(25)	(3.7)

4.6.2.1 Batch melting

The batch melting equation of Shaw (1970) is used.

$C^i_l / C^i_o = 1/F + D - (F.D)$ where C^i_l and C^i_o represent the concentrations of a trace element in the liquid and solid respectively. F is the weight fraction of liquid formed and D is the bulk distribution coefficient for the residual solids when the melt is removed from the system.

The results of batch melting calculations are illustrated graphically in Fig. 4.24. The curves show how D must change to keep C_l / C_o (constrained by the trace element abundances in sample KND 1.1 and average Kuiseb schist) constant for each trace element at different values of F for this melting model. Ta is the most incompatible trace element, showing the greatest enrichment in the liquid relative to the source. The Ta curve intersects the D = 0 line at an F value of 0.36. This implies that the maximum amount of batch melting possible is 36% (Fig 4.24). Batch melting assumes that the liquid remains in chemical equilibrium with the solid residue until the liquid is allowed to escape as a single discrete batch of primary magma. Other melting models e.g. Rayleigh partial melting, aggregrated Rayleigh partial melts and zone refining have also been applied to the Bloedkoppie granite data and are discussed below.

abundances in sample KND 1.1 and average Kuiseb schist) constant for each trace element at different values of F for this melting model. Ta is the most incompatible trace element, showing the greatest enrichment in the liquid relative to the source. The Ta curve intersects the D = 0 line at an F value of 0.36. This implies that the maximum amount of batch melting possible is 36% (Fig 4.24). Batch melting assumes that the liquid remains in chemical equilibrium with the solid residue until the liquid is allowed to escape as a single discrete batch of primary magma. Other melting models e.g. Rayleigh partial melting, aggregrated Rayleigh partial melts and zone refining have also been applied to the Bloedkoppie granite data and are discussed below.

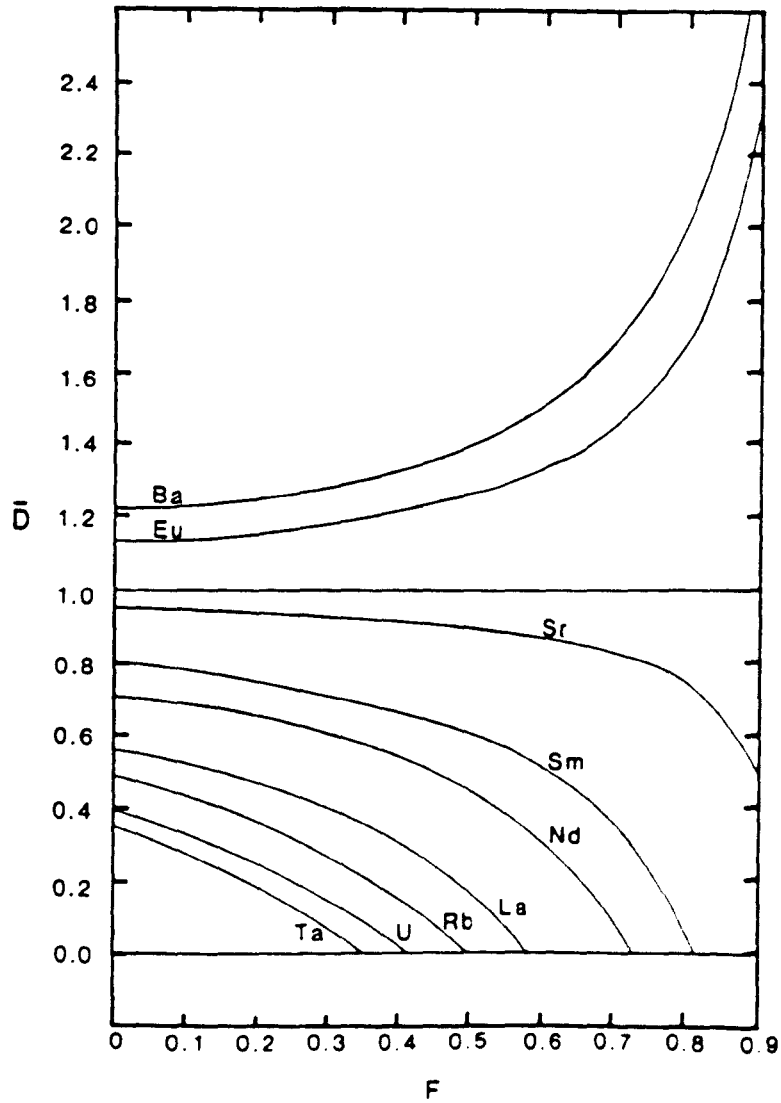

Fig. 4.24 Curves showing how bulk D must change as a function of F to produce the observed trace element distributions in the Bloedkoppie leucogranite assuming a batch melting model. C_l/C_o is constrained for each trace element by trace element distributions in the least evolved sample (KND 1.1) and the assumed source composition. The maximum F value is constrained at 36% by the Ta curve.

4.6.2.2 Raleigh partial melting

This melting model envisages the formation of infinitesimally small volumes of liquid which are instantaneously removed from the system. Each small volume melt fraction is assumed to be in chemical equilibrium with the solid residue. Although this melting model may be physically unlikely it serves to illustrate the limiting case of extreme trace element enrichment (of incompatible trace elements) in the liquid relative to the source. The equation used is from Shaw (1970), $C_l / C_o = 1 / D \ (1 - F)^{(1/D - 1)}$ ..... equation 4.3

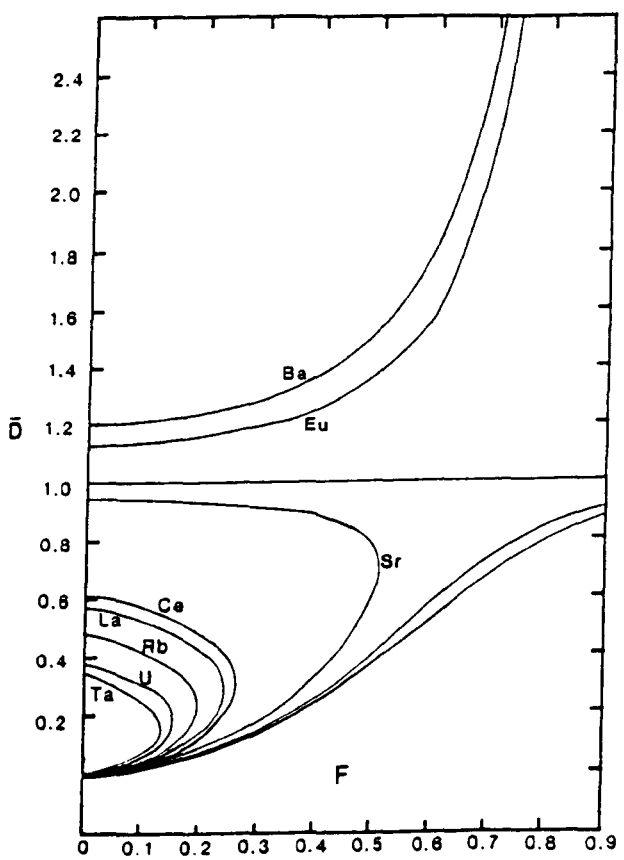

Fig. 4.25 Curves showing how bulk D must change as a function of F to produce the observed trace element distributions in the Bloedkoppie leucogranite assuming a Rayleigh fractionation model. C_l/C_o is constrained for each trace element by trace element distributions in the least evolved sample and the assumed source. The maximum F value is constrained at 14% by the Ta curve.

The most incompatible trace element (Ta) constrains the maximum degree of partial melting permitted by the data. A maximum F value of 0.14 i.e. about 14% partial melting is inferred from the Ta curve on Fig. 4.25. It is noted that for every F value substituted into the Rayleigh equation there are two possible D values which satisify the equation.

4.6.2.3 Aggregated Rayleigh partial melts

Shaw (1970) gives an equation which describes several Rayleigh partial melts collected together into a common resevoir where they are perfectly mixed. Results from this model in which $C_f/Co = 1/F\ (1- (1 - F)^{1/D})$, are indistinguishable from those obtained using the batch melting model i.e. F must be less than 0.36.

4.6.2.4 Zone refining

Zone refining is a melting process whereby magmas interact with unmelted source material. Under ideal conditions complete equilibration occurs between melt and the unmelted material through which the melt front proceeds. In effect, compatible elements are relatively unaffected by this process while incompatible elements are enriched in the magma according to the equation $C_f/C_o = 1/D - [1/D]\ e^{-nD}$ where n is the number of equivalent volumes processed by the liquid. Fig. 4.26 shows D values required to produce the observed C_f/C_o ratios for several trace elements as n changes. For n values greater than about 11 even the most incompatible trace element (Ta) is buffered at 1/D, while a compatible trace element e.g. Ba is buffered at 1/D for n values greater than about 3. However at least 1.8 zone lengths

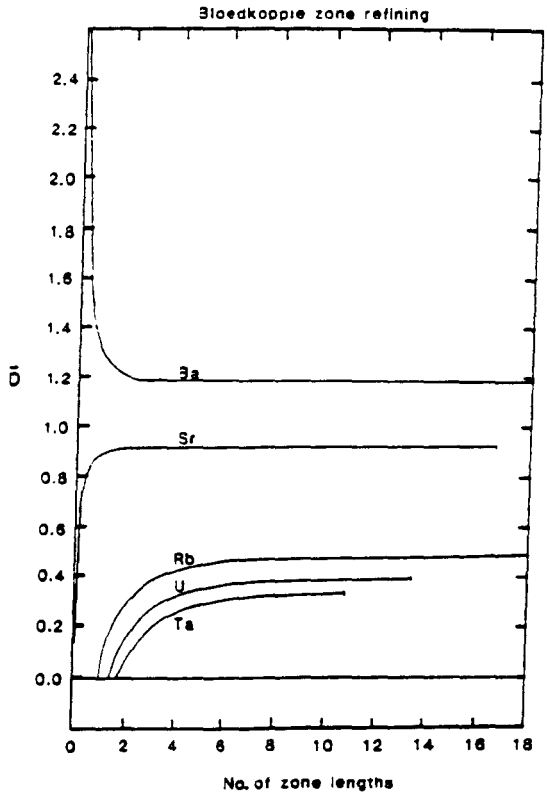

Fig. 4.26 Curves showing how bulk D must change as a function of n (no. of equivalent volumes) to produce the observed trace element distributions in the Bloedkoppie leucogranite assuming a zone refining model. C_l/C_o is constrained for each trace element by trace element distributions in the least evolved sample and the assumed source.

are required to produce the observed Ta enrichment relative to the source. The maximun n value is constrained by Ba (D = 1.20). Above 15.55 equivalent volumes the C_l/C_o ratio observed for Ba can no longer be maintained. Therefore the observed trace element patterns in the Bloedkoppie primary magma can be generated by zone refining if $1.8 < n < 15.5$.

4.6.2.5 Summary

The Bloedkoppie magma can be generated by batch melting of an average Kuiseb schist composition if F is less than 36%. It is interesting to note that if the trace element abundances for average upper crust (Taylor and Mc Clennan, 1985) are used as a source

material the calculated maximum F value is about 30% for the batch melting model, in good agreement with maximum value (36%) calculated on the basis of an average Kuiseb schist composition. Rayleigh partial melting is considered to be physically inprobable since the Rayleigh partial melting equation is satisfied by two D values at any given F value. Moreover, the Rayleigh melting model requires the removal of very small melt volumes as soon as they are formed. In the case of high viscosity granitic melts this is virtually impossible (e.g. Mc Kenzie, 1985).

Although all melting models represent oversimplifications of physically realistic situations the batch melting model is considered to be more realistic than any of the other melting models investigated. Assuming a batch melting model and the source compositions listed in Table 4.4 the maximum amount of partial melting must be less than 36%. The observed range of trace elements may be generated by Rayleigh fractional crystallisation if about 44% fractional crystallisation occurred. Ba, Sr, Eu, Zr, Hf and all the REE except Yb and Lu behave compatibly during fractional crystallisation of the Bloedkoppie magma while Lu, Yb, Pb, Hf, Nb, Ta, U, Th and Y are incompatible.

4.6.3 Goanikontes alaskite

For the purposes of trace element modelling it is assumed that the observed trace element variations within the Goanikontes alaskite intrusion were produced by Rayleigh fractional crystallisation of a primary magma. It is also assumed that the least evolved sample of the suite (sample G0) is representative of the primary magma composition while the most evolved sample (sample G9) is assumed to represent the "final liquid". Average bulk D values for the fractional crystallisation process have been calculated using the approach outlined above. U and Nd are highly incompatible and are assumed to have bulk D values close to zero.

Table 4.5 Calculated average bulk D values for the Goanikontes alaskite

	Eu	Sr	Ba	La	Ce	Nd	Sm	Yb	Lu	Zr
Nd	0.95	1.28	1.59	0.38	0.17	-	0.20	0.35	0.32	0.26
U	0.95	1.28	1.59	0.39	0.18	0.01	0.20	0.35	0.33	0.27

	Rb	Pb	Hf	Nb	Y	Th	U	Ta
Nd	1.12	0.95	0.40	0.86	0.56	0.54	0.01	1.12
U	1.12	0.95	0.41	0.86	0.57	0.55	-	1.12

Sr, Ba, Ta and Rb behave as compatible trace elements while other trace elements, listed in order of increasing incompatibility have D values < 1 (e.g. Pb, Eu, Nb, Y, Th, Hf, La, Yb, Lu, Zr, Sm, Ce, Nd, U).

Using the D values calculated above (based on Nd as a hygromagmatophile element) it is calculated that about 90% Rayleigh fractional crystallisation is required to produce the observed trace element variations. This extremely high degree of fractional crystallisation is required by the extreme enrichments in U and Nd relative to the inferred primary liquid.

In conclusion, it is possible to produce the extreme U and Nd enrichments in the most "evolved" Goanikontes alaskite samples only if > 90% fractional crystallisation of the primary magma occurred (assuming that U and Nd enrichment resulted only from magmatic enrichment processes).

4.6.3.1 Melting models to produce Goanikontes alaskite primary liquid

The calculations presented here assume that the parental Goanikontes alaskite magma was produced by anatexis of crustal rocks having the composition of an average Kuiseb schist, similar to the starting material used to model the Bloedkoppie granite magma. A number of melting models are applied in which C_l/C_o is kept constant i.e. constrained by the trace

element composition of the Kuiseb schist starting material and the most "least evolved" alaskite sample (sample no. G0).

4.6.3.2 Batch melting

A batch melting model predicts a maximum F value of 24% partial melting. Above 24% partial melting the observed U or Nd enrichment cannot be produced by simple batch melting (Fig. 4.27). The next most incompatible trace element is Rb which requires that f is less than 0.29 i.e. < 29% partial melting (Fig. 4.27).

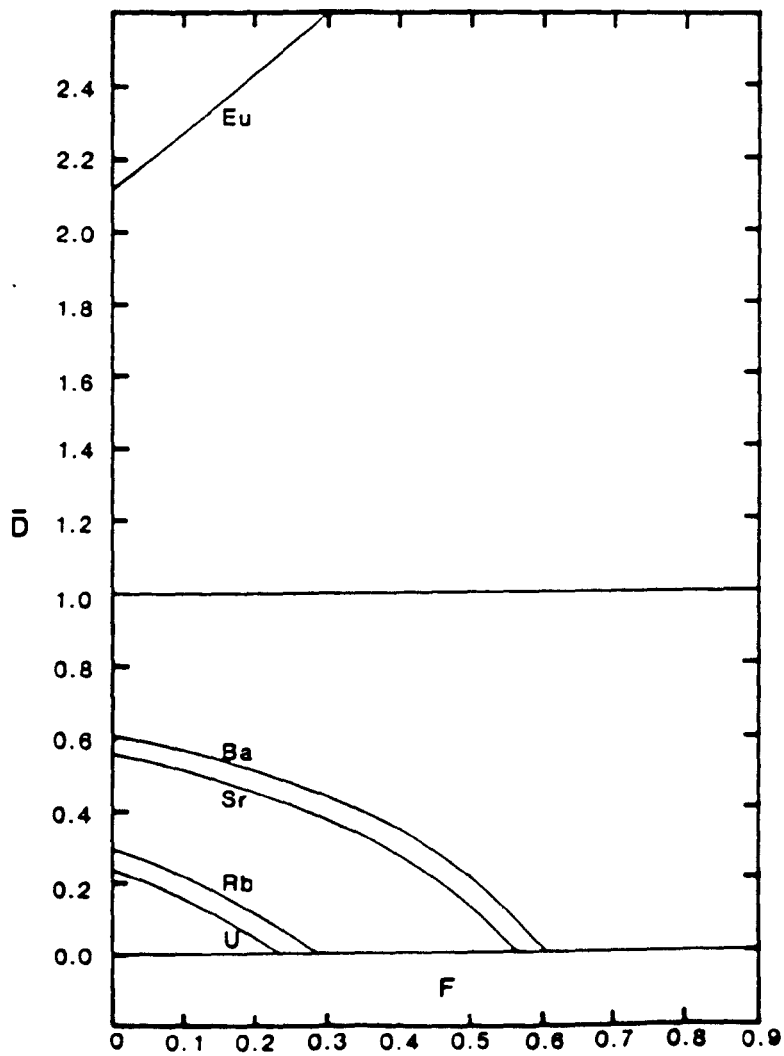

Fig. 4.27 Curves showing how bulk D must change as a function of F to produce the observed trace element distributions in the Goanikontes alaskite assuming a batch melting model. C_f/C_o is constrained for each trace element by trace element distributions in the least evolved sample and the assumed source.

If the trace element abundances of average upper crust (Taylor and Mc Clennan, 1985) in Table 4.4, are used as a source material the maximum amount of partial melting is constrained at 24%, in good agreement with that estimated using the average Kuiseb schist composition (24-29%).

4.6.3.3 Rayleigh partial melting

Fig. 4.28 shows how D changes with increasing F in order to keep C_l/C_0 constant during Rayleigh partial melting. The maximum amount of partial melting possible is ~9% (F = 0.09) (Fig. 4.28). The observed U enrichment in the primary liquid relative to the source cannot be produced if F > 0.09.

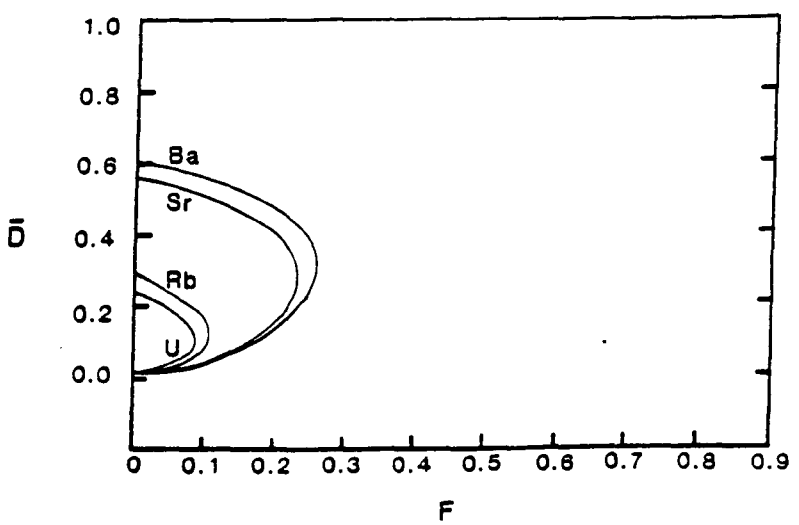

Fig. 4.28 Curves showing how bulk D must change as a function of F to produce the observed trace element distributions in the Goanikontes alaskite assuming a Rayleigh melting model. C_l/C_0 is constrained for each trace element by trace element distributions in the least evolved sample and the assumed source.

4.6.3.4 Zone refining

At least 3.25 zone lengths are required to produce the observed U enrichment. Ba provides a constraint on the maximum number of zone lengths. Above about 27 zone lengths the observed C_l/C_o ratio for Ba can no longer be maintained (Fig. 4.29).

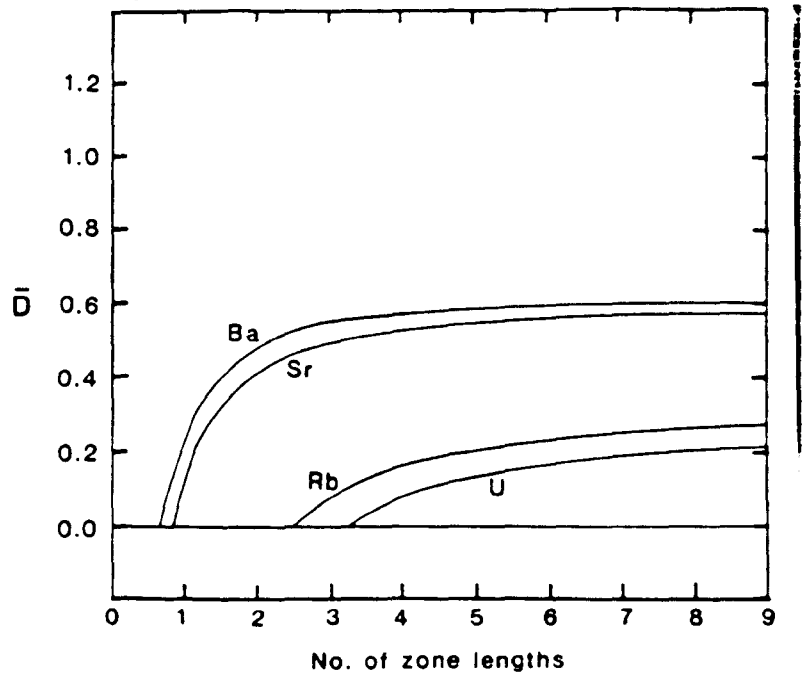

Fig. 4.29 Curves showing how bulk D must change as a function of n (no. of equivalent volumes) to produce the observed trace element distributions in the Goanikontes alaskite assuming a zone refining model. C_l/C_o is constrained for each trace element by trace element distributions in the least evolved sample and the assumed source.

4.6.3.5 Summary

In summary, the Goanikontes alaskite primary magma may be produced by batch melting of average Kuiseb schist or average upper crust if the degree of partial melting is less than about 24%. Rayleigh partial melting can produce the observed trace element abundances if the degree of partial melting is less than 9%. However as discussed above the Rayleigh melting equation is unlikely to represent a physically realistic melting model. More than 90%

fractional crystallisation is required to produce the observed U and Nd enrichments in the most evolved samples (defined on the basis of major and trace elements). With the exception of Sr, Ba, Ta and Rb trace elements behave incompatibly.

4.6.4 Inferred residual mineralogies for crustal-melt granitoids

Fig. 4.30 shows inferred source bulk D values for a range of trace elements in the Bloedkoppie granite and Goanikontes alaskite. Source bulk D values were calculated on the assumption that the least evolved sample from each intrusion was derived by batch partial melting of a source with trace element abundances of the average Kuiseb schist as shown in Table 4.4. F values used were as calculated above i.e. 0.36 and 0.24 for the Bloedkoppie granite and Goanikontes alaskite respectively.

The most striking feature of inferred bulk D values is that with the exception of Rb and U, most trace elements are preferentially retained in the residue. Ba, Sr and Eu behave compatibly suggesting residual feldspar in the source. The extremely high inferred (source) bulk D values for the REE are interpreted as reflecting REE control by residual minor phases. In the case of the Goanikontes alaskite the high inferred bulk D values for Zr, Hf and the HREE may reflect residual zircon during partial melting.

Source bulk D values inferred for the Goanikontes alaskite are higher than those inferred for the Bloedkoppie leucogranite. The higher inferred bulk D values (Ba and Sr excepted) for the Goanikontes alaskite may reflect a smaller volume partial melt whereby refractory minor phases remained unmelted and so retained significant amounts of the REE and HFS elements in the source. In the case of the Bloedkoppie granite for which larger degrees of partial melting (36%) have been inferred, minor phases may have been partially melted or incorporated into the melt so that the inferred source bulk D values for several trace

elements are lower. Inferred source bulk D values for Ba and Sr are lower for the Goanikontes alaskite suggesting that relatively large quantities of feldspar had melted. This is consistent with alaskite generation by relatively small volume partial melting (< ~ 20%) of a quartzo-feldspathic source dominated by K-feldspar ± plagioclase ± quartz anatexis to produce K rich melts enriched in U and Rb but depleted in the REE and HFS elements.

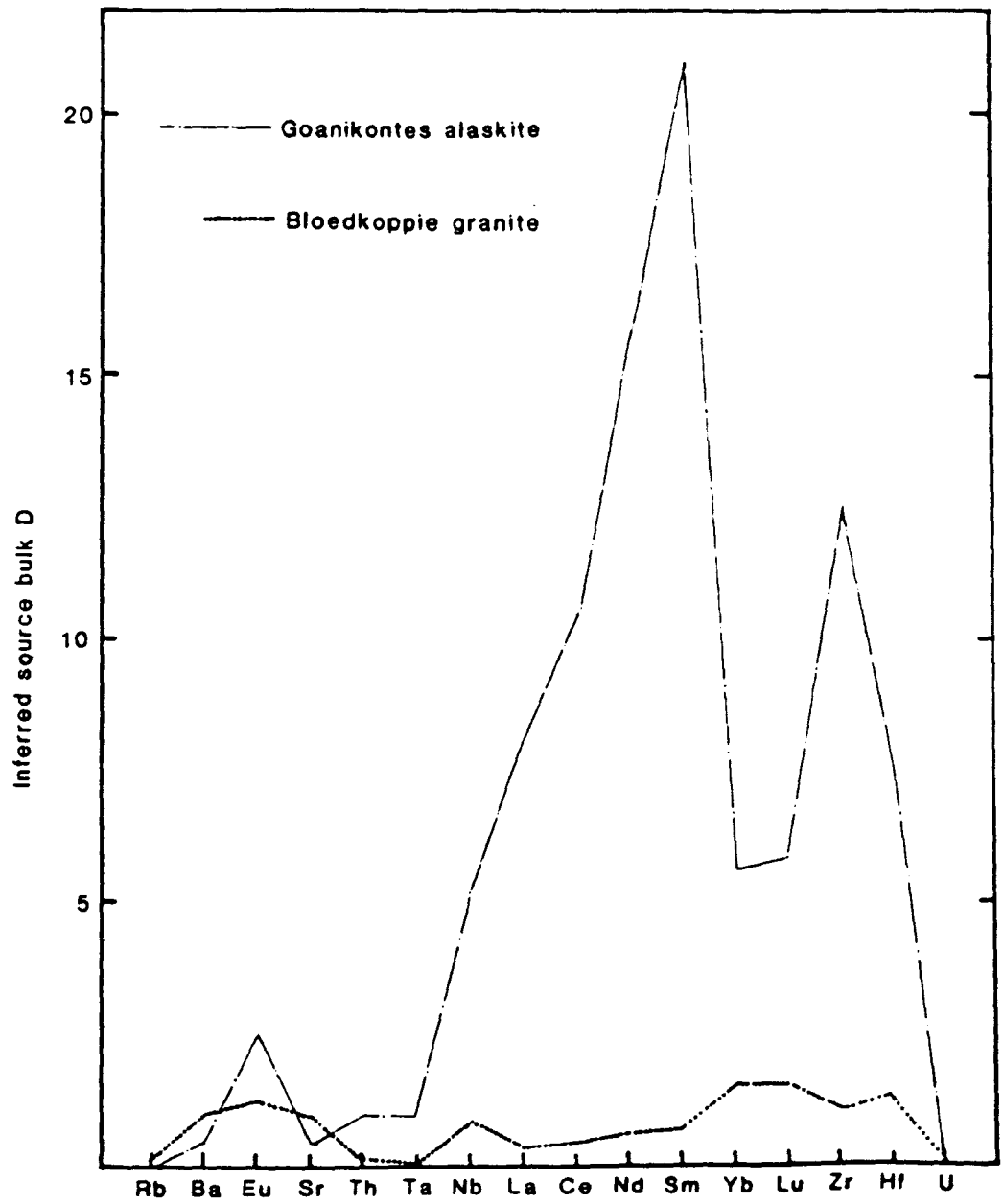

Fig. 4.30 Inferred source bulk D values for the Bloedkoppie leucogranite and Goanikontes alaskite intrusion. Bulk D values are calculated by assuming batch partial melting of a metasedimentary source (Table 4.4) using F values of 0.24 and 0.36 for the alaskite and leucogranite respectively.

4.6.5 The within-plate Sorris-Sorris granite

Trace element variations in the Sorris-Sorris granite are modelled in order to place constraints on the petrogenetic processes which produce high-field strength element enriched, within plate granitoids. Within-plate granitoids (Pearce *et al.*, 1983) are characterised by high Nb, Ta and Th abundances and significant crustal involvement in their genesis is unlikely (Weiss, 1983 Pearce *et al.*, 1984). However, Damara within-plate granitoids have model Nd ages in the range 1.0 - 1.3 Ga so that they cannot have been derived from a mantle source during the Damara orogeny.

A mantle derived undersaturated igneous rock (e.g. a nepheline syenite) is a likely precursor from which a trace element enriched within-plate granitoid may be generated. For the purposes of trace element modelling it is assumed that the Sorris-Sorris magma was derived by partial melting of a nepheline syenite.

The least evolved (on the basis of both major and trace elements) Sorris-Sorris granitoid sample analysed (RM 673) is the best available representative of the Sorris-Sorris primary magma. A sample from the Lofdal syenite in northern Namibia (sample 28/29) is chosen as a typical parental syenite material. This syenite merely provides a convenient parental composition from which to model within-plate granitoids and it is emphasised that no direct genetic link is implied between the Lofdal syenite and the Sorris-Sorris granitoid.

4.6.5.1 Variations within the Sorris-Sorris granitoid

LIL element variations are shown as logarithmic plots of Rb vs Ba and Sr vs Ba (Fig. 4.31). Ba and Sr behave as compatible trace elements (Fig. 4.11) while Rb is clearly incompatible over the observed compositional range. Vectors for the removal of plagioclase,

K-feldspar and biotite by Raleigh fractional crystallisation are shown in Fig. 4.31 with F values shown at 0.1 intervals along each vector.

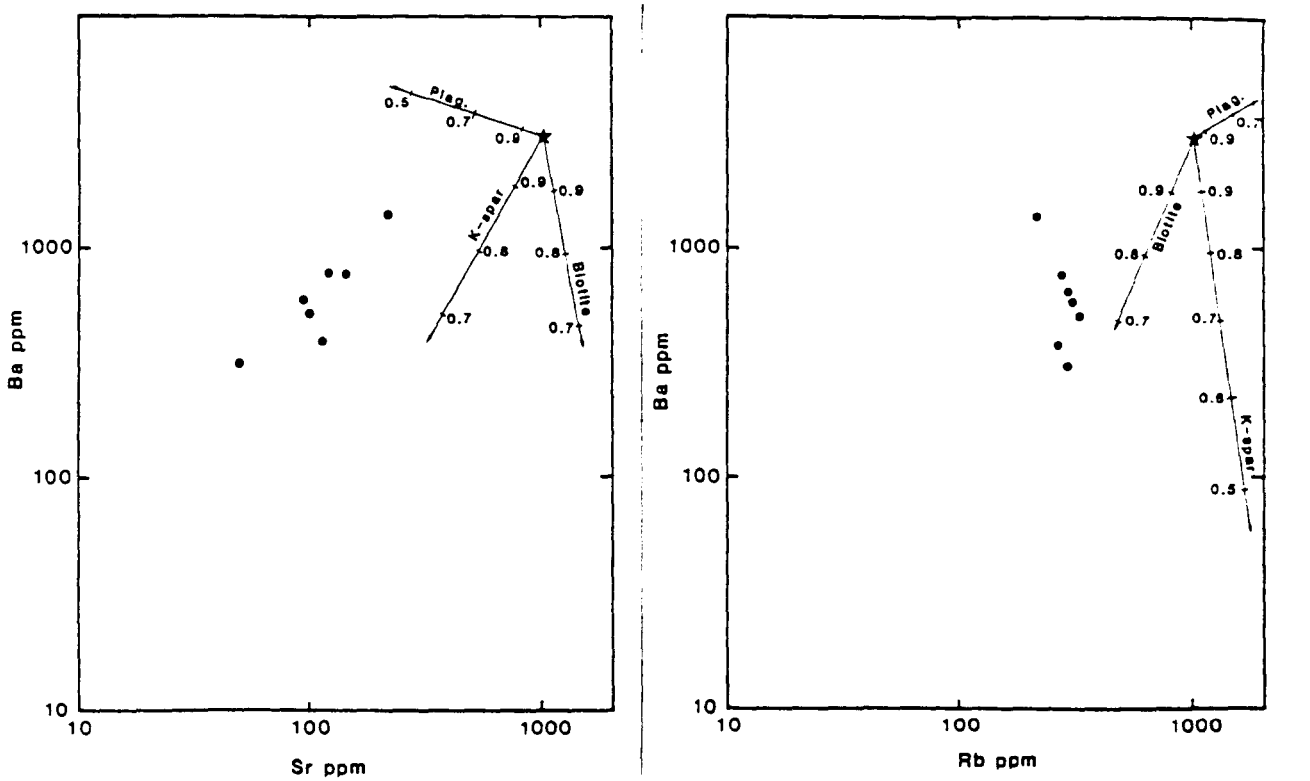

Fig. 4.31 Log-Log Ba vs. Sr and Ba vs. Rb diagrams for the Sorris-Sorris granitoid. Vectors are drawn for Rayleigh fractional crystallisation with F values shown as ticks at 0.1 intervals along each vector.

Assuming that the observed range in trace element variations result from Rayleigh fractional crystallisation mean bulk D values are calculated for a range of trace elements using the approach outlined in section 4.6.1 above. Based on major and trace element data, samples RM 673 and RM 663 are chosen to represent the least and most evolved Sorris-Sorris granitoid compositions respectively.

Lu is the most incompatible trace element while Yb and Pb also behave incompatibly. Since Lu most closely approaches a hygromagmatophile trace element bulk D values calculated using Lu variations are used in subsequent calculations of F. The calculated D values are tabulated in Table 4.6.

Table 4.6 Calculated average bulk D values for Rayleigh fractional crystallisation of the Sorris-Sorris granite

	Eu	Sr	Ba	La	Ce	Nd	Sm	Yb	Lu
Yb	3.84	5.67	5.81	4.53	4.43	4.21	3.35	-	-
Lu	3.19	4.60	4.71	3.72	3.65	3.44	2.81	0.23	-
Pb	3.84	5.66	5.81	4.53	4.42	4.20	3.35	-	0

	Zr	Hf	Rb	Pb	Sc	Ta	Th	Nb	Y
Yb	5.66	4.24	0.71	-	1.56	0.79	3.73	2.08	0.38
Lu	4.60	3.49	0.78	0.23	1.44	0.84	3.10	1.83	0.52
Pb	5.66	4.23	0.71	-	1.56	0.79	3.72	2.08	0.38

Assuming Rayleigh fractional crystallisation and the bulk D values tabulated in Table 4.6, the calculated F value is 0.78 i.e. ~ 22% fractional crystallisation of the primary Sorris-Sorris magma (sample RM 673) can produce the observed trace element variations.

4.6.5.2 Melting models for the Sorris-Sorris magma

The melting models presented here assume that the Sorris-Sorris primary magma was generated by anatexis of a pre-existing syenite intrusion. As discussed above, the Lofdal syenite is used here as a typical syenite parental material although it is not implied that the Sorris-Sorris magma was actually derived by anatexis of this particular syenite. Comparisons with other syenites (e.g. those from N.E. Africa ; Harris, 1978 and pers. comm.) show that trace element abundances in the Lofdal syenite are typical for syenite intrusions.

The trace element abundances in a typical Lofdal nepheline syenite sample are tabulated in Table 4.7. Trace element abundances in sample RM 673 (assumed to represent the Sorris-Sorris primary magma) are also given in Table 4.7.

Table 4.7 Trace element abundances (ppm) of RM673 and syenite model parent.

	Sr	Ba	Rb	Nb	Y	Zr	La	Ce	Nd	Sm
L. syenite	1254	299	169	172	25	868	58	102	33	4.9
RM 673	117	762	279	43	72	229	99	188	67	4.9

	Eu	Yb	Lu	Hf	Ta	Th	U
L. syenite	1.24	3.3	0.55	16.3	4.15	5.02	8.8
RM 673	1.20	7.1	1.18	6.69	4.10	53.6	10.8

Th and Y are extremely enriched in the Sorris-Sorris magma relative to the nepheline syenite magma. Most Sorris-Sorris granitoid samples have 50-60ppm Th whereas the average (n = 11) Th content of the analysed Lofdal syenite samples is about 9ppm.

4.6.5.3 Batch melting

In order to maintain the observed C_l/C_o ratio for Th the maximum amount of batch partial melting is about 9.4 %. Even if the higher Th value of 8.64ppm (average of 11 Lofdal syenite samples) is used as the source the degree of partial melting must be < 16%.

4.6.5.4 Rayleigh melting

A Rayleigh partial melting model restricts the maximum possible degree of partial melting to about 4%. The observed Th enrichment in the Sorris-Sorris magma cannot be produced if the degree of partial melting is more than about 4%.

4.6.5.5 Combined assimilation and fractional crystallisation

AFC calculations using an assimilation/fractional crystallisation ratio of 0.2 suggest that an F value of about 0.16 i.e. 84% fractional crystallisation is required, assuming the assimilated material had trace element abundances similar to average Kuiseb schist (i.e. containing about 14ppm Th). If the ratio of assimilation/fractional crystallisation is increased to 0.3, the observed Th enrichment can be achieved by approximately 80% combined AFC.

4.6.5.6 Summary

Since the Sorris-Sorris granitoid has model Nd (D.M.) ages in the range 1.2-1.4 Ga this intrusion cannot have been derived from the mantle at ~ 500 Ma (Rb/Sr age = 495 ±15 Ma). Assuming that the Sorris-Sorris magma was derived by partial melting of a syenite source rock, relatively small degrees of partial melting (<16% batch melting) are required to produce the observed trace element enrichments. AFC models require large degrees of fractional crystallisation (~ 80%) to produce the observed Th enrichments in the Sorris-Sorris granitoid. However AFC is considered to be an unlikely petrogenetic process since $\delta^{18}O$ values for the Sorris-Sorris granitoid are low (~ 7.0 ‰) suggesting that insignificant quantities of high $\delta^{18}O$ metasediments were assimilated.

4.6.6 Palmental diorite trace element modelling

Trace element variations in the calc-alkaline Palmental diorite are modelled in order to assess differences in the petrogenetic processes between calc-alkaline diorites and other granitoid types. It is assumed that variations within the Palmental diorite were produced

by Rayleigh fractional crystallisation of a primary magma. Major and trace element variations in this intrusion have been shown in Harker diagrams in Fig. 4.10. On major and trace element grounds samples P2094 and P2186 have been chosen to represent the least evolved and most evolved compositions respectively.

The procedure outlined above (section 4.6.1) was followed to estimate bulk D values for several trace elements using equation 4.2. U, Cs and Th were found to be the most incompatible trace elements and were used as hygromagmatophile trace elements to estimate bulk D values for other trace elements. Estimated average bulk D values for fractional crystallisation of the Palmental diorite are tabulated in Table 4.8.

Table 4.8 Calculated average bulk D values for Palmental diorite fractional crystallisation

	La	Ce	Nd	Sm	Eu	Gd	Tb	Yb	Lu	Cs
U	0.74	0.83	1.03	1.18	1.60	1.15	1.49	1.31	1.36	0.001
Cs	0.74	0.83	1.03	1.18	1.60	1.15	1.49	1.31	1.36	-
Th	0.69	1.04	1.04	1.21	1.71	1.18	1.58	1.36	1.42	-0.17

	Hf	Ta	Th	U	Sr	Rb	Zr	Y	Nb	Ba
U	0.71	0.64	0.15	-	0.74	0.43	0.63	1.34	0.31	0.59
Cs	0.70	0.64	0.14	-	0.74	0.43	0.63	1.34	0.31	0.59
Th	-	0.58	-	-0.17	0.69	0.33	0.56	1.39	0.20	0.52

U is the most incompatible trace element although Cs is almost equally incompatible. Th is slightly less incompatible than either U or Cs but the average bulk D values calculated using U, Cs or Th are very similar. This, combined with the coherent behaviour of U on the Harker diagram (Fig. 4.10) suggests that the observed variation in U reflects fractional crystallisation and has been relatively unaffected by alteration.

Perhaps the most striking feature of bulk D values calculated for Palmental diorite

fractional crystallisation is that most trace elements behave incompatibly. This is in marked contrast to trace element behaviour in the within-plate Sorris-Sorris granitoid or the crustal melt Bloedkoppie granitoid. Eu and the HREE behave compatibly while the LIL elements Ba, Sr and Rb are incompatible. In marked contrast to the Sorris-Sorris, Bloedkoppie and Goanikontes intrusions Ba and Sr behave incompatibly suggesting that no significant K-feldspar fractional crystallisation occurred. Hf and Zr behave as incompatible trace elements whereas in other granitoid types these trace elements are partitioned into zircon.

The compatible behaviour of the REE is interpreted as reflecting amphibole fractionation. Fourcadre and Allegre (1981) have shown that hornblende (the dominant phase in this diorite) hosts significant quantities of the REE in dioritic rocks. Furthermore the HREE S are preferentially partitioned into hornblende while La and Ce are slightly less compatible (Fourcadre and Allegre, *op. cit.*) This is consistent with estimated bulk D values (Table 4.8) which suggest that La and Ce behave incompatibly while the HREE s are more compatible (Fig. 4.32).

Sr behaves incompatibly suggesting that insufficient plagioclase feldspar fractional crystallisation occurred to produce a bulk D for Sr greater than unity. Eu behaves compatibly and has a high bulk D value, suggesting that at least some fractional crystallisation of plagioclase occurred. This is consistent with the relatively high bulk D value (0.74) calculated for Sr. Sphene occurs in trace amounts in the Palmental diorite and may have exerted some control on REE distribution although this accessory phase incorporates less REE than hornblende in dioritic magmas (Fourcadre and Allegre, *op. cit.*).

Assuming the bulk D values as outlined in Table 4.9, an F value of 0.28 is required, i.e. the observed range in compositions represent 71% fractional crystallisation (assuming that the most primitive sample P2094 is represents the "initial" liquid).

4.7 Comparison of D values estimated for each granitoid type

Estimated bulk D values during fractional crystallisation for each granitoid type are illustrated in Fig. 4.31. The Sorris-Sorris granitoid and the Palmental diorite represent within-plate and calc-alkaline granitoids respectively.

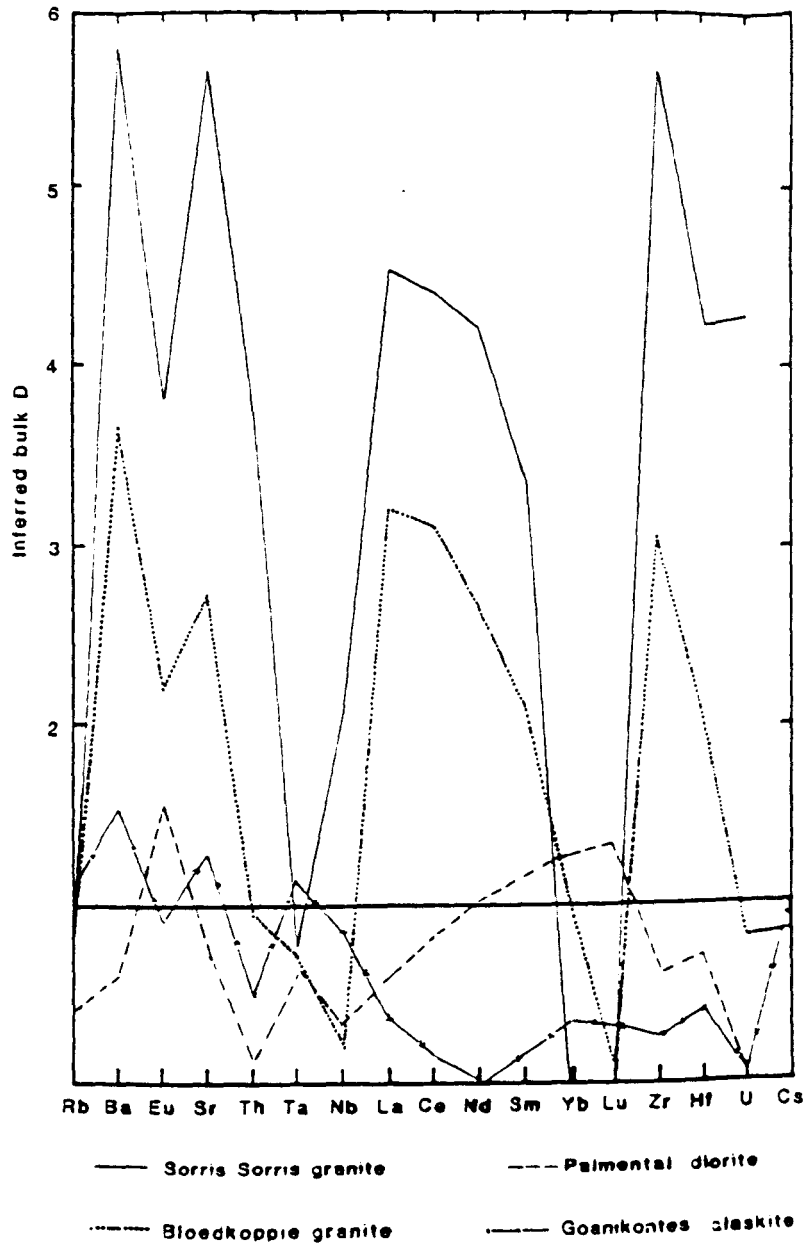

Fig. 4.32 Inferred bulk D values for fractional crystallisation of the Sorris-Sorris, Palmental, Bloedkoppie and Goanikontes intrusions.

The Bloedkoppie granite and Goanikontes alaskite are representative of crustal-melt granitoids, although clearly there are significant differences between bulk D values calculated for the Bloedkoppie and Goanikontes intrusions. The within-plate Sorris-Sorris granitoid displays the largest inferred bulk D values. The Bloedkoppie crustal-melt granitoid has relatively high bulk D values whereas the Palmental diorite and the Goanikontes alaskite have relatively low bulk D values for most trace elements. The following conclusions can be drawn from Fig. 4.32 ;

1. In the calc-alkaline Palmental diorite inferred bulk D values for both Ba and Sr are less than unity which is in marked contrast to the behaviour of these trace elements in the other granitoids. This strongly suggests that no significant K-feldspar fractional crystallisation occurred.

2. The estimated bulk D values for the REE strongly suggest that hornblende fractional crystallisation controlled the distribution of the REE in this intrusion.

3. Only the LIL elements Rb, Ba and Sr behave compatibly during fractional crystallisation of the Goanikontes alaskite magma suggesting that fractional crystallisation is dominated by K-feldspar.

4. Inferred bulk D values for Zr are high for the Sorris-Sorris and Bloedkoppie intrusions reflecting zircon fractional crystallisation. However, Zr behaved incompatibly during fractional crystallisation of the Palmental diorite and Goanikontes alaskite intrusion. The Sorris-Sorris and Bloedkoppie intrusions also have higher Zr abundances than the other intrusions suggesting that the behaviour of a trace element such as Zr during fractional crystallisation may be controlled by it's abundance in the magma. Similarily, the intrusions which have the highest LREE contents also display the highest inferred bulk D values for these trace elements during fractional crystallisation suggesting LREE removal by minor phases in which the LREE are crystallographic constituents.

4.9 Summary

In summary, three geochemically distinct granitoid types have been distinguished. The principal geochemical characteristics of each granitoid type are outlined in Table 4.1. Of the crustal-melt granitoids, alaskites were derived by relatively small volum(~ 20%) batch partial melting of a metasedimentary source while two-mica leucogranites (e.g. Bloedkoppie granite) may be modelled as larger volume (~36%) batch partial melts. Trace element enriched within-plate granitoids may be modelled as relatively small volume partial melts of syenite sources. Fractional crystallisation in within-plate granitoids is dominated by K-feldspar resulting in high inferred bulk D values for Ba and Sr. In marked contrast, Ba andSr behave as incompatible trace elements during fractional crystallisation of the calc-alkaline Palmental diorite while the REE are controlled by amphibole fractional crystallisation.

CHAPTER 5

Isotope geochemistry

5.1 Introduction

Since a good geochronological framework was already established by previous workers emphasis was placed on using radiogenic and stable isotopes to further constrain granitoid petrogenetic processes. In addition, radiogenic isotope determinations on metasediments were used to investigate crustal evolution during and subsequent to the Damara orogeny.

5.1.1 Previous work

Previously published whole-rock Rb/Sr ages for Damara granitoids are tabulated in Table 5.1. Granitoid sample localities are shown in Fig. 5.1. Published Rb/Sr whole-rock ages range from about 840 Ma to 460 Ma, although most granitoids yield ages in the range 590 - 550 Ma (Marlow, 1981 ; Kroner, 1982 ; Downing, 1982 ; Hawkesworth *et al.*, 1983 ; Marlow, 1983). The youngest intrusions were emplaced between 490 and 460 Ma ago and are confined to the high temperature west Central Zone (Fig 1.3), (Haack *et al.*, 1980 ; Hawkesworth *et al.*, 1983).

Hawkesworth and Marlow (1983) examined variations in Sr, Nd and Pb isotopes with depth in the Damara metasediments. $^{87}Sr/^{86}Sr$ ratios recalculated to 500 Ma show a striking increase with depth in the Damara metasedimentary pile. This trend is accompanied by a decrease in $^{143}Nd/^{144}Nd$. In contrast, Pb isotopic compositions of conformable and crosscutting sulphide ores do not show any systematic variation with depth.

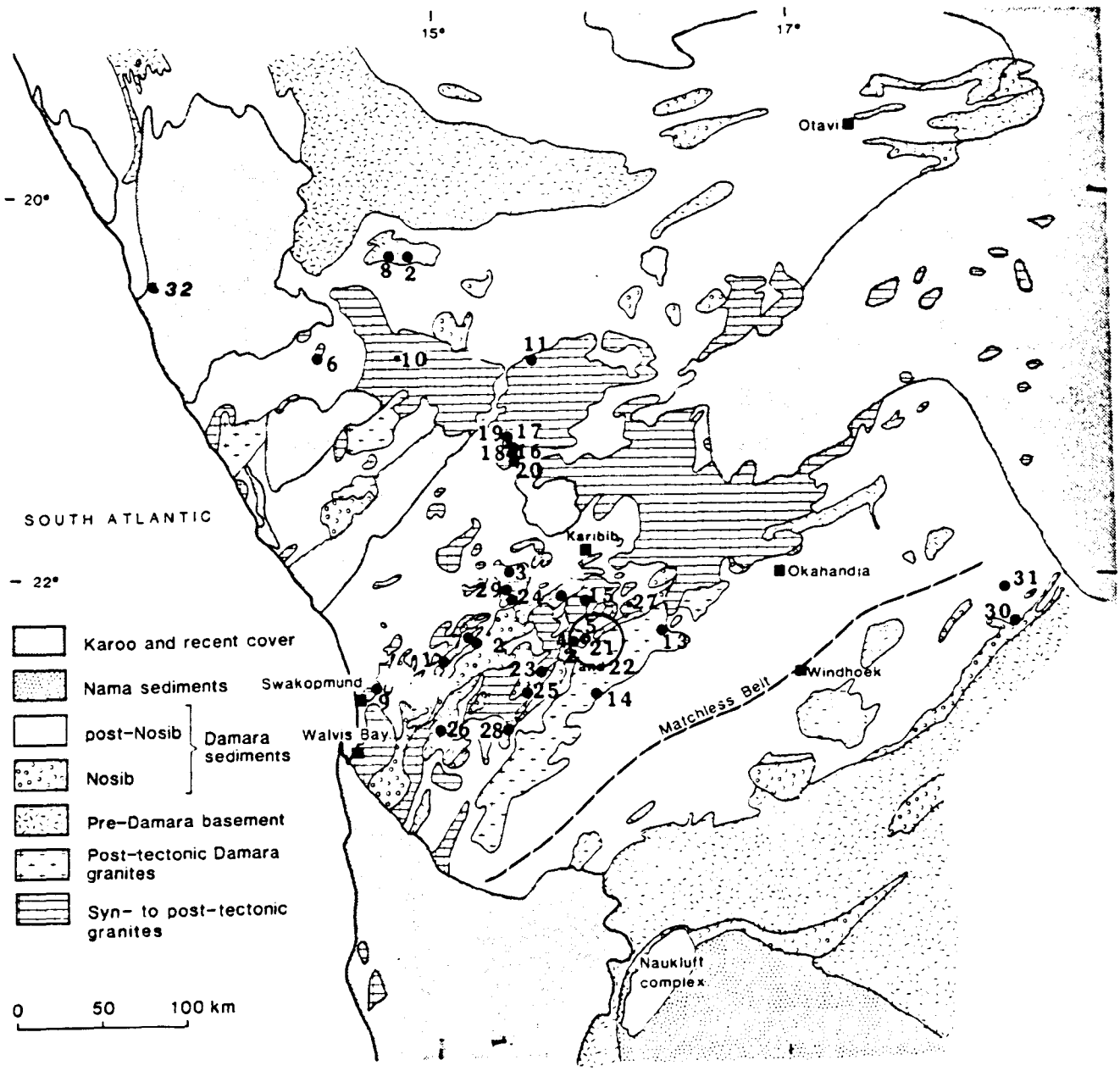

Fig. 5.1 Map of the Damara orogen showing the localities of granitoids listed in Table 5.1. Locality 21 (encircled) is the Palmental locality from which granitoids have been sampled for age determinations in this study. Locality 32 (close to the coast, in the north-west part of the area is the Huab-river diorite locality.

Table 5.1 Previously published Rb/Sr whole-rock ages for the Damara granitoids

	Intrusion	Age	Initial $^{87}Sr/^{86}Sr$	Reference
1	Rossing Alaskite	458 ±8	0.759 ±1	Kroner and Hawkesworth (1977)
2	Oas syenite	840 ±12	0.7036 ±13	Kroner (1982)
3	Abbabis dykes	766 ±78	0.7032 ±12	Kroner (1982)
4	Palmental diorite	750 ±18	0.7048 ±1	Kroner (1982)
5	Palmental granodiorite	651 ±20	0.7057 ±1	Kroner (1982)
6	Doros syenite	573 ±33	0.7058 ±1	Kroner (1982)
7	Outlet gorge granite	554 ±17	0.7140 ±4	Kroner (1982)
8	Lofdal syenite	764 ±60	0.7030 ±4	Hawkesworth *et al.*(1983)
9	Swakopmund Salem g.	563 ±63	0.707 ±4	Hawkesworth *et al.*(1983)
10	Sorris-Sorris granite	495 ±15	0.7092 ±15	Hawkesworth *et al.*(1983)
11	Otjosondjou Salem	546 ±30	0.7054	Hawkesworth *et al.*(1983)
12	Valencia alaskite	495 ±12	0.724 ±2	Hawkesworth *et al.* (1983)
13	Donkerhuk granite$_1$	523 ±8	0.7074 ±2	Blaxland *et al.* (1979)
14	Donkerhuk granite$_2$	521 ±15	0.7117 ±10	Blaxland *et al.* (1979)
15	Goas Salem-type	515 ±20	0.7166 ±6	Blaxland *et a.l* (1979)
16	Omaruru Salem-type	552 ±19	0.7056 ±4	Haack *et al.* (1980)
17	Omaruru leucocratic	517 ±11	0.7120 ±16	Haack *et al.* (1980)
18	Omaruru Salem-type	479 ±10	0.7076 ±3	Haack *et al* (1980)
19	Omaruru Salem-type	474 ±26	0.714 ±3	Haack *et al.* (1980)
20	Omaruru Salem-type	462 ±19	0.7087 ±5	Haack *et al.* (1980)
21	Palmental diorite	756 ±36	0.707 ±2	Kroner (1982)
22	Palmental diorite	748 ±38	0.706 ±2	Kroner (1982)
23	Horebis river granite	633 ±39	0.712 ±6	Downing (1982)
24	Stinkbank Salem-type	601 ±79	0.710 ±6	Marlow (1981)
25	Onanis Salem-type	554 ±33	0.712 ±6	Downing (1982)
26	Ida-dome alaskite	542 ±33	0.724 ±7	Marlow (1981)
27	Otjua red granite	516 ±23	0.721 ±4	Marlow (1981)
28	Bloedkoppie granite	510 ±9	0.717 ±1	Downing (1982)
29	Stinkbank granite	484 ±25	0.739 ±15	Marlow (1981)
30	Osombahe granite	651 ±20	0.708	Esquevin and Merendez (1974)
31	Dachsberg granite	508 ±5	0.722	Esquevin and Merendez (1974)

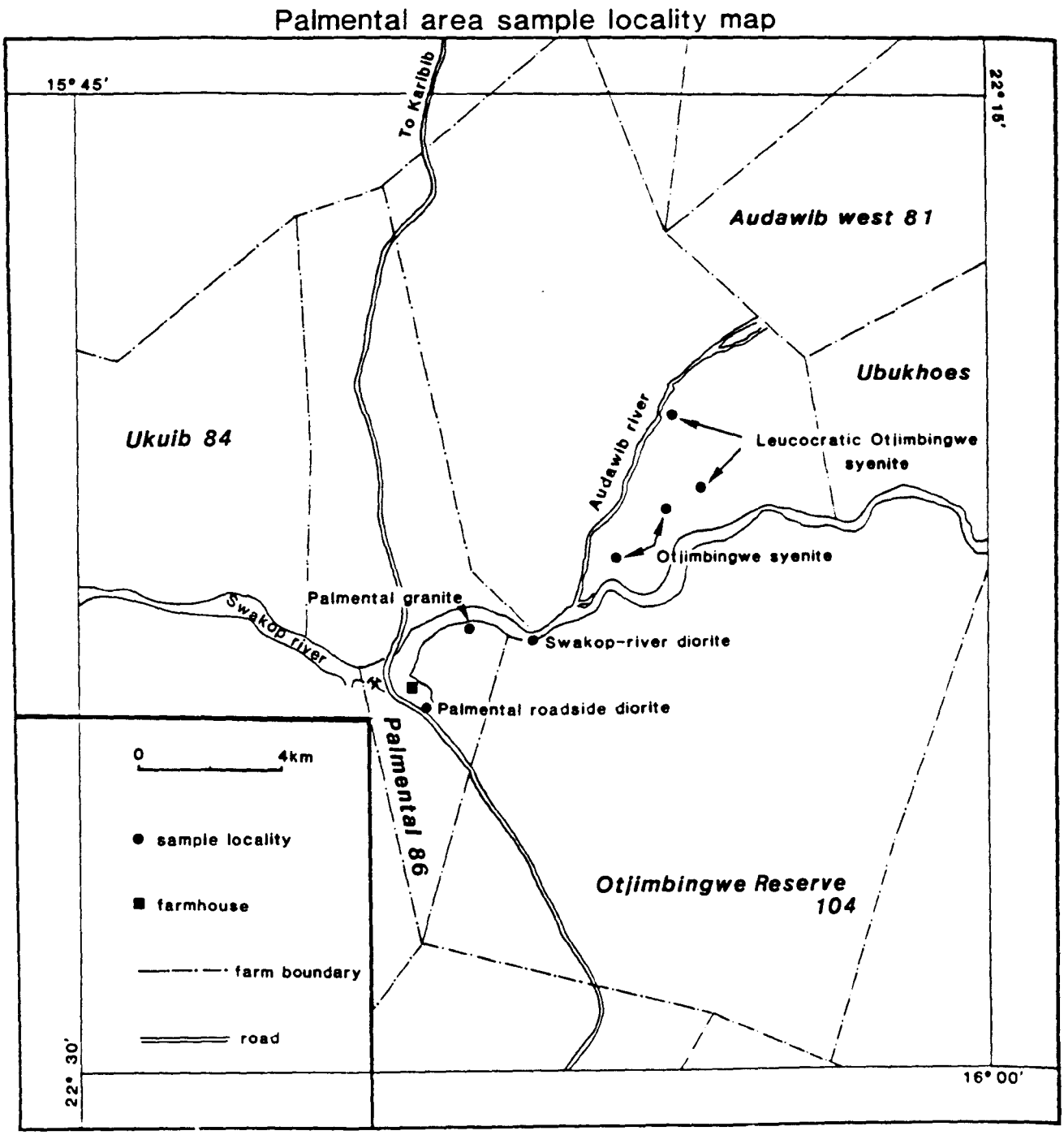

Fig. 5.2 Map of the Palmental area showing the sites sampled for geochronological studies.

Hawkesworth and Marlow (*op. cit.*) concluded that the Nosib Group (oldest Damara sediments) were derived from the underlying pre-Damara basement. Model Nd ages (CHUR ages) from the Nosib Group are about 2.0 Ga while the schists of the Kuiseb Formation have model Nd ages of about 1.0 Ga reflecting sediment input from younger source terrains during deposition of the Kuiseb Formation.

5.2 Geochronology

Rb/Sr whole-rock age determinations have been carried out on six granitoid intrusions. Localities are given in Fig. 5.1. Five of the six intrusions studied are from the Palmental area (Fig. 5.2) and are referred to in this work as the Palmental granite, the Palmental roadside diorite, the Swakop-river diorite, the Otjimbingwe syenite and the leucocratic Otjimbingwe syenite. Field relations are discussed in Ch 2. The Huab-river diorite outcrops about 12 Km north of the mouth of the Huab-river (R. Mc G. Miller pers. comm. 1985), (Fig. 5.1).

Analytical techniques are described in Appendix 1. $^{87}Sr/^{86}Sr$ ratios were determined to better than ±0.01% (2 standard errors on the mean). Rb/Sr elemental ratios were determined by X.R.F. and errors are estimated to be ±2% (at 2 sigma level). For all isochron calculations 2 sigma errors of 0.01% and 2% were used for $^{87}Sr/^{86}Sr$ and elemental Rb/Sr ratios respectively. Isochron regression lines were calculated using a computer programme written by D.W. Wright using the least squares approximation method of York (1969). A regression is termed an errorchron when the M.S.W.D. exceeds 5. Rb/Sr whole rock isotope data are listed in Appendix 2.

5.2.1 The Palmental granite

Seven samples from the Palmental granite define an isochron which corresponds to an age of 545 ± 46 Ma (Fig. 5.2).

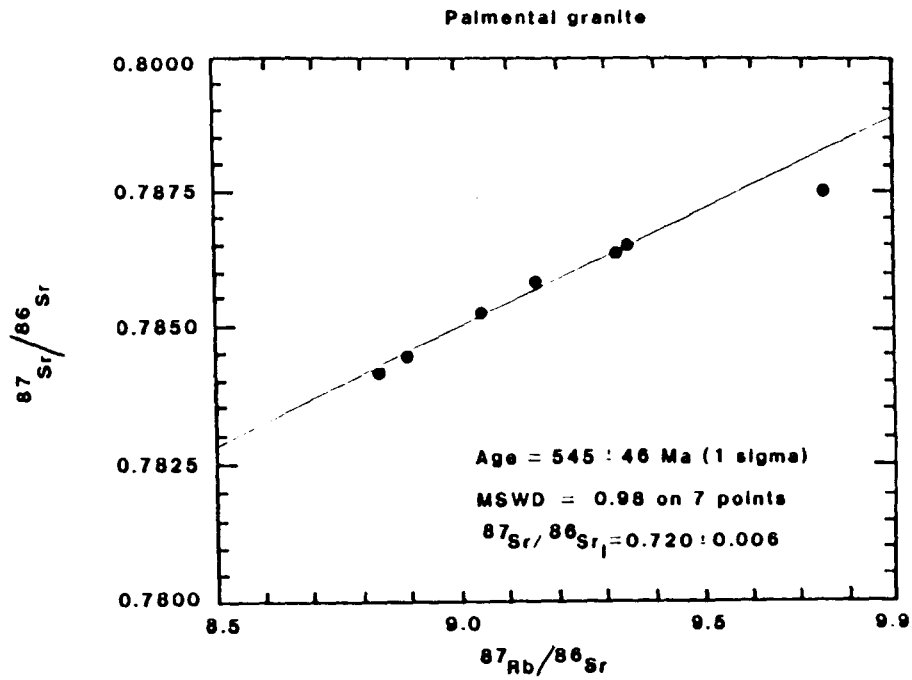

Fig. 5.3 Isochron diagram for the Palmental granite. See Fig. 5.2 for locality.

The large error on the calculated age, despite the relatively low M.S.W.D. of 0.98 is due to the restricted Rb/Sr range of the analysed samples, (Rb/Sr = 3.03 - 3.34). The relatively high initial $^{87}Sr/^{86}Sr$ ratio (0.72002) is consistent with the peraluminous major element geochemistry of the granite suggesting an upper-crustal source which had time integrated high Rb/Sr ratios. This age is indistinguishable from that of the large Donkerhuk batholith which outcrops about 1.5Km to the south of the sampled locality. However, the Palmental granite has a significantly higher initial $^{87}Sr/^{86}Sr$ ratio (~ 0.723) than that of the Donkerhuk granite (~ 0.712) at 521 Ma ago suggesting that these intrusions were not comagmatic.

5.2.2 The Palmental roadside diorite

This intrusion outcrops on the east side of the Karibib-Anschluss road as shown in Fig. 5.2. This diorite has a strong penetrative fabric and is demonstrably older than the Swawop river diorite (Ch. 2). Five samples yield an age of 564 ± 55 Ma (M.S.W.D. = 1.5) with an initial $^{87}Sr/^{86}Sr$ ratio of 0.7070 ± 0.0003 (Fig. 5.4).

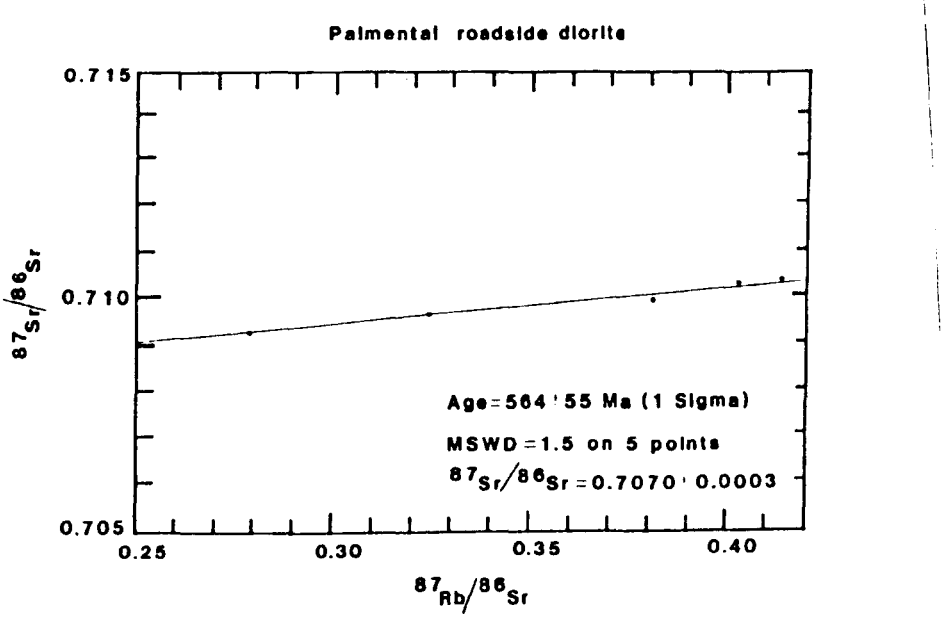

Fig. 5.4 Palmental "roadside diorite" isochron diagram. See Fig. 5.2 for localitiy.

This 564 ± 55 Ma age is in marked contrast to the 756 ± 35 Ma age reported by Kroner (1982) for this intrusion. However, as discussed in Ch. 2, four of the five samples which define Kroner's (*op. cit.*) isochron are co-linear on a 1/Sr vs. $^{87}Sr/^{86}Sr$ diagram (Fig. 5.5) suggesting that the 756 ± 35 Ma "isochron" is a mixing line and does not yield the age of diorite intrusion.

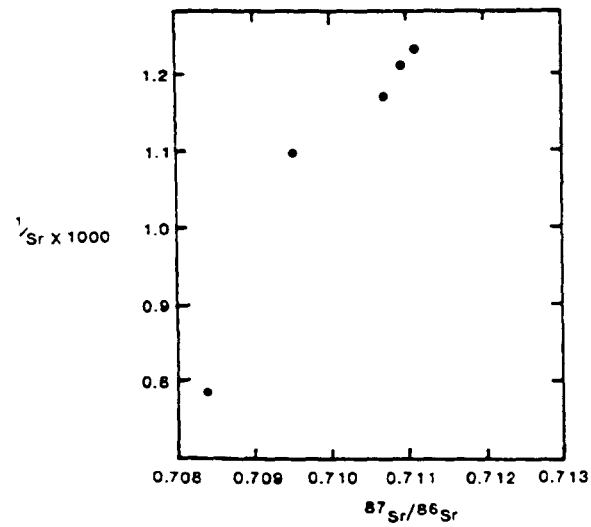

Fig. 5.5 1/Sr vs. $^{87}Sr/^{86}Sr$ diagram for Kroner's (1982) Palmental diorite data. The good correlation between 1/Sr and $^{87}Sr/^{86}Sr$ suggests that the c. 750 Ma isochron obtained by Kroner (*op. cit*) is a mixing line.

5.2.3 Swakop river diorite

Six samples from a small outcrop on the south bank of the Swakop river (Fig. 5.2) yield an "age" of 449 ± 31 Ma (M.S.W.D. = 2.2) with an initial $^{87}Sr/^{86}Sr$ ratio of 0.708909 ± 0.00011, (Fig. 5.6). These samples represent a relatively small rock volume (all the samples were collected from a 3 sq. metre outcrop) and the age is interpreted as reflecting the time at which the small sampled volume became a closed system with respect to Sr.

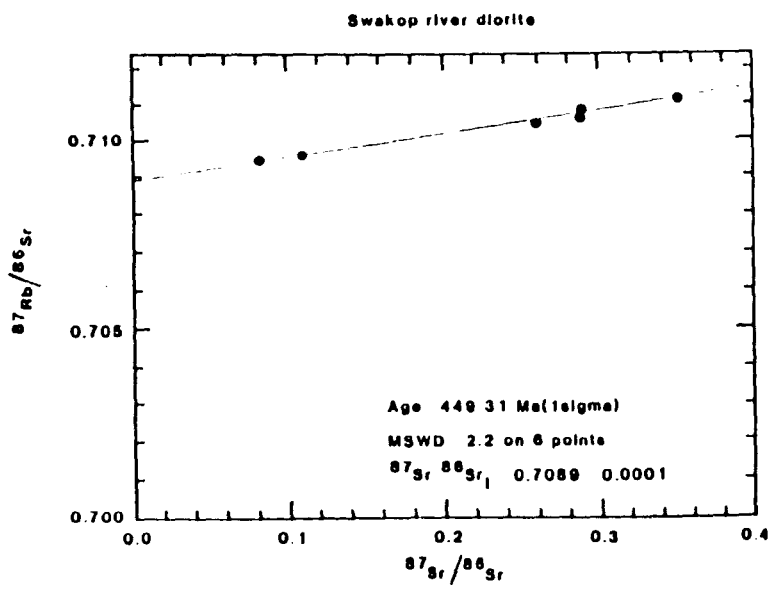

Fig. 5.6 Isochron diagram for the Swakop river diorite. See Fig. 5.2 for locality.

5.2.4 The Otjimbingwe syenite

The seven point isochron calculated for the Otjimbingwe syenite is shown in Fig. 5.7. The calculated age is 403 ± 14 Ma (M.S.W.D = 4.6) with an initial $^{87}Sr/^{86}Sr$ ratio of 0.7086 ± 0.0002. However, field evidence strongly suggests that this intrusion was emplaced before about 520 Ma because xenoliths of this syenite occur within the Donkerhuk granite near this locality (Ch .2). In addition, this syenite has the same penetrative fabric as the Palmental roadside diorite and so is pre - D_2 (Ch. 2).

The 403 ± 14 Ma age is difficult to interpret since the last major magmatic event in the area was the emplacement of the Donkerhuk granite at about 520 Ma ago. The youngest biotite (K/Ar) cooling age recorded near the margins of the Donkerhuk granite is 420 Ma (Haack and Hoffer, 1976) so that the 403 ± 14 Ma age is probably too young to reflect resetting by Donkerhuk granite contact metamorphism.

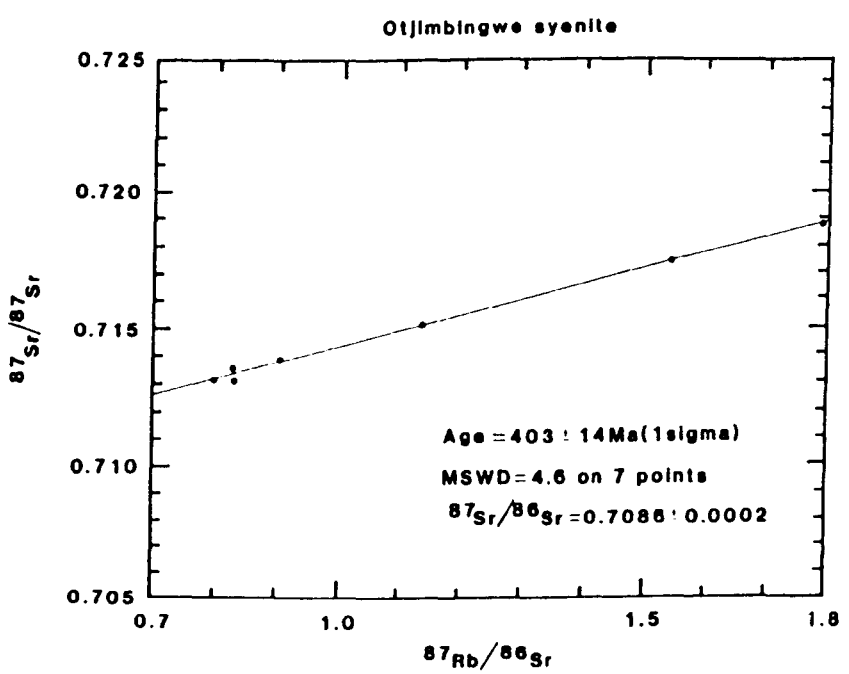

Fig. 5.7 Isochron diagram for the Otjimbingwe syenite. Sample localities are given in Fig. 5.2

5.2.5 The leucocratic Otjimbingwe syenite

Five samples define an age of 512 ± 21 (M.S.W.D. = 0.6) with an initial $^{87}Sr/^{86}Sr$ ratio of 0.7067 ± 0.0001, (Fig. 5.8). It is noted that this age is indistinguishable from that of the nearby (< 1 Km) Donkerhuk batholith (age = 521 ± 15 Ma, Blaxland *et al.*, 1979).

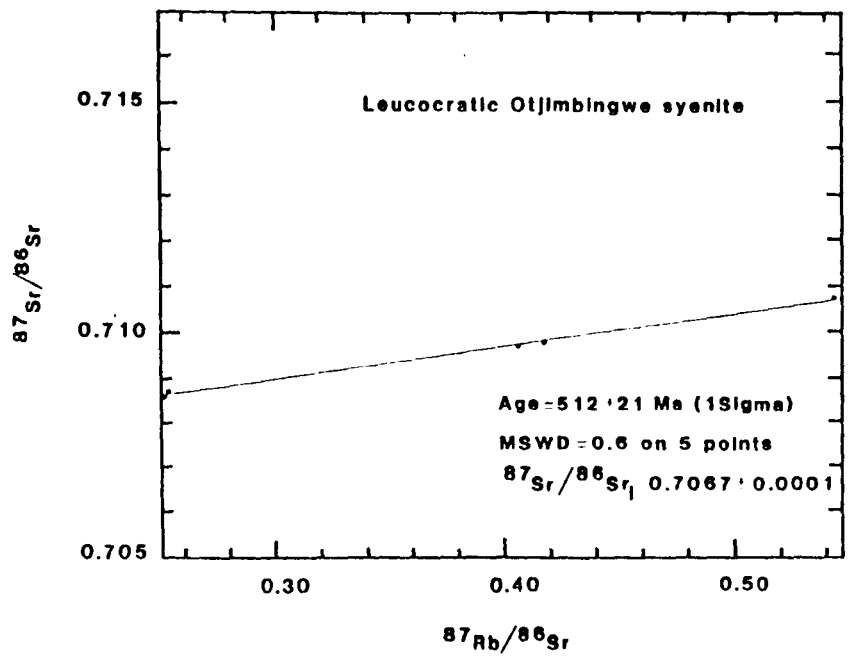

Fig. 5.8 Isochron diagram for the leucocratic Otjimbingwe syenite

5.2.6 The Huab river diorite

Five samples define an errorchron (Fig. 5.9a) corresponding to an age of 862 ± 74 Ma with an initial $^{87}Sr/^{86}Sr$ ratio of 0.70645 ± 0.00052 (M.S.W.D. = 7.5). However this diorite is post-tectonic and has a U/Pb zircon age of 570 ± 20 Ma (R. Mc G. Miller, pers. comm.). Therefore, the calculated Rb/Sr whole-rock age cannot represent the age of emplacement. A plot of $^{87}Sr/^{86}Sr$ vs. 1/Sr (Fig. 5.9b) shows that there is a good correlation between 1/Sr and

$^{87}Sr/^{86}Sr$ suggesting that the line defined by the data on the isochron diagram (Fig. 5.9a) is a mixing line and does not have any direct age significance.

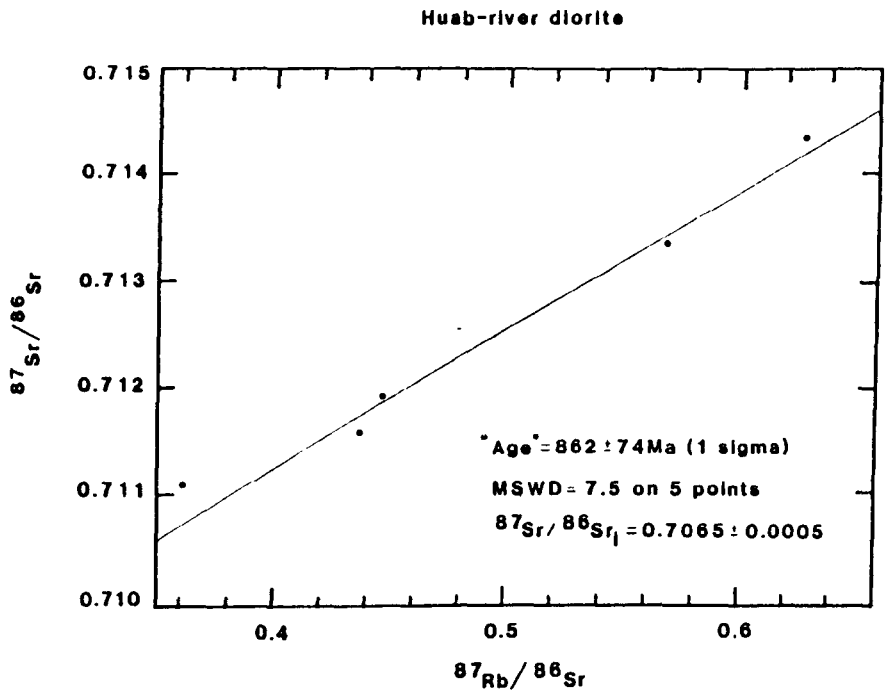

Fig. 5.9a Isochron diagram for the Huab-river diorite. See Fig. 5.2 for locality.

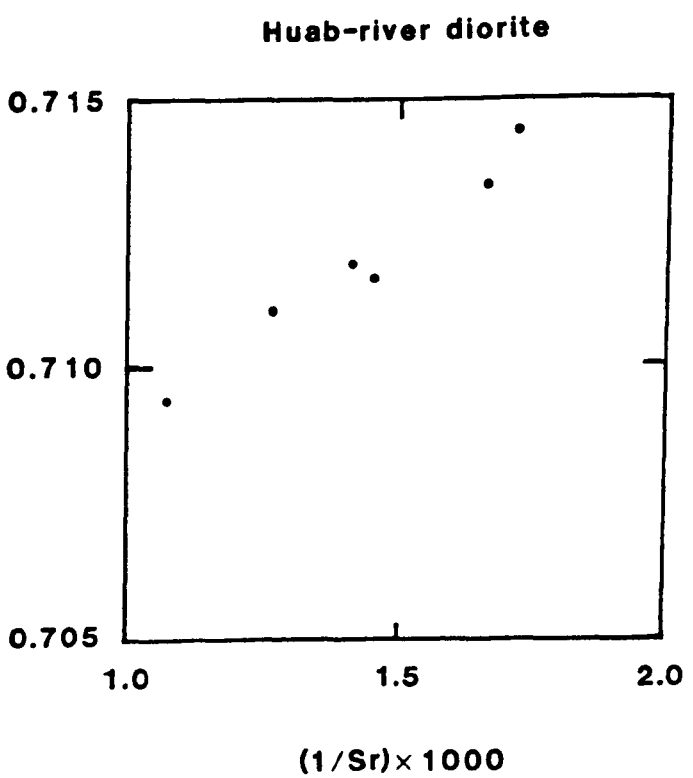

Fig.5.9b 1/Sr vs.$^{87}Sr/^{86}Sr$ diagram for the Huab-river diorite. The good correlation suggests that the "isochron" in Fig. 5.9a is a mixing line.

5.2.7 Summary

The 564 ± 55 Ma age obtained for the post-D_1, pre-D_2 (Ch. 2) strongly foliated Palmental "roadside" diorite contrasts with the 749 ± 34 Ma age reported by Kroner (1982). It is argued that Kroner's (*op. cit.*) c.750 Ma isochron represents a mixing line (Fig. 5.5) and does not have any direct age significance. The age of 545 ± 45 Ma obtained for the Palmental granite is similar to that of the Donkerhuk batholith (Blaxland *et al.*, 1979), although initial $^{87}Sr/^{86}Sr$ ratios recalculated to 521 Ma for the Palmental granite (~ 0.723) are significantly higher than those of the Donkerhuk granite (~0.712).

The 862 ± 74 Ma age obtained for the Huab-river diorite is clearly too old since this diorite is post-tectonic and has a U/Pb zircon age of 570 ± 20 Ma (R. Mc G. Miller, pers. comm.). The good correlation between $^{87}Sr/^{86}Sr$ and 1/Sr (Fig. 5.9b) strongly suggests that the "isochron" is a mixing line and does not yield the age of diorite intrusion.

5.3 Nd isotope geochemistry

Nd isotopic ratios have been determined for selected granitoid samples. Nd isotope ratios, Sm/Nd ratios and calculated model Nd ages are tabulated in Appendix 2. Analytical techniques are described in Appendix 1.

Damara granitoids are characterised by low $^{143}Nd/^{144}Nd$ ratios reflecting time integrated depletions in Sm/Nd. Sm/Nd remains relatively constant during intracrustal processes e.g. erosion and sedimentation and magmatic remobilisation (Mc Culloch and Wasserburg, 1978). The measured $^{143}Nd/^{144}Nd$ ratio is a measure of how long since the Sm/Nd ratio was significantly fractionated. Crustal extraction from the mantle significantly fractionates Sm/Nd so that the measured $^{143}Nd/^{144}Nd$ ratio is a measure of the time elapsed since the isotopic system was extracted from the mantle.

The assumption that Sm/Nd ratios remain relatively unchanged by intracrustal processes allows model Nd ages to be calculated. Model Nd ages are simply a measure of time since the sample had a Sm/Nd ratio similar to CHUR (Chondrite Uniform Resevoir) or a depleted mantle (DM) resevoir, and so provide an estimate of the time elapsed since the granitoids (or their precursors) were derived from the upper mantle. Damara granitoids are characterised by old model Nd ages (Hawkesworth *et al.*, 1981) - all the Damara granitoids studied have T_{DM} model Nd ages greater than 1.0 Ga even though they were intruded in the period 840 - 460 Ma.

Both Sr and Nd data are reported using the ε_i notation which compares $^{143}Nd/^{144}Nd$ or $^{87}Sr/^{86}Sr$ at the time of granitoid emplacement to that of bulk-earth at that time. Samples which reflect low time integrated Sm/Nd ratios have negative ε Nd values while time integrated high Rb/Sr results in positive ε Sr values.

5.4. Combined Sr and Nd isotopic evolution

Granitoid Sr and Nd isotope data are presented on a conventional $^{87}Sr / ^{86}Sr$ vs. $^{143}Nd/^{144}Nd$ diagram (Fig. 5.10). Damara granitoid data define a hyperbolic array in the lower right hand quadrant, indicating high time integrated Rb/Sr and low Sm/Nd ratios relative to bulk earth. Conventionally, such hyperbolae are interpreted as mixing lines between depleted mantle and old continental crust end-members (e.g. Allegre and Ben Othman, 1980 ; De Paolo, 1981 ; Mc Culloch and Chappell, 1982 ; Juteau *et al.* 1986). However a number of alternative explainations are explored below.

Firstly, it is important to distinguish between two possible mixing mechanisms which could generate the observed hyperbolae on $^{87}Sr / ^{86}Sr$ vs. $^{143}Nd/^{144}Nd$ diagrams. A binary mixing process whereby a mantle derived magma is contaminated by, and mixes with, a

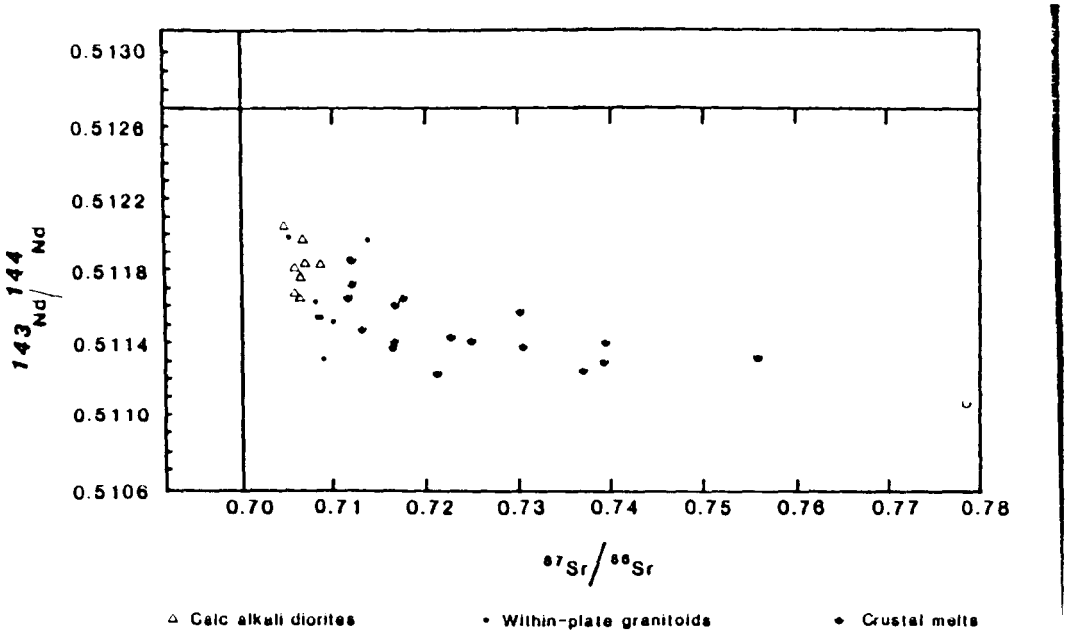

Fig. 5.10 $^{87}Sr/^{86}Sr$ vs. $^{143}Nd/^{144}Nd$ diagram for the Damara granitoids. The three granitoid types (Ch. 4) are distinguished.

component of old continental crust is termed "contemporaneous mixing" since the resulting magma has a direct contribution from continental crust and contemporaneous mantle. In contrast, where mixed crustal sources (e.g. volcano-sedimentary sequences) are remobilised to produce a magma, the mantle component may be significantly older than when the mixed magma was generated. In subsequent discussions of mixing mechanisms, the process in which contemporaneous mantle is mixed with old continental crust is modelled since this is the binary mixing mechanism which is frequently invoked to explain hyperbolae on $^{87}Sr/^{86}Sr$ vs. $^{143}Nd/^{144}Nd$ diagrams. A process of combined fractional crystallisation and assimilation (AFC) is also modelled, and finally, the preferred model of repeated intracrustal remobilisation is presented.

5.4.1. Binary mixing model

Binary mixing curves (Langmuir *et al.* 1978) between sample RM 586 which is considered to be a mantle derived diorite (T_{CHUR} = Rb/Sr whole rock age = 600 Ma) and three possible old continental crust compositions are shown on Fig. 5.11. The relevant isotopic and trace element data of the end-members are given in Table 5.2.

Table 5.2 Isotope and trace element parameters used in binary mixing calculations

Sample	Rb/Sr	Sm/Nd	$^{143}Nd/^{144}Nd$	$^{87}Sr/^{86}Sr$
RM 586	0.068	0.179	0.512290±3	0.70636
B2	2.069	0.185	0.511290±1	0.82150
Ros 5	10.364	0.332	0.511789±7	0.913674
Ic	1.106	0.142	0.511080±2	0.79852

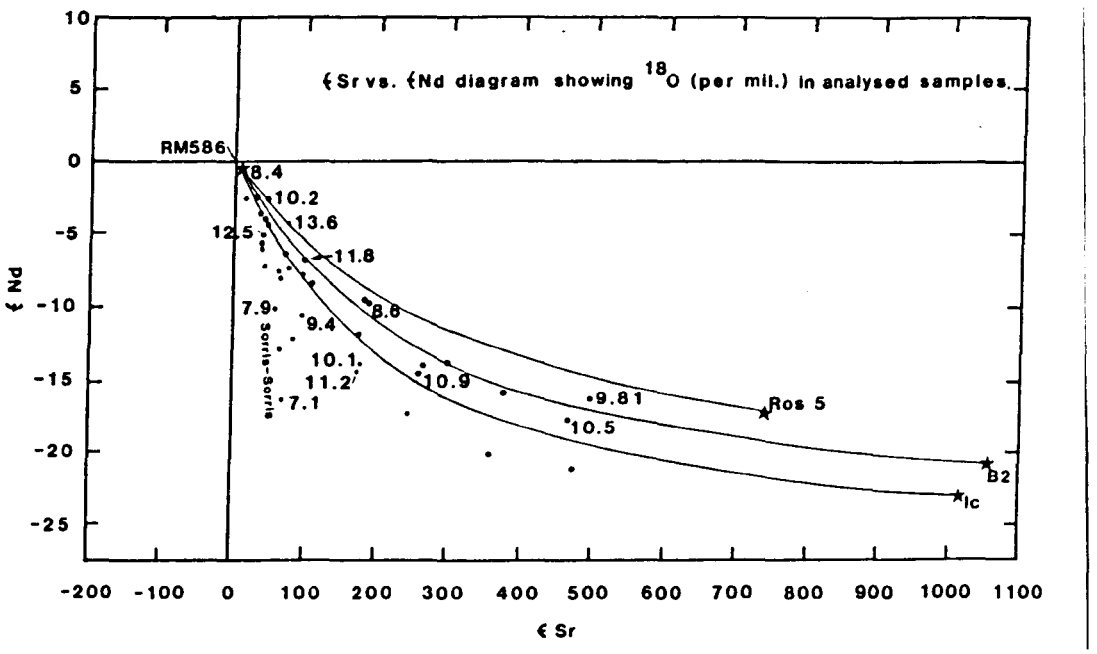

Fig. 5.11 Binary mixing curves between sample RM 586 and various crustal end member compositions are shown on this ε Sr vs. ε Nd diagram. Isotopic and trace element data of end-members are given in Table 5.2. $\delta^{18}O$ values in ‰ are shown adjacent to several sample points.

The continental crust end-member is poorly constrained since ε Sr is quite variable in old continental crust. However the envelope enclosed by the upper and lower mixing curves (Fig. 5.11) is considered to represent typical mixture compositions between a mantle component plotting close to ε Sr = ε Nd = 0 and a component of old continental crust (e.g. sample B2 which is 2.0-2.2 Ga pre-Damara basement). Although most granitoid data plot

close to or within the mixing envelope, simple binary mixing is considered to be an unlikely petrogenetic process for the following reasons ;

1. Trace element geochemistry (notably high-field strength element and REE data, Ch. 4.) require three geochemically distinct end-member compositions (Fig 4.1).

2. A significant number of samples, notably those from the Palmental diorite and Sorris-Sorris intrusions plot below the hyperbola defined by binary mixing lines. Clearly, these samples cannot be generated by simple binary mixing between a mantle composition which plots close to bulk earth, and old continental crust end-members.

3. Binary mixing models (e.g. De Paolo,1981 ; Allegre and Ben Othman, 1980) imply that each granitoid which lies on a mixing hyperbola has a component of mantle material extracted from the mantle contemporaneously with magma genesis. However, some samples which lie along the "mixing" hyperbolae on Fig. 5.11 have formed by in-situ melting of pre-existing crustal rocks (Ch. 3) and have no component of contemporaneous mantle derived material.

4. A binary mixing model predicts that $\delta^{18}O$ in granitoids should vary systematically along the hyperbola reflecting the relative proportions of end-members and their relative $\delta^{18}O$ values. However no such systematic variation is observed (Fig. 5.11) suggesting that simple binary mixing is unlikely.

5.4.2 Combined assimilation and fractional crystallisation (AFC)

An alternative interpretation of hyperbolae on ε Sr vs. ε Nd diagrams is by a process of combined assimilation and fractional crystallisation i.e. assimilation of a high εSr, low εNd, old continental crust end-member by a mantle derived magma while the mantle derived magma undergoes fractional crystallisation. The AFC equation of De Paolo (1981) was used.

$$m = \frac{\frac{r}{r-1}\frac{C_a}{Z}(1-F^{-Z})\varepsilon_a + C^o_m F^{-Z}\varepsilon^o_m}{\frac{r}{r-1}\frac{C_a}{Z}(1-F^{-Z}) + C^o_m F^{-Z}}$$

where m = the isotope ratio of the final magma

m^o = the isotope ratio of the original magma

ε_a = the isotope ratio of the assimilated material

$C_m{}^o$ = concentration of element in original magma

C_a = concentration of element in assimilated material

$Z = \frac{r + D - 1}{r-1}$ where D is the bulk distribution coefficient

r = the ratio of mass assimilated (M_a) to mass of crystals fractionated (M_c).

F is the mass of magma remaining as a function of the original mass. The r value used in AFC modelling is critical to the calculated isotopic variations. For the purposes of these calculations an r value of 0.2 is assumed. This value is based on thermal constraints provided by Taylor (1980). According to Taylor (*op. cit.*) the assimilation of 1g of country rock (at 150°C) requires the crystallisation of about 5g of cumulate crystals assuming an initial magma temperature of about 850°C. This suggests that an r value of 1: 5 i.e. 0.2 is geologically reasonable.

Assumptions must also be made about the bulk distribution coefficients for Sr and Nd in the assimilating phases. Some constraints on bulk D values are provided by the fact that if $D_{Sr} < 2.6$ all the magma must crystallise before the high $^{87}Sr/^{86}Sr$ end-member is reached (assuming the other AFC parameters as outlined in Table 5.3 are applied) as the AFC magma moves along an AFC line towards the high $^{87}Sr/^{86}Sr$ end-member (Fig. 5.12).

Sample RM 586 (Otjosondjou diorite) was chosen to represent the initial magma

(lowest $^{87}Sr/^{86}Sr$, highest $^{143}Nd/^{144}Nd$ observed) and sample B2 (basement orthogneiss) was chosen to represent the material being assimilated during AFC. Isotopic ratios were recalculated to initial ratios, and ratios at 500 Ma for the diorite (RM 586) and the orthogneiss (B2) end-member samples respectively. The isotopic and trace element parameters used in AFC modelling are given in Table 5.3.

Table 5.3 Isotopic and trace element parameters of the end-members used in AFC modelling

Sample		Rb	Sr	Sm	Nd	$^{87}Sr/^{86}Sr$	$^{143}Nd/^{144}Nd$
RM 586	initial magma	71	1045	14.1	79	0.704820	0.511902
B2	assimilant	329	159	10.9	58.8	0.778471	0.5109235

Parameters used in different AFC calculations as shown in Figs. 5.12a-d.

Figure No.	D_{Sr}	D_{Nd}	r value
Fig. 5.12a	1.5	1-10 as shown	0.5
Fig. 5.12b	2.0	1-10 as shown	0.2
Fig. 5.12c	2.6	1-10 as shown	0.2
Fig. 5.12d	3.5	1-10 as shown	0.2

Figs. 5.12 (a-d) show a number of AFC curves for different values of D_{Nd} as shown in circles adjacent to each curve. D_{Sr} varies between diagrams in the range 1.5-3.5 as listed in Table 5.3. With the exception of Fig. 5.12a (r = 0.5) r values of 0.2 are used. Most data lie in the envelope defined by the D_{Nd} = 2 and D_{Nd} = 5 curves while the Sorris-Sorris data require a D_{Nd} of about 10 in order to generate the observed low $^{87}Sr/^{86}Sr$, low $^{143}Nd/^{144}Nd$ values, assuming the D_{Sr} and r values outlined in Table 5.3.

In summary, the observed isotopic variations can be generated by AFC processes if geochemically reasonable parameters are used for r, D_{Sr}, D_{Nd}, C_a, C_m^o, ε_a and C_m^o. However, geological observations suggest that AFC is an unlikely process to

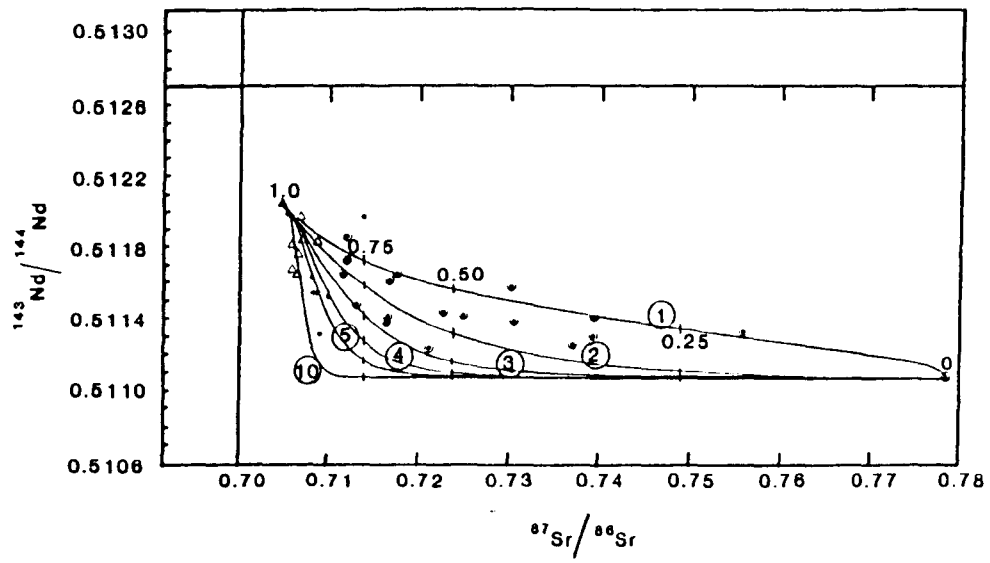

Fig. 5.12a $^{87}Sr/^{86}Sr$ vs. $^{143}Nd/^{144}Nd$ diagram for Damara granitoids. AFC curves are shown for different values (1 - 10) of D_{Nd} in the assimilating phases as shown in circles adjacent to each curve. An r value of 0.5 is assumed and D_{Sr} in the assimilating phases is 1.5 for all curves. Vertical ticks mark F values (fraction of the liquid remaining) at 0.25 intervals along curves. The isotopic and trace element parameters of the initial magma and the assimilant are given in Table 5.3.

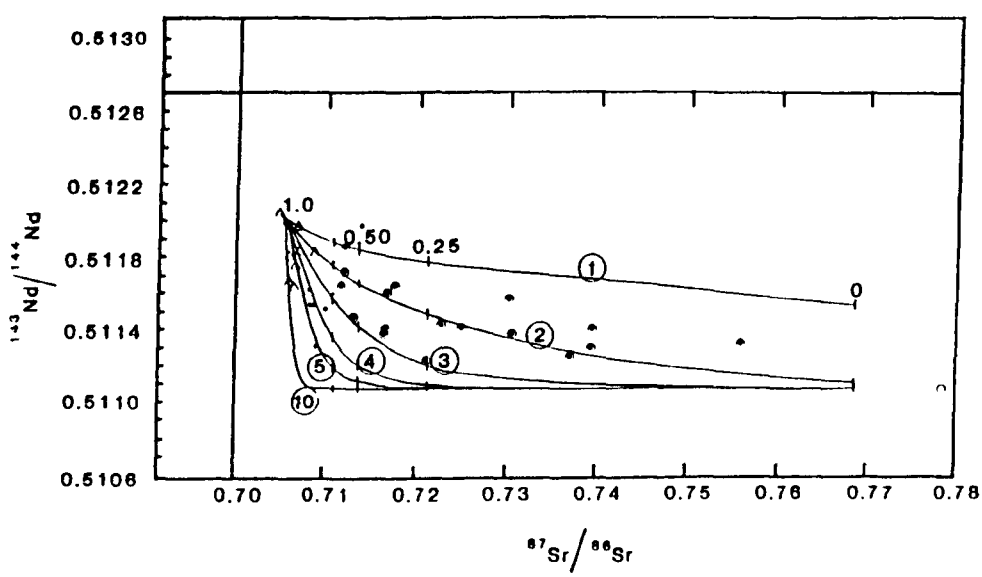

Fig. 5.12b AFC curves calculated assuming D_{Sr} in the assimilating phases is 2.0 and r = 0.2. Values for D_{Nd} in the assimilating phases are shown in circles adjacent to each curve. End member parameters are as listed in Table 5.3. Vertical ticks on curves mark F values at 0.25 intervals.

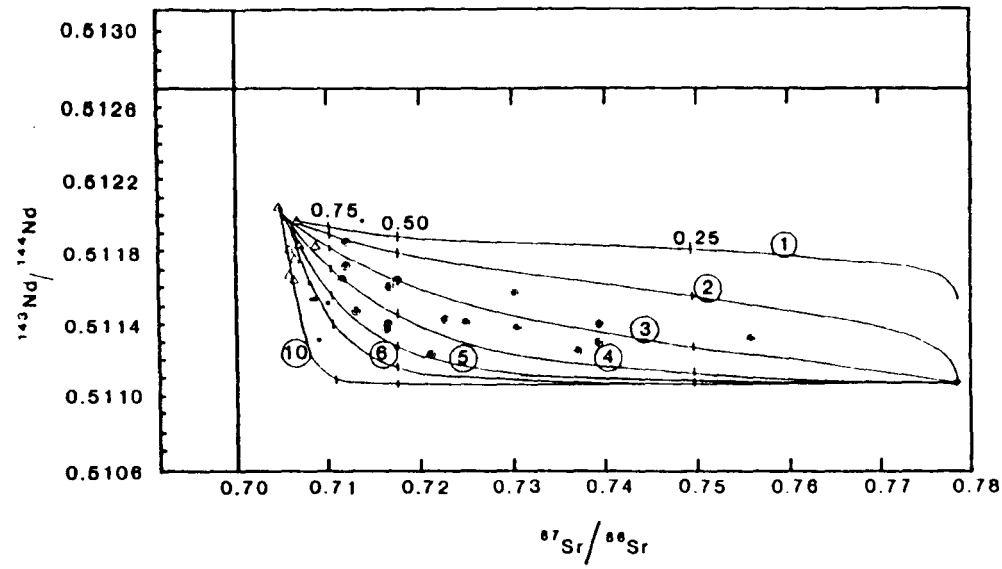

Fig. 5.12c AFC curves calculated assuming D_{Sr} in the assimilating phases is 2.6. An r value of 0.2 is assumed and the different curves are for various D_{Nd} values in the assimilating phases as shown in circles adjacent to each curve. Vertical ticks mark 0.25 intervals in F. The isotopic and trace element paremeters of the initial magma and the assimilant are given in Table 5.3.

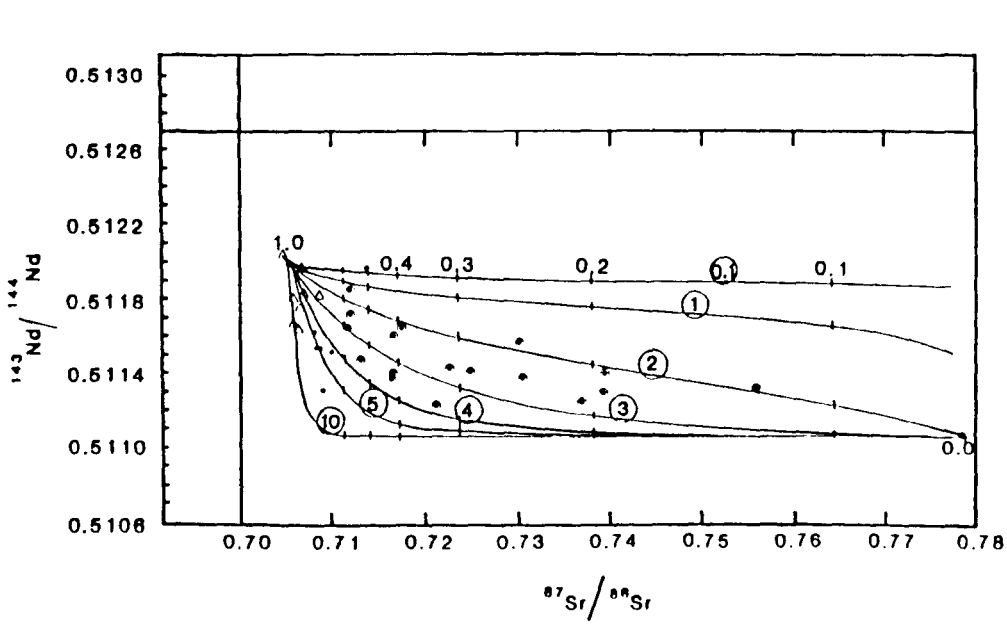

Fig. 5.12d AFC curves calculated assuming D_{Sr} in the assimilating phases is 3.5. An r value of 0.2 is assumed and the different curves are for D_{Nd} values in the assimilating phases as shown in circles adjacent to each curve. Vertical ticks are shown at F values of 0.1 - 0.4 and 1.0. End member parameters are as listed in Table 5.3.

generate the observed isotopic variations. The AFC process implies that each granitoid has a component of mantle derived material (derived from a contemporaneous mantle source) while field evidence strongly suggests that some granitoids which lie on AFC lines in $^{87}Sr / ^{86}Sr$ vs. $^{143}Nd / ^{144}Nd$ diagrams are derived by anatexis of crustal material and have no contemporaneous mantle component.

5.4.3 Episodic intracrustal remobilisation model

This model is proposed as an alternative explaination of hyperbolae defined by granitoid data on ε Sr vs. ε Nd diagrams. The model also explains the observed relationship between ε Sr and model Nd ages in the Damara granitoids. In this model, multistage episodic intracrustal remobilisation of granitoid protoliths during periods of orogenic activity increases Rb/Sr ratios but Sm/Nd ratios remain relatively unaffected. Between periods of orogenesis the isotopic ratios of the granitoid protoliths have relatively constant Rb/Sr and Sm/Nd ratios and so evolve along straight lines in ε Sr vs. ε Nd space. It is assumed that Rb/Sr is increased during each successive orogenic episode whereas Sm/Nd ratios remain constant. A fundamental implication is that the position of a granitoid sample in ε Sr vs. ε Nd space is primarily a function of how long the granitoid protolith has been in the continental (upper ?) crust. The model also requires that each orogenic event results in some addition of new material from the mantle to the crust as well as intracrustal remobilisation of pre-existing crustal material. Some new mantle derived material must be added to the crust during each orogenic episode in order to generate the observed range in ε Nd and ε Sr.

For the purposes of this model it is assumed that the protolith of an individual granitoid was remobilised every 500 Ma on average. Clearly, this applies only to granitoids which were not derived from the mantle during the last (Pan African) orogeny. In southern Africa orogenic events have been recognised at about 500 Ma ago (Pan African),1.0-1.1 Ga

ago (Watters, 1976 ; Malling 1978), 1.4-1.5 Ga ago (Kibaran event) and at about 2.0 Ga ago (Eburnian event) suggesting that there is a good geological basis for remobilisation (and consequent Rb/Sr increase) every 500 Ma. Geological processes by which Rb/Sr is increased relative to Sm/Nd are discussed below.

Fig 5.13 shows two evolution paths along which samples derived from a mantle source with an isotopic composition close to bulk earth may evolve with time if Rb/Sr is episodically increased but Sm/Nd remains constant. The upper line is shown for Rb/Sr increases by a factor of 3 every 500 Ma in granitoid protoliths. Similarily, the lower evolution path is shown for Rb/Sr increases of 2 every 500 Ma. Both evolution paths assume that the Sm/Nd ratio remained constant at 0.2. The main trend defined by the Damara granitoid data lies between lines corresponding to increases of Rb/Sr by between 2 and 3 every 500 Ma.

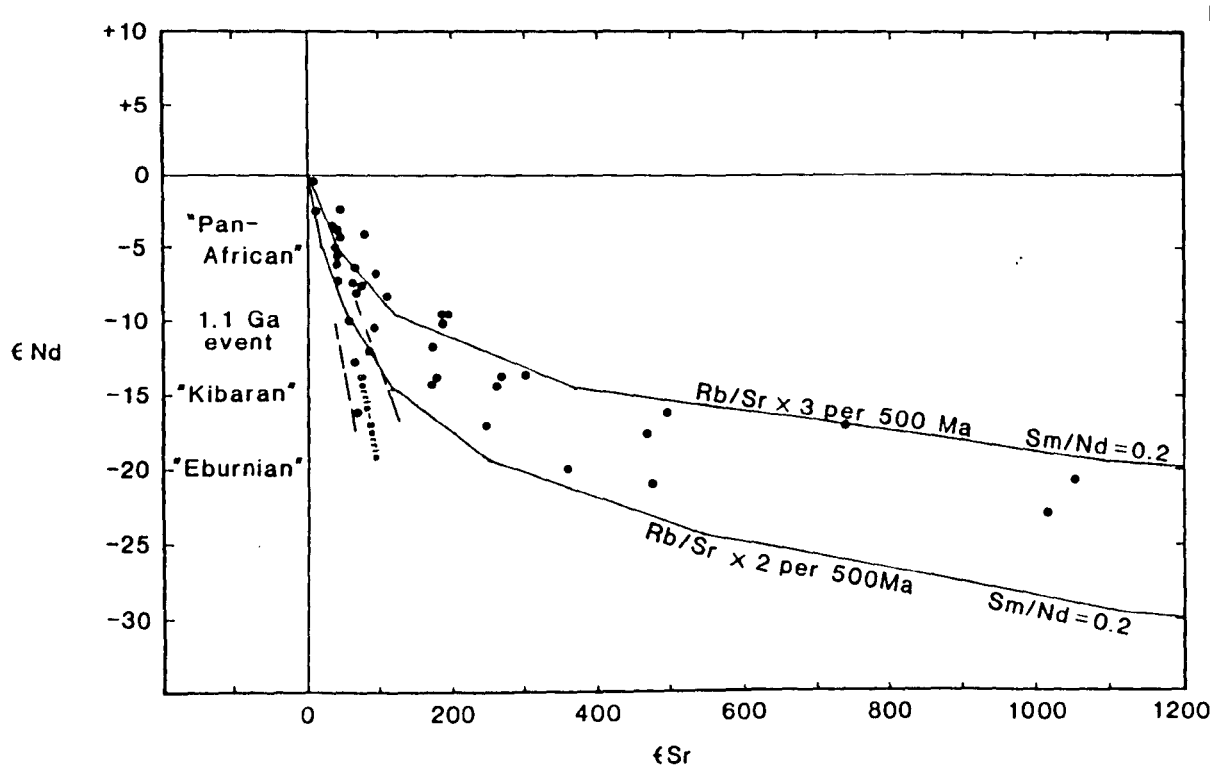

Fig. 5.13 ε Sr vs. ε Nd diagram for the Damara granitoids. Two evolution paths for Rb/Sr x 2 and x 3 per 500 Ma are shown. Sm/Nd is assumed to remain constant at 0.2.

The relationship between ε Sr and model Nd ages in the granitoids can provide further constraints on model evolution paths. Most of the granitoid data, (Sorris-Sorris and Palmental diorite intrusions excepted) plot within an envelope defined by Rb/Sr x 2 and Rb/Sr x 3 per 500 Ma (Fig. 5.14).

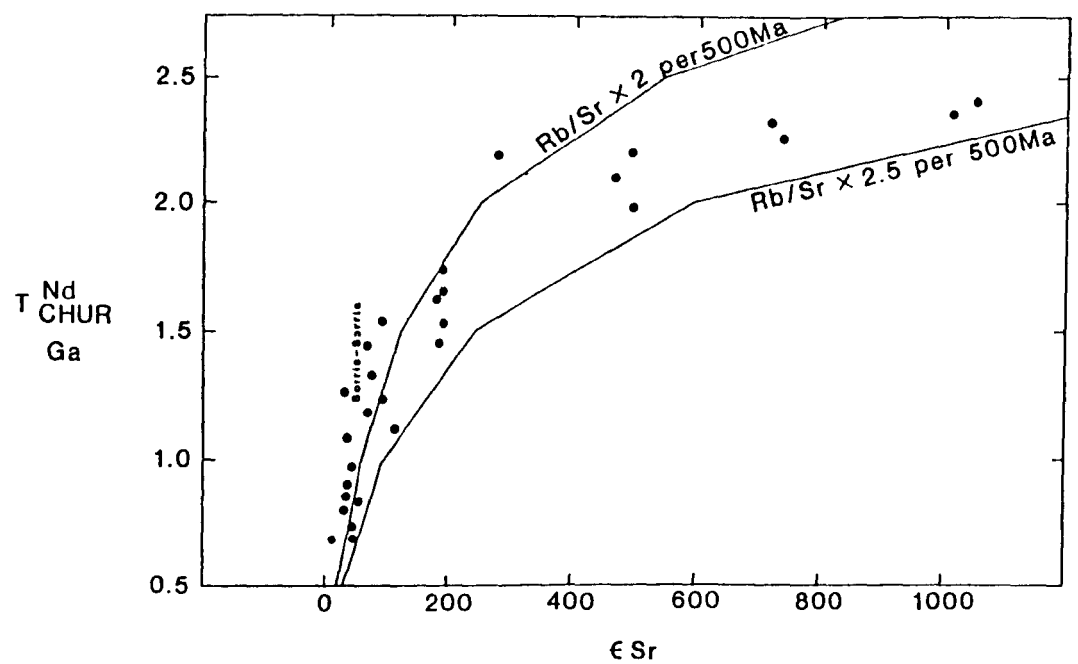

Fig. 5.14 ε Sr vs. model Nd age (CHUR) for Damara granitoids. With the exception of Sorris-Sorris and Palmental granitoid samples which define a steep trend most samples plot between the Rb/Sr x 2 and Rb/Sr x 3 per 500 Ma curves.

Samples from the Sorris Sorris and Palmental granitoids define steeper trends on Figs. 5.13 and 5.14 reflecting their restricted range of ε Sr. This implies insignificant Rb/Sr fractionation of their crustal precursors (both intrusions have model Nd ages significantly older than Rb/Sr whole-rock ages) which is consistent with their trace element geochemistry. The Palmental diorite and Sorris Sorris granitoid are characterised by low Rb/Sr and high HFS element abundances respectively. These trace element characteristics suggest granitoid derivation from precursors which had undergone little or no intracrustal remobilisation since intracrustal remobilisation decreases HFS element abundances and results in high Rb/Sr ratios.

In summary, the combined Sr and Nd isotope data are consistent with an episodic intracrustal remobilisation model in which Rb/Sr is increased by a factor of between 2 and 3 every 500 Ma.

5.4.4 Intracrustal Rb/Sr fractionation mechanisms

Since Rb behaves more incompatibly than Sr during partial melting processes (e.g. Ch. 4), magmas produced by intracrustal anatexis have higher Rb/Sr ratios than their source rocks. In addition, Rb/Sr ratios are increased by fractional crystallisation processes in granitic magmas. Examples of high Rb/Sr ratios produced by crustal anatexis include those of the alaskites of the Central Zone of Namibia (Ch. 4). Crustal anatexis and consequent increases in Rb/Sr, occur episodically, at or close to the peak of regional metamorphism during periods of orogenesis. However Rb/Sr is also increased by inter-orogenic processes which are quasi-continuous e.g. cycles of erosion and sedimentation (Martin and Meybeck, 1979). The balance between Rb/Sr increases as a result of episodic (magmatic) remobilisation and quasi-continuous (erosion and sedimentation) processes is difficult to assess. However stable isotopic ratios of crustal melt granitoids e.g. $\delta^{18}O$ of quartz separates, may provide a tool to assess the relative importance of episodic and quasi-continuous Rb/Sr increases in granitoid precursors since near-surface processes may increase $\delta^{18}O$. Clearly, the possible effects of post-magmatic fluid interactions must also be taken into consideration in such studies.

5.5 Sr and Nd isotope variations in the Damara metasediments

New Sr and Nd isotopic data (A. R. Gledhill, unpubl. data and this study) confirm the isotopic variations and trends in the Damara flysch succession (Kuiseb schists) as reported by Hawkesworth and Marlow (1983). These trends are accentuated by the younger molasse

sequence samples (Nama Group). $^{143}Nd/^{144}Nd$ shows a striking decrease with stratigraphic depth in sediments older than the Rossing Formation whereas $^{87}Sr/^{86}Sr$ ratios increase dramatically over the same stratigraphic interval (Figs. 5.15 and 5.16). All metasediment isotope data are tabulated in Appendix 2.

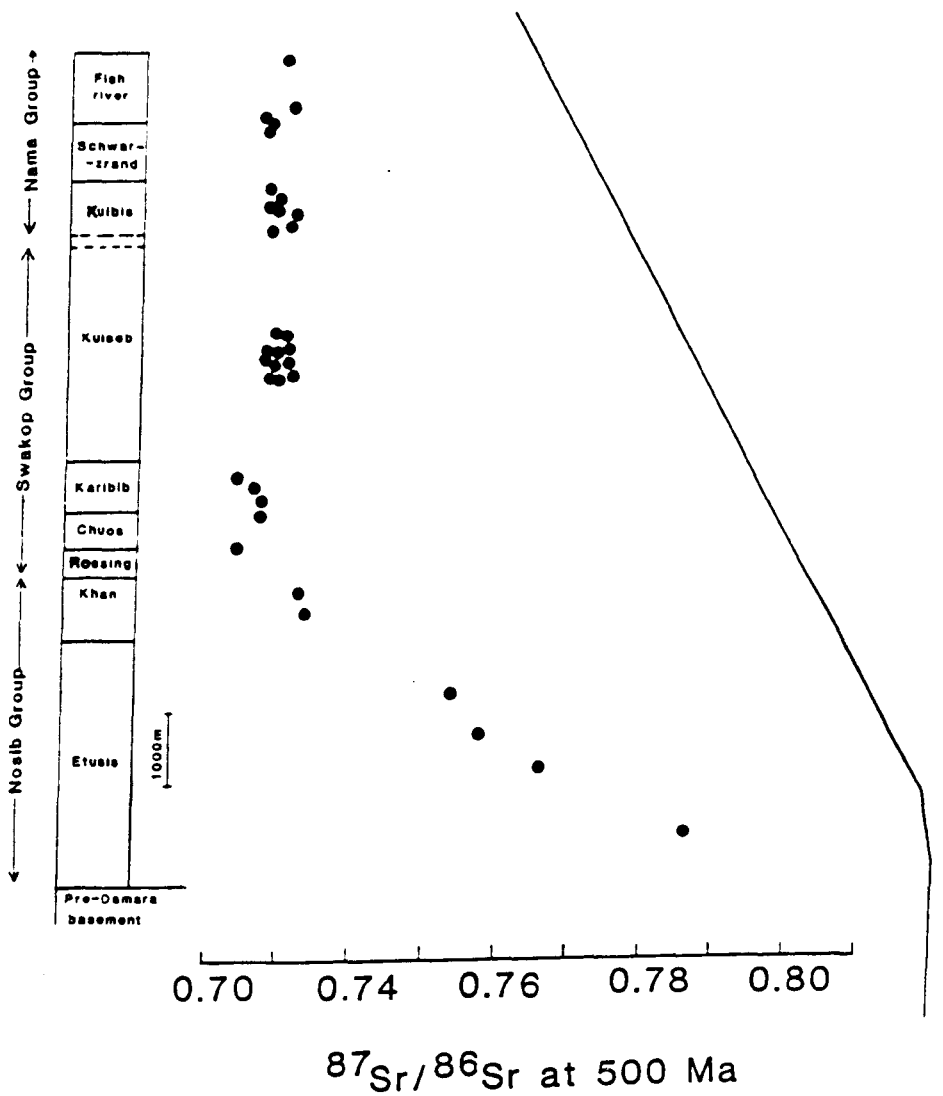

Fig. 5.15 Variations in $^{87}Sr/^{86}Sr$ with depth in the Damara metasedimentary pile. Ratios are recalculated to 500 Ma.

5.5.1 Metasediment isotope data

As shown in Fig. 5.16 $^{143}Nd/^{144}Nd$ decreases sharply with depth in the Nosib Group. This is also reflected in the calculated model Nd ages (Appendix 2). Most Nosib Group samples are characterised by model Nd ages of about 2.0 Ga whereas those of the younger Damara sediments (Kuiseb schists and Nama Group) have model Nd ages (CHUR) of about 1.0-1.2 Ga.

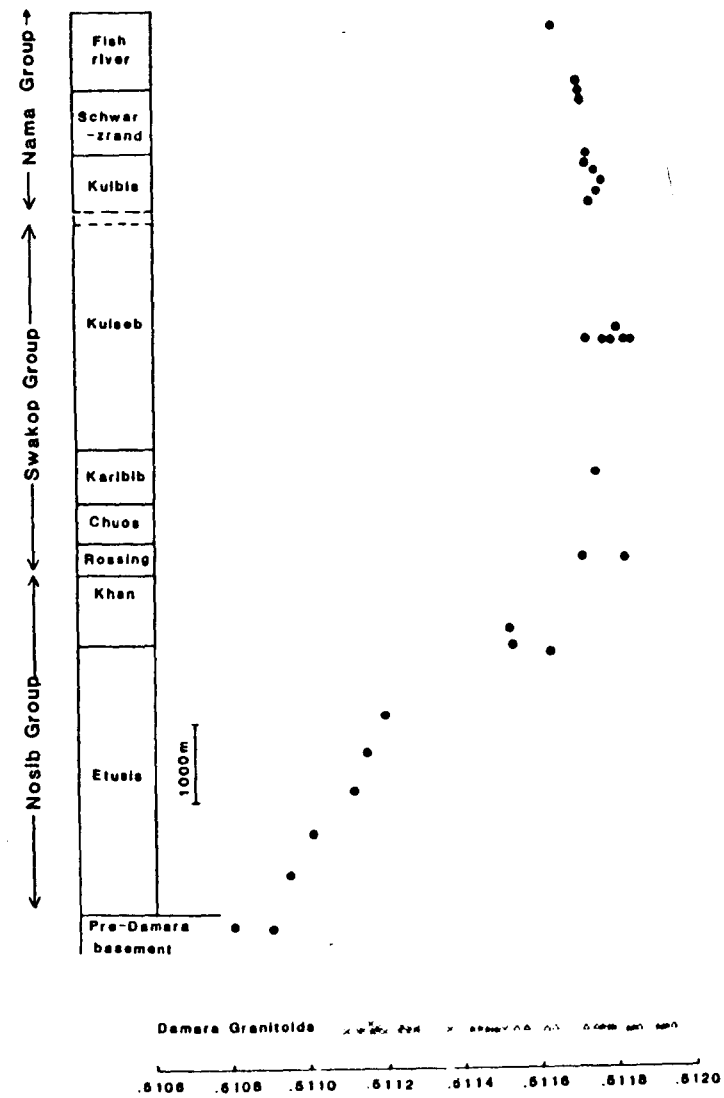

Fig. 5.16 Variations in $^{143}Nd/^{144}Nd$ with depth in the Damara metasediments. Isotopic ratios have been recalculated to 500 Ma.

It is assumed that Sm/Nd is not fractionated significantly by intracrustal processes (Mc Culloch and Wasserburg, 1978) so that model Nd ages calculated for metasediments represent an average model age for their source terrains. Therefore, sediments which are older than the Rossing Formation (Nosib Group) were derived from source terrains which had significantly older model ages than those sampled by the Kuiseb schists or the Nama Group.

5.5.2 Model age ratios

The ratio of model ages $T^{Nd}_{CHUR} / T^{Sr}_{BE}$ is used to assess the amount of intracrustal reworking, since this ratio provides a measure of Rb/Sr fractionation relative to Sm/Nd (Davies *et al.*, 1985). If no intracrustal reworking occurred, model Nd and model Sr ages should be identical, since both provide a measure of the time elapsed since the sample was derived from a source which had the isotopic ratio of CHUR or bulk earth for Nd and Sr respectively. However intracrustal reworking fractionates (increases) Rb/Sr but not Sm/Nd so that calculated model Sr ages are lower as Rb/Sr is fractionated (increased) by intracrustal reworking. Therefore, the ratio $T^{Nd}_{CHUR} / T^{Sr}_{BE}$ increases with intracrustal reworking and so provides a measure of the amount of intracrustal reworking (by magmatic remobilisation and erosion / sedimentation processes).

The ratio $T^{Nd}_{CHUR} / T^{Sr}_{BE}$ increases sharply in the older Damara metasediments (Nosib Group) (Fig. 5.17) suggesting sediment derivation from source terrains which had undergone relatively large amounts of Rb/Sr fractionation. Model age ratios remain relatively constant in samples of the Swakop and Nama Group, although the ratio increases somewhat in most of the Nama Group samples, suggesting that the Nama Group was derived from source terrains which had suffered slightly more intracrustal reworking than those sampled by the Kuiseb formation. This is consistent with derivation of the Nama sediments as molasse from the granitic source terrains of central Namibia (Germs , 1983).

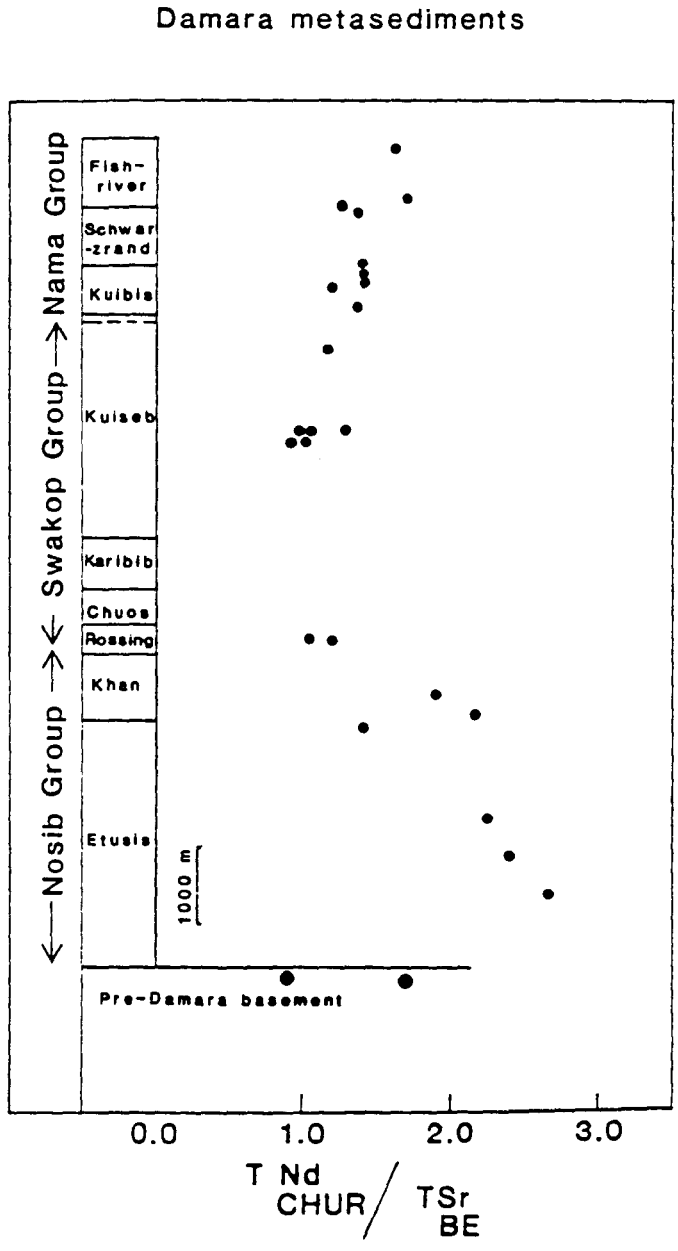

Fig. 5.17 Variations in the model age ratio $T^{Nd}_{CHUR} / T^{Sr}_{BE}$ with depth in the Damara metasediments. The source terrains of the older Damara metasediments (Nosib Group) have suffered the largest amount of intracrustal reworking.

Metasediment isotopic data are plotted on a $T^{Nd}_{CHUR} / T^{Sr}_{BE}$ vs. T^{Nd}_{CHUR} diagram in Fig. 5.18. Samples with the oldest model Nd ages (Nosib Group) have highest model age ratios and so were derived from source terrains which had undergone the greatest

Rb/Sr fractionation. The rate of change of Rb/Sr with time in source terrains of a sample may be estimated from Fig. 5.18 since the slope defined by data from a given sedimentary unit is indicative of the rate of change of Rb/Sr with time.

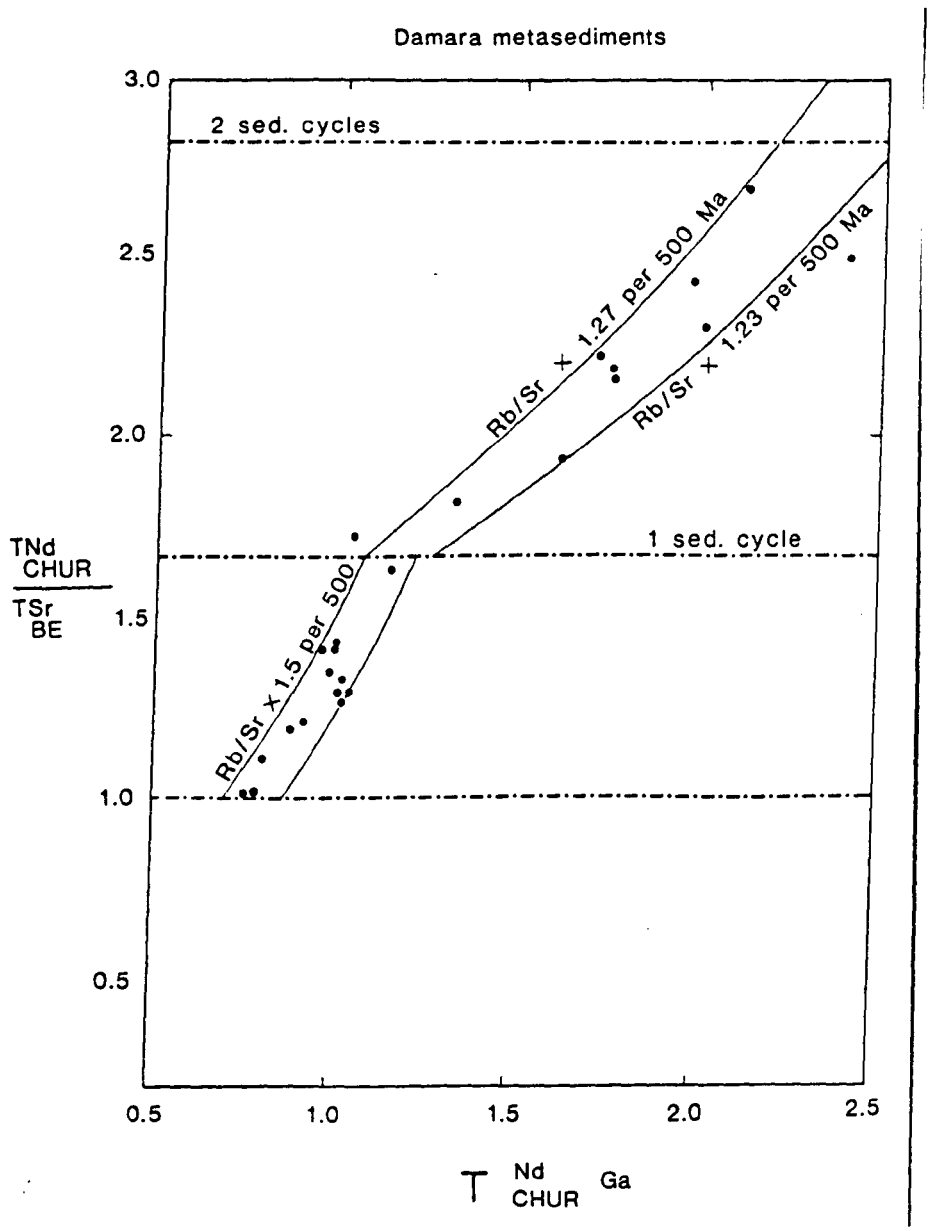

Fig. 5.18 $T^{Nd}_{CHUR}/T^{Sr}_{BE}$ vs. T^{Nd}_{CHUR} diagram for the Damara metasediments showing that higher rates of Rb/Sr fractionation are reflected in younger Damara metasediments. Horizontal lines at 1.68 and 2.82 are based on Martin and Meybeck's (1979) observation that Rb/Sr increased by a factor of 1.68 in a single sedimentary cycle.

On this diagram (Fig. 5.18) a system in which Rb/Sr increases by a constant factor per unit time e.g. Rb/Sr x 1.5 per 500 Ma defines a curve since $T^{Nd}_{CHUR} / T^{Sr}_{BE}$ increases according to a power law where $y = x^n$, (y = model age ratio, $x = T^{Nd}_{CHUR}$ in Ga. , n = factor by which Rb/Sr increases per Ga).

Data from the Etusis, Khan and Rossing formations define a slope which lies between the Rb/Sr x 1.23 and 1.27 per 500 Ma curves, while data from the Kuiseb and Nama Groups define a steeper slope which parallels the Rb/Sr x 1.5 per 500 Ma curve. This implies that the stratigraphically younger sediments have sampled source terrains in which Rb/Sr had increased at higher (average) rates than those sampled by the oldest sediments. Thus, while the oldest sediments (Nosib Group) sampled source terrains which had undergone the greatest amount of Rb/Sr fractionation, the rate of Rb/Sr fractionation is greatest in the terrains sampled by the stratigraphically younger sediments (Kuiseb schists and Nama Group).

In summary the sediment isotopic data is consistent with source terrain Rb/Sr increase rates in the range 1.23-1.5 per 500 Ma.

5.5.3 Granitoid and sediment isotopic data - a comparison

Rates of change of Rb/Sr of between 2 and 2.5 per 500 Ma have been inferred from Damara granitoid data (Fig. 5.13). Rb/Sr ratios have also been calculated for the granitoid sources. Calculated source Rb/Sr ratios are time integrated ratios which represent minimum estimates. They are Rb/Sr ratios required to produce the "initial" $^{87}Sr/^{86}Sr$ ratio in the time interval T^{Nd}_{CHUR} - Rb/Sr whole rock for each sample. It is assumed that each sample had a bulk earth $^{87}Sr/^{86}Sr$ ratio at the time of extraction from the mantle i.e. at $t = T^{Nd}_{CHUR}$.

The calculated Rb/Sr ratios are plotted against T^{Nd}_{CHUR} in Fig 5.19. With the exception of three Sorris-Sorris (within-plate) granitoid samples which define a subhorizontal trend most samples lie between the Rb/Sr x 1.5 and Rb/Sr x 2.0 per 500 Ma evolution paths.

The Rb/Sr x 1.68 line is shown for reference since Rb/Sr has been shown to increase locally by a factor of about 1.68 per erosion and sedimentation cycle (Martin and Meybeck, 1979).

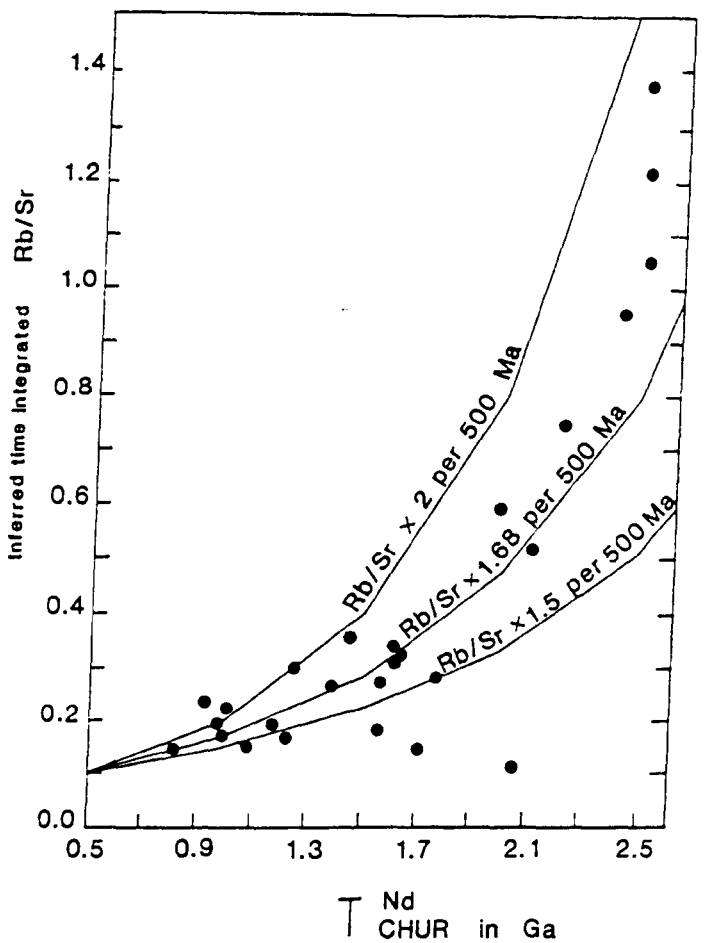

Fig. 5.19 Inferred time integrated granitoid source Rb/Sr ratios vs. T^{Nd}_{CHUR} for Damara granitoids. Most granitoid data lie between Rb/Sr x1.5 and Rb/Sr x 2.0 per 500 Ma lines. Three within-plate (HFS enriched) Sorris-Sorris granitoid samples define a subhorizontal trend suggesting low rates of Rb/Sr increases in their precursors.

In summary, source terrain rates of change of Rb/Sr inferred are as follows, inferred from ;

Older sediments (Nosib Group) - Rb/Sr x 1.23 - 1.27 per 500 Ma

Younger sediments (Kuiseb and Nama) - Rb/Sr x 1.5 per 500 Ma

Granitoid data - Rb/Sr x 2 - 2.5 per 500 Ma

Granitoid sources - Rb/Sr x 1.5 - 2.0 per 500 Ma.

It is interesting to note that the difference between rates inferred from granitoids and those inferred from granitoid sources is about 22% while those inferred from older and younger sediments also differ by about 20%. In both cases the differences in inferred Rb/Sr rates of change may reflect the effect of a single crustal melting event.

5.6 Lead isotopic data

Lead isotopic ratios have been determined for a range of Damara granitoids. Isotope data for whole-rock and K-feldspar separates are presented in Tables 5.4 and 5.5 respectively. Since K-feldspars have low U/Pb ratios their lead isotopic composition is believed to approximate that of the magma from which the feldspars crystallised (Patterson and Tatsumoto, 1964). In contrast, lead isotopic composition of whole-rocks have evolved isotopically since the magmas crystallised.

Whole-rock samples have $^{206}Pb / ^{204}Pb$, $^{207}Pb / ^{204}Pb$ and $^{208}Pb / ^{204}Pb$ ratios in the range 17.59 - 134.78, 15.60 - 22.46 and 37.99 - 44.37 respectively, (Table 5.4, Figs. 5.20 and 5.21) while feldspar separates have a more restricted range of 17.29 - 46.75, 15.61 - 17.32 , 37.54 - 45.56 for $^{206}Pb / ^{204}Pb$, $^{207}Pb / ^{204}Pb$ and $^{208}Pb / ^{204}Pb$ respectively. (Table 5.5, Figs. 5.22 and 5.23). Whole rock samples and feldspar separates from the Rossing alaskite show extremely radiogenic $^{206}Pb / ^{204}Pb$ and $^{207}Pb / ^{204}Pb$ compositions. The within-plate (Fig 4.1) granitoids typically display the most radiogenic $^{208}Pb / ^{204}Pb$ ratios. Aside from the uranium mineralised alaskites, crustal-melt granitoids display the least radiogenic lead ratios (Fig. 5.20 and 5.21).

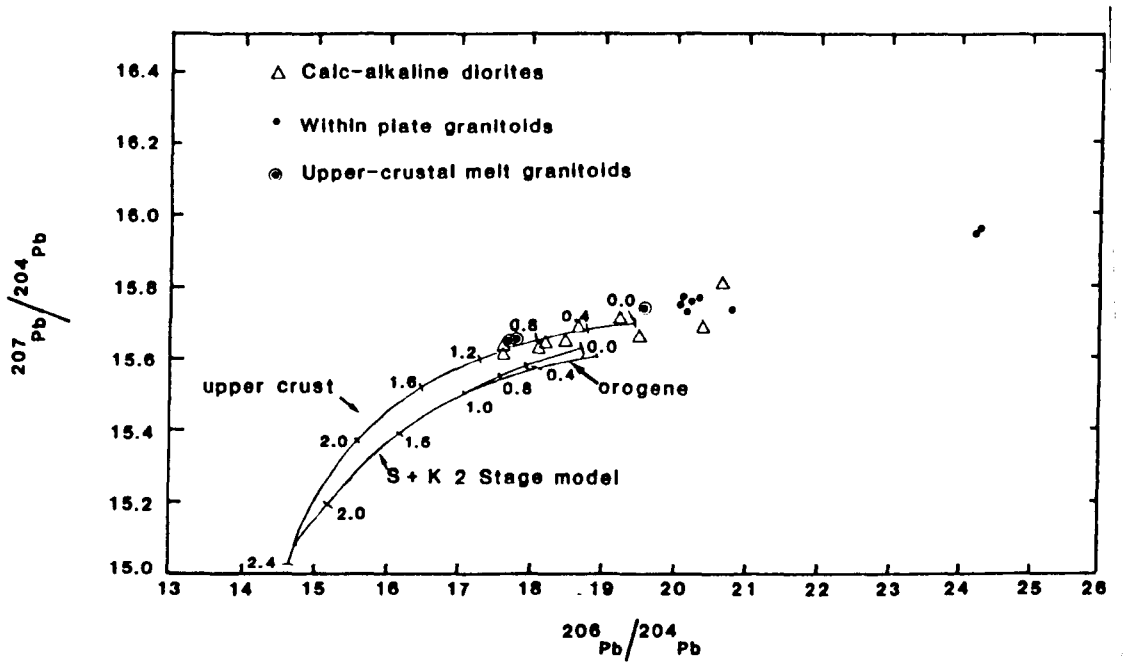

Fig. 5.20 $^{206}Pb/^{204}Pb$ vs. $^{207}Pb/^{204}Pb$ diagram for Damara granitoid whole-rock data. Most data plot above the Stacey and Kramers (1975) growth curve and the upper crust and orogene curves of Zartman and Doe (1981).

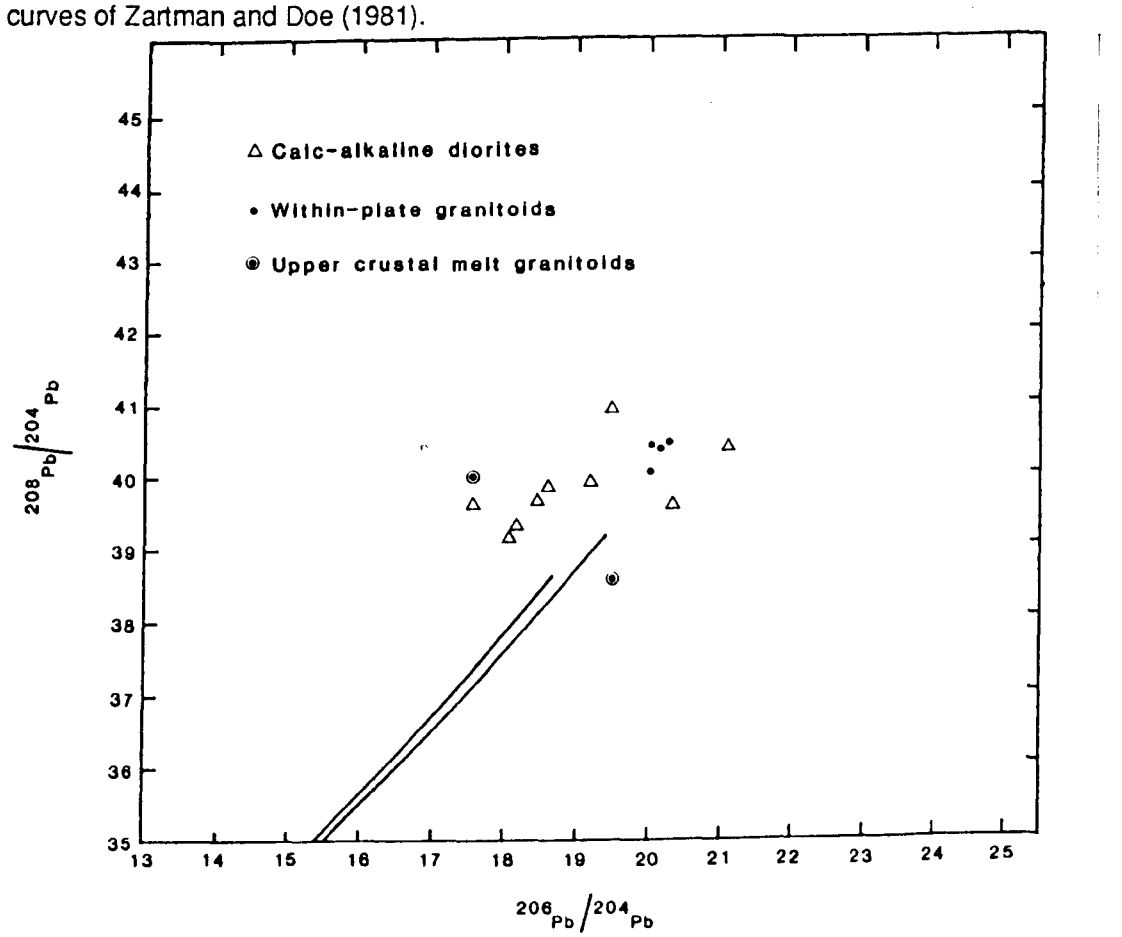

Fig. 5.21 $^{206}Pb/^{204}Pb$ vs. $^{208}Pb/^{204}Pb$ diagram for Damara whole-rock granitoid data. The orogene and upper crust curves after Zartman and Doe (1981) are also shown.

Table 5.4 Whole - rock Pb data

Sample		$^{206}Pb / ^{204}Pb$	$^{207}Pb / ^{204}Pb$	$^{208}Pb / ^{204}Pb$
Crustal - melt granitoids				
R 73	Donkerhuk granite	19.531 ± 0.002	15.747 ±0.002	38.548 ±0.005
PG 2175	Palmental granite	17.585 ±0.001	15.638 ±0.001	39.641 ±0.002
ROS 5*	Rossing alaskite	134.776±0.014	22.460 ±0.003	42.134 ±0.005
Calc-alkaline diorites				
P2139	Swakop - river diorite	19.216 ±0.002	15.718 ±0.002	39.987 ±0.005
P 2140	Swakop - river diorite	21.122 ±0.003	15.816 ±0.002	40.373 ±0.001
P 2141	Swakop - river diorite	17.598 ±0.001	15.639 ±0.001	40.000 ±0.001
P2092	Palmental diorite	18.164 ±0.004	15.649 ±0.004	39.267 ±0.013
P 2094	Palmental diorite	18.095 ±0.005	15.604 ±0.004	39.146 ±0.011
P 2095	Palmental diorite	18.628 ±0.001	15.693 ±0.001	39.841 ±0.003
P 2096	Palmental diorite	19.497 ±0.013	15.668 ±0.009	40.929 ±0.028
P 2097	Palmental diorite	18.478 ±0.006	15.654 ±0.005	39.655 ±0.013
Within-plate granitoids				
OT 2179	Otjimbingwe syenite	20.090 ±0.003	15.780 ±0.003	40.486 ±0.008
OT2180	Otjimbingwe syenite	20.301 ±0.005	15.778 ±0.004	40.465 ±0.012
OT2181	Otjimbingwe syenite	20.024 ±0.003	15.761 ±0.002	40.430 ±0.001
OT2182	Otjimbingwe syenite	20.192 ±0.001	15.775 ±0.001	40.365 ±0.003
S 2203	Sorris-Sorris granite	20.768 ±0.007	15.754 ±0.006	44.366 ±0.018
S 2204	Sorris-Sorris granite	20.264 ±0.003	15.740 ±0.003	43.767 ±0.008
28/27A	Lofdal syenite	24.160 ±0.002	15.963 ±0.002	37.988 ±0.004
28/34	Lofdal syenite	24.186 ±0.003	15.964 ±0.002	40.720 ±0.005

* Denotes sample from the U mineralised Rossing alaskite.

Table 5.5 Feldspar Pb data

Sample		$^{206}Pb/^{204}Pb$	$^{207}Pb/^{204}Pb$	$^{208}Pb/^{204}Pb$
Crustal - melt granitoids				
ROS 5*	Rossing alaskite	28.099 ±0.003	16.270 ±0.002	39.617 ±0.004
ROS 7*	Rossing alaskite	46.749 ±0.002	17.321 ±0.001	40.102 ±0.002
R 114	Donkerhuk granite	18.357 ±0.001	15.685 ±0.001	38.043 ±0.002
G 0	Goanikontes alaskite	18.352 ±0.003	15.664 ±0.003	38.508 ±0.006
V3	Valencia alaskite	17.762 ±0.005	15.647 ±0.001	38.367 ±0.002
O9	Otjua red granite	21.561 ±0.001	16.187 ±0.001	38.441 ±0.002
S1	Stinkbank leucogranite	17.920 ±0.001	15.680 ±0.001	38.670 ±0.002
PG 2175	Palmental granite	17.293 ±0.001	15.611 ±0.001	38.163 ±0.002
GG5	Salem Onanis granite	17.444 ±0.003	15.639 ±0.003	38.103 ±0.007
Calc-alkaline diorites				
129.13		17.808 ±0.001	15.645 ±0.001	38.238 ±0.001
P 2186		17.719 ±0.001	15.640 ±0.001	38.341 ±0.002
P 2094		17.724 ±0.001	15.647 ±0.001	38.745 ±0.002
Within-plate granitoids				
OT 2181	Otjimbingwe syenite	18.289 ±0.001	15.681 ±0.001	38.737 ±0.003
OT 2182	Otjimbingwe syenite	18.716 ±0.005	15.665 ±0.004	39.013 ±0.012
S 2204	Sorris - Sorris granite	18.725 ±0.001	15.683 ±0.001	39.451 ±0.002
NN 10	Naauwpoort volcanics	17.833 ±0.006	15.544 ±0.005	37.536 ±0.012
28/41	Lofdal syenite	18.135 ±0.003	15.638 ±0.003	38.433 ±0.009
1013	Dachsberg granite	24.753 ±0.015	16.109 ±0.009	45.558 ±0.032
YC 3	Horebis - river granite	18.782 ±0.003	15.729 ±0.002	39.136 ±0.007
YC 6	Horebis - river granite	19.490 ±0.002	15.807 ±0.001	39.949 ±0.004
UIS2210	Uis Sn pegmatite	23.626 ±0.006	15.932 ±0.004	37.869 ±0.010

* Denotes sample from the U mineralised Rossing alaskite.

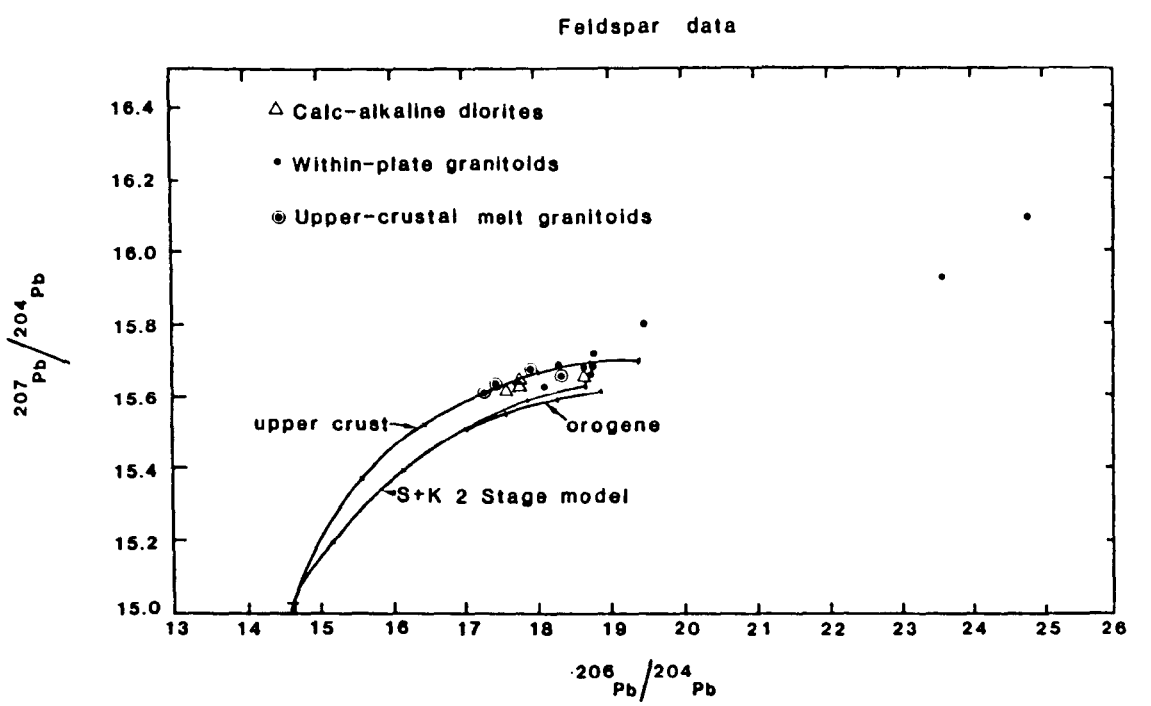

Fig. 5.22 $^{206}Pb/^{204}Pb$ vs. $^{207}Pb/^{204}Pb$ diagram for feldspar separates from Damara granitoids. Since feldspars have low U/Pb ratios the measured Pb isotopic composition reflects the isotopic composition of the magma from which the feldspars crystallised.

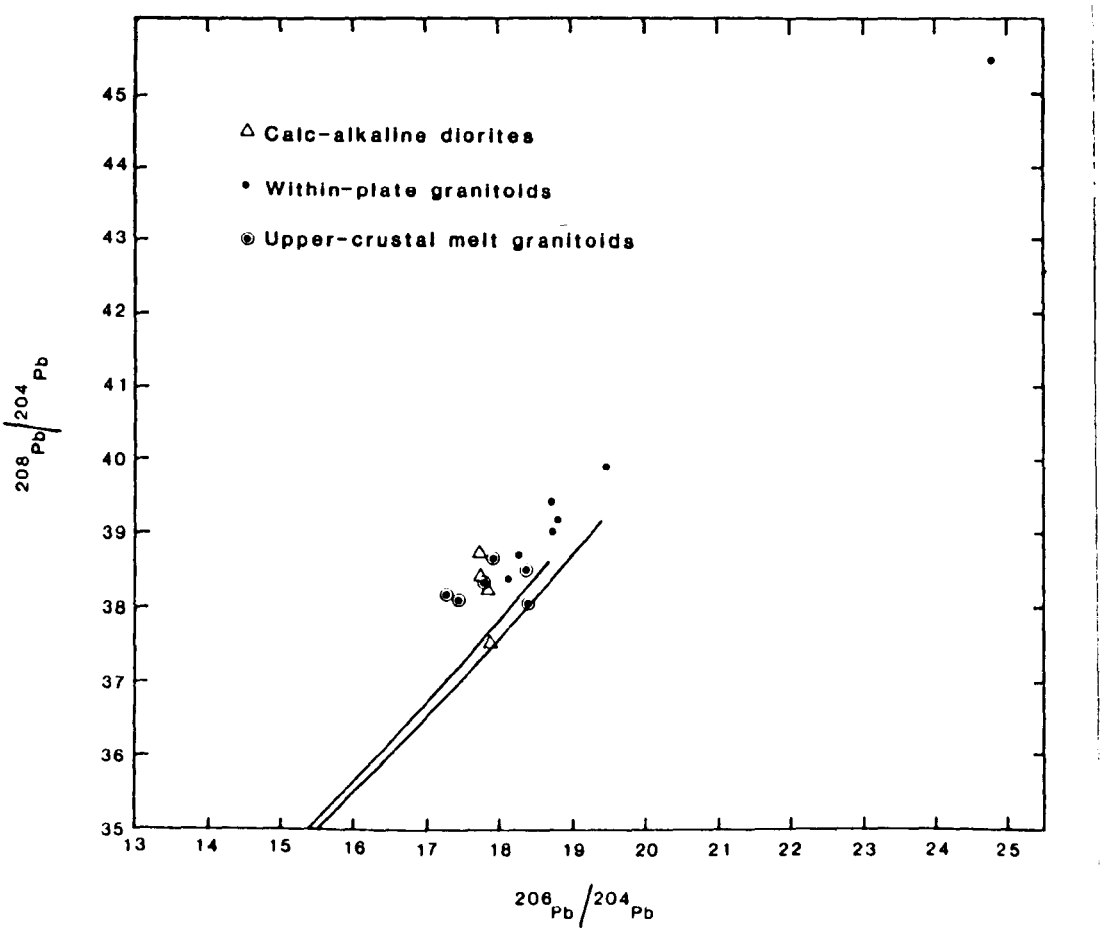

Fig. 5.23 $^{206}Pb/^{204}Pb$ vs. $^{208}Pb/^{204}Pb$ for Damara granitoid feldspar separates. The orogene and upper crust curves of Zartman and Doe (1981) are shown for reference.

5.6.1 K-feldspar data

Isotope data for K-feldspar separates are discussed and interpreted first, since feldspar isotopic ratios reflect those of the granitic magmas from which they crystallised and unlike whole-rock data do not have a significant component of radiogenic lead produced since magmas crystallised. The feldspar data plot above (i.e. have higher ^{207}Pb / ^{204}Pb) the Stacey and Kramers (1975) two stage model growth curve for terrestrial lead indicating a relatively ancient enrichment in U relative to Pb, to produce the observed high ^{207}Pb / ^{204}Pb ratios, (Fig.5.22).

If a simple single-stage evolution is assumed, μ values may be calculated using the primordial lead compositions of Tatsumoto *et al.* (1973). These, and subsequent multistage calculations assume that t_{final} equals the Rb/Sr whole-rock age of the granitoid i.e. it is assumed that no in-situ decay of U to Pb has occurred since the feldspars crystallised. Calculated model μ values range from 8.29 to 10.94 (Table 5.6) while model κ values are in the range 37.59 to 70.40. In Table 5.6 ages in parentheses denote assumed ages where Rb/Sr ages are uncertain. Model time parameters are T = 4.57 Ga and t_1 = Rb/Sr whole rock age for each intrusion.

Unlike previously published Pb isotopic data for granitoid feldspars e.g. (Vitrac *et al.* 1981) no systematic regional geographical control appears to exist on model μ or κ values. Instead, measured lead isotopic ratios reflect the granitoid compositional type, i.e. the threefold granitoid classification based on major and trace element geochemistry as outlined in Ch. 4.

However a single-stage model is geologically unrealistic for most Damara granitoids since it is likely that U/Pb was fractionated during intracrustal reworking and remobilisation associated with previous orogenies. For example, granitoids which yield T_{DM}^{Nd} model ages of about 2.0 Ga are derived from protoliths which may have suffered multistage episodic intracrustal remobilisation during previous orogenic events in which the U/Pb ratio may

have been fractionated. Therefore, the apparent μ and κ values of Table 5.6 serve only to illustrate the values required by the different granitoid types in the simplest situation where T is the same for all granitoid samples.

Table 5.6 Calculated μ and κ values assuming a single-stage model

Sample	Intrusion	Rb/Sr age	Model μ	Model κ
Crustal melt granitoids				
Ros 5	Rossing alaskite	458 ± 8	9.30	43.89
Ros 7	Rossing alaskite	458 ± 8	10.94	45.99
GG5	Salem onanis	544 ±33	8.33	38.14
PG 2175	Palmental granite	545 ± 33	8.29	38.33
S1	Stinkbank leucogranite	484 ± 25	8.39	40.02
09	Otjua red granite	516 ±23	9.18	39.30
G0	Goanikontes alaskite	508 ± 2*	8.37	39.52
V3	Valencia Salem-type granite	(500)	8.34	38.84
R114	Donkerhuk granite	521 ±15	8.40	37.59
Calc-alkaline diorites				
P2186	Palmental diorite	(650)	8.35	40.06
129.13	Huab-River diorite	570 ± 20*	8.35	38.88
P2094	Palmental diorite	(650)	8.36	41.89
Within-plate granitoids				
1031	Dachsberg granite	508 ±5	9.06	70.41
Uis 2210	Uis Sn pegmatite	(500)	8.78	36.66
YC3	Horebis river granite	633 ±39	8.49	43.49
YC6	Horebis river granite	633 ±39	8.61	47.15
OT 2181	Otjimbingwe syenite	(550)	8.40	40.91
OT 2182	Otjimbingwe syenite	(550)	8.40	40.91
S 2204	Sorris-Sorris granitoid	495 ±15	8.39	43.55
28/41	Lofdal syenite	764 ±60	8.37	41.58

* U/Pb zircon (Huab - river diorite, Miller, pers. comm.) or U/Pb monazite (Goanikontes alaskite, Briqueu *et al*, 1980) age. Ages in parentheses are assumed ages where Rb/Sr age is uncertain.

In subsequent modelling it is assumed that granitoids evolved in three stages characterised by different μ and κ values for each stage. It is assumed that the first two stages occurred according to the Stacey and Kramers growth curve for terrestrial lead (Stacey and Kramers, 1975) and these first two stages will be referred to as the S.K. model. According to the S.K. model the first stage (T to t_1) is for the time period 4.5-3.7 Ga (Fig. 5.24) with a μ value of 7.19 and a κ value of 32.21.

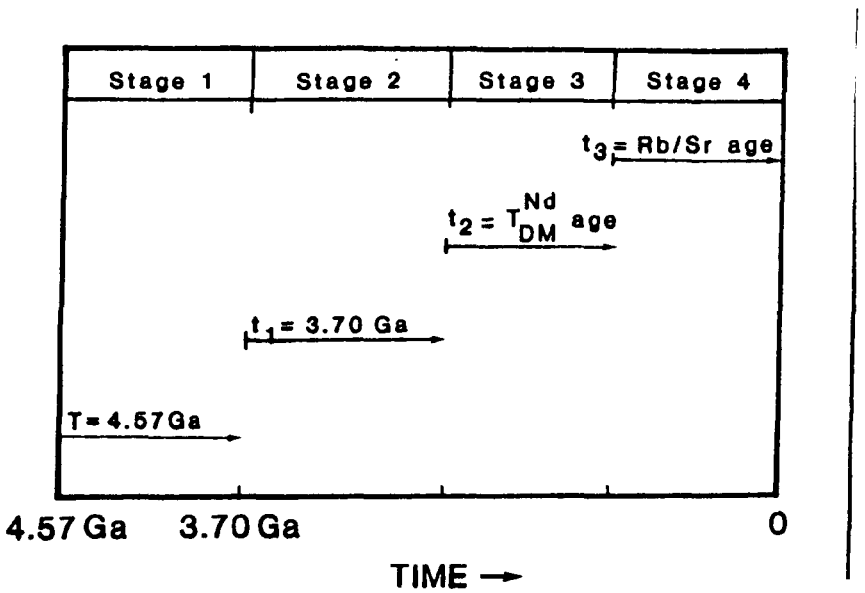

Fig. 5.24 Schematic representation of the parameters used in the three stage model as outlined in the text.

Similarily, the second stage is assumed to have the μ and κ parameters of the S.K. model, but the duration of the second stage varies from granitoid to granitoid since the end of the second stage is taken as the depleted mantle model Nd age (T_{DM}^{Nd}). Therefore the second stage is for the period 3.7 Ga until T_{DM}^{Nd} for each sample i.e. t_2 ends at T_{DM}^{Nd}. Finally, the third stage is for the period T_{DM}^{Nd} until the Rb/Sr whole rock age for each granitoid sample i.e. t_3 ends when the granitoid was emplaced and the feldspars crystallised.

It should be noted that since T_{DM}^{Nd} and Rb/Sr whole rock ages vary between intrusions, the duration of stages 2 and 3 are different for each intrusion. It is likely that U/Pb and Th/Pb ratios are fractionated by crustal extraction from the mantle so that T_{DM}^{Nd} ages (which reflect Sm/Nd fractionation by crustal extraction events) represent geologically reasonable times at which to change μ and κ values in a Pb isotope evolution model.

This model also assumes the following conditions ;

1. The initial system became closed at time T (4.57 Ga ago) to migration of Pb and U across its boundaries and was homogenous with respect to both the U/Pb ratio and to the isotopic composition of each element.

2. From time T to t_1 (4.57 to 3.7 Ga) the system evolved according to the S.K. model.

3. At t_1 (3.7 Ga.), a short lived differentiation took place within the closed system which produced different U/Pb ratios in the system. It is assumed that no isotopic fractionation of either U or Pb occurred at t_1 or subsequent times of differentiation.

4. The system evolved isotopically (as a series of subsystems with different μ and κ values) between times t_1 and t_2. At t_2 another differentiation event occurred which resulted in the homogenisation of the diverse isotopic compositions between subsystems. In addition this event at t_2 ($t_2 = T_{DM}^{Nd}$ for each sample) produced a range of different U/Pb ratios so that subsequent to t_2 (until t_3) a new series of subsystems developed, each characterised by different μ and κ values, which in time resulted in a range of isotopic compositions.

5. At time t_3 (assumed to be the Rb/Sr whole rock age of each intrusion) the isotopic ratios were effectively "frozen" as the lead was isolated in low U/Pb feldspars.

6. From t_3 to the present day no isotopic evolution occurred by virtue of the low U/Pb ratios of feldspars.

Some of the parameters of this model may be tested in a way which is model independent, and so provide independent constraints on the model. The parameter t_2 (the start of the third stage in the model outlined above) may be estimated independently by considering Fig. 5.22. The feldspar data plot above the S.K. two stage growth curve in Fig. 5.22 and so must have evolved in more than two stages.

The start of the third stage may be estimated by considering the geometry of the S.K. curve and possible evolution paths to produce the least radiogenic sample observed. A tangent to the S.K. growth curve which passes through the least radiogenic sample observed (PG 2175) intersects the S.K. curve at the youngest possible age at which a differentiation event could have produced the isotopic ratios of this sample. Therefore the point at which this tangent intersects the S.K. growth curve yields a minimum estimate for t_2, the start of the third stage. By comparing t_2 values estimated in this way to T_{DM}^{Nd} ages for samples with the least radiogenic Pb isotope ratios for each granitoid type it is possible to assess how well T_{DM}^{Nd} approximates to t_2, and so provide an independent test on this critical model parameter.

Using the tangent method described above, the least radiogenic sample analysed (PG2175, Palmental granite) yields a time for t_2 of 1.75 Ga. This minimum age accords well with the 1.7 Ga. minimum age suggested by Marlow (1981) for the start of the third stage (t_2) of growth of anomolous sulphide leads from the region. This age is also consisent with the model age of about 2.0 Ga for most Damara crustal-melt granitoids. Similarily the least radiogenic within-plate granitoid analysed (OT 2179, Otjimbingwe syenite) yields a minimum "age" of about 1.2 Ga for t_2. This age is in good agreement with T_{DM}^{Nd} model ages for within-plate granitoids (typically 1.1-1.5 Ga) suggesting that granitoid model Nd ages represent reasonable estimates of t_2 for this Pb isotope evolution model.

Model μ and κ values have been calculated for each feldspar separate using T, t_1 and t_2 parameters as outlined in Fig. 5.24. Decay constants λ_1 and λ_2 for ^{238}U and ^{235}U

are taken as 0.155125 x 10^{-9} yr^{-1} and 0.98485 x 10^{-9} yr^{-1} respectively, after Jaffey *et al.* (1971). The ^{232}Th decay constant used is the value given by Le Roux and Glendenin (1963) i.e. 0.049475 x 10^{-9} yr^{-1}. Calculated μ and κ values for the third stage of the model (i.e. T_{DM}^{Nd} - Rb/Sr whole-rock age) for each intrusion are tabulated in Table 5.7.

Table 5.7 Calculated model μ and κ values for the three stage model described in the text.

Sample		Rb/Sr age (t_3)	T^{Nd}_{DM} age (t_2)	Model μ	Model κ
Crustal - melt granitoids					
ROS 5	Rossing alaskite*	458 ± 8	2.57	18.27	53.09
ROS 7	Rossing alaskite*	458 ± 8	2.57	31.45	57.39
GG 5	Salem Onanis	554 ± 33	1.46	13.11	47.38
PG 2175	Palmental granite	545 ± 46	2.06	10.48	43.58
S 1	Stinkbank leucogranite	484 ± 25	2.27	11.42	46.69
O 9	Otjua red granite	516 ± 23	(2.0)	24.89	46.61
G 0	Goanikontes alaskite	508 ± 2	2.19	11.33	45.99
V 3	Valencia Salem - type	(500)	1.46	13.09	50.08
R114	Donkerhuk (Onanis)	521 ± 15	2.0	12.33	41.64
Calc- alkaline granitoids					
P 2186	Palmental diorite	(650)	1.45	14.25	58.80
RM 129.13	Huab - river diorite	570 ± 20	1.52	13.23	50.21
P 2094	Palmental diorite	(650)	1.42	14.92	69.73
Within - plate granitoids					
1031	Dachsberg granite	508 ± 5	1.31 Ga	46.31	226.35
UIS 2210	Uis Sn pegmatite	(500)	(1.4 Ga)	30.29	40.31
YC 3	Horebis - river granite	633 ± 39	1.13	28.57	102.18
YC 6	Horebis - river granite	633 ± 39	1.13	37.71	87.17
OT 2182	Otjimbingwe syenite	(550)	1.41	14.94	68.18
SOR 2204	Sorris-Sorris granite	495 ± 15	1.18	18.35	85.93
OT 2181	Otjimbingwe syenite	(550)	1.27	17.73	66.99
28/41	Lofdal syenite	764 ± 60	1.40	16.32	73.68

* Denotes U mineralised alaskite. Ages in parentheses are assumed where Rb/Sr or model ages are uncertain.

The within-plate granitoids are characterised by significantly higher model μ and κ values than crustal-melt or calc-alkaline granitoids. While μ and κ values calculated here (Tables 5.6 and 4.7) are model dependent the relative values of μ and κ fdor the three granitoid types are model independent. The high $^{206}Pb/^{204}Pb$, $^{207}Pb/^{204}Pb$, $^{208}Pb/^{204}Pb$ ratios of the within-plate granitoids reflect time-integrated high U/Pb and Th/Pb ratios in within-plate granitoid sources. In general, crustal-melt granitoids have the lowest model μ and κ values. The relatively high μ and κ values calculated for the Rossing alaskite samples (Ros 5 and Ros 7) are interpreted as being due to incorporation of tiny amounts of uranium bearing minerals in the separated feldspar samples.

5.6.2 Age significance of Pb data

The slope defined by data on a ^{206}Pb / ^{204}Pb diagram depends only on the time elapsed since the last stage began. The distribution of points along the isochron depends on the range of μ values of the last evolution stage while the "goodness of fit" of data to a straight line depends on how efficiently the lead isotopic ratios were homogenised at the beginning of the last stage and on subsequent closed system behaviour. The simple relationship between time elapsed since the last evolution stage began and the slope of the line defined by data points on a ^{206}Pb / ^{204}Pb diagram may be demonstrated by considering the Pb isochron equations and is illustrated in Appendix 1. Compatible values of t and $(^{207}Pb/^{206}Pb)^*$, (ratio of radiogenic ^{207}Pb to radiogenic ^{206}Pb) have been worked out (Stacey and Stern, 1973) so that t can be calculated from the slope of the isochron.

5.6.2.1 Whole rock data

In the case of whole-rock data (Fig. 5.20 and 5.21), in which the decay of uranium to lead has continued up to the present-day the slope defined by data points is a measure of the average age of granite formation. Whole rock data points (excluding U mineralised samples) define a regression line with a slope of 0.05813 ± 2 which corresponds to an age of 531 Ma. This "age" reflects an average age of the Damara granitoids which define this slope and is in good agreement with Rb/Sr whole rock ages for the granitoids

5.6.2.2 Feldspar data

Unlike whole-rock samples, feldspar separates retain the lead isotopic signature of the magma from which they crystallised since their low U/Pb ratios inhibit in-situ production of radiogenic lead. $^{207}Pb/^{206}Pb$ ages may be calculated for feldspars by determining the slope defined by the data on a $^{207}Pb/^{204}Pb$ vs. $^{206}Pb/^{204}Pb$ diagram since this slope gives the $^{207}Pb/^{206}Pb^{*}$ ratio (the ratio of radiogenic ^{207}Pb to ^{206}Pb). The feldspar data (19 samples) define a slope of 0.05784 ± 3 on a $^{207}Pb/^{204}Pb$ vs. $^{206}Pb/^{204}Pb$ diagram which corresponds to an age of 519 Ma. However, the slope of this line is strongly dependent on two Rossing alaskite samples (Ros 5 and Ros 7) which have high $^{207}Pb/^{204}Pb$ and $^{206}Pb/^{204}Pb$ ratios. Since this intrusion is relatively young (458 ± 8 Ma) the regression line is weighted to yield a relatively young average age of 519 Ma. If the two Rossing alaskite samples are excluded from the regression calculation the remaining 17 feldspar separates yield slope of 0.0599 ± 4 which corresponds to an age of 600 Ma. This age is interpreted as reflecting the "mean" age of granitoids which define the regression line.

5.6.3 Whole-rock / Feldspar data comparison

Both feldspar and whole rock data have been obtained for six samples. Since feldspar data effectively represents "initial ratios" the μ and κ values required to produce the observed whole-rock isotopic ratios may be calculated since the age of the granitoids are known. Calculated μ and κ values are tabulated in Table 5.8.

Table 5.8 Calculated μ and κ values - assuming feldspar ratios represent "initial ratios"

Sample No.	Intrusion	Age in Ma	μ	κ
Calc -alkaline diorite				
P2094	Palmental diorite	(650)*	3.49	1.27
Crustal-melt granitoids				
PG2175	Palmental granite	546 ± 45	3.31	54.07
Ros 5	Rossing alaskite	458 ± 8	114.80	109.80
Within-plate granitoids				
P2181	Otjimbingwe syenite	(650)*	16.27	51.78
P2182	Otjimbingwe syenite	(650)*	13.91	41.33
S2204	Sorris-Sorris	495 ± 15	19.20	173.90

* Age of the Palmental diorite and Otjimbingwe syenite is assumed to be 650 Ma.

Calculated μ and κ values for the Rossing alaskite (sample Ros 5) are extremely high reflecting associated U mineralisation. Sample P2094 (Palmental diorite) is characterised by low μ and κ values. The crustal melt granitoid sample PG2175

(Palmental granite) has a relatively low μ value but is distinguished from the diorite sample by a high κ value (54.07). The within-plate granitoid samples P2181, P2182 and S2204 have highest μ and κ values (aside from mineralised alaskites). Two point ages may be calculated (defined by the slopes of lines joining feldspar and whole-rock data on a $^{207}Pb/^{204}Pb$ vs. $^{206}Pb/^{204}Pb$ diagram) for feldspar/whole-rock pairs. In most granitoids the differences in ratios between whole-rock and feldspar data are insufficiently large to define meaningful slopes. However, in the case of the Rossing alaskite sample, (Ros 5) the differences between feldspar and whole-rock ratios are relatively large (Tables 5.4 and 5.5) and define a slope of 0.0580 which corresponds to an age of 526 Ma.

5.6.4 Summary of lead isotope results

1. Granitoid compositional type appears to control the $^{206}Pb/^{204}Pb$, $^{207}Pb/^{204}Pb$ and $^{208}Pb/^{204}Pb$ ratios. With the exception of U mineralised samples, crustal melt granitoids are characterised by relatively low $^{206}Pb/^{204}Pb$, $^{207}Pb/^{204}Pb$ and $^{208}Pb/^{204}Pb$ ratios, whereas within-plate granitoids display the highest values, being especially enriched in $^{208}Pb/^{204}Pb$. These patterns are observed in both whole-rock and feldspar data suggesting that relatively long lived differences in μ and κ values between the sources of each granitoid type.

2. The minimum age for the start of the third stage (assuming a three stage model for feldspar leads) is about 1.75 Ga for crustal melt granitoids and 1.2 Ga for within-plate granitoids. These ages accord well with model Nd ages for these granitoid types.

3. Comparison of whole-rock and feldspar data for the same samples suggest that (alaskites excluded) μ and κ values for the last stage are greatest for within-plate and lowest for crustal melt granitoids, with intermediate values for the

calc-alkaline diorites. Within-plate granitoids consistently show the highest μ and κ values suggesting that their sources had high time integrated U/Pb and Th/Pb ratios.

5.7 Oxygen isotope data

Oxygen isotope ratios have been determined for 18 quartz separates from a variety of granitoid types. The results are tabulated iin Appendix 2. Mineral separation and analytical techniques are described in Appendix 1.

Measured $\delta^{18}O$ values for quartz separates are in the range 8.7-15.4‰, the majority being very heavy. Fig. 5.25 is a histogram of all available oxygen isotope data for the Damara granitoids (Haack *et al.* 1982 and this study).

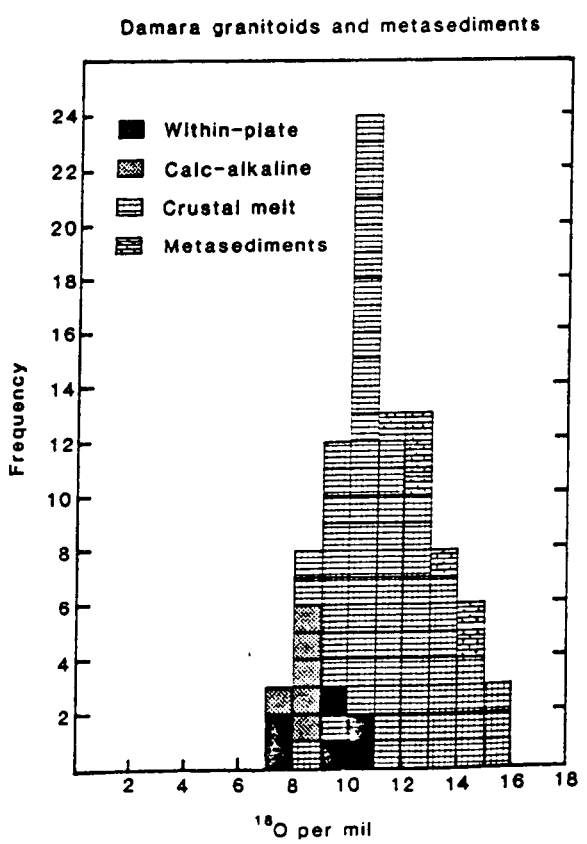

Fig. 5.25 Histogram of δ^{18} O ‰ for Damara granitoids and metasediments. Data from this study and after Haack *et al.*, 1982.

Most $\delta^{18}O$ values are extremely heavy with more than 70% of the analyses greater than +10‰, i.e. "high" $\delta^{18}O$ granitic rocks of Taylor (1978). The within-plate granitoids from Sorris-Sorris (Haack *et al. op. cit.*) and from the Horebis-river intrusion (this study) display the lowest $\delta^{18}O$ values, (Fig. 5.26).

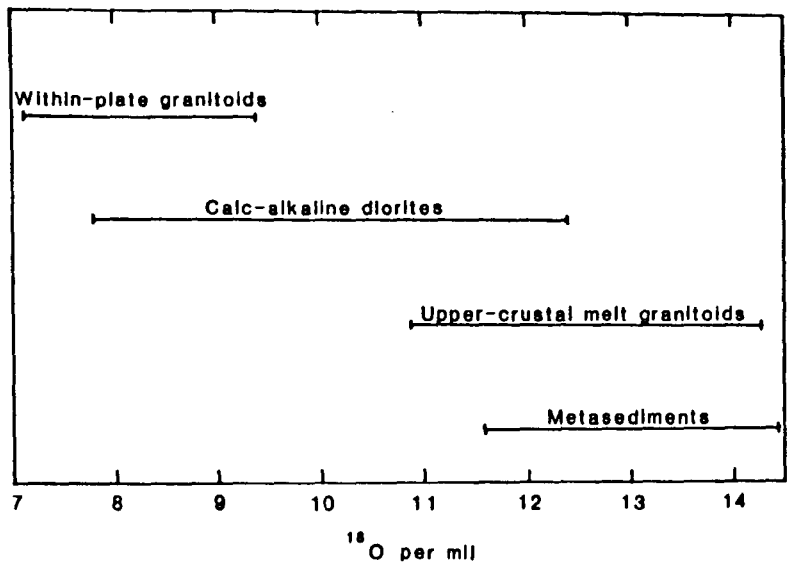

Fig. 5.26 Diagram showing the range in $\delta^{18}O$ ‰ for the three granitoid types and Damara metasediments. Within-plate granitoids display the lowest and most restricted range in $\delta^{18}O$.

It has been demonstrated (Giletti *et al.* 1978) that isotopic equilibration in silicate minerals takes place by volume diffusion rather than by dissolution-reprecipitation. Diffusion rates are several orders of magnitude lower and activation energies are significantly higher in quartz than in other silicate minerals e.g. feldspars (Giletti and Yund, 1984). Thus quartz remains relatively unaffected by late-stage magmatic or hydrothermal fluids as granitic plutons cool. For this reason it is assumed that quartz effectively retains the isotopic signature of the magma from which it crystallised and so yields information on magma petrogenetic processes. The resistance of quartz to isotopic exchange has also been convincingly demonstrated by Criss and Taylor (1983) for the Idaho batholith.

In the case of the Damara granitoids it appears that no large scale homogenisation of oxygen isotopes occurred (e.g. Wickham and Taylor, 1985) since samples from less than 0.5 Km apart have significantly different quartz $\delta^{18}O$ values e.g. +11.2 and 14.5 ‰ for the Palmental diorite and granite respectively.

The high $\delta^{18}O$ (> +10‰) of many granitoid quartz samples strongly suggest that significant amounts of metasedimentary material or altered volcanic rocks were involved in the intracrustal melting which produced most of the Damara granitoids (Taylor *et al.* 1977, Taylor, 1978). This is consistent with the peraluminous nature of many of the Damara granitoids. The relatively high $\delta^{18}O$ values of quartz from the Palmental diorite (+11.18 to +12.4‰) is thought to reflect relatively large scale assimilation of metsedimentary material for which there is abundant field evidence (Plate 2.2, Ch. 2). Similarily, the relatively high $\delta^{18}O$ values for the Otjimbingwe syenite (Ch. 2) quartz separates (+10.6 to +11.6‰) may reflect assimilation of high $\delta^{18}O$ metasedimentary material.

It is significant that the within-plate granitoids (e.g. Sorris-Sorris and Horebis river granitoids) display the lowest $\delta^{18}O$ values.This suggests that within-plate granitoid protoliths have not been involved in low temperature, near-surface alteration/weathering processes which increase $\delta^{18}O$. This interpretation is consistent with the restricted range in ε Sr values calculated for within-plate granitoids which is interpreted as reflecting little or no intracrustal reworking of within-plate granitoid protoliths. The elevated HFS element abundances in within-plate granitoids require that their protoliths had undergone little or no intracrustal reworking or magmatic remobilisation since these processes result in HFS element depletion (Ch.4).

Furthermore, there is a correlation between quartz $\delta^{18}O$ and model Nd age (T^{Nd}_{DM}) for the granitoid samples. Exceptions to this trend are the within-plate Sorris-Sorris granitoid samples (Fig. 5.27).

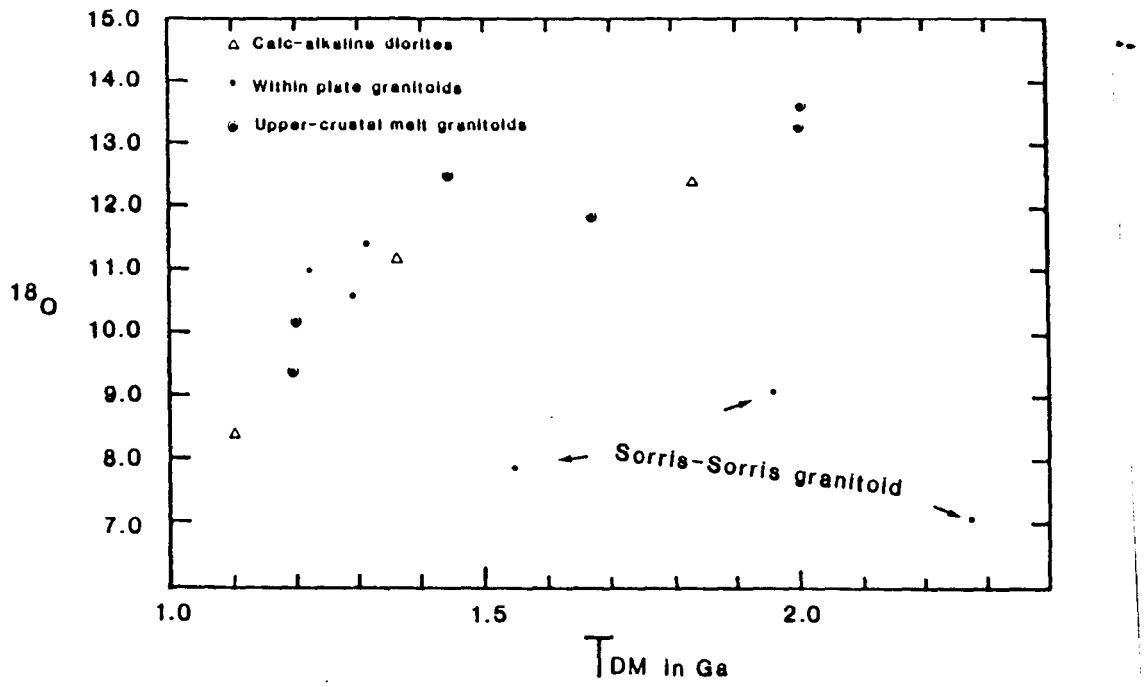

Fig. 5.27 Plot of $\delta^{18}O$ ‰ vs. model Nd age (T^{Nd}_{DM}). Most granitoids define a positive correlation between $\delta^{18}O$ and T^{Nd}_{DM}. In contrast, the within-plate Sorris-Sorris granitoid defines a subhorizontal trend.

The positive correlation between $\delta^{18}O$ and T^{Nd}_{DM} suggests that the $\delta^{18}O$ value of a granitoid quartz separate is a function of how long a granitoid protolith has been in the upper crust and so "available" for intracrustal reworking. This is consistent with a multistage episodic reworking model outlined above since granitoid protoliths with a long crustal history may have undergone many erosion and sedimentation cycles which may have increased $\delta^{18}O$.

In summary, $^{87}Sr/^{86}Sr$ increases systematically with depth in the Damara metasediments. This trend is accompanied by a decrease in $^{143}Nd/^{144}Nd$. The oldest Damara metasediments (Nosib Group) have model Nd ages (CHUR) in the range 2.0 - 2.2 Ga whereas the younger sediments (Kuiseb Formation and Nama group) have model Nd ages in the range 1.0 - 1.3 Ga. This indicates sediment input from a younger source terrain during deposition of the Kuiseb schists and Nama Group. The ratio of model ages ($T^{Nd}_{CHUR}/T^{Sr}_{BE}$) is used as an index of intracrustal reworking. The older Damara metasediments have the highest model age

ratios suggesting that their sources suffered the largest amounts of intracrustal reworking. However the rate of intracrustal reworking inferred from the younger metasediments is higher than that inferred from the older metasediments. This is a reflection of higher average rates of intracrustal reworking since about 1.3 Ga.

Hyperbolae defined by granitoid data on ε Sr vs. ε Nd diagrams may be explained by an episodic intracrustal reworking model in which Rb/Sr ratios are increased with time but Sm/Nd remains relatively constant. The high $\delta\ ^{18}O$ values of quartz separates from Damara crustal-melt granitoids suggest that their crustal precursors were involved in near-surface processes e.g. erosion and sedimentation which also increased Rb/Sr while Sm/Nd remained relatively unchanged.

Lead isotope data for Damara granitoids distinguish the three granitoid types classified on the basis of major and trace element data. Within-plate granitoids are characterised by radiogenic lead isotope ratios suggesting that their precursors had time integrated high U/Pb and Th/Pb ratios.

CHAPTER 6

Discussion and conclusions

6.1 Introduction

In this chapter geochemical constraints on the petrogenesis of each of the three granitoid groups (Ch. 4) are summarised. Since Damara intrusions are dominated by crustal-melt granitoids, emphasis is placed on how crustal melts are generated and extracted from their source regions. Rheological constraints on the generation and extraction of crustal melts are also discussed. Results and interpretations of Sr and Nd studies on metasediments (Ch. 5) are summarised and the implications for Damara crustal evolution are explored. Finally, the results of geological, geochemical and geochronological investigations from this and previous studies are collated and incorporated into a geotectonic model for the evolution of the orogen.

6.2 Crustal anatexis

Since the classical experimental studies of Tuttle and Bowen (1958) several authors have discussed high grade metamorphism and incipient anatexis of metasedimentary rocks (e.g. Hoffer, 1973 ; Busch *et al*, 1974 ; Winkler, 1976 ; Thompson and Algor, 1977 ; Wyllie, 1977 ; Thompson, 1985 ; Grant, 1985). Experimental studies confirm that initial melting of quartz-feldspar mixtures can produce liquid compositions close to the granite minimum in the $NaAlSi_3O_8$ (Ab) + $KAlSi_3O_8$(Or) + SiO_2 (Qtz) + H_2O(V) system, as originally determined by Tuttle and Bowen (*op. cit.*). In general, the Qtz-Ab-Or-H_2O system is an oversimplification and is inadequate to model crustal anatexis because the paths followed by liquid compositions may vary considerably depending on the An/Ab ratio of the system (Winkler, 1976). However, since the early stages of fusion are dominated by the minerals of this simple assemblage (Winkler, *op. cit.*) the results of Tuttle and Bowen (*op. cit*) and more recent melting experiments based on

this simplified assemblage are applicable to the generation of small volume crustal melts.

The effect of Ca bearing plagioclase on equilibria in the system $KAlO_2$ - $NaAlO_2$ - Al_2O_3 - SiO_2 - H_2O is discussed by Thompson and Tracy (1979) who conclude that the most calcic plagioclase compositions observed in high grade pelitic rocks (An_{25} - An_{40}) increase subsolidus and solidus temperatures by less than 30 °C. It is also necessary to distinguish the melting of peraluminous biotite ± plagioclase ± K-feldspar ± quartz assemblages from the melting of this assemblage plus a more aluminous phase (e.g. muscovite, Al_2SiO_5, cordierite etc.) because initial melting of an assemblage containing excess alumina may occur at a lower temperature (Thompson, 1982)

Although petrologists have long been aware of the influence of excess H_2O during crustal anatexis (Tuttle and Bowen, 1958) and several authors (e.g. Brown and Fyfe, 1970 ; Carmichael *et al.*, 1974) have pointed out that most crustal melts are H_2O undersaturated, most experimental studies have been conducted with excess H_2O. Thompson and Tracy (*op. cit*) and Thompson (*op. cit)* argue that in the absence of H_2O saturated melting the optimum conditions for anatectic melt generation occur in the pressure range 4-6 Kb between about 640 °C and 720 °C where muscovite dehydration and initial melting reactions overlap. This "dehydration melting" occurs when H_2O released from mica dehydration is released directly to an H_2O undersaturated melt without the generation of a fluid (vapour) phase. Anatexis of pelitic rocks is likely to occur under H_2O undersaturated conditions whereas H_2O saturated conditions are probably rarely achieved unless an external H_2O supply is available. Thompson and Tracy (*op.cit.*) used the model system CaO-K_2O-Na_2O-Fe_2O_3 -MgO-Al_2O_3 -SiO_2- H_2O (CKNFMASH) to represent metapelite anatexis. At about 3Kb, (similar to conditions of anatexis in the Central Zone), dehydration melting in the system (CKNFMASH) begins in the temperature interval 720 to 760 °C depending upon plagioclase composition. It is noted that H_2O undersaturatred crustal melts are characterised by high viscosities which inhibit their extraction and ascent unless the temperatures achieved are considerably higher than those required to generate "minimum melts", or volatiles are available to increase the melt volume and lower it's viscosity.

6.3 Crustal melt granitoids

The principal geochemical characteristics of crustal melt granitoids have been summarised in Table 4.1. Petrogenetic models for crustal-melt granitoids must account for their peraluminous major element geochemistry, high Rb/Sr ratios, low HFS element abundances, high initial $^{87}Sr/^{86}Sr$ and low $^{143}Nd/^{144}Nd$ ratios. In addition, petrogenetic models for alaskites must account for their high K_2O and U abundances. Crustal anatexis and granite petrogenesis models must also adress the problem of how high viscosity crustal-melts are extracted from their sources and coalesce to form granite intrusions.

For the purposes of this discussion two distinct crustal melting regimes are distinguished. It is argued that low volume partial melts (< ~ 20% melt) produced by anatexis of metasediments may be extracted from their sources only in exceptional circumstances. In contrast, partially molten systems with relatively large melt fractions (> ~ 35% melt) have dramatically lower yield strengths (Arzi, 1978) and may be extracted with their restites if the density contrast with surrounding country rocks is sufficient to allow buoyant ascent. Relatively large melt fractions are characterised by a suspension-like behaviour (Arzi, 1978) in which slow thermal convection may homogenise partially molten migmatitic rocks (e.g. Wickham, 1984) to produce restite-bearing granites. The transition from small melt fraction, granular/matrix controlled flow behaviour to suspension-like behaviour occurs at a critical melt fraction (Arzi, 1978 ; Van der Molen and Paterson, 1979) where the yield strength of partially molten granitic rock decreases by several orders of magnitude over a small (<10%) increase in melt fraction (Fig. 6.1).

In the context of Damara crustal-melt granitoids, trace element modelling (Ch. 4) indicates that the two melt regimes are represented by alaskites and leucogranites respectively. Alaskites are relatively small volume (< 20%) crustal melts whereas leucogranites

are large volume (> 40%) melts (Ch.4.). Rheological constraints on melt extraction indicate that relatively small volume (10-15%) crustal melts (e.g. alaskites) are rarely extracted from their sources. This may explain why migmatites are commonly observed in high grade metamorphic terrains while alaskite-type intrusions are rarely present.

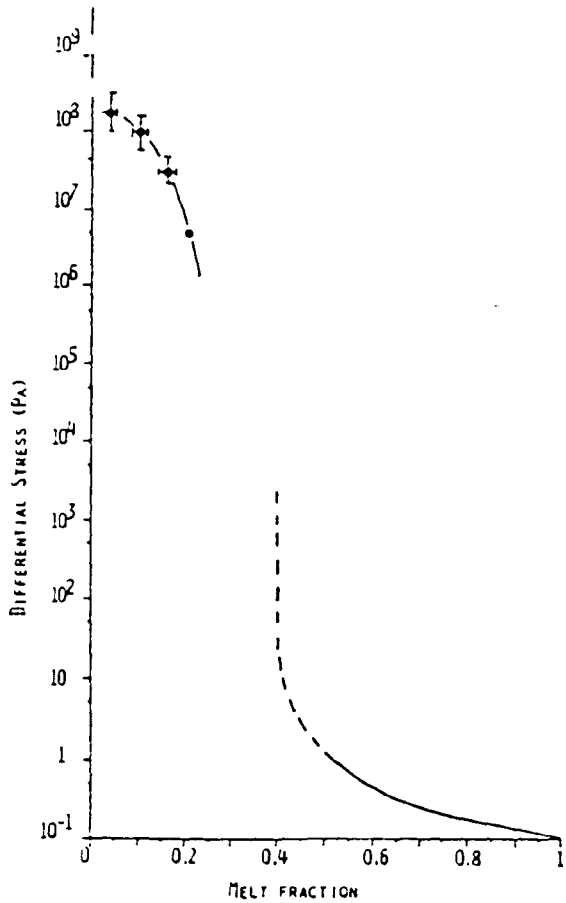

Fig. 6.1 Rheological behaviour of partially molten granite as a function of melt fraction. This diagram shows maximum differential stress as a function of melt fraction for a constant strainrate of 10^{-5} S^{-1} in a partially molten granite (After Van der Molen and Patterson (1979).

6.4 Rheological behaviour of crustal-melts

In order to understand how relatively small volume crustal melts (~10% melt) coalesce and are extracted from their sources it is necessary to understand how incipient melts are distributed among residual (matrix) grains. The dynamics of melt segregation place important physical constraints on how small volume melts may be extracted and have important geochemical implications which are discussed below.

Recently, geologists have applied interfacial energy relationships to predict and explain the equilibrium distribution of partial melts in igneous systems (Waff and Balau, 1979, 1982 ; Cooper and Kohlstedt, 1982 ; Watson, 1982). These experiments demonstrated that a basaltic melt will penetrate the grain edges of an olivine aggregate to form an interconnected network of channels throughout the system when the dihedral angle is less than 60^{o}. This behaviour is consistent with materials science melting theory based on interfacal energy arguments (e.g. Smith, 1964 ; Berre, 1975 ; Balau et al., 1979). Until recently the extrapolation of this melt behaviour to granitic systems was hampered by a lack of experimental data. However, Jurewicz and Watson (1985) have demonstrated average dihedral angles of 44, 49 and 59 degrees for K-feldspar/K-feldspar, K-feldspar/Quartz and Quartz/Quartz dihedral angles respectively in a partially molten granitic system. Jurewicz and Watson (*op. cit.*.) also noted that some of the melt fraction was isolated in randomly distributed pools suggesting that the shape of melt at grain edges deviates slightly from the idealised three sided geometry predicted by previous theories (e.g. Berre, 1975). The pooling of melt is due to the relatively large degrees (up to 24%) partial melts produced during the experiments of Jurewicz and Watson (*op. cit).* At lower melt fractions the melt forms an interconnecting framework along all grain edges since the measured dihedral angles are less than 60^{o}. In subsequent discussions it is assumed that the dihedral angles measured by Jurewicz and Watson (*op. cit.*) are generally applicable to granitic systems so that the partial melt forms an interconnected three dimensional network which may be extracted by matrix compaction.

6.4.1 Melt extraction

It is assumed that melt extraction occurs primarily by upward expulsion of a low-density melt by a more dense compacting matrix. The equations used are taken from Mc Kenzie (1984,1985), Richter and Mc Kenzie (1985) and Richter, (1986). The reader is referred to Mc Kenzie (1984) for derivation of the governing equations. A number of parameters which are used to describe the compacting regime require definition.

The compaction length (δ_c) is the thickness of the compacting region. More rigorously defined, it is the characteristic length (vertical height in metres) over which the compaction rate decreases by a factor of e. The compaction rate is simply a function of the rate of change of porosity (ϕ) with time i.e. $d\phi/dt$. Mc Kenzie (1984) has shown that the compaction length (δ_c) can be given by the equation

$$\delta_c = \left(\frac{\zeta + 4/3\eta K_\phi}{\mu}\right)^{1/2} \quad \ldots\ldots\ldots\ldots \quad 6.1$$

where : δ_c is the compaction length

ζ is the bulk viscosity of the matrix (residue)

η is the shear viscosity of the matrix

μ is the melt viscosity

K_ϕ is the permeability of the matrix.

ζ and η are the effective bulk and shear viscosities of the matrix respectively. The values of these parameters change as compaction proceeds by variations in matrix porosity and deformation by shear. Values for ζ and η are not well determined so that the value of 10^{18} Pas is used for ($\zeta + 4/3\eta$) following Richter and Mc Kenzie (*op. cit.*).

The matrix permeability K_ϕ is a function of matrix porosity which depends on the relative number of connecting and non-connecting pores. The equation of Richter and Mc Kenzie (*op. cit.*) is used

$$K_\phi = \phi_o^{\,3}\ a^2/1000 \quad \ldots\ldots\ldots\ldots \quad 6.2$$

where ϕ_o is the initial porosity of the matrix and a is the matrix particle radius.

The compaction time τ_o is the time required for the porosity at the base of the compacting layer to change from ϕ to ϕ/e, assuming that compaction ocurs at the initial compaction rate $d\phi/dt$. Mc Kenzie (1985) argued that instabilities in melt percolation may allow the melt to be extracted into melt channels. Under these circumstances the parameter τ_o

(compaction time) is an appropriate measure of time and this is the time parameter used in this discussion,

$$\tau_o = \delta_c / W_o \quad \ldots\ldots\ldots\ldots \quad 6.3$$

where δ_c is the compaction length as previously defined and W_o is the fluid velocity. Mc Kenzie (1984) has shown that

$$W_o = K_\phi (1 - \phi_o) \Delta\rho g / \mu \quad \ldots\ldots\ldots \quad 6.4$$

where K_o , and μ are as defined above

g = acceleration due to gravity

$\Delta\rho$ = density contrast between the matrix and the melt.

The simple compaction models described by these equations represent over-simplifications of how natural siicate systems are likely to behave. In particular, the effects of instabilities on melt percolation are poorly understood. Instabilities may allow the melt to be extracted into melt channels which facilitate the extraction of high viscosity melts. This melt channelling effect may explain the melt pools observed by Jurewicz and Watson (1985) during experimental melting of granitic systems. However, the equations do serve to demonstrate the major constraints on the rates at which crustal melts may be extracted from their sources. The equations show that melt viscosity is the major constraint on melt extraction rate.

Fig. 6.2 shows how compaction time τ_o varies with increasing melt fraction. In Fig. 6.2 curves are calculated assuming matrix grain sizes of 1, 2 and 3 mm for a melt of constant viscosity (5×10^4 Pas). Clearly, larger grain size matrices facilitate melt extraction. However Fig. 6.2 shows that it is virtually impossible to extract a melt with a viscosity of 5×10^4 Pas irrespective of the degree of partial melting or the grain size of the matrix, since compaction times in excess of 10^5 years are required. The value of 5×10^4 Pas for melt viscosity are based on that given by Shaw (1972) for "wet" granite magma at 800°C (5% H_2O) so that granitic magmas are unlikely to have appreciably lower viscosities unless they are extremely volatile

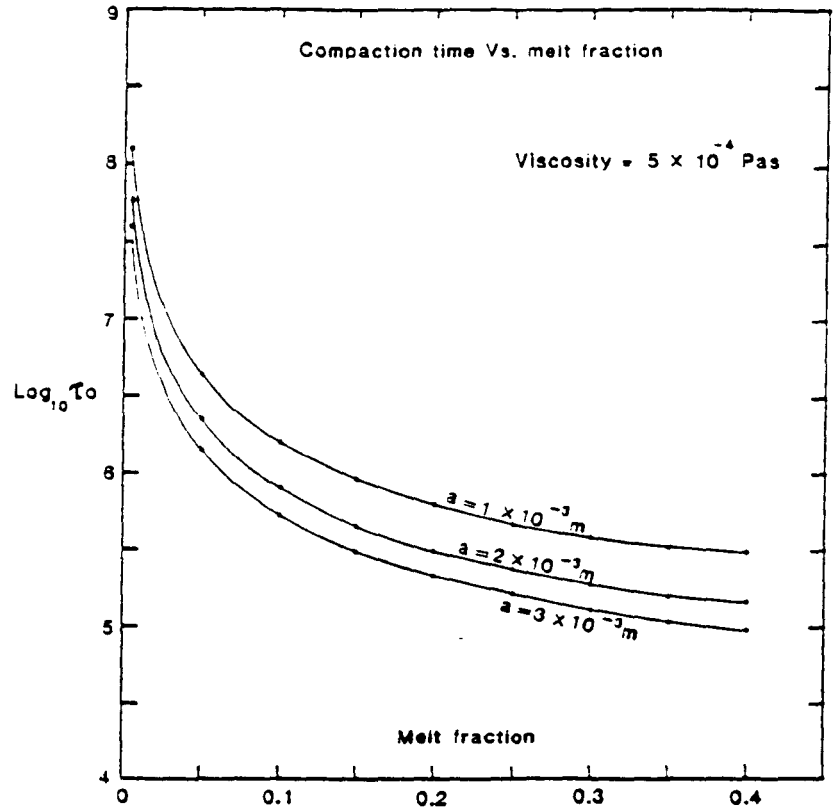

Fig. 6.2 Compaction time τ_o in years as a function of melt fraction for a constant melt viscosity of 5 x 10^4 Pas. The three curves are for matrix grain sizes of 1, 2 and 3 mm.

rich. Fig 6.3 shows the effect of matrix grain size on compaction time assuming a constant melt fraction of 10%. Curves have been drawn for different melt viscosities. The curve corresponding to a low melt viscosity of 1 x 10^2 Pas is shown as a limiting case, since such low viscosities are uncharacteristic of granitic melts unless they are extremely volatile rich. Even if an improbably low melt viscosity of 1 x 10^4 Pas is assumed, a compaction time in excess of 30,000 years is required if the matrix grain size is 2mm. It should be noted that volatiles have two important effects, both of which facilitate melt extraction

1. Volatiles (e.g. F^-, Cl^-, OH^-) break the Si-O bridges of aluminosilicate tetrahedra and depolymerise the melt resulting in a decrease in melt viscosity, (Burnham, 1979)

2. Relatively soluble volatiles e.g. HF, H_2O increase the melt volume and so enhance the melt/matrix density contrast.

In summary, it is unlikely that granitic magmas can be extracted from their sources by a matrix compaction mechanism alone, unless the melt is extremely volatile rich and the matrix grain size is large, (several mm).

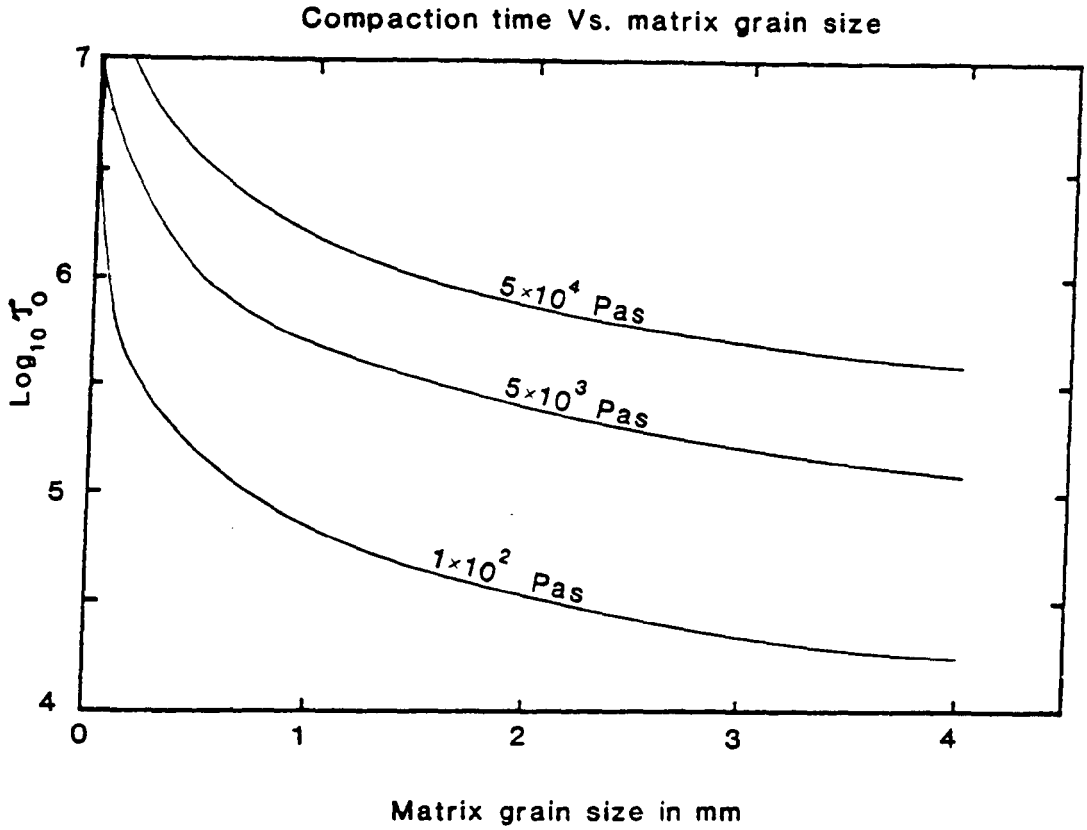

Fig. 6.3 Compaction time τ_o in years as a function of matrix grain size in mm. Three curves shown are for melt viscosities of 1 x 10^2, 5 x 10^3 and 5 x 10^4 Pas. The 1 x 10^2 Pas curve is shown as a limiting case only since such low melt viscosities are improbable for granitic melts.

Since matrix compaction is a very inefficient expulsion mechanism for high viscosity melts it is suggested that small volume crustal melts can only be extracted from their sources if the matrix is deformed by relatively large scale (regional ?) deformation events. It is noted that the alaskites of the Central Zone are syn-D_3 (Marlow, 1981 ; Miller, 1983), suggesting that relatively large-scale regional deformation events are required to "squeeze" small volume high viscosity melts out of their residual matrices. An intriguing implication is that the age of alaskite dykes in high T metamorphic terrains may constrain the age of regional deformation events.

6.4.2 Geochemical implications

Assuming that small volume granitic partial melts can be extracted from their sources (albeit in exceptional circumstances) the process of melt extraction has important implications for melt geochemistry. Depending on the melt / matrix distribution coefficients trace elements move at different velocities as the melt fraction moves relative to the matrix. Mc Kenzie (1984) has derived an equation which gives the effective transport velocity (W_e) for a given trace element as a function of it's bulk distribution coefficient, matrix porosity, and melt / matrix density contrast.

$$W_e/W = (((1 / \phi) - 1)\ (P_s / P_f)\ K_c + 1\ )^{-1} \quad \text{..... 6.5}$$

where ;

W_e = effective transport velocity of a trace element

W = melt velocity

ϕ = matrix porosity

P_s = matrix density

P_f = melt density

K_c = solid / melt bulk distribution co-efficient.

Clearly W_e/ W must be less than unity since a trace element cannot be transported faster than the melt. A simple model is outlined here to illustrate the magnitude of this effect during crustal anatexis. Assuming that a small volume granitic melts is extracted from a quartzo-feldspathic source with the mineralogy 30% quartz, 35% albite and 35% K-feldspar, calculated bulk distribution coefficients for Rb, Sr, Ba, Eu and U are as follows

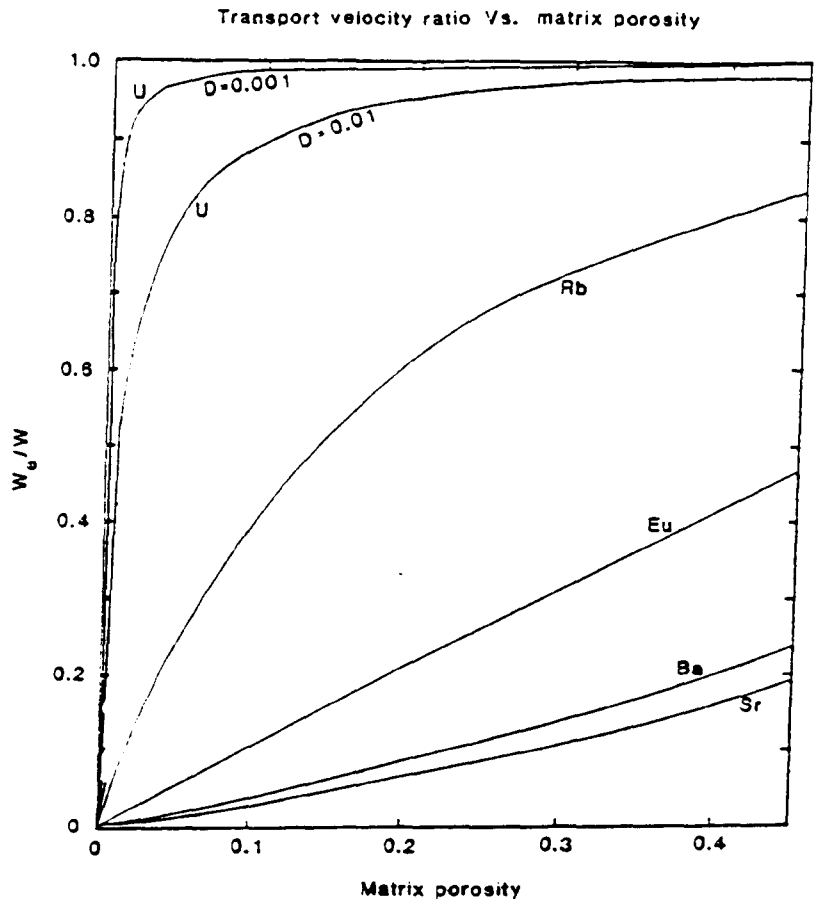

Fig. 6.4 Transport velocity ratio (W_e/W) for several trace elements as a function of matrix porosity. Curves are shown as dashed lines for matrix porosity values greater than 0.2 since the matrix may disaggregate at high porosity values (Mc Kenzie, 1984). These curves assume the melt is extracted from a quartzofeldspathic matrix as described in the text. K_d values are after Arth and Hanson (1975).

Trace element	Rb	Sr	Ba	Eu	U
Bulk D value	0.136	2.89	2.25	0.78	0.001 and 0.01

Kd values used from the compilation of Arth and Hanson (1975). Rb, Sr, Ba and Eu have been chosen since these elements are largely controlled by the major rock-forming minerals of the source and are relatively unaffected by trace-element enriched minor phases. U is modelled to illustrate the behaviour of a very incompatible trace element. Since Kd values for U are not well known two calculations have been carried out assuming bulk D values of 0.01 and 0.001.

Fig. 6.4 shows ratios of effective transport velocities as a function of matrix porosity. Assuming a matrix porosity of 3% (as used by Mc Kenzie, 1984 in similar calculations) U is transported out of the matrix about 3 times faster than Rb (assuming $D_U = 0.01$). Similarily Rb is transported about 1.7 times faster than Sr.

It is emphasised that these trace element fractionations result from relative movement between the melt and matrix. The matrix effectively acts as a separation column for the migrating melt. Therefore, trace element fractionation occurs within the melt fraction. These effects are superimposed on and accentuate trace element fractionations produced during melting. This "separation column" effect has several important consequences for trace element behaviour - for example

1. Incompatible trace-elements (e.g. U and Rb) may become highly enriched in the melt relative to trace elements which are transported more slowly out of the matrix

2. For small volume partial melts the combined effect of partial melting and separation of the trace elements by the residual martix column can theoretically produce enrichments in excess of 1/D for extremely incompatible trace elements (e.g. U).

3. This effect may produce trace element enrichments for which a process of volatile phase enrichment was previously invoked e.g. U and Rb enrichment in some granitoids. It is demonstrated quantitatively in a model below that this effect may enrich Rb relative to the high field strength (HFS) elements.

Figs. 6.5 and 6.6 demonstrate how Rb is preferentially transported relative to Nb or Y in a simple matrix / melt model based on that of Mc Kenzie (1984). The model shows how Rb / HFS element ratios may be increased without addition of Rb via a fluid phase as invoked by Pearce *et al.* (1984) to explain the high Rb/ HFS ratios of volcanic-arc granites. Although the magnitude of the enrichments documented here are model dependent, the trace element fractionations produced depend primarily on melt / matrix bulk distribution coefficients and so for a given source are independent of model parameters. In effect, the process accentuates trace element fractionations produced during the melting process.

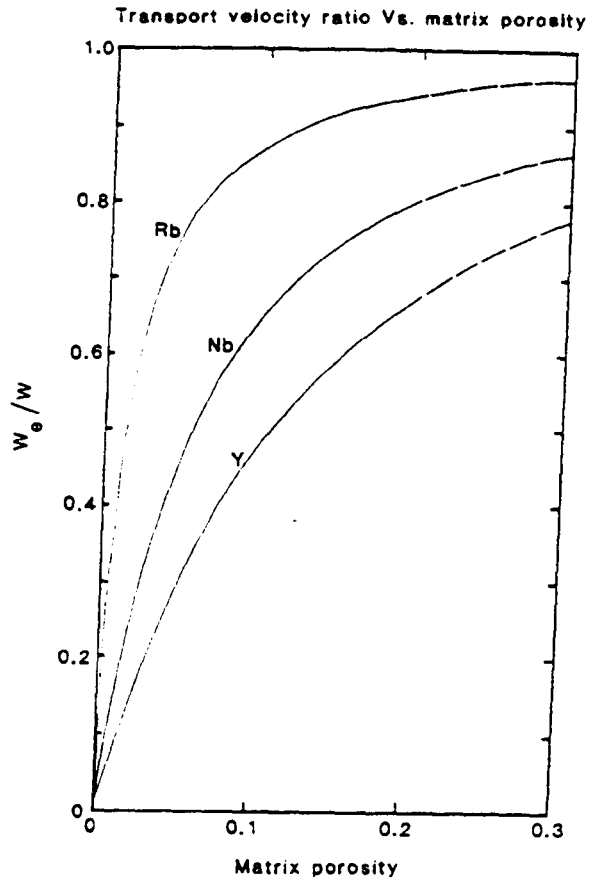

Fig. 6.5 Transport velocity ratios for Rb, Nb and Y as a function of matrix porosity assuming a matrix of olivine, orthopyroxene and clinopyroxene after Pearce *et al.* (1984). Kd values are from Pearce and Norry (1979) and Arth and Hanson (1975).

Fig. 6.5 is a plot of matrix porosity against element / melt velocity ratios for Rb, Nb and Y. The residual mineralogy used here is the same as that used by Pearce *et al.* (1984) to model petrogenetic paths for volcanic-arc granites, i.e. 67% olivine, 10% clinopyroxene and 23% orthopyroxene. Using this source mineralogy and the Kd values of Pearce and Norry (1979) and Arth and Hanson (1975) the following bulk distribution co-efficients were calculated.

Trace element	Rb	Nb	Y
Bulk D	0.013	0.05	0.103

These bulk D values are used in equation 6.5 to calculate effective transport velocities for Rb, Nb and Y. Rb is transported faster than the HFS elements reflecting it's lower melt / matrix bulk distribution co-efficient. The effects of preferential transport of Rb within the melt may be demonstrated by a simplified model based on that of Mc Kenzie (1984). It is assumed that trace elements are inhomogeneously distributed within the melt fraction before it begins to migrate relative to the matrix. The cause of local heterogeneties is irrelevant to the model but they may be due to small variations in the degree of partial melting in different parts of the system, or simply due to source heterogeneties. It is also assumed that the concentrations of trace elements decrease smoothly away from regions of local enrichment.

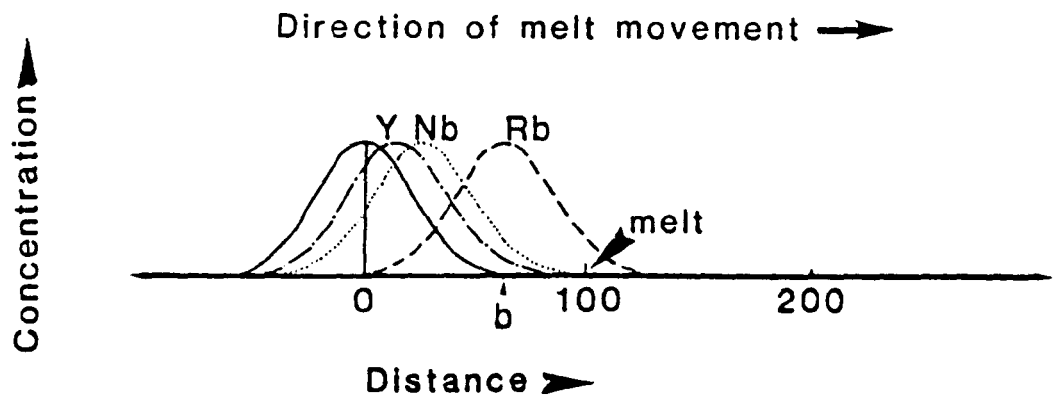

Fig. 6.6 Heterogeneties in trace element concentrations are assumed to have a normal distribution about the point of maximum concentration. Before the melt begins to migrate it is assumed that all three trace elements Rb, Nb and Y have equal concentrations with peaks centered on point 0 as shown by the solid-line profile. When the melt begins to migrate relative to the matrix (melt moves from left to right) the concentration profiles move to the right at different rates.

For simplicity, the approach of Mc Kenzie (1984) is adopted and it is assumed that trace element concentrations decrease uniformly away from regions of highest concentration to give a normal distribution about the maximum value, Fig. 6.6. For convenience, and so that the fractionations are easily visualised it is assumed that initially the peak concentrations of the Rb, Nb and Y are centred on point 0 in Fig. 6.6, and that the three trace elements are present in equal abundances before melt migration begins. In this model, melt moves from left to right so that the concentration profiles migrate in this direction at different velocities. If a constant matrix

porosity of 3% is assumed the trace elements move with relative velocities (relative to the melt velocity) of 0.69, 0.33 and 0.2 for Rb, Nb and Y respectively, i.e. Rb moves out of the matrix 3.45 times faster than Y and more than twice as fast as Nb. If the concentration profiles have widths at their bases of 100 length units (e.g. metres, mm etc.) then the Rb peak will have moved to a point 70 length units to the right of the original position (point b on Fig 6.6) when the melt has moved by 100 units. However the Nb and Y peaks "lag behind" Rb and have concentrations of 0.37 and 0.07 of their original concentrations respectively at point b, Fig. 6.6. Thus a rock sampled at point b would have a Rb/Nb ratio = 2.7 and a Rb/Y ratio ~ = 14 even if all three elements were present in equal abundances at point 0 (i.e. Rb/Nb = Rb/Y =1).

It is suggested that these effects are only applicable to granite petrogenesis in situations where the melt fraction is efficiently expelled from the residual matrix, since the effect depends on relative movement between the melt and matrix. The alaskite dykes of the Central Zone are examples of small melt fractions which were extracted from their source matrices, albeit over relatively small distances. This "separation column" effect may have produced local U enrichments in alaskites and accentuated U enrichments in the alaskite magma produced during relatively small volume (~ 15%) partial melting. As discussed below, relatively large volume crustal melts (~50%) do not efficiently separate from their residual matrices so that this "separation column" effect may be less effective in producing trace element fractionations.

It is interesting to note that the magnitude of these enrichments are sufficient to produce the Rb enrichments observed in syn-tectonic granites. Pearce *et al.* (1984) invoked Rb enrichment via a Rb-rich, (Nb + Y)-poor fluid phase to model Rb rich syn-tectonic granites. The magnitude of trace element fractionations produced by this process depends primarily on the length scale of melt migration relative to the length scale of initial heterogeneities. In the simple model outlined above for example, the distance of melt migration (100 units) is assumed to equal the peak width of the trace element concentration profiles (i.e. also 100 length units). More complex models which take account of dispersion (flattening of the concentration profile as it moves), concentration profiles in three dimensions, continuous variation in melt viscosity, matrix porosity and melt / matrix density contrasts are required to quantitatively model this

"separation column" effect for syn-tectonic granites. However, these simplistic preliminary calculations suggest that the magnitude of this effect is sufficient to produce the high Rb / HFS element ratios required by Pearce *et at.* (1984) to model Rb rich syn-tectonic granites.

6.4.3 Large volume crustal melts

The rheological behaviour of relatively large volume crustal melts (> ~30% melt) is significantly different to that of small volume partial melts. Large volume melts will be accompanied by matrix disaggregation (Mc Kenzie, 1984) and a suspension - like rheological behaviour (Arzi, 1978 ; Van der Molen and Patterson, 1979). The critical melt fraction at which this transition from melt/matrix behaviour to suspension like behaviour occurs is termed the rheological critical melt percentage by Arzi (*op. cit.*) and is in the range 25-40 volume % melt (Fig. 6.1). For melt fractions above this critical value the yield strength of the partially molten suspension is reduced by several orders of magnitude. If, at lowered yield strengths the Rayleigh number of the system increases sufficiently thermal convection may homogenise the partially molten system and disperse the matrix throughout the system (e.g. Wickham, 1984). It is interesting to note that thermal convection will occur irrespective of the Rayleigh number of the system if a horizontal temperature gradient is present across the partially molten system (Mc Kenzie, 1984). In the case of the large Donkerhuk granite batholith for example, it seems likely that a significant horizontal thermal gradient was present since there were longlived temperature differences in the areas to the north and south of this intrusion (Haack,1983). This process is perhaps easiest to visualize where migmatites have been produced by relatively large melt fractions (~ 50%). If the yield strength of the migmatitic system is lowered sufficiently thermal convection may homogenise the originally separate melt/matrix layers to produce a restite bearing granitic suspension (Wickham, 1984).

6.5 Summary of granite petrogenetic studies

6.5.1 Crustal-melt granitoids

In summary, rheological properties of crustal-melt granitoids distinguish two melt regimes characterised by contrasting melt yield strengths. The two melt regimes are also distinguished using trace element ratios (Fig. 6.7). Alaskites have high Rb/Zr ratios reflecting efficient melt separation from residual minor phases (e.g. zircon) during small volume partial melting i.e. Zr is preferentially retained in the source. In contrast, leucogranites are relatively large volume partial melts in which the melt fraction does not efficiently separate from trace element enriched residual phases so that the magma inherits the Rb/Zr ratio of their sources (Fig. 6.7).

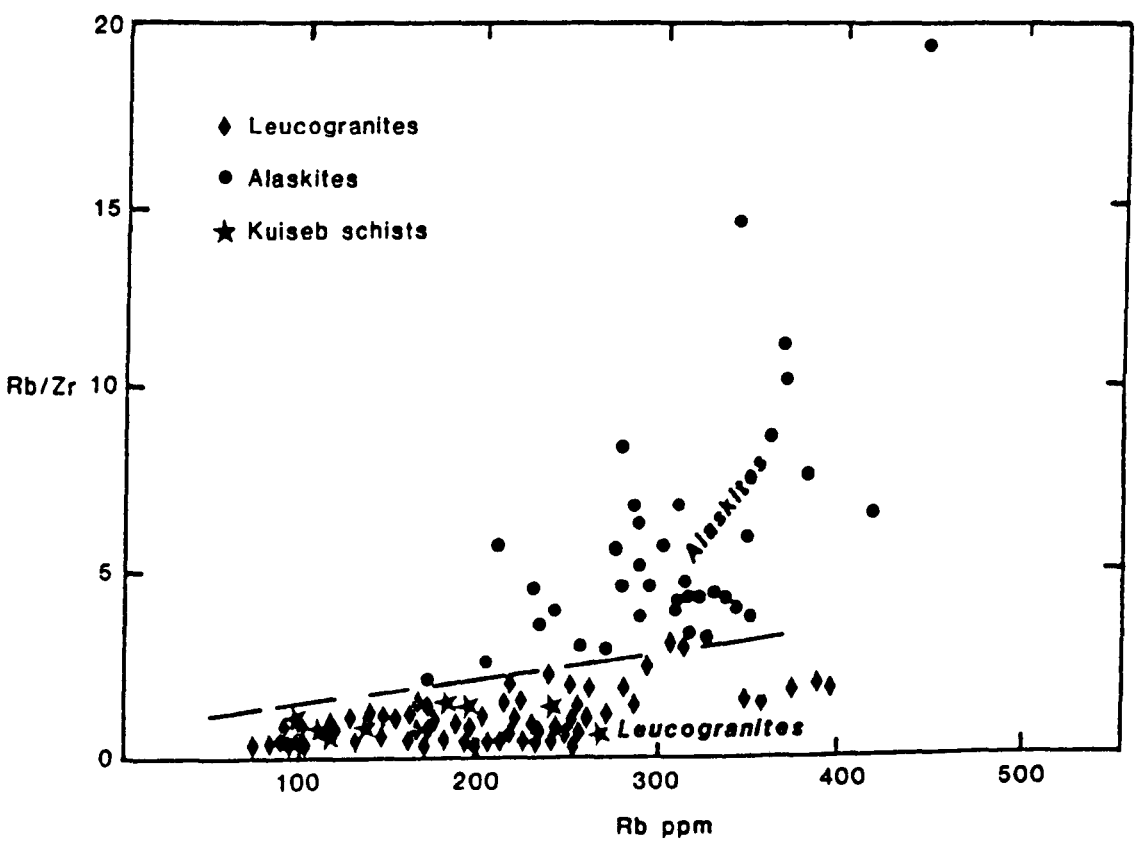

Fig. 6.7 Rb/Zr vs. Rb for Damara leucogranites and alaskites. Alaskites have relatively high Rb/Zr ratios due to low Zr abundances and relatively high Rb contents. Leucogranites are large volume partial melts which inherit the Rb/Zr ratios of their sources so that Rb/Zr ratios of leucogranites are similar to those of Damara metasediments. In contrast, alaskites are small volume melts in which Rb behaves as an incompatible trace element but Zr is preferentially retained in residual minor phases in the source e.g. residual zircon.

Most upper-crustal melt granitoids represent relatively large melt fractions (>~40% melt, Ch. 4) i.e. above the rheological critical melt percentage of Arzi (1978). In contrast, alaskites are generated by relatively small degrees of upper-crustal melting (Ch. 4). However such small volume high viscosity upper-crustal melts may be expelled only if their residual matrices are deformed during regional deformation events, perhaps accounting for the syn-D_3 age of Damara alaskites.

Dehydration melting is the most plausible mechanism by which large volumes of peraluminous granitoids may be generated. Dehydration melting proceeds without the appearance of a H_2O fluid (or vapour) phase. Melts produced by metapelite dehydration melting are peraluminous (Thompson and Algor, 1977 ; Thompson and Tracy, 1977 ; Thompson, 1982).

Low HFS element abundances in upper-crustal melt granitoids are a reflection of HFS element retention by HFS enriched residual minor phases during crustal anatexis.

High Rb/Sr ratios in crustal melt granitoids are due to the relatively incompatible behaviour of Rb during upper-crustal anatexis (Ch. 4) and increases in Rb/Sr ratios are due to Sr removal by feldspar fractional crystallisation, while Rb behaves incompatibly during fractional crystallisation of most upper-crustal granitoids (Ch. 4). In Namibia, upper-crustal melt granitoids typically have old model Nd ages (T^{Nd}_{DM} = ~ 1.5-2.5Ga) and have high $T^{Nd}_{DM} / T^{Sr}_{BE}$ ratios (Ch. 5) reflecting significant intracrustal reworking of their precursors. Intracrustal reworking of upper-crustal melt granitoid precursors may have been a combination of magmatic remobilisation during previous orogenic events and/or sedimentary reworking.

6.5.2 Calc-alkaline diorites

Calc-alkaline diorites i.e. diorites from Palmental, Otjosondjou and the Huab-River intrusions are characterised by metaluminous major element geochemistry, relatively low initial $^{87}Sr/^{86}Sr$ ratios and low HFS element abundances. As discussed above, incompatible trace elements (e.g. Rb) may be preferentially transported out of a residual matrix relative to the HFS

elements. Trace element fractionations produced during partial melting are accentuated by this "separation column" effect so that the combined effects may be sufficient to produce the high Rb/HFS ratios observed in calc-alkaline diorites without invoking a Rb-enriched fluids. However further constraints on the relative length scales of initial melt heterogeneities in three dimensions and the distances over which melts move from their residues are required before the magnitude of this effect can be quantified.

Trace element modelling (Ch. 4) shows that fractional crystallisation in Damara calc-alkaline diorites is dominated by hornblende fractional crystallisation while plagioclase plays a subordinate role. In contrast to within-plate granitoids in which trace element enriched minor phases control the REE's (Chs. 3 and 4), REE distribution in calc-alkaline granitoids is controlled by hornblende.

6.5.3 Within-plate granitoids

Within plate granitoids are characterised by low Ca contents, high HFS element abundances and variable $^{87}Sr/^{86}Sr$ ratios. Damara within-plate granitoids typically have T^{Nd}_{DM} model ages of about 1.1 to 1.3 Ga, strongly suggesting a widespread HFS enriched magmatic event at this time. Within-plate granitoids intruded during the Damara orogeny represent remobilised HFS enriched rocks which were first derived from the mantle in the period 1.0-1.3 Ga. Within-plate granitoids retain a HFS element enriched trace-element signature because their precursors have not been involved in significant intracrustal magmatic remobilisation which reduces HFS element abundances. Furthermore, relatively low $T^{Nd}_{DM} / T^{Sr}_{BE}$ ratios and low $\delta^{18}O$ values of within-plate granitoids (Ch. 5) preclude any significant intracrustal reworking of within-plate granitoid precursors. Within-plate granitoids display the highest $^{207}Pb/^{204}Pb$ and $^{208}Pb/^{204}Pb$ ratios observed in Damara granitoids reflecting time integrated enrichments in U and Th relative to Pb.

6.6 Summary of crustal evolution studies

Results and interpretations of a combined Sr and Nd isotopic study (Ch. 5) on Damara metasediments are summarised here. The principal conclusions are ;

1. $^{87}Sr/^{86}Sr$ and $^{143}Nd/^{144}Nd$ ratios show progressive increases and decreases respectively, with depth in the Damara metasedimentary pile.

2 . Model Nd ages for the oldest Damara metasediments (Nosib Group) are in the range 2.0-2.3 Ga, whereas the younger Kuiseb schists and Nama Group molasse sediments have T^{Nd}_{DM} ages in the range 1.0 -1.3 Ga. This is interpreted as reflecting a change in sediment provenance - the younger sediments were derived from younger source terrains.

3. The ratio $T^{Nd}_{DM} / T^{Sr}_{BE}$ which reflects intracrustal reworking (Ch. 5) of Rb/Sr relative to Sm/Nd, increases with depth in the Damara metasedimentary pile suggesting that the oldest sediments reflect source terrains which had undergone the largest amounts of intracrustal reworking. Intracrustal reworking processes which increase model age ratios may be a combination of magmatic remobilisation and sedimentary reworking.

4. The rate of increase of the ratio $T^{Nd}_{DM} / T^{SR}_{BE}$ with time, inferred from the stratigraphically oldest sediments (Nosib Group) is lower for than that inferred from younger sediments. This implies that the rate of intracrustal reworking reflected by sediments increased with time from about 2.0 Ga to about 1.0 Ga ago in this crustal segment.

6.7 Geotectonic evolution of the Damara orogen

6.7.1 Post-orogenic uplift and cooling

Variations in mineral cooling ages recorded in different parts of the orogen may be used to reconstruct the pattern of post-orogenic uplift, and may place constraints on the geotectonic evolution of the region. Several studies have documented variations in mineral cooling ages across the orogen e.g. Haack, 1978 ; Hawkesworth *et al.*, 1983 ; Haack, 1983.

Although the concept of a blocking temperature is an oversimplification it is assumed that minerals begin to record time over narrow discrete temperature intervals so that a mineral ages are a measure of the time elapsed since the mineral last cooled through their respective "blocking temperatures". For the purposes of this discussion the following blocking temperatures are adopted, after Haack (1983).

$^{40}Ar/^{39}Ar$ in hornblende - 500-550 °C

Rb/Sr in biotite - 300-350 °C

Rb/Sr in muscovite - 350 °C

K/Ar in biotite - 300 °C

Garnet fission track - 270 °C

Apatite fission track - 80 °C

The terms "Central Zone" and "Southern Zone" are used to refer to the areas north and south of the Okahandja lineament (OKL) respectively. The term "west Central Zone" refers to the high temperature area around Swakopmund where metasediment anatexis occurred during regional metamorphism (Fig. 6.8).

A K/Ar biotite study by Haack and Hoffer (1976) revealed an area of relatively young (~ 430 Ma) cooling ages in the west Central Zone whereas biotite ages from elsewhere in the orogen yield ages of about 485 Ma. Hawkesworth *et al.* (1983) confirmed that the west Central Zone preserves Rb/Sr biotite ages which are significantly younger than ages recorded in the remainder of the orogen and concluded that prograde metamorphism in the west Central Zone continued for some 40-50 Ma after the margins of the orogen had cooled below about 300 °C. Using ages obtained for hornblende, muscovite and biotite separates from single samples, a cooling rate of about 10 °C/Ma was deduced from two Salem-type granite samples from the Northern Zone and the northern part of the Central Zone (Hawkesworth *et at.,op. cit.*). This cooling rate is identical to that inferred from Central Zone granitoids by Haack (1983).

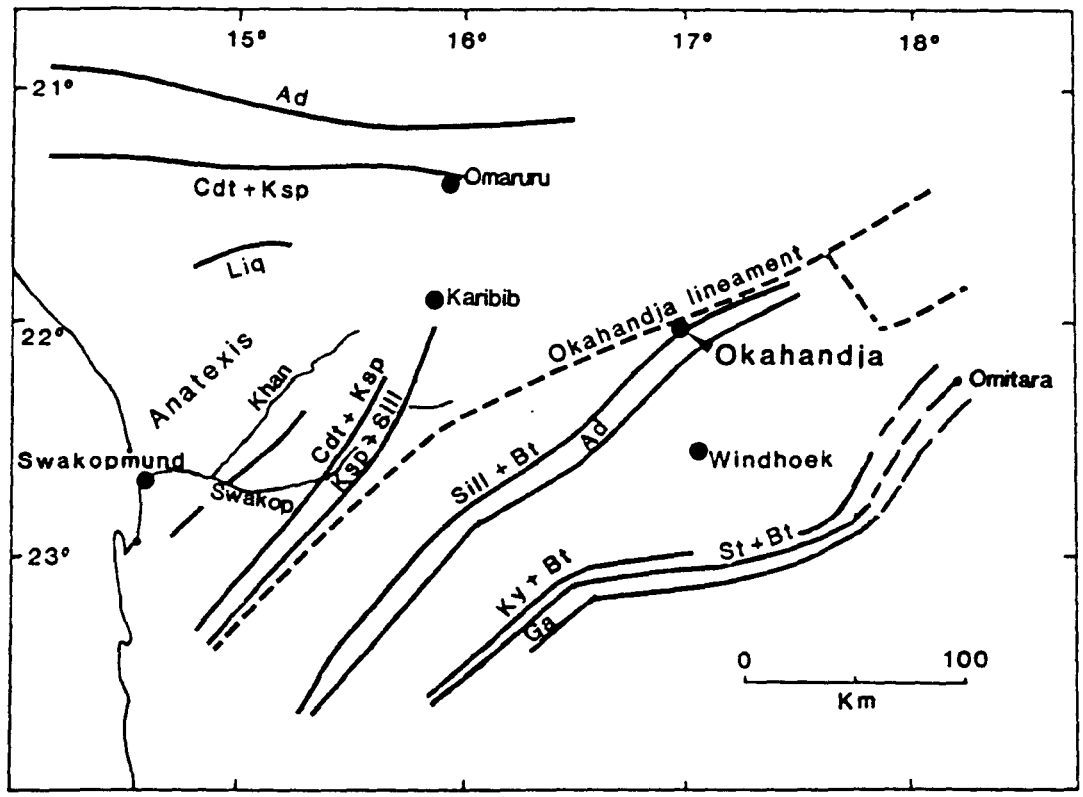

Mineral abbreviations

Ky - Kyanite	St - Staurolite
Ad - Andalusite	Ksp - K-feldspar
Sill - Sillimanite	Ga - Garnet
Cdt - Cordierite	Bt - Biotite
Liq - Liquid	

Fig. 6.8 Map of the Damara orogen showing the main reaction isograds in metapelites, (after Kasch, 1983). In Figs. 6.9 and 6.10 profiles of mineral ages are shown projected on to section lines from Swakopmund to Okahandja. In Fig. 6.9b the north - south line is drawn at 15°E.

Fig 6.9 a and 6.9b are profiles across the orogen showing variations in biotite cooling ages in north-south and east-west directions across the orogen (see Fig. 6.9 for lines of section). Fig. 6.9 shows that the area around Swakopmund (i.e. the West Central Zone) is surrounded to the north, south and east by areas which yield older mica ages.

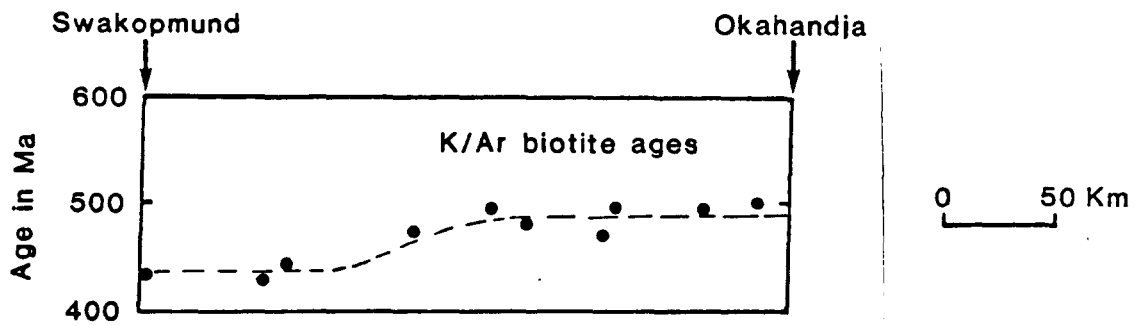

Fig. 6.9a Profile of K/Ar biotite ages along an approximately E-W traverse between Swakopmund and Okahandja, (after Haack, 1983). This profile shows that biotite ages in the west Central Zone are 50-60 Ma younger than those further east in the Central Zone. All data points are from north of the Okahandja lineament, (see Fig. 6.8 for profile line).

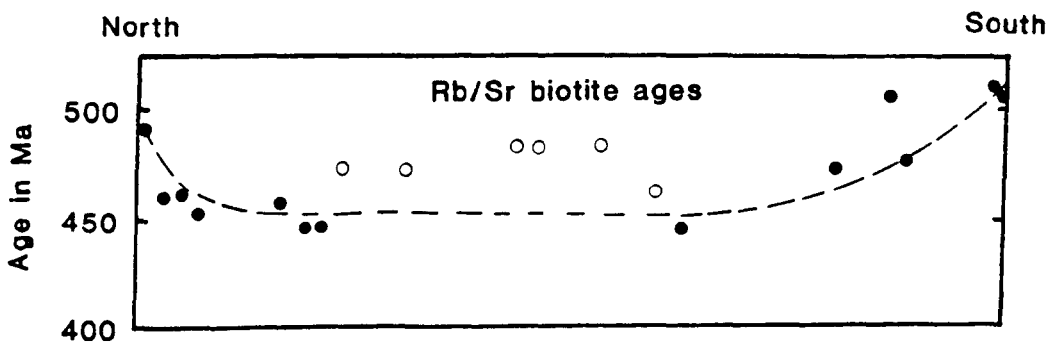

Fig. 6.9b Profile of Rb/Sr biotite ages projected onto a north-south line (15°E, Fig. 6.8) after Hawkesworth *et al.* 1983. Open circles are data projected from the east reflecting the older biotite ages shown in Fig. 6.9a. The age "trough" is due to the young ages of the west Central Zone as shown in Fig. 6.9a.

In Fig. 6.10 garnet and apatite fission track ages projected on to an approximately east-west traverse between Swakopmund and Okahandja show long-lived slow cooling rates in the western Central Zone.

The importance of the Okahandja lineament as a "hinge" along which substantial uplift of the Southern Zone relative to the Central Zone occurred soon after the peak of

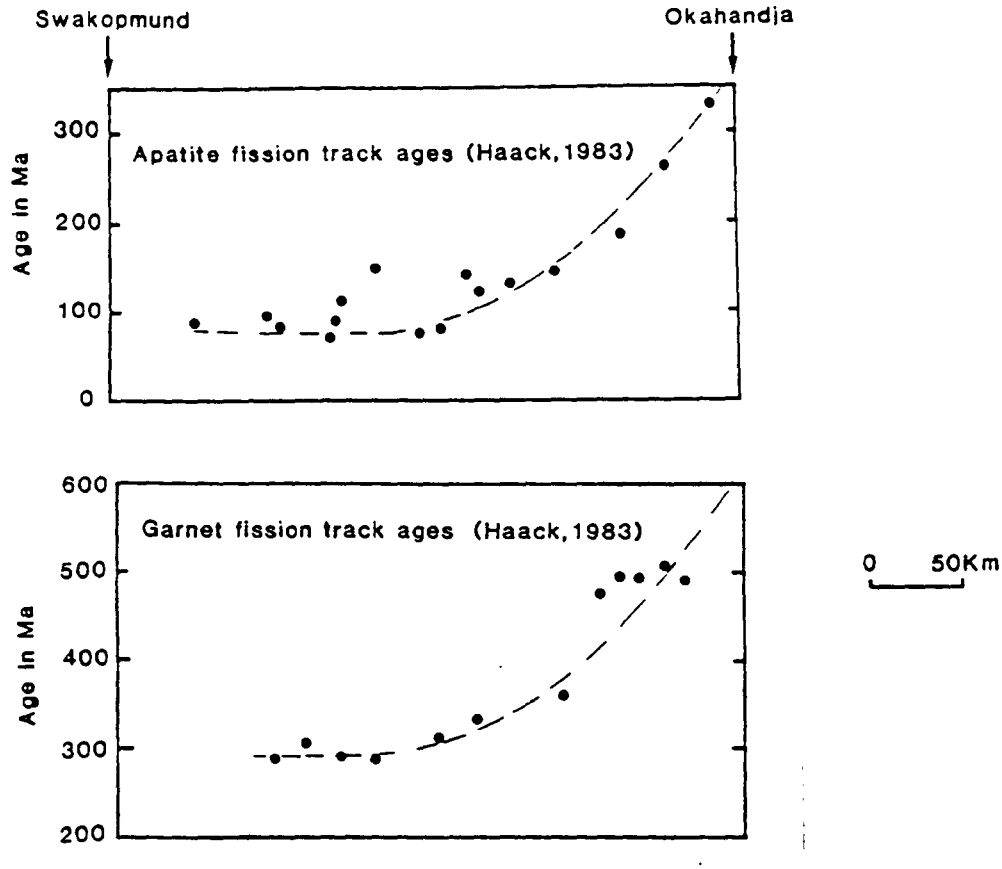

Fig. 6.10 Fission track age profiles (data from Haack, 1983) along an approximately E-W traverse between Swakopmund and Okahandja. Fission track age profiles for garnet and apatite demonstrate long lived differences in cooling rates between the west Central Zone and the remainder of the Central Zone. All data points are from north of the Okahandja lineament.

regional metamorphism is emphasised by Haack (1983). Samples to the south of the lineament yield relatively old garnet fission track ages which are virtually indistinguishable from K/Ar biotite ages from the same area. These data indicate that the Southern Zone had cooled rapidly to below 270 °C before about 480 Ma ago. Similarily, apatite fission tracks which reflect the time elapsed since cooling below about 80 °C yield ages in excess of 300 Ma south of the lineament whereas those from north of the lineament yield ages of about 120 Ma.

Cooling curves for the Central and Southern Zones (after Haack, 1983) are shown in Fig. 6.11. In the absence of cooling ages for hornblende in the Southern and Central Zones uniform cooling rates from peak metamorphic temperatures to about 300 °C (biotite cooling temperature) are assumed.

The Central Zone is characterised by relatively slow cooling rates and in the period 460-340 Ma cooling almost ceased resulting in a cooling curve plateau in the temperature interval 300-270°C, (Fig. 6.11). In contrast, south of the lineament cooling

proceeded steadily and no cooling curve plateau is observed. The west Central Zone cooled at the slowest rate and records the youngest cooling ages at every mineral "blocking temperature" (Figs. 6.9 and 6.10). In summary, three distinct cooling "regimes" may be distinguished in the Damara orogen

1. South of the Okahandja lineament where high pressure, relatively low temperature conditions are recorded (up to 580°C at 8-10Kb), uplift occurred rapidly after the peak of metamorphism so that all mineral ages are relatively old e.g. garnet and biotite ages are concordant, (Haack, 1983)

2. In contrast, north of the Okahandha lineament cooling proceeded relatively slowly, especially in the time interval 450-350 Ma (Fig. 6.11). In this 100 Ma time interval temperatures appear to have decreased by about 30°C only (from 300 to 270°C).

3. In the west Central Zone where youngest mineral ages are recorded, cooling rates were slowest (Figs. 6.9 and 6.10). In this area, prograde metamorphism continued for 40-50 Ma after the margins of the orogen had cooled below 300°C (Hawkesworth *et al.*, 1983).

Rapid cooling rates, deduced from concordant mineral ages can be used to infer rapid uplift (e.g. in the area south of the Okahandja lineament). In contrast however, slow cooling rates are not necessarily due to slow uplift rates since cooling rates depend on the balance between uplift rates and radiogenic heat production (England and Thompson, 1984). In the west Central Zone many Damara granites have elevated heat production in the range 10-20 HGU (Haack, 1983) (1 HGU = 0.418×10^{-3} mWm^{-3}) whereas average granites have about 4-6 HGU (Turekian and Wedepohl, 1961). This enhanced heat production may account for the slow cooling of the west Central Zone inferred from mineral age data. Mass transfer of heat producing elements by magmas and hydrothermal fluids and their subsequent concentration in the upper crust may have been a critical process in maintaining high temperatures over a relatively long period at relatively shallow crustal levels in the west Central Zone (Hartmann *et al.*, 1983).

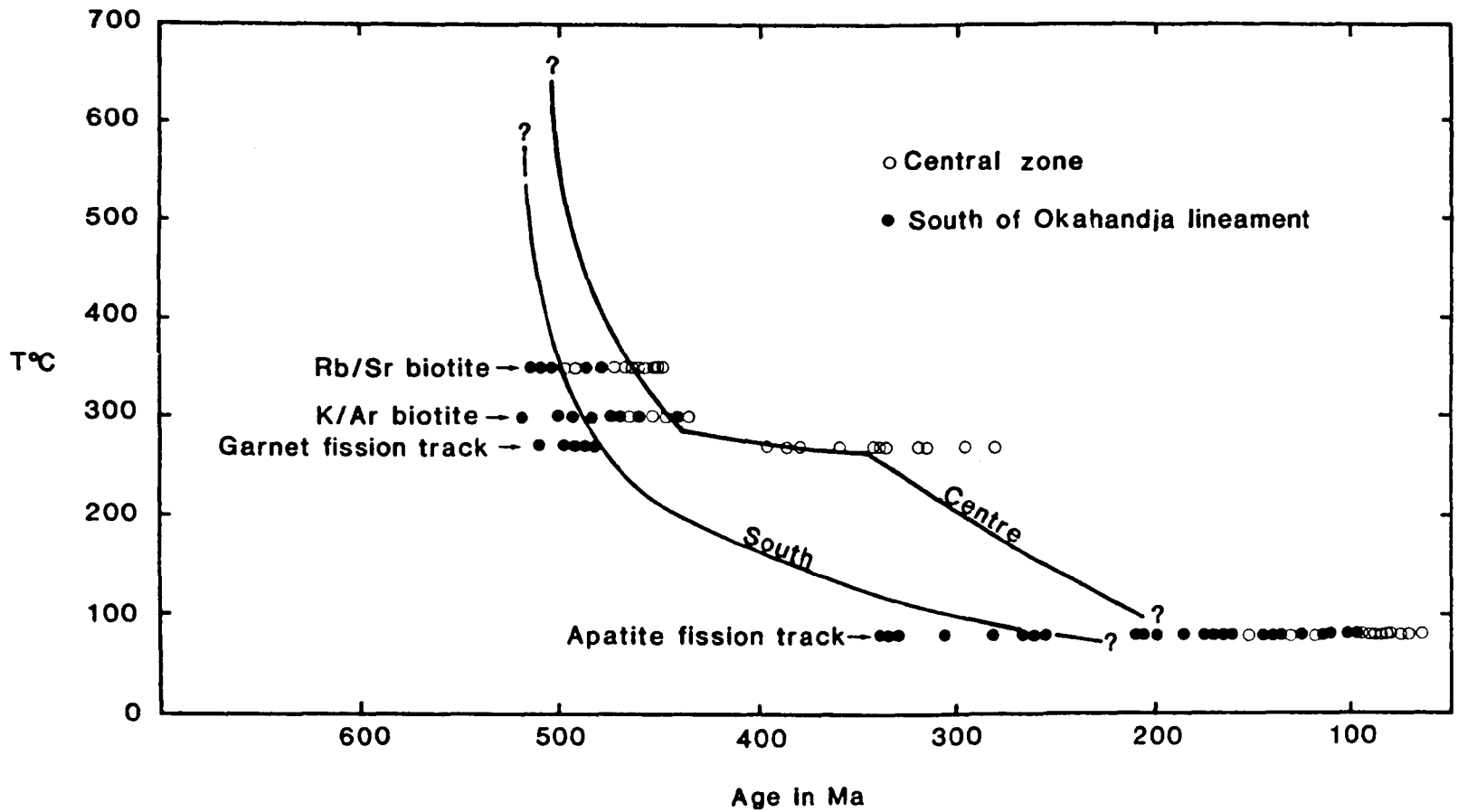

Fig. 6.11 Cooling curves for the Central Zone and the area south of the Okahandja lineament. Peak temperatures of about 670 °C and 580 °C occurred in the Central Zone and southern areas respectively. The open circles which extend to the youngest ages are for the west Central Zone.

6.7.2 A model for Damara belt evolution

A simplified model for the evolution of the orogen is proposed. This model accounts for the following key observations

1. The development of high pressure, relatively low temperature mineral assemblages in the area south of the Okahandja lineament

2. High-temperature, low-pressure metamorphism in the Central Zone which continued for 40-50 Ma after the margins of the orogen had cooled (Hawkesworth *et al.*, 1983)

3. Crustal melting occurred at shallower crustal levels with time (Hawkesworth *et al.*,1983)

4. The apparent absence of subduction related magmatism.

5. The structural and metamorphic asymmetry across the orogen.

In this model,high-pressure, relatively low-temperature metamorphism occurred in the area south of the Okahandja lineament due to crustal thickening during D_2 deformation. This area was uplifted by isostatic rebound within about 50 Ma after burial, and so yields old and concordant mineral ages. Uplift of the southern area relative to the rest of the orogen occurred along the Okahandja lineament. Schematic P-T-t paths for various segments of the orogen are shown in Fig. 6.12.

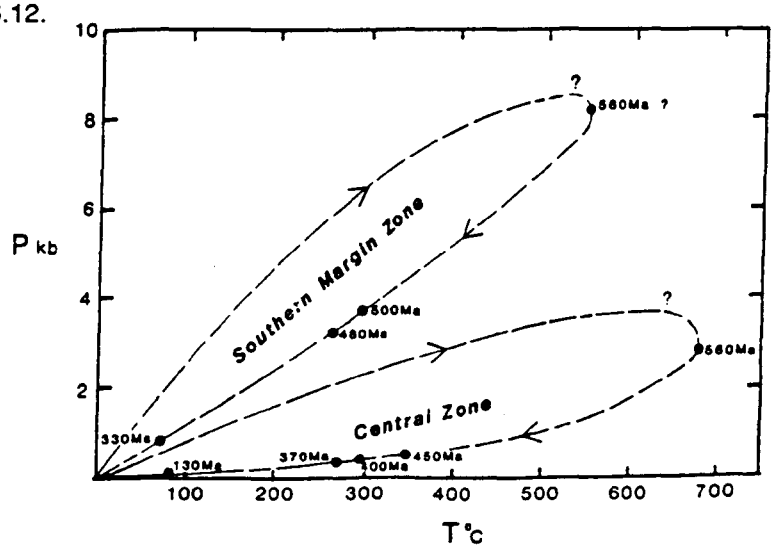

Fig 6.12 Schematic P-T-t paths for the Central Zone and the Southern Margin Zone of the Damara orogen deduced from P/T estimates (Kasch, 1983 ; Hartmann *et al.*, 1983) and mineral ages (Haack, 1983 ; Hawkesworth *et al.*, 1983). For simplicity, it is assumed that the peak of metamorphism occurred at about 560 Ma in both the Southern Margin Zone and the Central Zone. The Central Zone cooled at a slower rate than the Southern Margin Zone.

The area south of the Okahandja lineament was uplifted rapidly before thermal relaxation could occur so that metamorphic temperatures remained relatively low.

In contrast, high-temperature low-pressure metamorphism in the Central Zone was primarily due to advective heat transfer by magmas derived from deeper structural levels during the early rifting stage (e.g. Lux *et al.*, 1986). Heat producing elements may have been concentrated in the upper crust by magmas derived from lower crustal levels. U and Th may have been redistributed within the crust by zone-refining and/or upward transport by hydrous fluids released by dehydration reactions during prograde metamorphism.

In common with several previously published models two stages of evolution are distinguished - an early rifting stage followed by a phase of convergence and compression. Since there is no convincing evidence for subduction an ensialic orogenic evolution is proposed. The early rifting stage is critical to the model for the following reasons ;

1. To account for early geosynclinal development and sedimentation

2. To initiate a thermal perturbation at the base of the crust in the Central Zone

It is proposed that rifting was asymmetric so that attenuation of the lithosphere occurred by the "simple shear" model of Wernickie (1984). This contrasts with the symmetric "pure-shear" rifting models invoked by previous models for the orogen e.g. Martin and Porada, 1977 ; Martin, 1983. Asymmetric rifting is invoked to for the following reasons ;

1. It provides a mechanism whereby the regions of thinnest lithosphere and crust do not coincide. If symmetric rifting was invoked the regions of thinnest crust and lithosphere would be coincident so that high-temperature/low-pressure metamorphism (Wickham and Oxburgh, 1985) would occur early in the evolution of the orogen, whereas in the Damara orogen the observed high-T/low-P metamorphism is a relatively late-stage feature

2. It produces structural asymmetry across the belt. Reactivation of low-angle extensional features during compression can produce the observed structural asymmetry e.g. south-easterly directed thrusting.

It should be noted that the model differs substantially from recently published rift models for high-temperature/low-pressure metamorphic belts (Vielzeuf and Kornprobst, 1984 ;

Wickham and Oxburgh, 1985). In this model rifting is not invoked as the cause of high-temperature/low-pressure metamorphism insofar as high-T/low-P metmorphism does not occur in a region of thinned crust. Heat advection by magmas derived from the lower crust (e.g. the early Salem-type granite suite) are the primary heat source for high-T, low-P metamorphism in the west Central Zone. Enhanced radiogenic heat production in the upper-crust maintained relatively high temperatures in the west Central Zone and resulted in young mica ages.

The early rifting stage had the important effect of causing lower crustal melting below the Central Zone. These melts ascend in the crust resulting in advective heat transfer to higher crustal levels and a redistribution of heat producing elements. Therefore, the early asymmetric rifting stage sets up the conditions for later high-T/low-P metamorphism in the Central Zone but unlike the symmetric rift model of Wickham and Oxburgh (1985) does not directly cause high-temperature metamorphism at shallow crustal levels.

The symmetric rift model of Wickham and Oxburgh (*op. cit.*) cannot be readily applied to the Damara orogen for the following reasons ;

1. Kyanite bearing high-pressure relatively low-temperature assemblages occur in the Southern Margin Zone of the orogen. These high-pressure assemblages (8-10 Kb) are indicative of substantial crustal thickening. This is difficult to reconcile with a model which requires crustal extension in the Central Zone.

2. In the Damara belt there is no evidence for syn-metamorphism sedimentation - i.e. metamorphism of the lower parts of the sedimentary pile while deposition continued at the surface.

3. Nappe-type folds and thrusts occur on a regional scale in the southern part of the orogen (e.g. Bickle *et al.*, 1975).

Details of the model are shown in Fig. 6.13. Orogenic activity commenced with an early stage of asymmetric rifting (Fig. 6.13a). As illustrated by Mc Kenzie (1978) crustal extension causes thinning of the lithosphere and passive upwelling of the asthenosphere. As discussed above, an important feature of asymmetric extension is that the region of thinnest lithosphere is considerably displaced from the the region of maximum crustal thinning

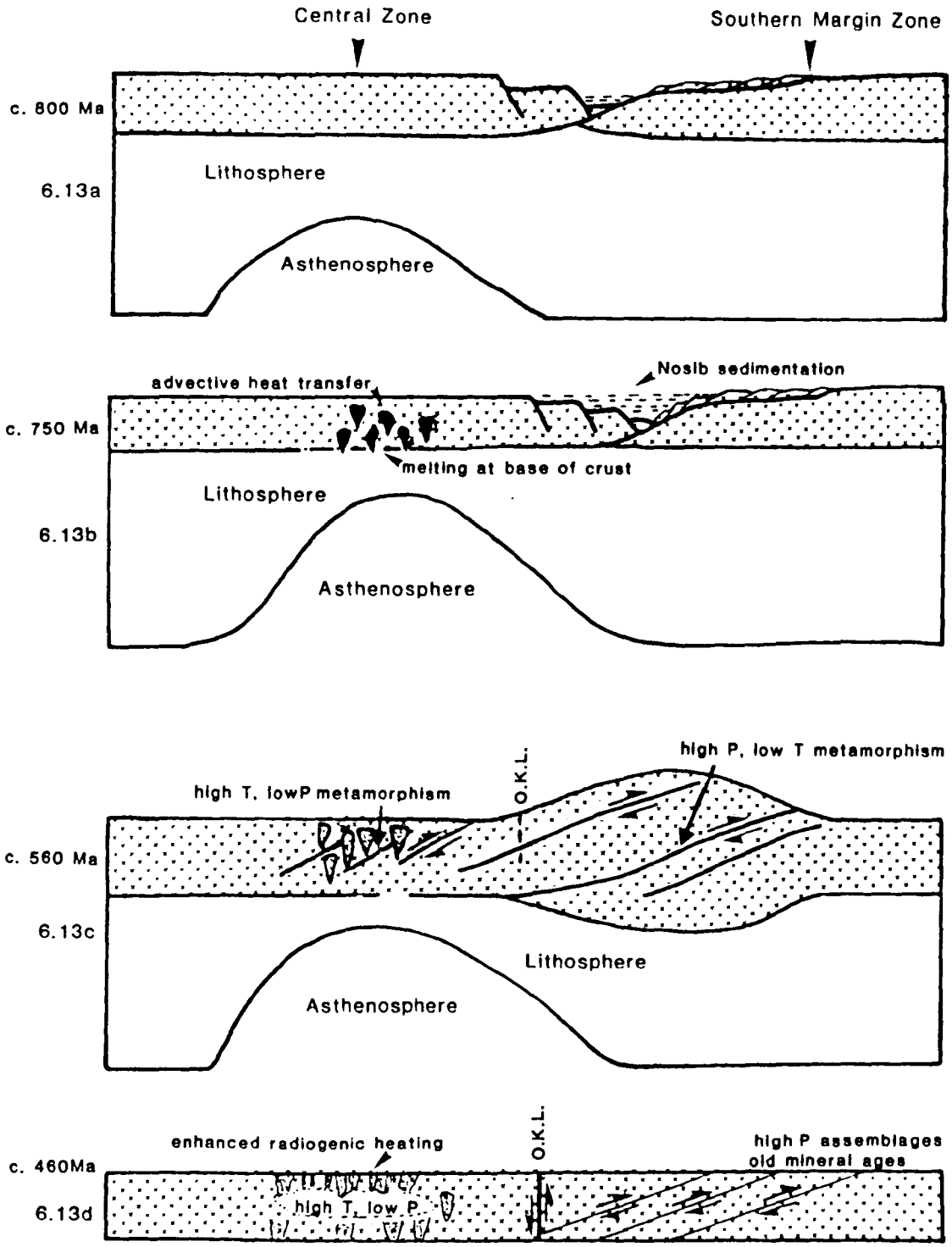

Fig. 6.13 An asymmetric rift model is invoked to produce a thermal perturbation at the base of the crust in the Central Zone. In this model, upwelling of asthenosphere resulted in melting at the base of the crust and the generation of early granitoids. These magmas advectively transported heat to higher levels in the crust. Rifting was followed by collision and southerly directed thrusting. This produced crustal thickening across the orogen but the largest amount of thickening occurred by thrusting in the Southern Margin Zone. However the Southern Margin Zone was uplifted rapidly along the Okahandja lineament relative to the Central Zone .

(Wernekie, 1984 ; Sandiford and Powell, 1986). In effect, the region in which the geotherm is most perturbed (where the lithosphere is thinnest) does not coincide with the region of thinnest crust In addition, magmas ascending in the crust redistribute heat-producing elements. This is shown schematically in Fig. 6.13a.

The replacement of lithosphere with hot asthenosphere as the lithosphere thins (Mc Kenzie, 1978) promotes melting of the lower crust and increases crustal conductive heat flow. These melts ascend in the crust and advectively transport heat to higher crustal levels (e.g. Soula, 1982). In addition, magmas ascending in the crust redistribute heat-producing elements. Lower crustal melting produces Damara diorites and early Salem-type granitoids. Advection of heat to shallower crustal levels and redistribution of heat-producing elements by ascending magmas causes perturbation of the crustal geotherm. This produces additional crustal melting and further advection of heat and transport of heat-producing elements to progressively shallower crustal levels with time.

The extension stage is followed by compression across the orogen (Fig. 4.13c). Detachment zones along which extension occurred are reactivated as thrust planes, thus accounting for the south-easterly directed thrusting in the Southern Margin Zone. The largest amount of crustal thickening occurs by thrusting in the Southern Margin Zone. Crustal thickening in the Southern Margin Zone produced low-temperature/high-pressure metamorphism. Isostatic rebound occurred soon after burial before thermal relaxation could occur so that high-P, low-T assemblages were produced. This is illustrated in the schematic P-T-t path (Fig. 6.12) for the Southern Margin Zone.

In the Central Zone, heat advected by magmas from deeper structural levels in the crust and the elevated heat generation of the Central Zone (Haack, 1983) produced high temperature metamorphism at relatively shallow (~ 10-12km) crustal levels. Enhanced radiogenic heat production maintained high-temperature/low-pressure metamorphism and this long-lived upper-crustal heat source explains the young mineral ages of the Central Zone.

6.8 Concluding remarks

Combined trace element and isotopic studies on Damara granitoids and metasediments have placed constraints on the evolution of the Damara crust. The following conclusions are worth emphasising

1. Little detectable crustal growth occurred during the Damara orogeny. Granitoids were derived by remobilisation of pre-existing continental crust. All intrusions have T_{Nd}^{DM} ages in excess of 1.0 Ga, indicating that no mantle derived granitoids were emplaced during Damara orogenesis.

2. Combined trace element and isotopic studies have identified three geochemically distinct granitoid types - crustal-melt granitoids, within-plate granitoids and calc-alkaline diorites.

Crustal-melt granitoids are peraluminous two-mica leucogranites and alaskites. These granitoids have high initial $^{87}Sr/^{86}Sr$ ratios (> 0.710) and have old model Nd ages (T_{Nd}^{DM} ages ~ 2.0 Ga). Crustal-melt granitoids are depleted in high field strength (HFS) elements and have high Rb/Sr ratios.

A model in which repeated intracrustal reworking of granitoid precursors fractionates Rb/Sr relative to Sm/Nd is proposed to explain observed hyperbolae on εSr vs. ε Nd diagrams. In this model the principal trace-element characteristics of crustal melt granitoids i.e. high Rb/Sr and low REE and HFS element abundances reflect a single process - intracrustal reworking of granitoid precursors. Some crustal-melt leucogranites and all alaskites are enriched in U.

Trace element modelling shows that alaskites are relatively small volume crustal melts (< 20%) whereas leucogranites are large volume (> 40 %) melts. Alaskites are generated when highly viscous small volume crustal melts are extracted from their sources. Extraction of high viscosity crustal melts can only be achieved if melt generation coincides with regional

deformation since matrix compaction mechanisms alone cannot expel high viscosity magmas from their sources. In contrast, large volume leucogranite crustal-melts have low yield strengths so that thermal convection may homogenise migmatitic rocks. Therefore large volume crustal melts may be emplaced *en masse* with their residual sources i.e. large volume melts are not expelled from their residual matrices.

Within-plate granitoids are characterised by high HFS and REE abundances. Damara within-plate granitoids typically have T^{Nd}_{DM} ages in the range 1.2-1.4 Ga, indicating a HFS enriched magmatic event in Namibia at that time. It is noted that HFS enriched granitoids in the Namaqua belt were intruded about 1.3 Ga ago (Harris *et al.*, in press). Combined Sr and Nd isotopic data indicate that within-plate granitoid precursors were not significantly reworked by intracrustal processes and so retain high HFS element and REE abundances. Inferred bulk distribution coefficients for a range of trace elements during fractional crystallisation are highest for the within-plate granitoids. Large bulk D values inferred for Ba and Sr suggest that fractionation of K-feldspar dominates within-plate granitoid crystallisation.

Damara calc-alkaline diorites are characterised by metaluminous major element geochemistry and low HFS abundances. Combined Sr and Nd isotopic data suggest that calc-alkaline diorite precursors were not involved in significant intracrustal reworking so that HFS element depletion is a source characteristic i.e. HFS element abundances were not reduced by intracrustal reworking.

3. Sr and Nd isotopic studies on Damara metasediments show that the oldest Damara sediments (Nosib Group) were derived from source terrains which had ~ 2.0 Ga T^{Nd}_{DM} ages. In contrast, younger sediments (Kuiseb Formation and Nama Group) have significantly younger T^{Nd}_{DM} ages (~ 1.0 Ga). This is interpreted as reflecting sediment input from younger source terrains during deposition of the Kuiseb schists and Nama Group.

Model age ratios are a measure of Rb/Sr fractionation relative to Sm/Nd fractionation. Since intracrustal reworking processes increase Rb/Sr but do not significantly change Sm/Nd model age ratios (T^{Nd}_{DM} / T^{Sr}_{BE}) are a measure of the amount of intracrustal

reworking. Model age ratios ($T^{Nd}_{DM} / T^{Sr}_{BE}$) are greatest for the oldest Damara sediments (Nosib Group) indicating that their sources had suffered the largest amounts of intracrustal reworking. However, the rate of intracrustal reworking was greatest in source terrains sampled by younger sediments (Kuiseb Formation and Nama Group). This suggests that the rate of intracrustal reworking increased with time in the period ~ 2.0-1.0 Ga in this region.

References

Abbey, S. (1980) Studies in "standard samples" for use in the general analysis of silicate rocks and minerals. Geostand. Newslett., 4, 163 - 190

Abbott, R.N. Jr. (1982) A petrogenetic grid for medium and high grade metabasites. Am. Mineral. 67, 865 - 876.

Ahrendt, H., Behr, H.R., Clauer, N., Porada, H. and Weber, K. (1983) K/Ar age determinations of the northern Damara branch and their implications for the structural and metmorphic evolution of the Damara orogen, S.W.A./Namibia, Spec. publ. Geol. Soc. S. Africa, No.11, 299-306

Allegre, C.J. and Ben Othman, D. (1980) Nd - Sr isotopic relationship in granitic rocks and continental crust development : a chemical approach to orogenesis, Nature 286 335 - 341

Allegre, C.J., Treuil, M., Minster, J.F., Minster,B. and Albarede, F. (1977) Systematic use of trace elements in igneous processes. Part 1 : Fractional crystallisation processes in volcanic suites. Contrib. Mineral. Petrol. 60, 57 -75

Arth, J.G. and Hanson, G.N. (1975) Geochemistry and origin of the early Pre-cambrian crust of northeastern Minnesota. Geochim. Cosmochim. Acta, 39, 325 -362

Arth, J.G. (1976) Behaviour of trace elements during magmatic processes - a summary of theoretical models and their applications. Jour. Res. U.S. geol. Survey 4, 41-47

Arzi, A.A. (1978) Critical phenomena in the rheology of partially melted rocks. Tectonophysics 44, 173-184

Balau, J.R., Waff, H. and Tyburczy, J.A. (1979) Mechanical and thermodynamic constraints of fluid distribution in partial melts. J. Geophys Res. 64, 6102 - 6108

Barber, J.P. and Yardley, B.W.D. (1985) Conditions of high-grade metamorphism in the Dalradian of Connemara, Ireland. J. Geol. Soc. Lond. 142, 87 - 96

Bateman, R. (1984) On the role of diapirism in the segregation, ascent and final emplacement of granitoid magmas. Tectonophysics 110, 211 - 231

Behr, H.J., Ahrendt, H., Martin, H., Porada, H., Rohra, J. and Weber, K. (1983) Sedimentology and mineralogy of upper Proterozoic playa-like deposits in the Damara orogen, 577 - 616, *in* Martin,H. and Eder,F.W. eds. Intracontinental fold belts - Case studies in the Variscan belt of Europe and the Damara belt of Namibia. Springer-Verlag, Berlin, 945pp.

Berning, J., Cooke, R., Haemstra, S.A., Hoffman, U. (1976) The Rossing uranium deposit, South West Africa. Economic Geology 71, 351 368.

Berre, W. (1975) A unifying theory of the stability of penetrating liquid phases and sintering pores. Acta Met. 23, 131 - 138

Bickle, M.J. and Coward, M.P. (1977) A major thrust in the southern Damara belt, Namibia. 20th Ann. Rep. Res. Unit for African Geology, Univ. of Leeds, 8 - 13

Bickle, M.J., Hawkesworth, C.J., England, P.C. and Athey, D.R. (1975) A preliminary thermal model for regional metamorphism in the Eastern Alps. Earth Planet. Sci. Lett. 26, 13 - 28

Blaine,J.L. (1977) Tectonic evolution of the Waldau ridge structure and the Okahandja lineament in part of the Central Damara orogen, west of Okahandja, S.W.A. Bull. Precambrian Res. Unit, Univ. of Cape town 21 , 99pp.

Blaxland, A., Gohn, E., Haack, U. and Hoffer, E. (1979) Rb/Sr ages of late tectonic granites in the Damara orogen, South West Africa / Namibia. N. Jb. Mineral Mh. 11, 489-508.

Bowden, A., Batchelor, R.A. , Chappell, B.W., Didier, J., Lameyre, J. (1984) Petrological, geochemical and source criteria for the classification of granitic rocks ; a discussion. Physics of the earth and Planetary interiors 35, 1 - 11.

Briqueu, L. and Lancelot, J.R. (1979) Rb/Sr systematics and crustal contamination models for calc-alkaline igneous rocks. Earth Planet. Sci. Lett. 43, 385 - 396.

Brown, G.C. (1970) A comment on the role of water in the partial fusion of crustal rocks. Earth Planet. Sci. Lett. 9, 355 - 358

Brown, G.C. and Fyfe W.S. (1970) The production of granitic melts during ultrametamorphism. Contrib. Mineral. Petrol. 28, 310 - 318

Brown, G.C. (1979) The changing pattern of batholith emplacement during earth history *in* Origin of granite batholiths - geochemical evidence. M.P. Atherton and J. Tarney (eds.). Shiva Publishing Ltd.

Brown, G.C., Thorpe, R.S. and Webb, P.C. (1984) The geochemical characteristics of granitoids in contrasting arcs and comments on magma sources. Jour. geol. Soc. Lond. 141, 413 - 426.

Bunting,F.J.L. (1977) Geology of part of the central Damara belt around the Tsumas river, east of Swakopmund, S.W. Africa. Unpubl. Phd. thesis, Rhodes University Grahamstown.

Busch, W., Schneider, G. and Mehnert, K.R. (1974) Initial melting at grain boundaries, Part II - Melting in rocks of granodioritic, quartzdioritic and tonalitic composition. N. Jb. Miner. Mh. 8, 345 – 370

Cawthorn,R.G. and Brown,P.A. (1976) A model for the formation and crystrallisation of corundum-normative calc-alkaline magmas through amphibole fractionation. Jour. Geol. 84, 467- 476.

Chappell, B.W. and White, A.J.R. (1974) Two contrasting granite types. Pacific Geology 8 , 173 - 174.

Clifford, T.N. (1967) The Damara episode in the upper Proterozoic - lower Palaeozoic strucyural evolution of southern Africa. Geol. Soc. Am. Spec. paper 92, 100pp.

Cobbing, D.E.J. (1982) Discussion on the origin of granites. J. Geol. Soc. Lond. 139, 103 - 105.

Collins, W.J., Beams, S.D., White, A.J.R. and Chappell, D.W. (1982) Nature and origin of A - type granites with particular reference to southeastern Australia. Contrib. Mineral. Petrol. 80, 189 - 200

Condie, K.C. and Hunter, D.C. (1976) Trace element geochemistry of Archaean granitic rocks from the Barberton region , South Africa. Earth Planet. Sci. Lett. 29, 389 - 400.

Condie, K.C. (1978) Geochemistry of Proterozoic granitic plutons from New Mexico, U.S.A.. Chem. Geol. 21, 131 - 149.

Corner, B. (1975) A preliminary report on the correlation between magmatic and radiometric data in the Damara orogenic belt, S.W.A.. Rep. S. Africa Atomic Energy Board 12pp.

Coward, M.P. (1981) The junction between Pan-African mobile belts in Nambia : it's structural history . Tectonophysics, 76, 59 - 73.

Coward, M.P. (1983) The tectonic history of the Damara belt. Spec. Publ. geol. Soc. S. Africa, 11 409 - 421.

Coward, M.P. and Daly, M.C. (1984) Crustal lineaments and shear zones in Africa ; their relationship to platemovements. Tectonophysics 24, 27 - 45.

Criss, R.E and Taylor H.P. (1983) An $^{18}O/^{16}O$ and D/H study of tertiary hydrothermal systems in the Southern half of the Idaho batholith. Geol. Soc. Amer. Bull. 94, 640 - 663.

De Paolo, D.J. (1981) Trace element and isotopic effects of combined wall-rock assimilation and fractional crystallisation. Earth Planet. Sci. Lett. 53, 189 - 202.

De Paolo, D.J. and Farmer, G.L. (1984) Isotopic data bearing on the origin of Mesozoic and Tertiary granitic rocks in the Western United States. Royal Soc. (London) Philos. Trans. A310, 745 - 753.

Downing, K.N. (1982) Tectonic significance of the Okahandja lineament. Unpubl. Phd. thesis, Univ. of Leeds. 238 pp

Downing, K.N. and Coward, M.P. (1981) The Okahandja lineament and it's significance for Damaran tectonics in Namibia. Geol. Rnd. Sch. 70, 3, 972 - 1000.

Eggert, R.G. and Kerrick, D.M. (1981) Metamorphic equilibria in the siliceous dolomite system : 6 Kb. experimental data and geologic implications. Geochim. Cosmochim. Acta 45, 1039 - 1049.

Ellis, A.J. and Mahon, W.A.J. (1967) Hydrothermal systems and experimental host water/rock reactions. Geochim. Cosmochim. Acta. 31, 519 - 538

England, P.C. and Thompson, A.B. (1984) Pressure - Temperature - Time paths of regional metamorphism I. Heat Transfer during the Evolution of Regions of Thickened Continental Crust. J. Petrology 25, 894 - 928

Thompson, A.B. and England, P.C. (1984) Pressure - Temperature - Time paths of regional metamorphism II, their inference and interpretation using mineral assemblages in metamorphic rocks. J. Petrology 25, 929 - 955

Ferry, J.M. and Spear, F.S. (1978) Experimental calibration of the partitioning of Fe and Mg between biotite and garnet. Contrib. Mineral. Petrol. 66, 113 - 117

Finnemore, S.H. (1978) The geochemistry and origin of the Matchless amphibolite belt, Windhoek district, S.W.A./Namibia. Spec. Publ. Geol. Soc. S. Africa. 11, 43 - 63

Flynn, R.T. and Burnham, C.W. (1978) An experimental determination of rare earth co-efficients between a chloride containing vapour phase and silicate melts. Geochim. Cosmochim. Acta 42, 685 -701

Fourcadre, S. and Allegre, C.J. (1981) Trace element behaviour in granite genesis - A study of the calc-alkaline association from the Queriquot Complex (Pyrenees, France). Contrib. Mineral. Petrol. 76, 177-195

Frets, D.C. (1969) Geology and structure of the Huab Welwitschia area, S.W. Africa. Bull. Precambrian. Res. Unit, Univ. of Cape Town, 24, 325pp

Ganguly, J. and Saxena, S.K. (1984) Mixing properties of aluminosilicate garnets ; constraints from natural and experimental data and applications th geothermo-barometry. Am. Min. 69, 88 - 97

Germs, G.J.B. (1983) Implications of a sedimentary facies and depositional enviroment analysis of the Nama Group in S.W.A./ Namibia. Spec. Publ. Geol. Soc. S. Africa. 11, 89-114

Giletti, B.J., Semet, M.P. and Yund, R.A. (1978) Studies in diffusion - III. Oxygen in feldspars ; an ionprobe determination. Geochim. Cosmochim. Acta. 42, 45 - 57

Gohn, E., Klein, J.A. (1980) Rb/Sr ages of granitic rocks along the middle reaches of the Omaruru river and the timing of orogenetic events in the Damara belt, Namibia. Contrib. Mineral Petrol. 74, 349 - 360

Gordon, T.M. and Greenwood, H.J. (1970) The reaction dolomite + quartz + water = talc + calcite + carbon dioxide. Am . Jour. Sci. 268, 225 - 242

Grant, J.A. and Weiben, P.W. (1971) Retrograde zoning in garnet near the second sillimanite isograd. Am. Jour. Sci. 270, 281 - 296

Grant, J.A. (1985) Phase equilibria in low-pressure partial melting of pelitic rocks. Am. Jour. Sci. 285, 409 - 435

Gray, D.R. (1979) Microstructure of crenulation cleavage ; an indicator of cleavage origin. Am. Jour. Sci. 279, 97 - 128

Green, T.H. and Ringwood, A.E. (1968) Genesis of the calc-alkaline igneous rock suite. Contrib. Mineral. Petrol. 18, 105-162

Greenwood, H.J. (1967) Wollastonite stability in H_2O - CO_2 mixtures and occurrence in a contact metamorphic aureole near Salmo, British Columbia, Canada. Am. Mineral. 52, 1669 - 1680

Gromet, L.P. and Silver, L.T. (1983) Rare earth element distributions among minerals in a granodiorite and their petrogenetic implications. Geochim. Cosmochim. Acta. 47, 925-939

Guj, P. (1970) The Damara mobile belt in S.Western Kaokoveld, S.W. Africa. Bull. Precambrian Res. Unit, Univ of Cape Town, 18, 168pp

Haack, U. and Hoffer, E. (1976) K/Ar ages of biotites from the Damara-orogen, South/West Africa. Trans. Geol. Soc. S. Africa 79, 213-216

Haack, U., Hoefs, J., and Gohn, E. (1982) Constraints on the origin of Damaran granites by Rb/Sr and δ^{18} O data. Contrib. Mineral. Petrol. 79, 279 - 289

Haack, U. (1983) On the content and vertical distribution of K, Th and U in the continental crust. Earth Planet. Sci. Lett. 62, 360-366

Haack, U. (1983) Reconstruction of the cooling history of the Damara orogen by correlation of radiometric ages with geography and altitude. *in* "Intracontinental Fold Belts" Ed. by Martin, H. and Eder, F.W. Springer - Verlag, Berlin 1983, 873 - 884

Haack, U., Gohn, E. and Hartmann, O. (1983) Radiogenic heat production in Damara rocks. Spec. Publ. Geol. Soc. S. Afr. 11, 225 - 231

Haack, U., Heinrichs, H, Boneb, M. and Schneider, A. (1984) Loss of metals from pelites during regional metamorphism. Contrib. Mineral. Petrol. 85, 116 - 132

Halbich, I.W. (1977) Structure and Tectonics along the Southern Margin of the Damara Mobile Belt, S.W.A. Annale Univ. Stellenbosch. Ser. Al. (Geol) 2, 149-247

Hanson, G.N. (1978) The application of trace elements to the petrogenesis of igneous rocks of granitic composition. Earth Planet. Sci. Lett. 38, 26-43

Hanson, G.N. (1980) Rare Earth Elements in petrogenetic studies of igneous systems. Ann. Rev. Earth Planet. Sci. Lett. 8, 371-406

Harris, N.B.W. (1981) The role of fluorine and chlorine in the petrogenesis of a peralkaline complex from Saudi Arabia. Chem. Geol. 31, 303-310

Harris, N.B.W. (1983) Possible source regions for "within-plate" magmatism in north - east Africa and Arabia. Bull. Fac. Earth Sci., King Adbulaziz Univ. 6, 249 - 257

Harte, B. (1975) Determination of a pelite petrogenetic grid for the eastern Scottish Dalradian. Yb. Carnegie Inst. Wash. 74, 438-446

Hart, S.R. and Davis, K.E. (1978) Nickel partitioning between olivine and silicate melt. Earth Planet. Sci. Lett. 40, 203-219

Hartmann, O., Hoffer, E. and Haack, U. (1983) Regional metamorphism in the Damara orogen - Interaction of crustal motion and heat transfer. Spec. Publ. Geol. Soc. S. Africa 11, 233-241.

Hawkesworth, C.J., Kramers, K.D. and Miller R. Mc G. (1981) Old model Nd ages in Namibian Pan-African rocks. Nature 289, 278-282

Hawkesworth, C.J., Menzies, M.A. and Van Calsteren, P. (1983) Geochemical and tectonic evolution of the Damara Belt, Namibia in Collision Tectonics, Coward, M.P. and Ries, A. eds, Spec. Publ. Geol. Soc. Lond. 19, 305-320

Hawkesworth, C.J. and Marlow, A.J. (1983) Isotopic evolution of the Damara Orogenic Belt. Spec/ Publ. Geol. Soc. S. Africa 11, 397-407

Hawkesworth, C.J., Gledhill, A.R., Roddick, J.C., Miller, R. Mc G. and Kroner, A. (1983) Rb/Sr and $^{40}Ar/^{39}Ar$ studies bearing on models for the thermal evolution of the Damaran belt, Namibia. Spec. Publ. geol. Soc. S. Afr. 11, 323 - 338

Hawkesworth, C.J. and Van Calsteren, P.V.C. (1983) Radiogenic isotopes - Some geological applications. Ch. 11 in Rare Earth Element Geochemistry, Developments in Geochemistry, edited by P. Henderson - Elsevier Science Publications B.V. Amstredam, pp 375 -421

Hedberg, R.M. (1979) Stratigraphy of the Ovamboland Basin, S.W.A. Bull. Precambrian Res. Unit., Univ. of Cape Town 24, 325pp

Helz, R.T. (1975) Phase relations of basalts in their melting ranges at PH_2O = 5 K.b., Part 2 - melt compositions. Journal of Petrology 17, 139 - 193

Hewitt, D.A. (1973a) The metamorphism of micaceous limestones from south-central Connecticut. Am. Jour. Sci. 273A, 444-469

Hewitt, D.A. (1973b) Stability of the assemblage muscovite-calcite-quatrz. Am. Mineralogist 58, 785-791

Hess, P.C. (1971) Prograde and retrograde equilibrium in garnet - cordierite gneiss in south - central Massachusettes. Contrib. Mineral. Petrol. 30, 177 - 195

Hoernes,S. and Hoffer, E. (1979) Equilibrium relations of prograde metamorphic mineral assemblages. A stable isotope study of rocks of the Damara Orogen from Namibia. Contrib. Mineral. Petrol. 68, 377-389

Hodges, K.V. and Spear, F.S. (1982) Geothermometry, geobarometry and the Al2SiO5 triple point at Mt. Moosilkauke, New Hamshire. Am. Mineral. 67, 1118 - 1134

Hoeschk, G. (1980) Phase relations of a simplified marly rock system with application to the Western Idaho Tauern (Austria). Contrib. Mineral. Petrol. 73, 53-68

Hoffer, E. (1977) Petrologische untersuchungen 2ur regionalmetamorphose Al-riche metapelite in sudlichen Damara Orogen (S.W.A). Habilitationsschrift, Univ. Gottingen, 150pp

Hoffman, K.H. (1983) Lithostratigraphy and facies of the Swakop Group of theSouthern Damara Belt, S.W.A./Namibia. Spec. Publ. Geol. Soc. S. Africa 11, 43-63

Huang, W.L. and Wyllie, P.J. (1973) Melting relations of muscovite granite to 35 kb as a model for the fusion of metamorphosed subducted oceanic sediments. Contrib. Mineral. Petrol. 42, 1 - 4

Huang, W.L. and Wyllie, P.J. (1974) Melting relations of muscovite with quartz and sanidine in the K_2O - Al_2O_3 - SiO_2 - H_2O system to 30 kb and an outline of paragonite melting relations. Am. Jour. Sci. 274, 378 - 395

Indares, A. and Martignole, J. (1985) Biotite - garnet geothermometry in the granulite facies ; the influence of Ti and Al in biotite. Am. Mineral. 70, 272 - 278

Jacob, R.E. (1974) Geology and Metamorphic Petrology of part of the Damara Orogen along the lower Swakop River, S.W.Africa. Bull. Precambrian Res. Unit, Univ. of Cape Town 17, 185pp

Jacobsen, S.B. and Wasserburg, G.H. (1979) The mean age of mantle and crustal resevoirs. Jour. Geophys. Res. 84, 7411 - 7426

Jaffey, A.H., Flynn, K.F., Glendenin, L.E., Bentley, W.C. and Essling, A.M. (1971) Precision measurements of half-lives and specific activities of U^{235} and U^{238}. Phys. Rev. C,4, 1889-1906

Jurewicz, S.R. and Watson, E.B. (1985) The distribution of partial melts in a granitic system ; the application of liquid phase sintering theory. Geochim. Cosmochim. Acta. 49, 1109 - 1121

Juteau, M, A., and Albarede, F. (1986) The Pb-Sr-Nd isotope geochemistry of some recent circum-Mediterranean granites. Contrib. Mineral. Petrol. 92, 331-340

Kasch, K.W. (1981) The structural geology, metamorphic petrology and tectonothermal evolution of the southern Damara Belt around Omitara S.W. Africa/Namibia. Unpubl. Ph.D. thesis, Univ. of Cape Town, 333pp

Kennedy, W.Q. (1964) The structural differentiation of Africa in the Pan-African (500 Ma) tectonic episode. 8th Ann. Rep. Inst. Afr. Geol., Univ. of Leeds, 48-49

Klein, J.A. (1980) Evolution of first generation folds in a marble unit (Damara Orogenic Belt, Namibia). Geol. Rundsch. 69, 770-800

Kroner, A., Harpern, M. and Jacob, R.E. (1978) Rb/Sr geochronology in favour of polymetamorphism in the Pan-African Damara belt of Namibia. Geol Rundsch 67, 688-705

Kroner, A. (1982) Rb/Sr geochronology and tectonic evolution of the Pan-African Damara Belt of Namibia/ South Western Africa. Am. Jour. Sci. 282, 1471 - 1507,

Kroner, A. (1982) Precambrian crustal evolution and continental drift. Geol. Rundsch. 70, 2, 412-428

Leake, B.E. (1978) Nomenclature of amphiboles. Min. Mag. 42, 533-563

Le Fort, P. (1981) Manasalu leucogranite : a collision signature of the Himalaya, a model for it's genesis and emplacement. Tour. Geophys. Res. 86, 10545-10568

Le Roux, L.J. and Glendenin, L.L. (1963) Half life of Thorium 232. Proc. Natl. Conf. on Nuclear Energy, Pretoria

Lux, D.R., De Yoreo, J.J., Guldotti, C.V. and Decker, E.R. (1986) Role of plutonism in low-pressure metamorphic belt formation. Nature 323, 794 - 797

Mahood, G. and Hildreth, W. (1983) Large partition co-efficients for trace elements in high silica rhyolites. Geochim. Cosmochim. Acta. 47, 11-30

Malling, S. (1978) Some aspects of the lithostratigraphy and tectonometamorphic evolution in the Nauchas - Rehoboth area S.W.A. 14th and 15th Ann. Rep. Precambrian Res. Unit, Univ. of Cape Town, 183-193

Marlow, A.G. (1981) Remobilisation and primary Uranium genesis in the Damara Orogenic Belt, Namibia. Unpubl. Ph.D. thesis, Univ. of Leeds

Marlow, A.G. (1983) Geology and Rb/Sr geochronology of alaskites, mineralised and radioactive granites, Namibia. Spec. Publ. Geol. Soc. S. Afr. 11, 289-298

Martin, H. (1975) The mineralisation of the ensialic Damara Orogenic Belt. Geol. Soc. S. Afr. 16th Geocong. Stellenbosch 95-98

Martin, H. and Porada, H. (1977) The intracratonic branch of the Damara Orogen in S.W. Afr. - Discussions of geodynamic models. Precambrian Res. 5, 339-357

Martin, J.M. and Meybeck, M. (1979) Elemental mass-balance of material carried by major world rivers. Marine Chem. 7, 173-206

Mc Carthy, T.S. and Hasty, R.A. (1976) Trace element distribution patterns and their relationship to the crystallisation of granitic melts. Geochim. Cosmochim Acta. 4, 1351-1358

Mc Carthy, T.S. and Groves, D.I. (1979) The Blue Tier Batholith, northern Tasmania. Contrib. Mineral. Petrol. 71, 193-209

Mc Culloch, M.T. and Wasserburg, G.J. (1978) Sm-Nd and Rb-Sr geochronology of continental crust formation. Times of addition to continents of chemically-fractionated mantle derived materials are determined. Science 200, 1003 - 1011

Mc Culloch, M.T. and Chappell, B.W. (1982) Nd isotopic characteristics of S and I-type granites. Earth Planet. Sci. Lett. 58, 51-64

Mc Kenzie, D. (1984) The generation and compaction of partially molten rock. J. Petrology 25, 713 - 765

Mc Kenzie, D. (1985) The generation of magma from the crust and mantle. Earth Planet Sci. Lett. 74, 81 - 91

Mc Kenzie, D. (1978) Some remarks on the development of sedimentary basins. Earth Planet Sci. Lett. 40, 25 - 32

Meetz, P. (1976) Experimental investigation of the metamorphism of siliceous dolomites, Part 3, Equilibrium data for the reaction 1 Tremolite + 11 Dolomite = 8 Forsterite +13 Calcite + $9CO_2$ +$1H_2O$ for the total pressures of 3,000 and 5,000 Bars. Contrib. Mineral. Petrol. 58, 137 - 148

Miller, C.F. and Stoddard, E.F. (1980) Origin of strongly peraluminous granite magmas ; a non-pelitic source? Geol. Soc. Amer. (Abs. with prog.) 12, 483-484

Miller, C.F. and Mittlefehldt, D.W. (1982) Depletion of the light Rare Earth Elements in felsic magmas. Geology 10, 129-133

Miller, C.F. (1985) Are strongly peraluminous magmas derived from pelitic sedimentary sources. Journal of Geology 93, 673 - 689

Miller, R. Mc G. (1973) The Salem granite suite, S.W. Africa ; Genesis by partial melting of the Khomas schist. Memoir 64, Dept. of Mines, Geological Survey

Miller, R. Mc G. (1979) The Okahandja lineamant ; a fundamental tectonic boundary in the Damara Orogen of S.W.Africa/Namibia. Trans. Geol. Soc. S. Afr. 82, 349-361

Miller, R. Mc G. (1980) Geology of a portion of Central Damaraland, S.W.Africa/Namibia. Mem. Geol. Surv. S. Afr. and S.W.Afr. 6, 78pp

Miller, R. Mc G. and Hoffman, K.H. (1981) Geology of the Damara Belt, Excurscion guide, Geocongress 1981, Geol. Soc. S. Afr. 115pp

Miller, R. Mc G. (1983) The Pan-African Damara Orogen of S.W.Afr./Namibia. Spec. Publ. Geol. Soc. S. Afr. 11, 431-515

Miller, R. Mc G. (1983) A possible model for the Damara orogen in the light of recent data, in Rast,_W. and Delaney,F.M eds. - "Profiles of Orogenic Belts". Geodynamic series, Am. Geophys. Un. 10, 31-34

Miller, R. Mc G. and Burger, A.J. (1983) Tectonic implications of the contrasting geochemistry of Damaran mafic volcanic rocks, S.W.A./Namibia. Spec. Publ. Geol. Soc. S. Afr. 11, 115-138

Miller, R. Mc G. and Burger A.J. (1983) Economic implications of plate tectonic models fo the Damara Orogen. Spec. Publ. Geol. Soc. S. Afr. 11, 115-138

Morgan, P. (1983) Constraints on rift thermal processes from heat flow and uplift. Tectonophysics 94, 277 - 298

Naney, M.T. (1983) Phase equilibria of rock forming ferromagnesian silicates in granitic systems. Am. Jour. Sci. 283, 993-1033

Nash, C.R. (1971) Metamorphic petrology of the S.J. area, Swakopmund district, S.W. Africa. Bull. 9, Precambrian Res. Unit, Univ. of Cape Town

Ng'Ambi, O., Boelrijk, N.A.I.M., Priem, H.N.A. and Daly, M.C. (1986) Geochronology of the Mkushi Gneiss Complex, Central Zambia. Precambrian Res. 24, 27 - 45

Parrish, D.K., Krivz, A.L. and Carter, N.L. (1976) Finite - element folds of similar geometry. Tectonophysics 32, 183 - 207

Peacock, M.A. (1931) Classification of igneous rock series. Journal of Geol. 39, 65-67

Pearce, J.A. and Norry, M.J. (1979) Petrogenetic implications of Ti, Zr, Y and Nb variations in volcanic rocks. Contrib. Mineral. Petrol. 67, 33 - 47

Pearce, A.J. , Harris, N.B.W. and Tindle, A.G. (1984) Trace element discrimination diagrams for the tectonic interpretation of igneous rocks. J. Petrol. 25, 956-983

Pidgeon, R.T. and Aftalion, M. (1978) Cogenetic and inherited zircon U-Pb systems in granites; Palaeozoic granites of Scotland. in Bowes, D.R. and Leake, B.E. (eds) - "Crustal evolution in northwestern Britain and adjacent regions". Geol. Soc. Spec. Pap. 10, 183-220

Pitcher, W.S. (1979) The anatomy of batholiths ; Jour. Geol. Soc. Lond. 135, 157-182

Porada, H. and Wittig, R. (1983) Turbidites and their significance for the geosynclinal evolution of the Damara Orogen, S.W.A./Namibia. Spec. Publ. Geol. Soc. S. Afr. 11, 21-36

Puhan, D. (1976) Metamorphic temperature determined by means of the Dolomite-Calcite solvus geothermometer - examples from the Central Damara Orogen, S.W.A. Contrib. Mineral. Petrol. 58, 23-28

Puhan, D. (1983) Temperature and pressure of metamorphism in the Central Damara Orogen. Spec Publ. Geol. Soc. S. Afr. 11, 219-223

Puhan, D. and Hoffer, E. (1983) Phase relations of Talc and Tremolite in metamorphic Calcite-Dolomite sediments in the southern portion of the Damara Belt. Contrib. Mineral. Petrol. 40, 207-214

Ramsay, J.G. (1980) The crack-seal mechanism of rock deformation. Nature 284, 135-280

Reeves, C.V. (1978) Interpretation of the reconnaissance aeromagnetic survey of Botswana. Rep. Geol. Surv. Botswana. 199pp

Rice, A. (1981) Convective fractionation; a mechanism to provide cryptic zoning (macrosegregation), layering, crescumulates, banded tuffs and explosive volcanism in igneous processes. Jour. Geophys. Res. 86, 405-417

Richter, F.M. and Mc Kenzie, D. (1984) Dynamic models for melt segregation from a deformable matrix. Journal of Geology 92, 729 - 740

S.A.C.S. (1980) The lithostratigraphy of Southern Africa ; 1 The lithostratigraphy of S. Africa, S.W.A./Namibia, and the republic of Bophuthatswana, Transkei and Venda. Handbk. Geol. Surv. S. Afr. 8, 690pp

Sandiford, M. and Powell, R. (1986) Deep crustal metamorphism during continental extension ; modern and ancient examples. Earth Planet. Sci. Lett. 79, 151 - 158

Sawyer, E.W. (1976) The geology of an area south-east of Walvis Bay ; lithology and field relationships. Rep. Geol. Surv. S. Afr. (Namibia) unpubl. 120pp

Sawyer, E.W. (1981) Damaran structural and metamorphic geology of an area south east of Walvis Bay, S.W.A./Namibia. Mem. Geol. Surv. S.W. Afr./Namibia 7, 94pp

Scott, D.R. and Stevenson, D.J. (1984) Magma solitons. Geophys. Res. Lett. 11, 1161 - 1164

Sekine, T., Wyllie, P.J. and Barker, D.R. (1981) Phase relationships at 30Kb for quartz eclogite compositions in CaO - MgO - Al_2O_3 - SiO_2 - H_2O with implications for subduction zone magmas. Amer. Mineral., 67, 865-876

Shand, S.J. (1951) Eruptive rocks. J. Wiley (publisher) N. York.

Shaw, H.R. (1965) Comments on viscosity, crystal settling and convection in granitic magmas. Am. Jour. Sci. 263, 120 - 152

Shaw, D.M. (1970) Trace element anatexis during anatexis. Geochim. Cosmochim. Acta. 34, 239-243

Smith, C.S. (1964) Some elementary principles of polycrystalline microstructure. Metall. Rev. 9, 1-48

Smith, D.A.M. (1965) The geology of the area around the Khan and Swakop rivers in S.W. Africa. Mem. 3, South West Africa series, Republic of South Africa, Dept. of Mines, Geological Survey, 113 pp

Stacey, J.S. and Stern,T.W. (1973) Revised table for the calculation of lead isotope ages. Natl. tech. Infor. Service, Springfield, Virginia, 22151, U.S.A. 35pp

Stacey, J.S. and Kramer J.D. (1975) Approximation of terestrial lead isotope evolution by a two stage model. Earth and Planet. Sci. Lett. 26, 207-221

Stern, C.R. and Wyllie, P.J. (1978) Phase composition through crystallisation intervals in andesite basalt - H_2O at 30 Kb. with implications for subduction zone magmas. Am. Mineral. 63, 641-663

Streckeisen, A. (1975) To each plutonic rock it's proper name. Earth Sci. Rev. 12, 1-33

Takahasi, E. (1978) Partitioning of Ni^{2+}, Co^{2+}, Fe^{2+}, Mn^{2+} and Mg^{2+} between olivine and silicate melts : compositional dependance of partition co-efficients. Geochim. Cosmochim. Acta 42, 1829-1845

Taylor, H.P. (1978) Oxygen and hydrogen isotope studies of plutonic granitic rocks. Earth Planet Sci. Lett. 38, 177 - 210

Taylor, H.P. (1980) The effects on assimilation of country rocks by magmas on $^{18}O/^{16}O$ and $^{87}Sr/^{86}Sr$ systematics on igneous rocks. Earth Planet. Sci. Lett. 47, 243 - 254

Taylor, R.P and Mc Clennan, S.M. (1985) The continental crust : it's composition and evolution. Geoscience Texts, Blackwell Scientific Publications

Taylor, R.P , Strong, D.F and Fryer, B.J. (1981) Volatile control of contrasting trace element distributions in peralkaline granitic and volcanic rocks. Contrib. Mineral. Petrol. 71, 267-271

Tatsumoto, M. (1978) Isotopic composition of lead in oceanic basalt and it's implications for mantle evolution. Earth Planet. Sci. Lett. 38, 63 - 87

Thompson, A.B. (1975) Mineral reactions in a calc-mica schist from Garretts, Vermont, U.S.A. Contrib. Mineral. Petrol. 53, 105-127

Thompson, A.B. (1976) Mineral reactions in pelitic rocks ; I, Prediction of P-T-X (Fe - Mg) phase relations. Am. Jour. Sci. 276, 401 - 424

Thompson, A.B. and Algor, J.R. (1977) Model systems for anatexisof anatectic rocks. Theory of melting relations in the system $KAlO_2$ - $NaAlO_2$ - Al_2O_3 - SiO_2 - H_2O. Contrib. Mineral. Petrol. 63, 247-269

Thompson, A.B., Lyttle, P.T. and Thompson, jnr. J.B. (1977) Mineral reactions and A - Na - K and A - F - M facies type in the Garretts schist, Vermont. Am. J. Sci. 277, 1124-1151

Thompson, A.B. and Tracy, R.J. (1979) Model systems for anatexis of pelitic rocks II, Facies series melting and reactions in the system CaO - $KAlO_2$ - $NaAlO_2$ - Al_2O_3 - SiO_2 - H_2O. Contrib. Mineral. Petrol. 70, 429 - 438

Tindle, A.G. and Pearce, J.A. (1981) Petrogenetic modelling of in-situ fractional crystallisation in the zoned Loch Doon pluton, Scotland. Contrib. Mineral. Petrol. 78, 198-207

Tindle, A.G. (1982) Petrogenesis of the Loch Doon granitic intrusion, Southern Uplands of Scotland. Unpubl. Ph.D. thesis, Open University

Tuttle, D.F. and Bowen, N.L. (1958) Origin of granite in the light of experimental studies in the system NaAlSi3O8 - $KAlSi_3O_8$ - SiO_2 - H_2O. Mem. Geol. Soc. Am. 74

Treuil, M. and Varet, J. (1973) Criteres volcanologiques, petrologiques et geochemiques de la geneses et de la differentation des magmas basaltiques : exemples de l'Afar. Bull. Soc. Geol. France 15, 401-644

Van der Molen, I. and Paterson, M.S. (1979) Experimental deformation of partially melted granite. Contrib. Mineral. Petrol. 70, 299 - 318

Vitrac, A.M., Albarede, F. and Allegre, C.J. (1981) Lead isotopic composition of Hercynian granitic K-feldspar constrains continental genesis. Nature 291, 460-464

Waff, H.S. and Balau, J.R. (1979) Equilibrium fluid distribution in an ultramafic partial melt under hydrostatic stress conditions. Jour. Geophys. Res. 87, 6109 - 6114

Watson, E.B. (1979) Zircon saturation in felsic liquids : Experimental results and applications to trace element geochemistry. Contrib. Mineral. Petrol. 70, 407-419

Watson, E.B. and Green, T.H. (1981) Apatite/Liquid partition co-efficients for the rare earth elements and strontium. Earth Planet. Sci. Lett. 56, 405-421

Watson, E.B. (1982) Melt infiltration and magma evolution. Geology 10, 236 - 240

Watson, E.B. and Harrison, T.M. (1983) Zircon saturation revisited : temperature and composition effects in a variety of crustal magma types. Earth Planet. Sci. Lett. 64, 295-304

Watson, E.B. and Harrison, T.M. (1984) Accessory minerals and the geochemical evolution of crustal magmatic systems : A summary and prospectus of experimental approaches. Physics of the Earth and Planetary Interiors 35, 19-30

Watters, B.R. (1978) Petrogenesis of the felsic rock units of the late Precambrian Sinclair Group, S.W. Africa. Geol Rundsch. 67, 743 - 773

Weiss, D. (1983) Pb isotopes of Ascension Island rocks: oceanic origin for the gabbroic to granitic plutonic xenoliths. Earth Planet. Sci. Lett. 62, 273-282

Wells, P.R.A. (1980) Thermal models for the magmatic accretion and subsequent metamorphism of continental crust. Earth Planet. Sci. Lett. 46, 253 - 265

Wendhlandt, R.F. and Harrison,W.J. (1979) Rare Earth partitioning between immiscible carbonate and silicate liquids and CO2 vapour : results and implications for theformation of light rare earth enriched rocks. Contrib. Mineral. Petrol. 69, 409-419

White, A.J.R., Clemens, J.D., Holloway, J.R., Silver, L.T., Chappell, B.W. and Wall, V.J. (1986) S-type granites and their probable absence in s.western North America. Geology 14, 115-118

Wickham, S.M. (1984) Crustal anatexis in the Trois Seigneurs Massif, Pyrenees France. Unpubl. Ph.D. thesis, Univ. of Cambridge

Wickham, S.M. and Oxburgh, E.R. (1985) Continental rifts as a setting for regional metamorphism. Nature 318, 330 - 333

Wickham, S.M. and Taylor, H.P. jr. (1985) Stable isotopic evidence for large scale seawater infiltration in a regional metamorphic terrane ; the Trois Seigneurs Massif, Pyrenees, France. Contrib. Mineral. Petrol. 91, 122 - 137

Wyborn, D. and Chappell, B.W. (1983) Chemistry of the Ordivician and Silurian greywackes of the Snowy Mountain, southeastern Australia : an example of chemical evolution of sediments with time. Chem. Geol. 39, 81-92

Wyllie, P.J. (1977) Crustal anatexis ; an experimental review. Tectonophysics 43, 41 - 47

Yardley, B.W.D., (1977) An experimental study of diffusion in garnet. Am. Mineral. 62, 793 - 800

York, D. (1969) Least squares fitting of a straight line with correlated errors. Earth Planet. Sci. Lett. 5, 320-324

Zartmann, R.E. (1984) Lead isotopic provinces in the Cordillera of the Western United States and their geologic significance. Economic geology 69, 792 - 805

Zen, E. and Hammarstrom, J.M. (1982) Magmatic epidote : host rocks, mineral composition and significance. Geol. Soc. Am. (Abs. with prog.) 14, p652

Zuber, M.T. and Parmentier, E.M. (1986) Lithospheric necking : a dynamic model for rift morphology. 77, 373 - 383

Appendix A - Analytical techniques

A (i) Sampling and crushing

Typically, granite samples were 3-5 kg in weight when collected. Care was taken to ensure that only the freshest material was sampled and freshly blasted sites were selected wherever possible. Powdered samples previously prepared for geochronological studies by A.Marlow (1981) and K.Downing (1982) were also used for geochemical investigations.

All samples were cleared of weathered surfaces and markings using a hydraulic splitter. Each sample was split into ~1 inch cubes which were washed in distilled H_2O and allowed to dry in order to remove any dust contaminant. These fragments were crushed in a hardened steel jaw crusher to minus 0.5 cm size pieces. At least 2kg of each sample was crushed in this way. A representative sample (about 150g) of this crushite was sampled by cone and quartering techniques to obtain a representative subsample. This subsample was then placed in an agate lined tema barrell and ground for 15-20 minutes until the resulting powder was less than 200 mesh size.

A (ii) XRF sample preparation

Trace elements were determined on pressed powder pellets while major elements were analysed on glass beads. For pressed pellets about 8g of rock powder was mixed with Moviol binder and pressed into a 3cm diameter pellet using a hydraulic press. Pellets were dried and hardened overnight in an oven at 110 ^{o}C. When dry, each pellet was labelled on it's edge and stored in a pill-box for analysis.

Glass beads were prepared by mixing a 4:1 lithium metaborate:tetraborate mixture (Spectraflux 100B) with pre-dried rock powder in the ratio 6:1 and fusing the mixture in a platinum-gold alloy crucible in a muffle furnace at 1100 °C for 20 minutes. A flux loss correction was applied to each batch of eight samples. Loss on ignition data were obtained by heating about 2.5g of rock powder in a silica crucible at 1000 °C for twenty minutes and calculating the percentage weight loss.

A (iii) XRF analyses

Most samples were analysed using both energy dispersive (EDXRF) and wavelength dispersive systems at the Open University and Nottingham University respectively. All samples were analysed by EDXRF for major and trace elements.

a. EDXRF

Rb, Sr, Y, Zr, Nb, Pb and Ni were determined by EDXRF. Samples were analysed using a Link Systems Meca 10-44 EDXRF spectrometer. This incorporates a low power (49W) silver anode side window X-ray tube operated in pulsed mode with maximum settings of 49Kv or 1MA, and a Si(Li) detector with a resolution of 125eV at 5.9KeV. The EDXRF has been calibrated using international standards and representative analyses of standards obtained over the period of this study are given inTable A1.1.

Table A1.1 Analyses of the standard AGV-1 over the period of this study compared to the recommended values, Abbey, (1980).

Element	Abbey (1980)	19/5/1982	16/11/1983	28/5/1985	7/4/1986
SiO_2	59.61	59.31	59.34	59.50	59.32
TiO_2	1.06	1.08	1.06	1.07	1.07
Al_2O_3	17.19	17.18	16.95	17.21	17.16
Fe_2O_3	6.78	7.07	6.98	6.98	6.98
MnO	0.10	0.09	0.10	0.10	0.09
MgO	1.52	1.69	1.69	1.60	1.52
CaO	4.94	5.09	5.07	5.05	5.02
Na_2O	4.32	4.30	4.57	4.38	4.33
K_2O	2.92	2.94	2.92	2.95	2.95
P_2O_5	0.51	0.47	0.47	0.51	0.49

	Abbey (1980	18/2/84	19/12/84	8/2/85	23/9/85
Ni	9	9	9	7	10
Nb	23	23	26	26	24
Rb	250	253	255	254	250
Sr	240	231	230	233	236
Y	29	30	28	27	30
Zr	500	499	493	502	497

For major element analyses, glass beads were counted in duplicate for 500 seconds at 10KV, 0.2mA with no primary beam filter. Powder pellets for trace element analyses were counted twice for 800 seconds at 45Kv, 0.3mA with a 127 micron silver primary beam filter in position. Instrument drift within single batches (16 samples and 4 standards per batch) was monitored by analysing USGS AGV-1 for major elements and USGS GSP-1 for trace elements several times during each run. An internal monitor sample (KND 1.1) was run several times over the period of this study to assess differences between calibrations. All XRF data are tabulated in Appendix B.

Detection limits for the major elements are generally 0.05wt% except for the light elements Na, Mg, Al and Si for which detection limits are between 0.2 (Si) and 0.96 wt% (Na). Precision is better than 1% relative (at 2 sigma) except for Al (2%), Mg (3%) and Na (10%). For trace elements detection limits are 6ppm for Rb, Sr, Y, Nb and Ni and 15 ppm for Zr. Precision for all trace elements is about 2% at the 100ppm level. Full details of the EDXRF system are given in Potts *et al* (1984).

b. Wavelength dispersive XRF

Trace elements Ba, Ce, Co, Cr, Hf, La, Ni, Nb, Pb, Rb, Sr, Ta, Th, U,V, Zr ,Y were analysed at Nottingham University on a Phillips PW1400 wavelength dispersive X-ray fluorescence spectrometer. Analyses were carried out on pressed pellets which had been previously analysed using EDXRF techniques. A rhodium X-ray tube was used for all wavelength dispersive analyses. Operating conditions are shown in Table 1.2. Detection limits are about 3ppm. Rb and Sr were determined separately from other trace elements. Both elements were analysed at 75KV, 40mA using a LiF 220 crystal. A detailed account of the technique is given by Harvey and Atkin (1981).

Table 1.2 Operating conditions for Nottingham University WDXRF system

Element	KV	mA	Crystal	Ct (peak) *	Ct (bkd)*
Ba	50	60	LiF 220	20	10
Co	60	50	LiF 220	20	20
Cr	50	60	LiF 220	20	8
Ni	70	40	LiF 220	10	4
Nb	75	40	LiF 220	10	8
Y	75	40	LiF 220	20	16
Zr	75	40	LiF 220	20	20

* Ct (peak) and Ct (Bkd) are normal counting times for peak and background positions respectively.

A (iv) Instrumental neutron activation analysis (INAA)

INAA was carried out on 36 samples to determine the concentrations of REE'S as well as the abundances of Th, Ta, Hf, U, Co and Sc. The techniques are described in detail by Potts *et al* (1981) and Potts *et al* (1985).

Rock powders were dried overnight in an oven at 110 °C. Approximately 0.3g of each powder was accurately weighed into polythene capsules. The capsule lids were sealed to prevent leakage of radioactive powder. Irradiation capsules were then stacked in a polythene

cylinder. A pre-weighed lacquered iron foil was placed between each irradiation capsule to monitor neutron flux variations along the length of the cylinder. Each irradiation cylinder contained nine samples and two standards. Standards used were the irradiation standard AC (OURS) and a sample of the Whin Sill which was used as an internal standard.

Samples were irradiated in a core tube at the Imperial College reactor centre, Silwood Park, Ascot in a thermal flux of $5x10^{12}$ n cm^2 S^{-1} for 24-30 hours. Following irradiation the samples were allowed to "cool" for about a week to allow short lived radioisotopes to decay. The samples were "counted" at the Open University using two detectors on either side of the sample capsule - a planar low energy photon spectrometer (LEPS) and a coaxial Ge(Li) detector. Each sample was counted for 800 seconds on the LEPS detector for Sm, and on the coaxial detector for La, Co and Sc. The other elements were determined by counting each sample for 2.5 x 10^4 to 5 x 10^4 seconds using the LEPS detector. The iron foils were "counted" using the coaxial detector for 300 seconds each, to assess variations in the neutron flux. Data were processed using spectroscopy amplifiers and a multichannel analyser. Photopeak data were corrected for neutron flux variations calculated using the iron foil data. Details of counting conditions, peak fitting, calibration and corrections are given in Potts *et al.* (1980) and in Potts *et al.* (1985).

A (v) Radiogenic isotope analysis

All isotopic analyses and sample preparations were carried out in a clean-air laboratory in which a positive air pressure is maintained. Sample dissolutions and beaker handling are carried out in laminar flow units whenever possible. Beakers and measuring cylinders are kept sealed with Parafilm. Sr dissolutions are carried out in teflon beakers while teflon bombs are used for Nd dissolutions to ensure complete dissolution of Nd bearing

accessory phases. Bombs and beakers are thoroughly cleaned between sample batches to prevent cross contamination between samples. All teflon is cleaned by washing in quartz distilled (QD) H_2O, soaking for at least 24 hours (usually for several days) in conc. HNO_3 at 80°C and finally by soaking in QD H_2O for at least 24 hours. Beakers are then rinsed and allowed to dry, inverted on clean tissue paper.

All H_2O is distilled by a two stage quartz still or produced by a Milli-Q reverse osmosis water purification system. HCl and HNO_3 are doubly distilled in quartz stills and finally purified in sub-boiling teflon stills. HF is also purified in teflon sub-boiling stills. Total procedural blanks for Sm and Nd are <1ng and about 8ng for Sr.

a. Sr chemistry

About 150mg of rock powder is weighed into a teflon beaker to which a couple of drops of QD H_2O are added to avoid spattering when acid is added. About 5ml of 40% HF and 2ml of concentrated HNO_3 is added to the powder/water mixture. This is allowed to stand cold overnight in a laminar flow unit, having sealed the beaker tops with Parafilm. The beakers (in batches of six) are then placed under the evaporating lamps and allowed to evaporate nearly to dryness. A further 2ml of conc. HNO_3 is added and evaporated to near dryness.Then, about 6ml of 6M QD HCl are added and allowed to warm up under the lamps. At this stage complete dissolution should occur and the solution should be a clear orange colour. If complete dissolution is not achieved at this stage the solution is evaporated again and the last two stages of acid addition are repeated until complete dossolution is achieved. The solution is then evaporated to near-dryness and the residue is redissolved in 1ml of QD 2.5M HCl for loading on to the cation exchange columns. Any residue is centrifuged off and the clear solution is

pipetted carefully on to pre-conditioned cation exchange columns taking care not to disturb the resin column. The sample is slowly washed into the column using two 1ml aliquots of 2.5M HCl (each aliquot is allowed to sink into the resin before the next is added). 40ml of 2.5M HCl is then allowed to percolate through the columns and the Sr fraction is collected with a further 10ml of 2.5M HCl (QD). The solution containiing the Sr fraction is then evaporated to dryness and the beakers are sealed with Parafilm and stored for isotopic analysis.

b. Nd chemistry

Dissolutions are carried out in sealed teflon bombs to ensure complete dissolution of Nd rich minor phases. About 150mg of rock powder was weighed into a PTFE bomb and one drop of QD H_2O is added followed by about 5ml of 40% HF and about 2ml of conc. HNO_3. This mixture is allowed to stand cold overnight in sealed bombs. The PTFE bomb is then placed in a polythene sleeve which holds the top of the bomb in position. This assembly is then placed in a monel jacket and allowed to stand for several days in an oven at 180 °C. The bomb is removed from the oven and the solution is evaporated down under evaporating lamps. When almost dry about 2ml of HNO_3 are added and when this has dried down about 6ml of 6M HCl are added. If complete dissolution does not occur at this stage the bomb is reassembled and returned to the oven for a further 24 hours.

When the sample is completely dissolved the solution is centrifuged and loaded on to the Sr columns as described for Sr separation. When the Sr fraction is collected the columns are washed with one ml of QD H_2O and eluted with ml of 3M HNO_3 after which ml of 3M HNO_3 are collected. This fraction is then evaporated to dryness.

c. Pb chemistry

About 20 mg of sample is weighed into a sevalex bomb in batches of five samples. About 1ml of TD HNO_3 followed by 2-3 mls of TD HF are added to each sample. This mixture is allowed to stand cold overnight. This solution is then evaporated down under the evaporating lamps. When dry, a further 2 mls of TD HNO_3 are added which are also evaporated to dryness. After evaporation, 3mls of 6M HCl are added and evaporated to dryness. 1 ml of 1M HBR is then added and this is allowed to stand cold overnight. The solution is then ready for ion exchange columns.

Ion exchange columns consist of polythene pipette tips loaded with 3-4 drops of Dowex 200-400 mesh anion exchange resin. The pipette tips are taken from a sealed container in which they have been imersed overnight in hot 6M HCl. The columns are placed in a covered perspex rack in a laminar flow unit and are flushed through with 16M HNO_3 followed by 1 column volume (c.v.) of QD H_2O. The resin is added at this stage (3-4 drops) followed by successive 1 c.v. washes of QD 6M HCl, QD H_2O and 6M HCl and 2 c.v. washes of TD H_2O and HBr.

Using a clean pipette tip, 1ml of HBr which contains the sample lead is carefully transferred from a sevalex bomb to the column taking care not to disturb the column resin. When the HBr has eluted into the resin 1c.v. of HBr is slowly added to the column. This is followed by the addition of three successive column volumes of HBr. When the HBr has eluted through the resin Pb is collected in a clean sevalex bomb by eluting the column with three c.v. of TD H_2O and collecting the elutant. A few drops of TD 16M HNO_3 are added to this solution before evaporating to dryness under lamps.

All Pb chemistry was carried out in a laboratory which is used exclusively for Pb chemistry. Special precautions were taken to ensure low Pb blanks which were in the range 0.7-1.1 ng during this study.

d. Mass-spectrometry

Sr and Nd are analysed on outgassed single Ta and triple Re/Ta filaments (Re centre filament). The Sr fraction is redisolved in about 0.5ml H_2O and loaded into a drop of H_3PO_4 on the centre of a single Ta filament using a micro-pipette. A current is allowed to pass through the filament and is gradually increased until a dull red glow is observed. The current is increased very slowly to prevent the solution from spreading on the filament. When the filament begins to glow the Phosphoric acid fumes off and the sample should remain close to the filament centre as it dries down.

Nd fractions are redissolved in a small drop of QD H_2O and carefully loaded on to the side filaments (Ta) of a triple filament. The current is increased slowly to dry down the solution.

Pb is loaded by dissolving the dried down sample in a small drop of phosphoric acid. Using a pipette tip a small drop of silica gel is placed on the centre of a single Re filament and the current is increased to about 0.45A. The silica gel is allowed to evaporate until it appears mushy, but not dry. The drop of phosphoric acid in which the sample has been dissolved is now loaded on to the silica gel and excess phosphoric acid is driven off by slowly increasing the current. When the filament begins to glow the current is slowly turned down. The filament is now ready for loading in the sample turret. All Pb sample loading is carried out in a laminar flow unit in a clean air laboratory.

Loaded filaments are carefully positioned in a clean sample turret of a V.G. 54E mass-spectrometer. Electrical connections are checked and the turret is allowed to stand in a vacuum oven at 80 °C until ready for loading into the mass-spectrometer.

All radiogenic isotope mass-spectrometry was carried out on a V.G. 54E mass-spectrometer interfaced with a HP 9845T computer which runs the analyses automatically using software developed by D.W. Wright and P.W.C. Van Calsteren

e. Sr isotope measurement

The computer adjusts the filament current until a beam intensity of 15pA is obtained. The measuring cycle is mass 88, 87, 86, 86.5, 85 and 84. When the Rb contribution to the 87 peak is < 0.01% the 85 peak is no longer counted. The intensities are calculated using a double interpolation algorithm (Dodson, 1978). Corrections are applied for zero, dynamic memory, and Rb interference where necessary. The $^{87}Sr / ^{86}Sr$ ratio is corrected for mass fractionation assuming that the fractionation is linearily dependant on mass difference, and that $^{86}Sr / ^{88}Sr = 0.1194$. As an analysis proceeds ratios are stored by the computer in sets of 10. Means and errors are calculated, and the ratios are rejected if Chauvenets criterion is not satisfied. If the total error for the set is greater or equal to 100 then the whole set is rejected. If the total error is greater than 500 the whole set is ignored. The run for an individual sample is terminated when at least 100 ratios have been accumulated and the $^{87}Sr / ^{86}Sr$ ratio error is better than 0.00002 (1σ).

f. Nd isotope measurement

Nd beams are run at an intensity of about 7pA. The measuring cycle is mass 146, 144, 142.5, 142, 147. The 147 peak is eliminated when the Sm contribution to the 144 peak is < 0.01%. The $^{143}Nd/^{144}Nd$ ratio is corrected for mass-fractionation assuming $^{146}Nd/^{144}Nd = 0.7219$. A run is terminated when at least 200 ratios are accumulated and the error is better than 0.000010 (1 σ).

g. Data representation

In several diagrams Sr and Nd data have been reported using the ε notation of De Paolo and Wasserburg (1976).

$$\varepsilon Nd = \frac{^{143}Nd/^{144}Nd \text{ sample at time t}}{^{143}Nd/^{144}Nd \text{ CHUR at time t}}$$

$$\varepsilon Sr = \frac{^{87}Sr/^{86}Sr \text{ of sample at time t}}{^{87}Sr/^{86}Sr \text{ of bulk earth at time t}}$$

Model Nd ages are reported relative to CHUR and depleted mantle (DM).

$$T^{CHUR}_{Nd} = 1/\lambda \ln\left[\left[\frac{^{143}Nd/^{144}Nd \text{ of sample} - ^{143}Nd/^{144}Nd \text{ CHUR}}{^{147}Sm/^{144}Nd \text{ of sample} - ^{147}Sm/^{144}Nd_{CHUR}}\right] + 1\right]$$

$$T^{DM}_{Nd} = 1/\lambda \ln\left[\left[\frac{^{143}Nd/^{144}Nd \text{ of sample} - ^{143}Nd/^{144}Nd \text{ DM}}{^{147}Sm/^{144}Nd \text{ of sample} - ^{147}Sm/^{144}Nd_{DM}}\right] + 1\right]$$

where $\lambda^{147}Sm = 6.54 \times 10^{-12}\ a^{-1}$

$(^{143}Nd/^{144}Nd)_{CHUR} = 0.51264$

$(^{147}Sm/^{144}Nd)_{CHUR} = 0.1967$

$(^{143}Nd/^{144}Nd)_{DM} = 0.51310$

$(^{147}Sm/^{144}Nd)_{DM} = 0.2238$

$\lambda^{87}Rb = 1.42 \times 10^{-11}\ a^{-1}$

$(^{87}Sr/^{86}Sr)_{BE} = 0.7047$

$(^{87}Rb/^{86}Sr)_{BE} = 0.0847$

A (vi) Wavelength dispersive electron microprobe analysis

Microprobe mineral analyses were carried out on polished carbon-coated thin sections using a Cambridge instruments Microscan 9 (M9) microprobe. The M9 incorporates a fully automated computerised system which automatically controls spectrometer angles, count times, crystal selection and specimen position. In addition on-line ZAF corrections are performed automatically.

An accelerating potential of 20 kV and a probe current of 30 nA were used for all wavelength dispersive analyses using a defocussed 15 micron diameter electron beam. The instrument was calibrated daily using the mineral standards and operating conditions listed in Table A1.3. An "in-house" standard (ABG - a basaltic glass) was analysed several times each day to monitor instrument precision.

Table A1.3 Calibration standards and operating conditions for microprobe analyses

Element	Mineral	Concentration (in %)	Crystal	Peak angles	Std.	Unk.
Si	wollastonite	2.05	TAP	16.04	20	30
Ti	rutile	5.95	PET	18.232	15	30
Al	jadeite	3.28	TAP	18.851	30	30
Cr	metal	100.00	LiF	34.639	20	50
Fe	fayalite	52.95	LiF	28.72	30	50
Mn	metal	100.00	LiF	31.45	20	50
Mg	forsterite	25.52	TAP	22.579	30	30
Ca	wollastonite	34.16	PET	22.494	20	30
Na	jadeite	11.20	TAP	27.573	40	30
K	KCl	52.45	PET	25.24	15	30
Ba	barite	57.11	PET	18.413	20	50
F	LIF	73.25	TAP	45.36	80	100
Cl	KCl	47.55	PET	32.64	20	30

A (vii) Oxygen isotope analyses

Quartz for oxygen isotope analyses was handpicked after magnetic separation to remove ferromagnesian minerals. Oxygen was extracted in an oxygen extraction line by reacting the quartz separate with chlorine trifluoride in sealed reaction vessels. The extracted oxygen was converted to CO_2 and isotope analyses were carried out on a Sira 34 mass-spectrometer. Typically, sample sizes were in the range 10 - 15 mg. Duplicate analyses were carried out for several samples and precision was about ± 0.3‰. The standard sample NBS 28 gave $\delta\ ^{18}O$ values in the range 9.64 to 9.78‰.

A (viii) Age significance of lead data

The simple relationship between time and the slope of a line defined by data on a $^{207}Pb/^{204}Pb$ vs. $^{206}Pb/^{204}Pb$ diagram may be demonstrated by considering the following equations. The equation of an isochron on a $^{207}Pb/^{204}Pb$ vs. $^{206}Pb/^{204}Pb$ diagram is

$$\frac{^{207}Pb/^{204}Pb - (^{207}Pb/^{204}Pb)_o}{^{206}Pb/^{204}Pb - (^{206}Pb/^{204}Pb)_o} = \frac{1}{137.8} \times \frac{e^{\lambda 2tn-1} - e^{\lambda 2tn}}{e^{\lambda 1tn-1} - e^{\lambda 1tn}}$$

where o refers to initial lead isotopic compositions and where λ_1 and λ_2 are the decay constants of U^{238} and U^{235} respectively. The slope of the line (isochron) is defined by

$$\frac{1}{137.8} \times \frac{e^{\lambda 2tn-1} - e^{\lambda 2tn}}{e^{\lambda 1tn-1} - e^{\lambda 1tn}}$$

however $\frac{^{207}Pb/^{204}Pb - (^{207}Pb/^{204}Pb)_o}{^{206}Pb/^{204}Pb - (^{206}Pb/^{204}Pb)_o}$ is also equal to $(^{207}Pb/^{206}Pb)^*$

where $(^{207}Pb/^{206}Pb)^*$ is the ratio of radiogenic ^{207}Pb to radiogenic ^{206}Pb. Therefore

$$(^{207}Pb/^{206}Pb)^* = \frac{1}{137.8} \times \frac{e^{\lambda 2tn-1} - e^{\lambda 2tn}}{e^{\lambda 1tn-1} - e^{\lambda 1tn}}$$

Compatible values of t and $(^{207}Pb/^{206}Pb)^*$ have been worked out (Stacey and Stern, 1973) so that t can be calculated from the slope of the isochron.

Appendix B - Analytical data

B (i) XRF DATA

Bloedkoppie granite

	KND1.1	KND1.2	KND1.3	KND1.4	KND1.5	KND2.1	KND2.2	KND2.3	KND2.4	KND2.5
SiO_2	73.25	74.55	74.42	75.99	75.54	74.96	74.19	74.52	73.89	75.07
TiO_2	0.21	0.23	0.15	0.07	0.07	0.20	0.20	0.20	0.20	0.19
Al_2O_3	13.72	13.25	13.62	14.04	13.92	13.23	13.57	13.32	13.73	13.58
Fe_2O_3	1.81	2.12	1.47	0.69	0.57	1.65	1.84	1.72	1.81	1.66
MnO	0.07	0.07	0.04	0.02	0.03	0.05	0.05	0.05	0.05	0.05
MgO	0.22	0.22	0.42	0.27	0.11	0.08	0.28	0.18	0.38	0.48
CaO	1.25	1.29	1.16	1.09	1.03	1.23	1.28	1.23	1.27	1.17
Na_2O	2.89	2.86	3.24	3.48	3.34	3.04	3.10	3.37	3.36	3.04
K_2O	5.56	5.30	5.42	5.27	5.31	5.44	5.48	5.55	5.36	5.48
P_2O_5	0.05	0.02	0.0	0.04	0.06	0.0	0.02	0.04	0.0	0.0
L.O.I.	0.56	0.66	0.46	0.51	0.36	0.42	0.41	0.34	0.61	0.35
Total	99.61	100.61	100.46	101.41	100.33	100.40	100.57	100.73	100.92	101.11
Ba	424	405	314	123	120	355	409	354	432	326
Ce	116	131	96	NA	NA	109	106	117	110	128
Co	NA	6	3	NA	NA	4	5	3	4	3
Cr	4	5	4	5	NA	6	6	6	6	5
Hf	NA	6	8	NA	NA	8	7	8	8	7
La	73	66	46	NA	NA	52	53	58	55	56
Ni	3	7	3	0	2	4	4	4	5	4
Nb	24	26	15	12	12	21	21	20	20	21
Pb	39	39	37	44	47	34	36	34	34	34
Rb	269	251	235	235	241	237	242	244	234	233
Sr	98	94	80	56	57	85	92	80	94	83
Ta	NA	2	2	NA	NA	2	3	2	4	2
Th	35	40	26	23	22	38	31	37	31	45
V	6	7	1	NA	NA	2	4	3	1	5
Y	31	39	20	13	13	31	29	32	29	29
Zr	182	173	112	45	45	148	139	135	154	152

Bloedkoppie granite XRF data (contd)

	KND 2.6	BL1	BL2	BL3
SiO_2	73.51	76.03	76.02	76.25
TiO_2	0.19	0.08	0.10	0.09
Al_2O_3	13.16	13.46	13.74	13.67
MnO	0.05	0.05	0.06	0.04
MgO	0.26	0.16	0.12	0.00
CaO	1.17	1.04	1.02	0.98
Na_2O	3.70	4.17	3.46	3.21
K_2O	5.28	5.04	5.04	5.17
P_2O_5	0.0	0.0	0.0	0.0
L.O.I	0.30	0.26	0.40	0.46
Total	99.26	101.28	101.23	101.01

Ba	300	106	92	176
Ce	115	33	42	33
Co	5	2	3	2
Cr	6	4	1	2
Hf	6	8	8	9
La	50	12	18	17
Ni	6	3	6	4
Nb	21	29	38	19
Pb	38	48	45	45
Rb	265	307	300	295
Sr	78	39	36	42
Ta	3	1	1	1
V	5	ND	1	ND
Y	32	33	46	29
Zr	123	47	55	49

Donkerhuk granite

	R73	R75	R76	R77	R78	R80	R100	R101
SiO_2	74.33	72.42	66.66	69.59	69.68	64.27	72.85	74.57
TiO_2	0.10	0.29	0.83	0.45	0.49	1.12	0.24	0.25
Al_2O_3	13.88	14.42	15.79	15.47	15.40	15.95	13.62	13.88
Fe_2O_3	0.83	1.84	5.06	3.24	3.41	5.68	1.65	1.81
MnO	0.03	0.03	0.08	0.08	0.07	0.12	0.05	0.06
MgO	0.32	0.69	1.55	1.14	1.25	1.95	0.56	0.58
CaO	0.85	0.91	2.50	2.19	2.18	3.32	1.10	1.10
Na_2O	3.42	2.52	3.73	3.17	3.16	3.51	3.23	3.33
K_2O	5.33	5.90	3.07	4.79	4.49	2.68	5.05	5.12
P_2O_5	0.07	0.13	0.37	0.15	0.13	0.30	0.07	0.11
L.O.I	0.81	0.83	0.92	0.83	0.82	0.87	0.45	0.56
Total	100.10	100.32	100.69	101.40	101.19	99.90	98.99	101.62
Ba	638	722	689	686	582	549	383	450
Ce	27	125	94	57	65	107	58	68
Co	4	5	11	7	10	12	4	4
Cr	12	10	12	14	13	13	12	11
Hf	7	5	6	6	6	9	9	6
La	17	54	45	28	30	47	27	33
Ni	6	7	10	13	10	9	7	4
Nb	9	11	24	18	16	23	12	13
Pb	44	44	29	37	35	29	38	26
Rb	130	194	210	226	225	149	222	95
Sr	102	136	203	148	148	220	82	231
Ta	2	2	ND	1	2	3	2	2
Th	15	60	11	18	25	16	17	16
V	6	21	59	47	45	84	18	24
Y	33	22	33	47	37	41	54	28
Zr	89	203	289	156	165	282	141	199

Donkerhuk granite (contd)

	R102	R105	R108	R100	R112	R114	R115	R117
SiO_2	73.66	73.26	71.32	73.40	72.68	72.36	71.74	71.64
TiO_2	0.22	0.22	0.40	0.18	0.18	0.16	0.21	0.24
Al_2O_3	13.86	13.98	14.59	14.97	14.30	14.37	14.44	14.62
Fe_2O_3	1.63	1.75	2.79	1.35	1.42	1.42	1.54	1.74
MnO	0.06	0.05	0.06	0.05	0.06	0.04	0.04	0.04
MgO	0.49	0.34	1.06	0.53	0.61	0.22	0.50	0.78
CaO	1.03	0.90	1.63	1.60	1.04	0.86	0.94	1.35
Na_2O	3.20	3.42	3.29	3.70	3.94	2.70	2.63	3.96
K_2O	5.39	5.46	4.94	4.25	4.70	6.03	6.37	4.52
P_2O_5	0.12	0.11	0.19	0.10	0.18	0.22	0.28	0.14
L.O.I.	0.40	0.39	0.58	0.58	0.59	0.68	0.79	0.62
Total	100.15	100.15	101.01	101.02	99.75	99.33	99.77	99.78
Ba	381	411	820	603	426	495	405	372
Ce	55	59	80	37	41	36	35	62
Co	1	4	4	2	3	3	2	3
Cr	12	11	13	11	11	12	12	11
Hf	7	7	3	5	4	6	5	6
La	29	39	42	19	18	18	18	26
Ni	9	8	9	7	6	7	6	5
Nb	15	12	19	9	16	14	17	19
Pb	38	41	39	50	47	42	46	36
Rb	259	291	187	147	218	237	170	154
Sr	78	86	175	169	113	89	80	99
Ta	4	3	4	2	4	3	2	3
Th	16	12	20	9	11	3	5	23
V	17	14	35	17	14	10	13	18
Y	38	44	31	26	22	25	27	23
Zr	133	129	182	101	107	99	125	160

Donkerhuk granite (contd)

	S101	S104	S105	S1113	S116	S117	S118	S119
SiO_2	71.06	72.99	73.96	73.14	74.17	72.15	69.01	72.92
TiO_2	0.34	0.30	0.21	0.24	0.20	0.31	0.44	0.28
Al_2O_3	14.74	15.06	14.35	14.83	14.72	15.10	15.21	15.16
Fe_2O_3	2.53	2.20	1.51	2.10	1.46	2.12	3.19	1.78
MnO	0.03	0.03	0.02	0.02	0.03	0.03	0.08	0.03
MgO	0.70	0.55	0.22	0.65	0.52	0.69	1.01	0.57
CaO	2.18	2.13	2.05	1.79	1.33	1.90	2.11	2.00
Na_2O	4.32	4.41	4.28	3.76	4.00	4.15	3.22	4.05
K_2O	2.38	2.58	2.39	3.45	4.45	3.11	4.74	3.34
P_2O_5	0.08	0.06	0.07	0.06	0.12	0.12	0.15	0.12
L.O.I.	1.02	0.52	0.70	0.73	0.55	0.66	0.65	0.44
Total	99.36	100.84	99.78	100.77	100.52	100.33	99.72	100.69
Ba	450	539	556	873	704	652	526	651
Ce	68	60	44	54	38	47	50	41
Co	4	4	4	2	2	5	2	6
Cr	11	11	10	10	10	10	10	6
Hf	6	6	7	7	6	9	6	5
La	33	32	22	30	23	23	27	21
Ni	4	6	2	6	5	4	3	3
Nb	13	10	6	4	9	12	10	9
Pb	26	28	26	26	30	26	26	28
Rb	95	90	82	87	115	98	88	98
Sr	231	239	225	280	220	271	281	275
Ta	2	2	1	2	2	1	2	1
Th	16	13	4	8	6	10	6	8
V	24	25	19	16	14	22	25	21
Y	28	28	16	28	18	16	18	17
Zr	199	186	162	165	108	163	169	144

Goanikontes alaskite

	GO	G1	G2	G3	G5	G7	G8	G9	G10
SiO_2	68.77	75.89	70.92	74.20	73.71	72.60	75.76	74.50	71.77
TiO_2	0.0	0.06	0.13	0.0	0.02	0.0	0.07	0.09	0.11
Al_2O_3	17.04	13.85	15.70	14.87	14.74	14.65	13.97	13.39	15.84
Fe_2O_3	0.0	0.22	0.71	0.0	0.14	0.0	0.17	0.19	1.27
MnO	0.0	0.02	0.04	0.0	0.02	0.03	0.01	0.02	0.03
MgO	0.16	0.29	0.76	0.12	0.0	0.24	0.26	0.09	0.54
CaO	0.68	1.25	2.37	0.94	1.47	0.32	1.48	0.87	2.96
Na_2O	2.26	2.56	3.52	2.39	2.90	1.86	2.48	1.84	3.93
K_2O	10.30	6.38	5.00	8.09	7.00	9.55	5.77	7.60	3.73
P_2O_5	0.0	0.02	0.05	0.06	0.05	0.0	0.0	0.0	0.11
L.O.I.	0.36	0.66	0.76	0.42	0.51	0.39	0.68	0.50	0.59
Total	99.64	100.53	99.96	101.16	100.55	99.64	100.60	99.07	99.89
Ba	839	234	233	369	314	1748	204	209	169
Ce	1	19	22	18	13	0	18	39	27
Co	1	4	4	0	2	2	1	5	1
Cr	9	10	10	8	9	11	9	9	8
Hf	9	3	4	4	4	7	7	6	6
La	7	8	8	7	8	4	11	15	11
Ni	4	3	6	3	2	4	3	2	5
Nb	5	6	11	6	4	4	7	7	13
Pb	32	41	40	35	21	30	37	36	50
Rb	458	310	276	382	344	419	264	347	209
Sr	166	90	104	107	107	197	85	86	102
Ta	2	2	2	2	1	13	3	4	3
Th	6	47	36	30	0	0	38	29	79
V	3	9	12	5	7	5	9	7	13
Y	9	25	26	24	16	8	29	25	49
Zr	19	0	2	5	0	65	71	107	0

Rossing alaskite

	PRU1	PRU2	PRU3	PRU4	PRU5	PRU6	ROS2	ROS3	ROS4
SiO_2	76.27	73.54	75.66	73.95	73.31	74.03	77.83	78.15	73.52
TiO_2	0.16	0.18	0.13	0.07	0.20	0.62	0.03	0.05	0.05
Al_2O_3	12.75	14.03	13.28	13.80	14.13	10.84	12.55	13.00	15.13
Fe_2O_3	0.80	0.86	0.44	0.31	1.29	3.65	0.17	0.27	0.29
MnO	0.02	0.01	0.01	0.01	0.02	0.05	0.01	0.01	0.01
MgO	0.28	0.39	0.25	0.10	0.39	1.30	0.15	0.25	0.15
CaO	0.53	0.69	0.62	1.03	0.56	0.73	0.36	0.36	0.46
Na_2O	2.73	2.87	2.93	3.76	3.24	1.67	3.31	3.56	4.16
K_2O	5.69	6.45	6.21	4.88	6.67	5.33	5.74	5.12	6.68
P_2O_5	0.09	0.09	0.09	0.15	0.13	0.38	0.07	0.05	0.10
Total	99.98	99.59	100.08	98.63	100.55	99.30	97.65	101.37	100.96
Ba	98	146	121	87	180	187	NA	NA	NA
Ce	ND	36	ND	ND	47	14	NA	NA	NA
Co	ND	ND	ND	ND	ND	5	NA	NA	NA
Cr	43	53	56	32	50	40	NA	NA	NA
La	8	23	5	6	29	7	NA	NA	NA
Ni	4	ND	ND	3	3	8	11	6	6
Nb	18	23	14	14	20	68	41	6	8
Pb	41	53	39	37	43	86	41	59	32
Rb	347	337	284	278	369	380	285	307	350
Sr	29	46	41	60	41	45	21	31	34
Th	11	48	12	1	52	53	40	54	68
V	4	13	6	0	9	55	NA	NA	NA
Y	10	19	12	14	14	54	31	28	35
Zr	92	80	41	61	42	50	45	77	60
U	59	437	47	25	48	919	384	260	214

Rossing alaskite (contd)

	ROS5	ROS6	ROS6A	ROS7	ROS9	ROS18R	ROS18W
SiO_2	76.59	75.09	75.71	77.51	76.10	73.82	74.61
TiO_2	0.03	0.06	0.01	0.03	0.04	0.04	0.06
Al_2O_3	13.87	14.44	13.52	13.19	14.48	14.11	13.91
Fe_2O_3	0.20	0.37	0.15	0.25	0.30	0.54	0.35
MnO	0.01	0.01	0.01	0.01	0.01	0.02	0.03
MgO	0.31	0.25	0.15	0.31	0.15	0.25	0.34
CaO	0.37	0.43	0.67	0.46	1.87	0.90	0.53
Na_2O	3.81	3.82	3.70	3.94	5.51	3.83	3.64
K_2O	5.84	6.18	5.28	5.46	1.81	5.99	6.17
P_2O_5	0.05	0.05	0.07	0.09	0.05	0.38	0.18
L.O.I	0.63	0.64	0.54	0.42	0.42	0.82	0.61
Total	101.69	101.33	99.61	101.68	100.55	100.70	100.41
Ni	4	6	4	6	6	6	6
Nb	7	14	5	16	15	12	17
Pb	48	51	44	35	57	63	67
Rb	342	331	314	287	101	340	349
Sr	33	36	59	26	23	36	38
Th	31	44	30	19	46	124	106
Y	24	37	7	29	51	74	62
Zr	134	78	67	74	101	85	129
U	456	538	21	236	540	772	886

Swakopmund Salem granite

	SM1	SM2	SM3	SM4	SM5	SM6
SiO_2	70.46	71.24	70.08	69.98	69.44	70.08
TiO_2	0.51	0.48	0.48	0.53	0.50	0.51
Al_2O_3	14.90	14.75	14.85	14.90	14.73	14.89
Fe_2O_3	3.14	2.95	3.00	3.31	3.35	3.23
MnO	0.05	0.05	0.05	0.07	0.0	0.05
MgO	1.15	1.14	0.95	1.12	1.23	1.15
Na_2O	2.74	3.46	2.97	2.89	3.38	3.10
K_2O	4.71	3.99	4.25	4.86	4.83	5.04
P_2O_5	0.11	0.12	0.14	0.10	0.14	0.13
LOI	0.65	0.97	0.95	0.49	0.55	0.49
Total	100.44	100.34	99.79	100.16	100.27	100.70
Ba	458	428	423	470	462	434
Ce	77	62	68	95	85	64
Co	8	5	9	7	9	7
Cr	33	36	34	37	33	32
Hf	9	8	7	7	6	7
La	40	28	34	45	36	34
Ni	10	10	10	12	11	11
Nb	32	29	28	37	28	30
Pb	36	36	38	37	37	37
Rb	271	186	207	232	237	248
Sr	138	132	130	137	142	137
Ta	3	3	2	3	3	3
Th	23	21	22	26	20	21
V	43	42	47	48	43	45
Y	47	43	43	42	49	42
Zr	184	179	173	187	181	177

Palmental diorite

	P2094	P2095	P2096	P2097	P2171	P2172	P2177	PUAT1
SiO_2	51.74	53.74	52.96	53.61	55.66	54.72	54.68	49.54
TiO_2	0.97	0.99	0.96	0.96	1.14	1.16	1.13	2.69
Al_2O_3	15.21	15.76	15.18	15.71	15.59	15.63	16.05	6.54
Fe_2O_3	8.53	8.93	8.96	8.78	8.45	8.92	8.92	15.01
MnO	0.18	0.18	0.14	0.17	0.16	0.16	0.15	0.36
MgO	4.82	4.88	4.48	4.75	3.41	0.16	3.72	8.24
CaO	8.82	8.80	8.79	8.47	7.29	7.81	7.73	11.80
Na_2O	2.64	3.12	2.47	2.92	3.56	3.18	3.61	1.00
K_2O	2.54	2.82	2.96	3.39	3.68	3.20	2.39	0.68
P_2O_5	0.38	0.47	0.40	0.38	0.48	0.50	0.51	0.77
L.O.I	1.76	0.91	1.29	1.08	0.64	0.76	0.82	0.82
Total	97.49	100.60	98.57	100.21	100.06	99.41	99.68	97.47
Ni	35	16	29	22	18	18	12	34
Nb	11	16	15	16	24	23	24	80
Pb	15	15	9	16	24	18	18	5
Rb	82	110	117	129	159	131	112	11
Sr	850	835	840	902	1148	1113	937	60
Th	8	12	8	12	15	16	12	35
V	227	192	203	198	221	242	183	432
Y	29	30	30	30	24	26	31	70
Zr	135	163	173	172	143	171	189	344

	Palmental diorite				
	P2178	P2184	P2186	P2196	P2197
SIO_2	56.68	61.98	62.42	58.24	55.99
TiO_2	1.03	0.69	0.61	1.00	1.06
Al_2O_3	16.34	16.69	15.97	15.62	16.13
Fe_2O_3	8.30	5.33	4.81	7.46	8.06
MnO	0.15	0.12	0.10	0.13	0.13
MgO	3.45	2.19	1.98	2.76	3.06
CaO	7.08	5.01	4.75	5.92	6.95
Na_2O	3.43	4.41	4.73	3.67	3.53
K_2O	2.85	3.68	3.43	4.27	3.35
P_2O_5	0.47	0.26	0.23	0.42	0.48
L.O.I.	0.86	0.54	0.74	0.68	0.70
Total	100.64	100.89	99.74	100.17	99.44
Ni	13	9	13	17	9
Nb	22	31	26	31	34
Pb	23	24	24	20	15
Rb	106	117	168	126	105
Sr	959	1348	1175	919	1043
Th	9	21	24	17	18
Y	27	23	19	31	32
Zr	192	258	216	232	216

Horebis- River granite

	YC1	YC3	YC4	YC5	YC6	YC8	YC9	YC10	YC11	YC12
SiO_2	77.05	76.50	74.35	73.19	73.31	77.48	76.28	74.28	76.60	72.98
TiO_2	0.23	0.25	0.31	0.37	0.35	0.11	0.25	0.36	0.23	0.34
Al_2O_3	12.04	12.36	13.38	12.87	13.05	12.77	12.24	13.19	12.24	13.05
Fe_2O_3	1.49	1.67	2.47	2.14	2.75	1.19	1.59	2.34	1.20	2.62
MnO	0.0	0.02	0.02	0.03	0.02	0.0	0.01	0.02	0.02	0.01
MgO	0.03	0.09	0.30	0.52	0.37	0.32	0.25	0.23	0.06	0.40
CaO	0.07	0.54	0.38	1.30	0.56	0.18	0.45	0.57	0.99	0.53
Na_2O	2.36	3.08	3.05	3.20	2.80	3.37	2.96	3.27	2.77	2.96
K_2O	6.44	5.71	6.24	5.92	5.94	5.45	6.36	5.58	5.87	6.34
P_2O_5	0.0	0.0	0.05	0.0	0.0	0.0	0.03	0.0	0.0	0.0
LOI	0.51	0.35	0.46	1.12	0.56	0.42	0.37	0.51	0.58	0.51
Total	100.22	100.56	101.12	100.65	99.70	101.28	100.80	100.36	100.55	99.75
Ba	226	351	438	427	521	204	300	630	239	471
Ce	104	110	118	177	166	127	162	128	153	170
Co	5	2	3	4	4	3	4	4	5	3
Cr	4	2	6	3	2	3	5	6	4	6
Hf	10	8	9	10	10	10	9	9	9	10
La	41	54	51	85	82	63	80	64	75	82
Ni	3	0	5	3	6	1	2	5	2	5
Nb	86	43	79	89	79	100	48	72	51	77
Pb	73	18	19	21	20	21	18	22	19	18
Rb	212	154	197	158	151	122	188	124	173	169
Sr	21	54	39	47	41	37	43	52	55	45
Ta	5	4	6	5	2	7	4	3	5	4
Th	32	17	26	26	26	40	33	18	36	29
V	3	8	8	8	8	7	9	4	5	12
Y	39	32	62	67	58	54	37	55	45	58
Zr	236	188	340	370	370	221	188	326	160	382

Salem Onanis granite

	GG1	GG2	GG3	GG4	GG5	GG6	GG7	GG8	GG9	GG10
SiO_2	73.25	72.20	71.65	70.55	71.46	71.66	72.03	71.59	72.09	72.96
TiO_2	0.48	0.34	0.32	0.35	0.34	0.49	0.31	0.33	0.37	0.49
Al_2O_3	13.25	14.62	14.24	14.83	14.51	13.81	14.35	14.24	14.22	13.17
Fe_2O_3	2.10	2.30	2.32	2.61	2.39	2.78	2.32	2.53	2.43	2.30
MnO	0.04	0.04	0.05	0.05	0.03	0.05	0.06	0.04	0.03	0.04
MgO	0.60	0.77	0.79	1.05	0.92	1.10	0.59	0.57	1.00	0.69
CaO	1.25	2.15	2.02	2.38	2.16	1.34	2.01	2.18	2.30	1.33
Na_2O	1.84	3.21	3.01	3.32	3.02	2.34	3.10	2.86	3.29	2.25
K_2O	6.08	4.42	4.58	4.21	4.55	6.23	4.89	4.67	3.82	6.21
P_2O_5	0.11	0.12	0.0	0.06	0.0	0.09	0.05	0.05	0.0	0.09
LOI	0.83	1.20	0.61	0.74	0.97	0.86	0.68	1.02	0.94	0.96
Total	99.92	101.18	99.59	100.14	100.35	100.76	100.47	100.09	100.49	100.49
Ba	1308	845	749	817	700	1278	699	582	817	1299
Ce	240	95	76	104	90	231	82	84	91	246
Co	7	5	5	8	0	8	7	6	5	5
Cr	4	16	14	15	17	12	13	16	6	15
Hf	8	9	7	3	NA	7	7	7	8	7
La	124	49	45	60	53	119	43	42	49	133
Ni	4	5	4	7	57	6	5	5	4	5
Nb	28	10	9	9	11	26	12	11	10	27
Pb	34	26	27	25	34	31	29	27	30	32
Rb	225	138	125	141	151	267	165	135	117	250
Sr	238	265	256	318	278	242	223	231	272	247
Ta	1	2	0	2	0	2	0	0	1	0
Th	34	17	16	18	19	30	6	20	17	34
V	26	26	29	39	33	40	27	30	33	31
Y	22	12	13	12	13	22	13	9	14	21
Zr	331	110	111	119	132	232	100	106	145	329

Sorris-Sorris granite

	654	662	663	664	665	666	667	673	2198	2199
SiO_2	72.85	72.59	75.26	72.74	73.99	73.78	71.26	72.55	75.15	74.05
TiO_2	0.22	0.28	0.12	0.17	0.23	0.27	0.40	0.26	0.13	0.19
Al_2O_3	14.31	14.01	13.39	13.53	13.94	13.78	13.85	13.91	13.67	13.38
Fe_2O_3	1.93	2.16	0.81	1.48	1.68	1.71	2.64	2.09	0.97	1.64
MnO	0.04	0.03	0.03	0.03	0.04	0.03	0.04	0.06	0.03	0.02
MgO	0.16	0.29	0.31	0.33	0.25	0.27	0.23	0.36	0.18	0.15
CaO	1.24	1.24	0.54	1.14	1.08	1.22	1.30	1.19	0.85	1.07
Na_2O	3.05	2.94	4.66	4.32	3.35	2.74	2.88	3.66	3.63	3.74
K_2O	5.18	5.65	5.51	5.13	5.25	5.91	6.12	3.36	4.75	4.86
P_2O_5	0.07	0.0	0.03	0.0	0.06	0.14	0.04	0.0	0.06	0.09
LOI	0.56	0.51	0.58	1.07	0.92	0.54	1.07	1.27	0.98	1.06
Total	99.23	99.68	101.25	99.97	100.78	100.04	99.78	100.88	100.40	100.23
Ba	NA	1392	304	503	742	371	590	762	NA	NA
Ce	NA	219	96	109	119	149	267	186	NA	NA
Co	NA	3	4	4	5	4	0	4	NA	NA
Cr	NA	279	261	227	231	281	230	244	NA	NA
Hf	NA	10	6	5	9	8	12	4	NA	NA
La	NA	120	47	60	62	68	131	92	NA	NA
Nb	22	20	25	32	33	44	62	43	47	60
Pb	29	31	23	26	27	24	22	19	31	35
Rb	244	219	295	321	297	261	301	279	204	210
Sr	170	213	48	98	140	115	92	117	79	83
Th	47	50	53	52	50	47	52	57	20	29
V	NA	19	3	7	13	9	13	19	NA	NA
Y	54	31	81	52	44	63	53	72	68	80
Zr	193	250	94	152	180	194	323	229	108	131

Salem Goas

	R126	R127	R128	R130	R131	R132	R133	R134	S149	S150
SiO_2	70.33	68.40	69.67	67.7	61.40	70.51	67.99	65.82	68.63	69.25
TiO_2	0.37	0.50	0.42	0.72	0.71	0.38	0.48	0.35	0.48	0.41
Al_2O_3	15.41	14.98	14.98	14.70	17.13	14.57	15.04	16.37	15.43	15.23
Fe_2O_3	2.56	3.38	2.90	5.20	5.09	2.67	3.43	2.47	3.44	2.89
MnO	0.05	0.07	0.06	0.11	0.11	0.06	0.08	0.05	0.07	0.06
MgO	1.00	1.22	1.27	2.18	2.06	1.04	1.42	1.09	1.37	1.06
CaO	2.07	2.39	2.20	2.75	2.56	2.34	2.49	1.74	2.40	2.18
Na_2O	3.15	3.12	3.47	3.26	3.19	2.84	3.14	3.01	3.84	3.41
K_2O	5.60	4.68	4.99	3.58	5.90	4.63	4.57	7.18	4.52	5.13
P_2O_5	0.13	0.11	0.05	0.29	0.19	0.06	0.11	0.07	0.18	0.09
L.O.I.	0.72	0.77	0.58	0.86	0.73	0.76	0.75	0.66	0.70	0.69
Total	101.37	99.63	100.68	101.24	99.06	99.80	99.51	98.82	101.07	100.40
Ba	918	1002	861	661	1226	952	909	1425	878	869
Ce	89	106	103	147	218	78	111	99	112	102
Co	4	6	8	10	12	5	6	7	6	6
Cr	12	14	12	17	24	14	15	23	13	12
Hf	7	4	6	8	7	5	5	6	6	7
La	50	55	54	75	113	43	57	56	59	55
Nb	14	15	15	22	21	13	15	13	19	15
Pb	42	39	39	31	41	38	38	48	38	39
Rb	167	162	161	193	254	161	171	218	165	164
Sr	252	275	249	220	287	249	249	281	261	253
Ta	0	4	2	1	3	1	2	1	5	3
Th	23	22	29	24	34	15	14	15	32	26
V	31	43	23	74	77	39	50	40	48	41
Y	22	25	23	33	35	20	26	23	26	24
Zr	164	197	171	232	245	152	169	136	197	177

Namibfontein red granite

	N1	N2	N3	N4	N6	N7	N8	N9
SiO_2	72.90	72.03	72.20	73.59	73.08	72.88	72.73	72.56
TiO_2	0.33	0.34	0.35	0.14	0.35	0.33	0.36	0.35
Al_2O_3	13.94	14.31	13.98	14.16	14.17	13.87	14.02	13.95
Fe_2O_3	2.40	2.47	2.30	1.24	2.41	2.41	2.27	2.24
MnO	0.05	0.05	0.03	0.023	0.05	0.04	0.04	0.04
MgO	0.45	0.52	0.34	0.14	0.38	0.48	0.51	0.38
CaO	1.33	1.28	0.99	1.10	1.34	1.40	1.27	1.49
Na_2O	3.06	2.96	2.66	2.29	2.78	3.22	2.75	2.71
K_2O	5.99	6.48	6.88	7.41	5.88	5.87	6.63	6.04
P_2O_5	0.12	0.15	0.14	0.05	0.12	0.09	0.06	0.10
L.O.I.	0.42	0.46	0.33	0.48	0.43	0.60	0.47	0.55
Total	100.98	101.05	100.20	100.62	100.99	101.17	100.85	100.41
Ba	633	596	667	557	610	581	625	545
Ce	123	121	94	19	131	100	109	113
Co	4	4	6	4	4	4	5	4
Cr	15	8	9	6	8	12	5	9
Hf	6	7	8	9	8	9	8	8
La	58	58	46	9	65	47	49	55
Ni	4	3	4	4	4	3	4	1
Nb	13	14	14	7	15	14	27	15
Pb	34	27	32	33	38	34	32	32
Rb	302	324	342	331	251	257	287	281
Sr	113	142	142	148	123	157	125	123
Ta	4	4	2	1	3	4	4	3
Th	61	62	49	3	68	47	49	69
V	15	16	20	11	17	24	13	20
Y	27	24	23	13	24	18	21	24
Zr	201	208	221	88	219	246	236	199

Otjua red granite

	O1	O2	O3	O4	O5	O6	O7	O8	O9	O10
SiO_2	75.41	75.87	75.56	75.42	75.59	75.54	74.39	77.24	76.55	74.79
TiO_2	0.12	0.11	0.17	0.09	0.09	0.14	0.13	0.07	0.09	0.10
Al_2O_3	14.54	13.57	13.23	13.65	14.25	13.79	13.87	13.58	13.41	14.35
Fe_2O_3	0.97	1.29	1.35	0.74	0.86	1.30	0.92	0.82	0.87	1.12
MnO	0.02	0.01	0.01	0.0	0.01	0.01	0.03	0.02	0.02	0.02
MgO	0.0	0.0	0.26	0.23	0.25	0.08	0.0	0.10	0.0	0.37
CaO	0.78	0.69	0.02	0.0	0.70	0.85	1.16	0.26	0.97	1.04
Na_2O	3.31	2.85	2.22	2.25	3.52	2.77	3.06	3.36	3.20	3.33
K_2O	5.94	6.02	8.23	8.41	6.10	6.07	5.50	5.65	5.47	5.87
P_2O_5	0.0	0.0	0.06	0.06	0.02	0.05	0.0	0.0	0.01	0.0
L.O.I	0.26	0.40	0.45	0.44	0.28	0.47	0.67	0.36	0.59	0.47
Total	101.35	100.82	101.56	101.28	101.69	100.05	99.97	101.45	101.20	101.45
Ba	118	191	358	336	251	208	93	113	85	96
Ce	28	30	45	25	33	37	24	18	26	26
Co	2	3	3	2	2	3	4	3	2	3
Cr	7	5	6	6	5	7	3	6	3	4
Hf	6	9	8	9	8	7	3	6	3	4
La	9	12	19	11	16	16	6	6	9	12
Nb	10	8	10	8	6	12	9	5	8	9
Pb	65	58	72	72	60	59	57	44	53	61
Rb	301	287	394	403	296	291	272	291	266	274
Sr	32	79	81	78	81	81	55	60	51	54
Th	37	34	42	24	30	38	28	8	24	21
V	5	9	11	7	11	9	6	6	6	6
Y	77	55	58	56	39	61	56	42	64	60
Zr	75	77	130	82	77	94	51	31	106	59

Dachsberg granite

	1012	1013	1014	1015	1030	1031	1032	1034	1035
SiO_2	74.90	75.12	74.41	74.14	75.51	77.13	75.96	76.67	75.28
TiO_2	0.27	0.28	0.25	0.26	0.13	0.13	0.11	0.10	0.13
Al_2O_3	13.11	12.80	12.77	13.02	12.46	12.77	12.76	13.16	12.49
Fe_2O_3	2.30	2.58	2.46	2.30	2.07	1.33	1.43	1.78	2.01
MnO	0.01	0.01	0.01	0.02	0.01	0.01	0.01	0.01	0.01
MgO	0.24	0.21	0.15	0.36	0.15	0.15	0.15	0.15	0.15
CaO	0.02	0.01	0.02	0.37	0.06	0.01	0.01	0.0 1	0.13
Na_2O	4.16	4.38	4.34	4.62	3.89	6.02	5.48	4.28	4.38
K_2O	5.35	5.22	5.15	5.01	5.12	2.36	2.88	4.60	4.47
P_2O_5	0.08	0.10	0.13	0.27	0.40	0.05	0.04	0.08	0.04
L.O.I.	0.52	0.37	0.50	0.57	0.38	0.47	0.66	0.50	0.45
Total	100.96	101.05	100.01	100.91	99.75	100.25	99.31	101.15	99.35
Nb	54	59	55	59	85	71	18	75	78
Pb	10	9	10	11	10	8	4	10	10
Rb	218	197	205	220	146	54	12	110	106
Sr	11	7	11	21	8	6	395	7	7
Th	15	6	14	31	22	22	3	16	16
Y	57	70	60	90	108	105	25	58	116
Zr	316	310	287	332	378	367	174	381	441
U	2	2	3	4	2	3	2	2	2

Leucocratic Stinkbank granite

	LS1	LS2	LS3	LS4	LS5	LS6	LS7	LS8	LS9	LS10
SiO_2	72.36	74.59	72.87	76.70	71.97	71.73	71.43	74.43	74.19	73.80
TiO_2	0.26	0.25	0.34	0.24	0.33	0.29	0.28	0.08	0.24	0.16
Al_2O_3	14.38	13.73	14.05	12.74	14.64	14.46	14.50	14.19	13.95	14.18
Fe_2O_3	2.21	1.99	2.63	1.79	2.75	2.44	2.11	0.78	0.04	0.03
MnO	0.05	0.03	0.06	0.04	0.06	0.05	0.04	0.03	0.04	0.03
MgO	0.46	0.46	0.42	0.33	0.64	0.47	0.40	0.18	0.43	0.21
CaO	1.74	1.54	1.83	1.43	1.75	1.55	1.40	1.00	1.64	1.23
Na_2O	4.26	3.05	3.35	3.85	3.13	2.91	2.97	3.62	3.50	3.66
K_2O	4.97	4.92	4.35	4.10	4.69	4.67	5.31	6.36	4.07	5.62
P_2O_5	0.09	0.0	0.12	0.11	0.13	0.13	0.11	0.14	0.07	0.09
L.O.I.	0.42	0.38	0.31	0.28	0.48	0.56	0.59	0.57	0.60	0.42
Total	101.17	100.94	100.21	100.53	100.56	99.16	99.13	101.16	100.84	100.55
Ba	445	4289	409	222	410	407	496	448	331	395
Ce	51	37	39	18	52	52	50	12	48	20
Co	NA	4	6	0	4	4	4	0	3	0
Cr	33	12	18	54	25	13	13	9	13	9
La	23	19	36	24	32	31	23	20	18	14
Nb	14	13	17	14	18	14	13	6	12	12
Pb	40	37	34	36	39	38	40	45	35	40
Rb	214	192	203	180	226	229	241	232	197	207
Sr	127	120	126	93	121	115	115	109	104	111
Th	25	19	17	34	26	26	18	12	17	13
V	21	14	27	13	20	20	20	5	13	7
Y	18	18	21	13	26	19	20	15	15	18
Zr	143	151	165	116	167	158	138	64	158	69

Lofdal syenite

	28/26	28/27A	28/27B	28/28	28/29	28/30	28/31	28/33	28/41
SiO_2	60.08	55.58	54.81	51.14	54.36	49.51	54.59	56.80	47.24
TiO_2	0.70	0.22	0.23	0.39	0.20	1.04	0.28	0.51	1.42
Al_2O_3	21.50	19.49	19.49	22.91	19.25	19.58	19.83	20.16	16.05
Fe_2O_3	7.01	5.42	5.60	5.22	5.75	6.81	4.48	6.59	10.84
MnO	0.07	0.19	0.19	0.29	0.24	0.23	0.31	0.35	0.19
MgO	1.45	0.18	0.08	0.49	0.12	0.93	0.32	0.35	0.19
CaO	0.32	1.86	2.02	2.30	2.56	4.99	2.32	2.12	7.14
Na_2O	0.14	8.98	9.58	10.49	9.89	8.00	10.13	11.05	3.19
K_2O	5.24	5.68	5.74	3.09	6.02	6.32	7.22	2.15	3.82
P_2O_5	0.08	0.00	0.00	0.05	0.0	0.30	0.0	0.0	1.52
L.O.I.	2.93	2.92	3.18	5.96	3.23	2.25	2.71	2.59	2.03
Total	99.38	100.44	100.98	102.26	101.51	99.57	100.11	102.74	98.17
Ba	1135	156	NA	216	299	2436	397	222	3822
Ce	123	78	NA	135	121	106	161	290	315
Co	12	3	NA	5	0	5	4	0	23
Cr	52	7	NA	7	22	26	14	25	41
La	65	39	NA	80	60	54	91	157	152
Ni	18	2	NA	0	5	2	3	0	23
Nb	17	303	273	177	172	215	217	556	44
Pb	9	34	38	13	19	10	21	29	24
Rb	141	164	166	210	169	174	275	191	151
Sr	47	1132	1253	926	1254	1199	841	1288	3257
Th	21	5	6	4	1	2	6	6	7
Y	80	22	22	30	25	20	32	32	46
Zr	243	1463	1217	93	868	516	851	32	335
U	4	29	23	5	3	0	18	43	0

	Palmental granite				
	PG 2174	PG2175	PG2176	PG2	PG6
SiO_2	72.17	71.88	71.57	72.21	72.09
TiO_2	0.30	0.27	0.27	0.26	0.28
Al_2O_3	14.18	14.29	14.84	14.10	13.69
Fe_2O_3	2.50	2.30	2.22	2.25	2.22
MnO	0.04	0.03	0.03	0.03	0.03
MgO	0.38	0.42	0.45	0.42	0.24
CaO	1.23	1.18	1.14	1.20	1.21
Na_2O	2.56	3.01	2.69	3.82	3.08
K_2O	6.14	6.11	6.00	6.21	6.01
P_2O_5	0.01	0.13	0.12	0.17	0.09
L.O.I.	1.20	0.94	0.91	0.78	0.95
Total	100.81	100.57	100.23	101.47	99.58
Nb	21	22	21	19	19
Pb	51	50	52	53	52
Rb	298	311	298	298	300
Sr	95	93	93	100	99
Th	53	47	49	48	46
Y	36	27	30	27	25
Zr	227	221	217	215	217

Huab-River diorite

	RM129.5	RM129.6	RM129.11	RM129.12	RM129.13
SiO_2	53.63	61.13	57.59	57.15	61.82
TiO_2	0.87	0.63	0.77	0.81	0.55
Al_2O_3	16.50	15.84	15.30	16.99	16.10
Fe_2O_3	7.85	5.17	7.34	6.60	4.84
MnO	0.13	0.08	0.13	0.10	0.08
MgO	5.04	2.92	4.72	0.10	2.52
CaO	6.69	4.57	6.00	6.20	4.40
Na_2O	3.11	3.57	2.70	3.36	3.21
K_2O	3.24	3.85	3.76	3.26	3.72
P_2O_5	0.39	0.27	0.27	0.28	0.19
L.O.I.	2.43	1.92	1.76	1.55	1.58
Total	99.85	99.89	100.31	100.70	98.89
Nb	16	13	12	11	12
Pb	32	31	32	29	32
Rb	109	118	104	98	126
Sr	706	600	689	786	580
Th	31	26	17	23	25
Y	38	27	31	26	25
Zr	214	204	202	231	189

Swakop River diorite

	SRD1	SRD2	SRD4	P2139	P2140	P2141
SiO_2	57.17	58.76	57.18	60.75	59.81	59.19
TiO_2	0.85	0.91	0.81	0.74	0.79	0.86
Al_2O_3	17.13	18.13	17.95	16.98	17.52	18.57
Fe_2O_3	5.85	3.22	5.88	5.82	2.74	3.11
MnO	0.12	0.07	0.12	0.13	0.07	0.08
MgO	2.80	2.21	2.76	2.42	2.30	2.50
CaO	7.54	6.89	6.67	5.56	9.71	9.50
Na_2O	3.67	3.61	3.77	3.63	4.75	5.24
K_2O	4.18	5.58	4.05	3.42	1.54	2.14
P_2O_5	0.32	0.29	0.87	0.29	0.29	0.34
L.O.I.	0.40	0.62	0.87	0.74	0.87	0.92
Total	100.02	100.29	100.30	100.48	100.36	101.42
Nb	23	27	18	28	25	26
Pb	19	24	22	23	15	16
Rb	138	201	132	115	47	65
Sr	1404	1626	1469	1151	1657	1709
Th	7	14	7	23	15	14
Y	29	26	21	32	25	26
Zr	274	307	256	231	241	256

Otjimbingje syenite

	2179	2180	2181	2182	OSY1	OSY2	OSY3	OSY4	OSY5
SiO_2	55.04	51.93	58.94	58.84	54.53	55.48	56.54	58.34	59.32
TiO_2	0.91	1.03	0.90	0.89	0.90	0.85	0.70	0.60	0.57
Al_2O_3	13.99	11.61	13.50	14.78	13.96	14.42	14.80	15.69	14.14
Fe_2O_3	7.26	8.53	6.09	6.48	7.36	6.94	6.06	5.21	5.98
MnO	0.12	0.16	0.11	0.09	0.13	0.12	0.11	0.09	0.11
MgO	4.20	6.65	3.79	3.28	4.48	3.99	3.53	3.09	3.49
CaO	5.61	7.99	4.26	3.65	5.85	5.34	4.88	4.22	4.53
Na_2O	2.90	2.97	3.08	3.57	2.76	2.84	2.82	3.50	2.89
K_2O	7.84	5.81	7.39	7.66	7.90	7.99	8.58	8.52	7.58
P_2O_5	0.84	1.00	0.45	0.53	0.72	0.67	0.51	0.53	0.59
L.O.I.	0.57	0.68	0.57	0.51	0.83	0.75	1.09	0.44	0.78
Total	99.25	98.35	99.08	100.28	99.41	99.40	99.64	100.24	99.98
Nb	37	32	64	46	30	29	30	18	30
Pb	25	22	26	30	32	28	29	36	27
Rb	412	479	419	411	355	364	369	370	256
Sr	1050	907	679	772	1237	1268	1201	1350	945
Th	29	21	26	34	26	23	21	11	13
Y	47	55	38	37	35	44	46	29	40
Zr	271	247	285	305	244	227	231	145	138

Leucocratic Otjimbingwe Syenite

	LSY 7	LSY 8	LSY 9	LSY 2183	LSY 2184
SiO_2	61.28	62.19	63.36	61.73	61.98
TiO_2	0.71	0.72	0.63	0.69	0.69
Al_2O_3	16.34	16.21	16.19	16.60	16.69
Fe_2O_3	5.46	5.26	5.17	5.29	5.33
MnO	0.12	0.11	0.10	0.13	0.12
MgO	2.30	1.96	1.98	2.08	2.19
CaO	5.09	4.80	4.62	5.03	5.01
Na_2O	5.61	4.60	4.65	4.74	4.41
K_2O	3.72	3.87	3.89	3.75	3.68
P_2O_5	0.28	0.28	0.26	0.31	0.26
L.O.I.	0.89	0.53	0.74	0.56	0.54
Total	101.79	100.55	101.57	100.90	100.89
Nb	27	32	27	30	31
Pb	27	26	27	22	24
Rb	164	180	191	118	117
Sr	1180	1236	1055	1350	1348
Th	17	26	25	21	21
Y	23	24	20	23	23
Zr	268	252	232	253	258

Valencia alaskite

	26/59 90m	26/59 120.4m	26/59 140m	26/59 155m	26/59 217m	26/69 85m	26/69 137m	V21	V31
SiO_2	75.92	84.75	77.23	74.18	73.15	72.99	74.63	75.34	75.48
TiO_2	0.09	0.02	0.03	0.10	0.18	0.05	0.13	0.07	0.06
Al_2O_3	14.47	8.54	12.58	14.36	13.58	13.64	13.72	13.45	14.00
Fe_2O_3	0.26	0.00	0.00	0.37	1.07	0.14	0.63	0.53	0.37
MnO	0.01	0.01	0.0	0.01	0.03	0.01	0.02	0.01	0.02
MgO	0.23	0.0	0.06	0.25	0.54	0.0	0.30	0.15	0.11
CaO	0.95	0.11	0.0	0.89	1.05	0.52	0.69	0.69	0.92
Na_2O	2.84	0.68	1.66	2.78	5.06	3.12	2.46	4.09	3.47
K_2O	6.05	4.85	8.17	7.07	5.50	7.04	5.84	5.68	4.99
P_2O_5	0.11	0.06	0.0	0.0	0.06	0.08	0.09	0.09	0.16
LOI	0.32	0.66	0.43	0.36	0.81	0.55	0.66	0.54	0.41
Total	101.16	99.57	100.15	100.37	101.01	98.13	1200.73	100.58	99.00
Ba	NA	NA	545	639	583	298	NA	NA	NA
Ce	NA	NA	4	27	39	18	NA	NA	NA
Co	NA	NA	ND	ND	4	1	NA	NA	NA
Cr	NA	NA	9	9	13	16	NA	NA	NA
Hf	NA	NA	6	8	8	4	NA	NA	NA
La	9	5	3	15	18	5	NA	25	5
Ni	2	5	4	5	8	5	NA	ND	2
Nb	10	4	4	13	17	7	21	10	7
Pb	41	30	50	40	35	39	40	58	41
Rb	228	169	300	257	229	367	323	293	154
Sr	72	46	75	128	125	74	64	30	63
Th	4	10	ND	17	30	ND	16	58	7
Y	15	5	10	32	65	19	34	33	14
Zr	49	56	52	83	113	33	105	66	49
U	33	54	NA	NA	NA	NA	17	16	5

Valencia Salem granite

	V1	V3	V4	V5	V6	V8	V9	V10	V11
SiO_2	64.05	74.44	74.14	64.73	64.74	65.23	67.09	63.88	64.75
TiO_2	0.91	0.07	0.06	0.85	0.99	0.82	0.75	0.95	0.82
Al_2O_3	15.26	13.37	14.58	15.42	15.48	15.07	15.38	15.31	15.32
Fe_2O_3	5.97	0.49	0.49	5.68	6.28	5.47	4.63	5.90	5.48
MnO	0.09	0.01	0.05	0.09	0.10	0.10	0.08	0.10	0.09
MgO	1.92	0.12	0.19	1.77	2.08	1.85	1.64	1.87	1.81
CaO	3.18	0.90	0.49	3.12	3.28	3.06	2.67	3.62	3.24
Na_2O	3.25	3.87	2.23	3.36	3.14	2.86	3.19	3.51	2.99
K_2O	4.30	4.90	7.69	4.27	4.21	4.40	4.90	4.01	4.16
P_2O_5	0.22	0.13	0.18	0.24	0.29	0.21	0.23	0.22	0.26
L.O.I	0.63	0.57	0.11	0.66	0.40	0.47	0.83	0.74	0.50
Total	99.78	98.91	100.11	100.11	100.83	99.26	100.28	100.11	99.30
Ba	NA	674	NA	NA	NA	824	NA	781	NA
Ce	NA	115	NA	NA	NA	124	NA	137	NA
Co	NA	10	NA	NA	NA	10	NA	11	NA
Cr	NA	33	NA	NA	NA	32	NA	37	NA
Hf	NA	7	NA	NA	NA	6	NA	9	NA
La	55	57	61	63	61	58	72	67	59
Nb	21	27	29	28	29	25	23	30	25
Pb	27	29	25	22	22	30	27	31	23
Rb	212	190	214	208	213	206	221	207	203
Sr	209	193	202	201	197	193	208	199	208
Th	24	24	24	25	24	25	32	25	32
Y	38	51	54	41	54	44	28	60	28
Zr	267	264	282	278	285	271	285	293	271

Neutron activation REE data

	La	Ce	Nd	Sm	Eu	Tb	Tm	Yb	Lu
Bloedkoppie granite									
KND 1.1	64.85	122.19	51.54	9.63	1.28	1.13	0.36	2.48	0.39
KND2.5	58.25	113.53	50.34	9.02	1.19	0.98	0.35	2.52	0.40
BL1	12.82	24.83	13.18	4.01	0.61	0.79	0.47	3.49	0.58
BL2	17.64	33.61	18.04	5.37	0.63	1.02	0.52	4.17	0.71
Stinkbank leucogranite									
S2	92.23	195.39	83.05	16.05	0.66	1.94	0.50	2.91	0.43
S5	93.35	189.98	80.81	15.80	0.66	1.81	0.37	2.37	0.34
Salem diorite									
RM615	69.83	136.56	54.43	10.81	1.24	1.43	0.73	4.79	0.80
RM617	75.26	144.86	60.92	11.65	1.30	1.75	NA	4.12	0.62
Otjua red granite									
06	24.69	53.19	22.10	6.27	0.53	1.39	NA	4.93	0.81
Sorris-Sorris red granite									
RM666	75.17	159.11	67.88	14.01	1.04	1.83	NA	6.6	1.02
RM663	49.86	96.39	35.40	8.03	0.70	1.59	1.20	8.63	1.51
RM664	63.27	118.53	41.34	8.02	0.75	1.29	0.73	5.75	1.07
RM673	97.82	184.97	64.87	12.57	1.20	1.93	1.08	7.13	1.17
SOR 2203	181.10	321.40	98.70	15.32	1.43	2.04	1.21	8.91	1.25
Salem Goas granite									
R131	128.55	233.0	82.56	13.34	1.88	1.40	0.41	2.57	0.46
R133	70.08	127.86	44.92	7.78	1.41	0.92	0.31	1.87	0.34
Naauwpoort lavas									
KN2	210.0	406.8	204.03	38.80	7.90	3.59	1.30	8.65	1.38
KN10	116.0	233	114.2	22.10	4.41	2.94	1.46	9.41	1.51

	La	Ce	Nd	Sm	Eu	Tb	Tm	Yb	Lu
Kuiseb schists									
KH16	40.39	81.10	41.10	8.23	1.56	1.20	0.48	2.84	0.45
KH27	35.40	72.59	35.13	7.28	1.34	1.04	NA	0.70	0.62
Alaskites									
26/69/78m	5.95	9.29	3.30	0.86	0.75	0.29	NA	2.19	0.45
Ida 3/2	7.30	8.99	2.57	0.62	0.23	0.21	0.30	2.06	0.40
Ida 4/1	5.80	7.60	2.59	0.30	0.43	0.27	0.25	1.55	0.26
G0	5.07	6.90	1.33	0.48	0.67	0.16	NA	0.72	0.11
G9	24.61	40.16	8.64	1.37	0.77	0.64	0.44	3.347	0.57
Lofdal syenite									
28/29	57.16	99.54	31.28	4.91	1.24	0.59	NA	3.28	0.55
28/26	56.00	111.1	51.52	9.29	1.51	1.27	NA	5.04	0.85
Otjimbingwe syenite									
OT 2181	77.40	159.5	75.71	13.86	2.98	1.53	0.66	2.80	0.39
Otjosondjou diorite									
RM586	81.95	177.0	84.70	14.41	3.12	1.64	0.63	3.79	0.56
Swakopmund Salem granite									
SM2	53.71	111.6	49.97	9.69	1.11	1.33	0.67	4.88	0.75
Palmental diorite									
P 2177	59.25	115.7	58.24	10.72	2.58	1.21	0.41	2.74	0.42
P 2172	56.88	105.6	51.61	9.47	2.49	1.05	0.32	2.11	0.33
Donkerhuk granite									
R 73	20.93	44.78	20.61	4.95	1.05	0.92	0.34	2.21	0.34
R 100	47.58	98.20	45.05	9.75	1.01	1.40	0.77	4.55	0.71
R 114	20.55	42.42	20.19	4.72	0.85	0.78	0.19	1.45	0.21
S119	28.99	51.16	21.39	4.03	0.88	0.50	NA	1.08	0.17

B (ii) GRANITOID GEOCHRONOLOGY DATA

Sample	Rb	Sr	$^{87}Sr/^{86}Sr$	$^{87}Rb/^{86}Sr$
Huab-River diorite	"Age" = 862 ± 74 Ma		Ri = 0.7065 ± 0.0005	MSWD = 7.5
RM129.5	109	706	0.711923±18	0.4470
RM129.6	118	600	0.713360±19	0.5695
RM129.10*	119	943	0.709432±19	0.3653
RM129.11	104	689	0.711575±15	0.4370
RM129.12	98	786	0.711106±15	0.3610
RM129.13	126	580	0.714362±20	0.6292
Otjimbingwe syenite	"Age" = 403±14 Ma		Ri = 0.708598 ±0.0002	MSWD = 4.6
OSY 2179	412	1050	0.715219±18	1.1366
OSY 2181	419	679	0.718780±15	1.7880
OSY 2182	411	772	0.717474±11	1.5424
OSY1	355	1237	0.713580±13	0.8297
OSY 2	364	1268	0.713096±11	0.8317
OSY 3	369	1201	0.713848±18	0.9047
OSY 4	370	1350	0.713143±12	0.8004
Leucocratic Otjimbingwe syenite	Age = 513±48 Ma		Ri = 0.706654±0.00026 MSWD = 5.2	
OSY 7	164	1180	0.709675±16	0.4067
OSY 8	180	1236	0.709751±16	0.4183
OSY 9	191	1053	0.710758±13	0.5243
OSY 10	151	1165	0.709305±14	0.3815
OSY 11	152	1204	0.709038±12	0.3642
OSY 2183	118	1350	0.708651±18	0.2530
OSY 2184	117	1348	0.708547±19	0.2512
Swakop River diorite	Age = 451±27 Ma		Ri = 0.708903±0.00007	MSWD = 2.6
SRD1	138	1404	0.710682±15	0.2897
SRD 2	201	1626	0.711573±11	0.3634
SRD 3	172	1418	0.711229±20	0.3522
SRD 4	132	1469	0.710439±20	0.2609
P 2139	115	1151	0.710876±15	0.2893

GRANITOID GEOCHRONOLOGY DATA (Contd)

Sample	Rb	Sr	$^{87}Sr/^{86}Sr$	$^{87}Rb/^{86}Sr$
P 2140	47	1657	0.709486±19	0.0821
P 2141	65	1709	0.709598±13	0.1101
Palmental "roadside" diorite	"Age" = 568±53 Ma		Ri = 0.706979±0.00027	MSWD = 10
P 2092	94	839	0.709623±19	0.3243
P 2094	82	850	0.709265±20	0.2792
P 2095	110	835	0.709929±19	0.3814
P 2096	117	840	0.710300±19	0.4032
P 2097	129	902	0.710373±17	0.4140
Palmental granite	Age = 546 ±45 Ma		Ri = 0.719945±0.0059	MSWD = 1
PG 2174	298	95	0.791627±17	9.1628
PG 2175	311	93	0.795026±19	9.7616
PG 2176	298	93	0.793005±19	9.3517
PGR 1	299	98	0.788928±14	8.9008
PGR 2	300	99	0.788335±20	8.8399
PGR 3	310	97	0.792777±19	9.3269
PGR 7	301	97	0.790499±19	9.0541

B (iii) Granitoid Sr isotope data

Sample	Intrusion	Age	Rb	Sr	$^{87}Sr/^{86}Sr$	$^{87}Rb/^{86}Sr$
PGR 1	Palmental granite	546±45	299	98	0.788928	8.90
PGR 2	Palmental granite	546±45	300	99	0.788335	8.839
PGR 3	Palmental granite	546±45	310	97	0.792777	9.327
PGR 5	Palmental granite	546±45	363	1255	0.792531	0.844
PGR 7	Palmental granite	546±45	301	97	0.790499	9.054
PG 2174	Palmental granite	546±45	298	95	0.791627	9.164
PG 2175	Palmental granite	546±45	311	93	0.795026	3.124
R 73	Donkerhuk granite	521±15	130	102	0.752667	3.705
R110	Donkerhuk granite	521±15	150	172	0.73089	2.53
R115	Donkerhuk granite	521±15	174	83	0.75760	6.12
S118	Donkerhuk granite	523±8	75	229	0.7144	0.95
S119	Donkerhuk granite	521±15	98	275	0.71524	1.032
KND 1.1	Bloedkoppie granite	510±9	259	95	0.77456	7.927
KND 1.5	Bloedkoppie granite	510±9	233	55	0.80768	12.381
LS9	L. Stinkbank granite	601±79	197	104	0.76011	5.467
S1	Stinkbank leucogranite	486±31	380	66	0.85585	16.83
S7	Stinkbank leucogranite	486±31	349	73	0.83405	14.02
O6	Otjua red granite	516±23	279	84	0.79397	9.87
O2	Otjua red granite	516±23	275	80	0.79782	10.04
Ida 4/2	Ida dome alaskite	542±33	207	132	0.75742	4.56
26/59155	Valencia alaskite	495±12	257	128	0.76389	5.94
DG 58	Rossing alaskite	458±8	334	28	0.98537	35.46
Ros 5	Rossing alaskite	458±8	342	33	0.913674	30.601
Ros 7	Rossing alaskite	458±8	287	26	0.943933	32.69
G0	Goanikontes alaskite	508±2	458	166	0.78690	7.81
G9	Goanikontes alaskite	508±2	347	86	0.82439	11.74

Sample	Intrusion	Age	Rb	Sr	$^{87}Sr/^{86}Sr$	$^{87}Rb/^{86}Sr$
R 131	Salem Goas	515±20	254	287	0.73571	2.598
R 133	Salem Goas	515±20	171	249	0.73153	2.046
GG11	Salem Onanis	554±33	129	237	0.72402	1.548
P 2172	Palmental diorite	(650)	131	1113	0.709289	0.341
P 2186	Palmental diorite	(650)	168	1175	0.709869	0.414
P 2094	Palmental diorite	568±53	82	850	0.709265	0.279
P 2097	Palmental diorite	568±53	129	902	0.710373	0.414
P 2140	Swakop river diorite	(650)	47	1657	0.709486	0.082
SRD 1	Swakop River diorite	(650)	140	1399	0.710695	0.289
SRD 2	Swakop river diorite	(650)	201	1615	0.711573	0.361
SRD 3	Swakop River diorite	(650)	173	1422	0.711229	0.352
RM 586	Salem Otjosondjou diorite	548±31	71	1045	0.70636	0.197
RM 662	Sorris-Sorris granite	495±15	219	213	0.72941	3.01
RM 664	Sorris-Sorris granite	495±15	321	98	0.77542	9.26
RM 654	Sorris-Sorris granite	495±15	240	167	0.73855	4.17
RM 673	Sorris-Sorris granite	495±15	279	117	0.75756	6.63
Sor 2203	Sorris-Sorris granite	495±15	215	131	0.760385	4.680
Sor 2204	Sorris-Sorris granite	495±15	216	134	0.739826	4.68
RM 666	Sorris-Sorris granite	495±15	232	106	0.75384	6.38
OSY 2179	Otjimbingwe syenite	(650)	412	1050	0.715219	1.137
OSY 2181	Otjimbingwe syenite	(650)	419	679	0.718790	1.788
OSY 2182	Otjimbingwe syenite	(650)	411	772	0.717474	1.543
OSY 1	Otjimbingwe syenite	(650)	355	1237	0.713524	0.829
OSY 3	Otjimbingwe syenite	(650)	369	1181	0.713848	0.905
OSY 4	Otjimbingwe syenite	(650)	372	1346	0.713143	0.80
OSY 5	Otjimbingwe syenite	(650)	263	957	0.713629	0.796
OSY 6	Otjimbingwe syenite	(650)	192	1054	0.709554	0.527
B2	Basement orthogneiss	~2.0 Ga	329	159	0.82150	6.039
YC7	Horebis river red granite	633±40	143	53	0.78465	7.834
SM2	Salem Swakopmund	563±63	186	132	0.74077	4.199

Sample	Intrusion	Age	Rb	Sr	$^{87}Sr/^{86}Sr$	$^{87}Rb/^{86}Sr$
OSY 7	L.Otjimbingwe syenite	513±48	164	1167	0.709675	0.407
OSY 8	L.Otjimbingwe syenite	513±48	179	1239	0.709751	0.418
OSY 9	L.Otjimbingwe syenite	513±48	192	1060	0.710758	0.514
OSY 10	L.Otjimbingwe syenite	513±48	157	1191	0.709305	0.382
OSY 11	L. Otjimbingwe syenite	513±48	153	1216	0.709038	0.364
OD 1	L. Otjimbingwe syenite	513±48	191	1327	0.710350	0.417
OD 2	L. Otjimbingwe syenite	513±48	136	1140	0.710259	0.345
OD 3	L. Otjimbingwe syenite	513±48	102	1471	0.709449	0.20
RM129.5	Huab-River diorite	570±20	109	706	0.711923±18	0.4470
RM129.6	Huab-River diorite	570±20	118	600	0.713360±19	0.5695
RM129.10*	Huab-River diorite	570±20	119	943	0.709432±19	0.3653
RM129.11	Huab-River diorite	570±20	104	689	0.711575±15	0.4370
RM129.12	Huab-River diorite	570±20	98	786	0.711106±15	0.3610
RM129.13	Huab-River diorite	570±20	126	580	0.714362±20	0.6292

B (iv) Granitoid Nd data

Sample	Intrusion	Age	Sm	$Nd^{143}Nd/^{144}Nd$		DM model age
YC7	Horebis river red granite	633±40	11.8	66	0.51227	1.13Ga
R 131	Salem Goas	515±20	13.34	83.23	0.51158	1.93Ga
R 133	Salem Goas	515±20	7.78	45.26	0.51159	2.05Ga
GG11	Salem Onanis	554±33	3.86	27.9	0.51180	1.46Ga
R 73	Donkerhuk granite	521±15	4.95	20.61	0.511763	2.93Ga
R110	Donkerhuk granite	521±15	3.59	18.4	0.51200	1.67Ga
R115	Donkerhuk granite	521±15	6.07	23.9	0.51226	2.00Ga
S118	Donkerhuk granite	523±8	4.42	25.3	0.51220	1.19Ga
S119	Donkerhuk granite	521±15	4.03	21.82	0.512247	1.19Ga
KND 1.1	Bloedkoppie granite	510±9	9.63	51.54	0.51184	1.83Ga
KND 1.5	Bloedkoppie granite	510±9	0.96	4.42	0.51193	2.08Ga
LS9	L. Stinkbank granite	601±79	2.99	17.5	0.51170	1.87Ga
S1	Stinkbank leucogranite	486±31	11.3	63.1	0.51149	2.27Ga
S7	Stinkbank leucogranite	486±31	11.7	64	0.51145	2.38Ga
O6	Otjua red granite	516±23	6.27	28.97	0.51166	-
O2	Otjua red granite	516±23	4.53	17.7	0.51167	-
Ida 4/2	Ida dome alaskite	542±33	1.02	3.01	0.51192	1.19Ga
26/59155	Valencia alaskite	495±12	4.73	21.6	0.51170	2.56Ga
DG 58	Rossing alaskite	458±8	1.44	7.04	0.51155	2.57Ga
Ros 5	Rossing alaskite	458±8	1.84	5.54	0.511789	-
Ros 7	Rossing alaskite	458±8	2.35	7.65	0.511787	-
G0	Goanikontes alaskite	508±2	0.643	2.98	0.51186	2.19Ga
G9	Goanikontes alaskite	508±2	4.18	30.9	0.51153	1.75Ga
R 131	Salem Goas	515±20	13.34	83.23	0.51158	1.93Ga
R 133	Salem Goas	515±20	7.78	45.26	0.51159	2.05Ga
GG11	Salem Onanis	554±33	3.86	27.9	0.51180	1.46Ga
P 2172	Palmental diorite	(650)	9.47	51.61	0.512129	1.36Ga
P 2186	Palmental diorite	(650)	6.96	41.5	0.511954	1.45Ga
P 2094	Palmental diorite	568±53	9.56	52.8	0.512078	1.42Ga
P 2097	Palmental diorite	568±53	6.81	34.5	0.512003	1.69Ga
P 2140	Swakop river diorite	(650)	8.71	50.2	0.511897	1.61Ga

Sample	Intrusion	Age	Sm	Nd	$^{143}Nd/^{144}Nd$	DM model age
RM 586	Salem Otjosondjou diorite	548±31	14.1	79	0.512291	1.09Ga
RM 129.6	Huab-River diorite	570±20	8.62	53	0.511903	1.51Ga
RM 129.13	Huab-River diorite	570±20	7.85	49.6	0.511870	1.52Ga
RM 662	Sorris-Sorris granite	495±15	14.5	101	0.51176	1.55Ga
RM 664	Sorris-Sorris granite	495±15	8.02	46.93	0.51175	2.06Ga
RM 654	Sorris-Sorris granite	495±15	9.48	51.7	0.51152	2.28Ga
RM 673	Sorris-Sorris granite	495±15	12.57	67.25	0.51184	1.92Ga
Sor 2203	Sorris-Sorris granite	495±15	15.32	98.7	0.512094	1.21Ga
Sor 2204	Sorris-Sorris granite	495±15	13.0	80.4	0.512149	1.18Ga
RM 666	Sorris-Sorris granite	495±15	14.01	71.17	0.51208	1.65Ga
OSY 2179	Otjimbingwe syenite	(650)	20.5	110	0.512198	1.28Ga
OSY 2181	Otjimbingwe syenite	(650)	20.9	110	0.512227	1.27Ga
OSY 2182	Otjimbingwe syenite	(650)	17.4	88.9	0.512164	1.41Ga
B2	Basement orthogneiss	~2.0 Ga	10.9	58.8	0.51129	2.66Ga
YC7	Horebis river red granite	633±40	11.8	66.0	0.51227	1.13Ga
SM2	Salem Swakopmund	563±63	7.79	41.2	0.51211	1.44Ga

B (v) Metasediment isotope data

Sample	Unit	$^{87}Sr/^{86}Sr$	$^{143}Nd/^{144}Nd$	Rb	Sr	Sm	Nd
CHN 1	Nama metasediment	0.75460	0.51213	82	77	4.61	21.5
CHN 5	Nama metasediment	0.71117		7	373		
CHN 6	Nama metasediment		0.51201	356	64	10.1	55.6
CHN 8	Nama metasediment	0.74043	0.51209	121	105	8016	40.3
CHN 9	Nama metasediment	0.73409	0.51209	58	64	4.17	21.6
CHN 17	Nama metasediment	0.82224	0.51208	175	37		
CHN 22	Nama metasediment	0.76080	0.51202	123	63		
CHN 27	Nama metasediment	0.73375	0.51188	73	128		
TS 2316	Nama metasediment	0.73834	0.51215	135	122	9.98	48.2
TS 2842	Nama metasediment	0.75422	0.51210	102	59		
TS 2874	Nama metasediment	0.75237	0.51212	119	68		
TS 3921	Nama metasediment	0.76792	0.51210	154	70		
Kh 11	Kuiseb schist	0.74252		171	139		
Kh 14	Kuiseb schist	0.75458		195	113		
Kh 15	Kuiseb schist	0.75177		196	121		

Sample	Unit	$^{87}Sr/^{86}Sr$	$^{143}Nd/^{144}Nd$	Rb	Sr	Sm	Nd
Kh 16	Kuiseb schist	0.75713	0.51220	142	82	8.23	41.1
Kh 17	Kuiseb schist	0.73745		106	102		
Kh 18	Kuiseb schist	0.75832		155	85		
Kh 20	Kuiseb schist	0.72838		76	150		
Kh 21	Kuiseb schist	0.73102		78	123		
Kh 22	Kuiseb schist	0.73661		123	118		
Kh 23	Kuiseb schist	0.73606		131	116		
Kh 24	Kuiseb schist	0.72817	0.51218	78	139	9.8	46.9
Kh 25	Kuiseb schist	0.75848		95	58		
Kh 26	Kuiseb schist	0.72762		37	206		
Kh 27	Kuiseb schist	0.74592	0.51214	81	65	7.28	35.13
Kh 28	Kuiseb schist	0.75052		89	63		
Kh 523	Kuiseb schist	0.73380	0.51221	93	101		
Kh 529	Kuiseb schist	0.72948	0.51222	94	134		
Chert	Matchless	0.93422	0.51215	77	7	6.03	32.3
560 Ros	Rossing	0.71172	0.51177	187	1197	1.51	7.9
DG 77	Karibib	0.73720	0.51223			5.96	29.2
G 12	Khan	0.75224	0.51179				
G 13	Khan	0.79724	0.51171	302	109	6.31	32.9
554	Khan	0.81886	0.51151	431	117	10.7	65.3
2159	Khan	0.78002		290	173	7.88	43.5
1009	Khan	0.79120		229	75	8.93	46.0
014	Etusis	0.80622	0.51146	116	42	0.344	1.86
015	Etusis	0.89805	0.51147	149	30	3.95	22.3
E 2	Etusis	0.79950	0.51154	108	73	3.44	19.5
E 8	Etusis	0.81805	0.51154	161	80	4.84	27.2
Lc	pre-Damara basement	0.79852	0.51108			8.89	62.6
B 2	pre-Damara basement	0.82150	0.51129	329	159	10.9	58.8

B (vi) Quartz separate - oxygen isotope data

Sample number	Intrusion	$\delta^{18}O$ ‰
Crustal melt granitoids		
PG 2175	Palmental granite	14.54
V 10	Valencia Salem-type	10.49
BL 1	Bloedkoppie granite	13.33
Ida I/2	Ida-dome alaskite	10.88
S7	Stinkbank leucogranite	10.54
S1	Stinkbank leucogranite	9.82
03	Otjuo red granite	10.70
O9	Otjua red granite	11.89
Calc-alkaline diorites		
P 2172	Palmental diorite	11.18
P 2140	Palmental diorite	12.41
Within-plate granitoids		
OT 2182	Otjimbingwe syenite	11.40
OT 2181	Otjimbingwe syenite	11.08
OT 2179	Otjimbingwe syenite	10.63
YC 3	Horebis-river granite	8.82
YC 6	Horebis-river granite	8.66

B (vii) Whole - rock Pb data

Sample		$^{206}Pb/^{204}Pb$	$^{207}Pb/^{204}Pb$	$^{208}Pb/^{204}Pb$
Crustal - melt granitoids				
R 73	Donkerhuk granite	19.531± 0.002	15.747 ±0.002	38.548 ±0.005
PG 2175	Palmental granite	17.585 ±0.001	15.638 ±0.001	39.641 ±0.002
ROS 5*	Rossing alaskite	134.776 ±0.014	22.460 ±0.003	42.134 ±0.005
Calc-alkaline diorites				
P2139	Swakop - river diorite	19.216 ±0.002	15.718 ±0.002	39.987 ±0.005
P 2140	Swakop - river diorite	21.122 ±0.003	15.816 ±0.002	40.373 ±0.001
P 2141	Swakop - river diorite	17.598 ±0.001	15.639 ±0.001	40.000 ±0.001
P2092	Palmental diorite	18.164 ±0.004	15.649 ±0.004	39.267 ±0.013
P 2094	Palmental diorite	18.095 ±0.005	15.604 ±0.004	39.146 ±0.011
P 2095	Palmental diorite	18.628 ±0.001	15.693 ±0.001	39.841 ±0.003
P 2096	Palmental diorite	19.497 ±0.013	15.668 ±0.009	40.929 ±0.028
P 2097	Palmental diorite	18.478 ±0.006	15.654 ±0.005	39.655 ±0.013
Within-plate granitoids				
OT 2179	Otjimbingwe syenite	20.090 ±0.003	15.780 ±0.003	40.486 ±0.008
OT2180	Otjimbingwe syenite	20.301 ±0.005	15.778 ±0.004	40.465 ±0.012
OT2181	Otjimbingwe syenite	20.024 ±0.003	15.761 ±0.002	40.430 ±0.001
OT2182	Otjimbingwe syenite	20.192 ±0.001	15.775 ±0.001	40.365 ±0.003
S 2203	Sorris-Sorris granite	20.768 ±0.007	15.754 ±0.006	44.366 ±0.018
S 2204	Sorris-Sorris granite	20.264 ±0.003	15.740 ±0.003	43.767 ±0.008
28/27A	Lofdal syenite	24.160 ±0.002	15.963 ±0.002	37.988 ±0.004
28/34	Lofdal syenite	24.186 ±0.003	15.964 ±0.002	40.720 ±0.005

* Denotes sample from the U mineralised Rossing alaskite.

B (viii) Feldspar Pb data

Sample		$^{206}Pb/^{204}Pb$	$^{207}Pb/^{204}Pb$	$^{208}Pb/^{204}Pb$
Crustal - melt granitoids				
ROS 5*	Rossing alaskite	28.099 ±0.003	16.270 ±0.002	39.617 ±0.004
ROS 7*	Rossing alaskite	46.749 ±0.002	17.321 ±0.001	40.102 ±0.002
R 114	Donkerhuk granite	18.357 ±0.001	15.685 ±0.001	38.043 ±0.002
G 0	Goanikontes alaskite	18.352 ±0.003	15.664 ±0.003	38.508 ±0.006
V3	Valencia alaskite	17.762 ±0.005	15.647 ±0.001	38.367 ±0.002
O9	Otjua red granite	21.561 ±0.001	16.187 ±0.001	38.441 ±0.002
S1	Stinkbank leucogranite	17.920 ±0.001	15.680 ±0.001	38.670 ±0.002
PG 2175	Palmental granite	17.293 ±0.001	15.611 ±0.001	38.163 ±0.002
GG5	Salem Onanis granite	17.444 ±0.003	15.639 ±0.003	38.103 ±0.007
Calc-alkaline diorites				
129.13		17.808 ±0.001	15.645 ±0.001	38.238 ±0.001
P 2186		17.719 ±0.001	15.640 ±0.001	38.341 ±0.002
P 2094		17.724 ±0.001	15.647 ±0.001	38.745 ±0.002
Within-plate granitoids				
OT 2181	Otjimbingwe syenite	18.289 ±0.001	15.681 ±0.001	38.737 ±0.003
OT 2182	Otjimbingwe syenite	18.716 ±0.005	15.665 ±0.004	39.013 ±0.012
S 2204	Sorris - Sorris granite	18.725 ±0.001	15.683 ±0.001	39.451 ±0.002
NN 10	Naauwpoort volcanics	17.833 ±0.006	15.544 ±0.005	37.536 ±0.012
28/41	Lofdal syenite	18.135 ±0.003	15.638 ±0.003	38.433 ±0.009
1013	Dachsberg granite	24.753 ±0.015	16.109 ±0.009	45.558 ±0.032
YC 3	Horebis - river granite	18.782 ±0.003	15.729 ±0.002	39.136 ±0.007
YC 6	Horebis - river granite	19.490 ±0.002	15.807 ±0.001	39.949 ±0.004
UIS2210	Uis Sn pegmatite	23.626 ±0.006	15.932 ±0.004	37.869 ±0.010

* Denotes sample from the U mineralised Rossing alaskite.